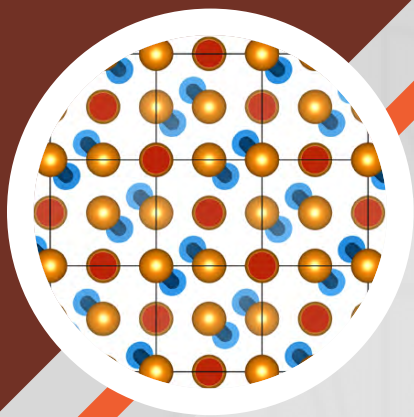
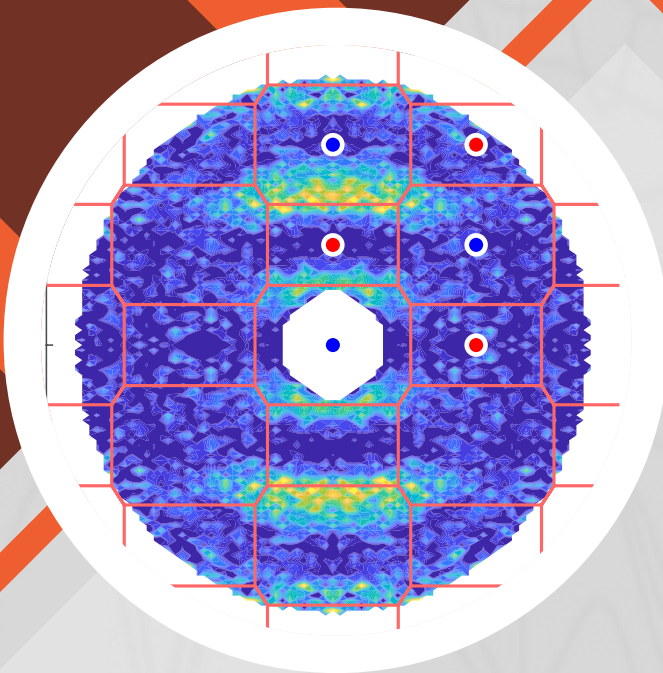




Check for
updates

NIST SP 1284



NIST
National Institute of
Standards and Technology
U.S. Department of Commerce

ACCOMPLISHMENTS AND OPPORTUNITIES

2022

NIST CENTER FOR NEUTRON RESEARCH



ON THE COVER

The NCNR's neutron source provides a valuable research tool for a wide variety of scientific fields from biological systems, engineering materials, to magnetic structures, and more. The cover features data from only a few of the experiments highlighted in this report.

NIST SPECIAL PUBLICATION 1284

2022 NIST Center for Neutron Research Accomplishments and Opportunities

Robert M. Dimeo, Director

Steven R. Kline, Editor

This publication is available free of charge from:

<https://doi.org/10.6028/NIST.SP.1284>

DECEMBER 2022



U.S. Department of Commerce
Gina M. Raimondo, Secretary

National Institute of Standards and Technology
Laurie E. Locascio, NIST Director and Under Secretary of Commerce for Standards and Technology

DISCLAIMER

Certain commercial entities, equipment, or materials may be identified in this document in order to describe an experimental procedure or concept adequately. Such identification is not intended to imply recommendation or endorsement by the National Institute of Standards and Technology, nor is it intended to imply that the entities, materials, or equipment are necessarily the best available for the purpose. Throughout the text, unless otherwise stated, q (or Q) refers to the momentum transfer. Error bars in figures and uncertainties in the text represent one standard deviation unless otherwise stated.

National Institute of Standards and Technology Special
Publication 1284, 87 pages (December 2022)
CODEN: NSPUE2

This publication is available free of charge from:
<https://doi.org/10.6028/NIST.SP.1284>

Table of Contents

2 FOREWORD

3 THE NIST CENTER FOR NEUTRON RESEARCH

4 NIST CENTER FOR NEUTRON RESEARCH INSTRUMENTS

BIOSCIENCES

- 6 Molecular origins of two-dimensional membrane viscosity measured by neutron and X-ray spectroscopies, M. Nagao, *et al.* (CHRNS)
- 8 *In-situ* monitoring of protein unfolding/structural states under cold high-pressure stress, D. C. Gomes, *et al.* (CHRNS)
- 10 Small-angle neutron scattering provides insight into the self-association of lactate dehydrogenase during freeze-thaw in buffered solutions, J. Sonje, *et al.* (CHRNS)
- 12 Probing protein-protein interactions in monoclonal antibody formulations with neutrons, A. Y. Xu, *et al.*

CHEMICAL PHYSICS

- 14 Dynamics of molecular associates in methanol water mixtures, Y. Zhai, *et al.* (CHRNS)
- 16 Aluminium formate, $\text{Al}(\text{HCOO})_3$: an Earth-abundant, scalable and highly-selective material for CO_2 capture, H. A. Evans, *et al.*

CONDENSED MATTER

- 18 Weyl-mediated helical magnetism in NdAlSi , J. Gaudet, *et al.* (CHRNS)
- 20 Magnetic fields induce a topological electronic transition leading to a new geometry for thermoelectric conversion in the itinerant ferromagnet $\text{Fe}_{3-x}\text{GeTe}_2$, P. P. Balakrishnan, *et al.*
- 22 Magnetic excitations: a window into the electronic interactions in a spin-triplet superconductor, N. P. Butch, *et al.* (CHRNS)
- 24 Chemical origin of magnetic dead shells in Ni nanoparticles deduced from polarized small-angle neutron scattering, B. Das. *et al.* (CHRNS)

ENGINEERING PHYSICS

- 26 Characteristic rotation of principal stress axes after friction stir welding, T. Gnäupel-Herold, *et al.*
- 28 Exploring microstructure development of tricalcium silicate for additive manufacturing in construction using rheoSANS, A. J. Allen, *et al.* (CHRNS)
- 30 NeXT provides insight on the durability of concrete structures, L. E. Dalton, *et al.*

GEOLOGY

- 32 Probing oil recovery in shale nanopores with small- and ultra-small-angle neutron scattering, C. W. Neil, *et al.* (CHRNS)

INSTRUMENTATION

- 34 High-flux, high-resolution neutron reflectometry with CHRNS CANDOR, D. P. Hoogerheide, *et al.* (CHRNS)
- 36 Upgrade of the BT-8 diffractometer for stress and texture, T. Gnäupel-Herold, *et al.*

NEUTRON PHYSICS

- 38 Pendellösung interferometry probes the neutron charge radius, lattice dynamics, and fifth forces, B. Heacock, *et al.*

SOFT MATTER

- 40 Structural and dynamical roles of bound polymer chains in rubber reinforcement, D. Salatto, *et al.* (CHRNS)
- 42 Neutron scattering techniques yield insight into the structure and dynamics of computationally designed coiled coil bundlemers and their supramolecular 1-D assemblies, N. J. Sinha, *et al.* (CHRNS)
- 44 Predicting the plateau modulus from molecular parameters of conjugated polymers, A. M. Fenton, *et al.*
- 46 Polymer architecture can change dynamics of polymer nanocomposites, S. Darvishi, *et al.* (CHRNS)
- 48 Understanding temperature dependent shear thinning of catalyst inks for fuel cells using small-angle neutron scattering, W. Yoshimune and M. Harada (*nSoft*)

ADVANCES IN MEASUREMENT

- 50 A versatile stopped-flow sample environment for time-resolved SANS studies, E. G. Kelley, *et al.* (CHRNS)
- 51 Large-area TKIDs for charged particle detection in neutron beta decay and beyond, E. M. Scott, *et al.*
- 52 ANDiE the autonomous neutron diffraction explorer, A. McDannald, *et al.*
- 53 Streamlining small-angle neutron scattering data collection under extreme conditions, C. V. L. Gagnon, *et al.*

54 NEUTRON SOURCE OPERATIONS

55 FACILITY DEVELOPMENT

58 SERVING THE SCIENCE AND TECHNOLOGY COMMUNITY

61 THE CENTER FOR HIGH RESOLUTION NEUTRON SCATTERING (CHRNS)

70 2022 AWARDS

74 PUBLICATIONS: AUGUST 1, 2021 TO JULY 31, 2022

86 INSTRUMENTS AND CONTACTS

87 NIST CENTER FOR NEUTRON RESEARCH CONTACTS

Foreword

In 2022, work continued towards restarting the reactor and the scientific program. Areas of focus included engaging with the Nuclear Regulatory Commission (NRC), implementing comprehensive corrective actions to prevent recurrence of the 2021 fuel damage event, and restoring the reactor to operational readiness.

In March, the NRC issued a final Special Inspection Report and, in August a Confirmatory Order. The Order did not present any showstoppers to restart and did not include a notice of cited violations. It did include several additional requirements for reactor operations at the NCNR which are currently being implemented.

At this time, the primary cooling system of the reactor, which was contaminated in the incident, has been cleaned sufficiently to allow the reactor to operate. Also, the corrective actions required to restart the reactor are complete. This includes revisions to many operational procedures, enhancements in training and proficiency assessments, implementation of a program supporting a healthy nuclear safety culture, and improvements in verifying that reactor refueling has been performed properly, thus preventing recurrence of the fuel damage incident. We are confident that the reactor is ready to operate safely.

The outage to upgrade the cold source and some neutron guides, originally scheduled for 2023, has been postponed until after the reactor operates for several cycles. Though this delays the implementation of significant performance increases, it allows us to restart the reactor when we receive authorization from the NRC. This delay will be used to accelerate the installation of the Neutron Spin Echo instrument being constructed by the University of Delaware and funded by the NSF.

The research produced by NCNR users and staff was excellent as evidenced by the highlights in this report. I am pleased to share this impressive work as well as details on facility developments. Thank you all for continued support as we progress towards restart.



The NIST Center for Neutron Research

Neutrons provide a uniquely effective probe of the structure and dynamics of materials ranging from water moving near the surface of proteins to magnetic domains in memory storage materials. The properties of neutrons (outlined below) can be exploited using a variety of measurement techniques to provide information not otherwise available. The positions of atomic nuclei in crystals, especially of those of light atoms, can be determined precisely. Atomic motion can be directly measured and monitored as a function of temperature or pressure. Neutrons are especially sensitive to hydrogen, so that hydrogen motion can be followed in H-storage materials and water flow in fuel cells can be imaged. Residual stresses such as those deep within oil pipelines or in highway trusses can be mapped. Neutron-based measurements contribute to a broad spectrum of activities including engineering, materials development, polymer dynamics, chemical technology, medicine, and physics.

The NCNR's neutron source provides the intense, conditioned beams of neutrons required for these types of measurements. In addition to the thermal neutron beams from the heavy water moderator, the NCNR has two liquid hydrogen moderators, or cold sources which supply neutrons to three-fourths of the instruments. One is a large area moderator and the other is smaller, but with high brightness. These moderators provide long wavelength guided neutron beams for industrial, government, and academic researchers.

There are currently 30 experiment stations: 12 are used for neutron physics, analytical chemistry, or imaging, and 18 are beam facilities for neutron scattering research. The subsequent pages provide a schematic description of our instruments. More complete descriptions can be found at <https://www.nist.gov/ncnr/neutron-instruments>.

The Center supports important NIST measurement needs but is also operated as a major national user facility with merit-based access made available to the entire U.S. technological community. Each year, approximately 2000 research participants from government, industry, and academia from all areas of the country are served by the facility (see pp. 58). Beam time for research to be published in the open literature is without cost to the user, but full operating costs are recovered for proprietary research. Access is gained mainly through a web-based, peer-reviewed proposal system with user time allotted by a beamtime allocation committee twice a year. For details see <https://www.nist.gov/ncnr/obtaining-beam-time>. The National Science Foundation and NIST co-fund the Center for High Resolution Neutron Scattering (CHRNS) that currently operates five of the world's most advanced instruments (see pp. 61). Time on CHRNS instruments is made available through the proposal system. Some access to beam time for collaborative measurements with the NIST science staff can also be arranged on other instruments.

WHY NEUTRONS?

Neutrons reveal properties not readily probed by photons or electrons. They are electrically neutral and therefore easily penetrate ordinary matter. They behave like microscopic magnets, propagate as waves, can set particles into motion, losing or gaining energy and momentum in the process, and they can be absorbed with subsequent emission of radiation to uniquely fingerprint chemical elements.

WAVELENGTHS – in practice range from ≈ 0.01 nm (thermal) to ≈ 1.5 nm (cold) ($1 \text{ nm} = 10 \text{ \AA}$), allowing the formation of observable interference patterns when scattered from structures as small as atoms to as large as biological cells.

ENERGIES – of millielectronvolts, the same magnitude as atomic motions. Exchanges of energy as small as nanoelectronvolts and as large as tenths of electronvolts can be detected between samples and neutrons, allowing motions in folding proteins, melting glasses and diffusing hydrogen to be measured.

SELECTIVITY – in scattering power varies from nucleus to nucleus somewhat randomly. Specific isotopes can stand out from other isotopes of the same kind of atom. Specific light atoms, difficult to observe with X-rays, are revealed by neutrons. Hydrogen, especially, can be distinguished from chemically equivalent deuterium, allowing a variety of powerful contrast techniques.

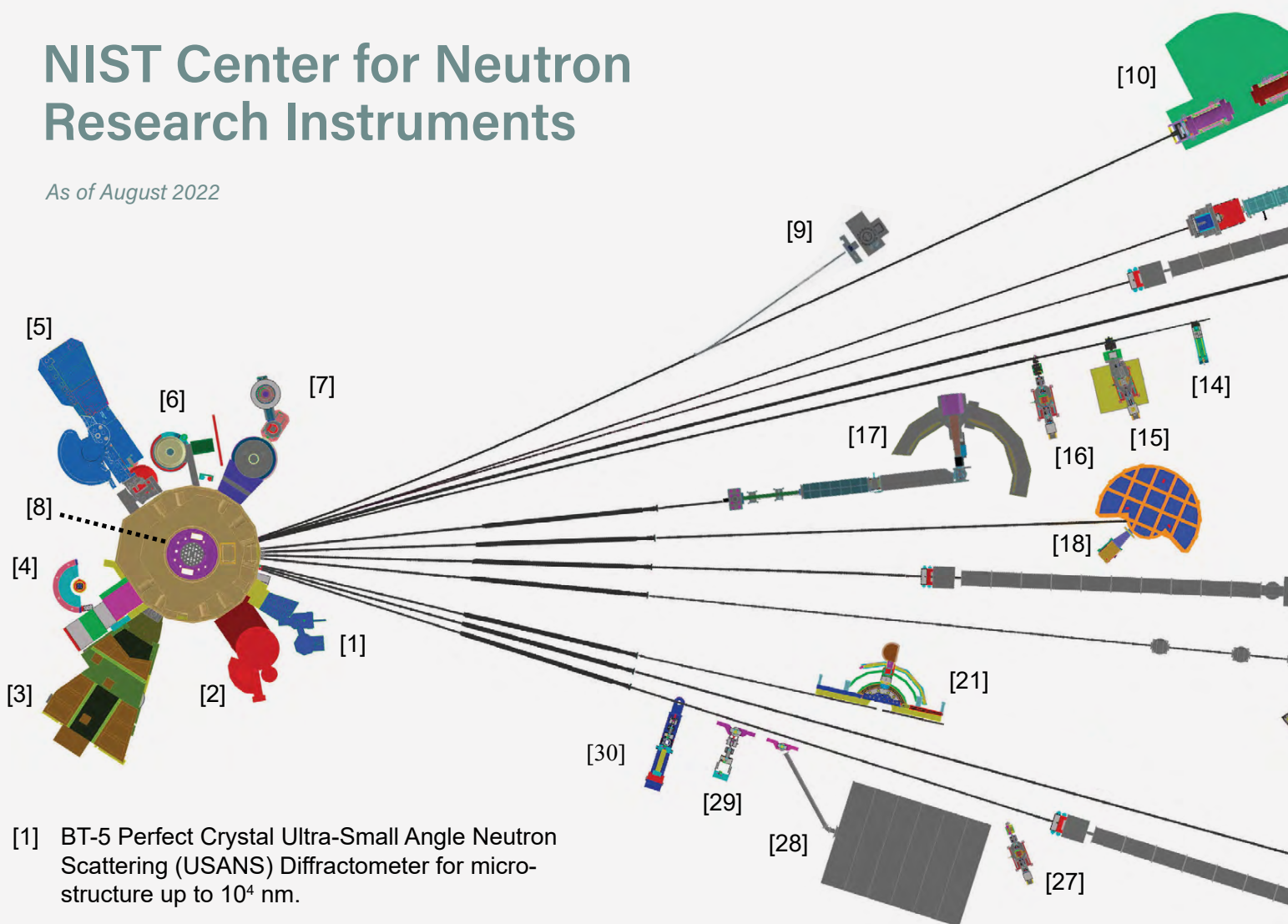
MAGNETISM – makes the neutron sensitive to the magnetic moments of both nuclei and electrons, allowing the structure and behavior of ordinary and exotic magnetic materials to be detailed precisely.

NEUTRALITY – of the uncharged neutrons allows them to penetrate deeply without destroying samples, passing through walls that condition a sample's environment, permitting measurements under extreme conditions of temperature and pressure.

CAPTURE – characteristic radiation emanating from specific nuclei capturing incident neutrons can be used to identify and quantify minute amounts of elements in samples as diverse as ancient pottery shards and lake water pollutants.

NIST Center for Neutron Research Instruments

As of August 2022



[1] BT-5 Perfect Crystal Ultra-Small Angle Neutron Scattering (USANS) Diffractometer for micro-structure up to 10^4 nm.

[2] BT-4 Filter Analyzer Neutron Spectrometer with cooled Be/Graphite filter analyzer for chemical spectroscopy and thermal triple axis spectrometer.

[3] BT-2 Neutron Imaging Facility for imaging hydrogenous matter in large components such as water in fuel cells and lubricants in engines, in partnership with General Motors and DOE.

[4] BT-1 Powder Diffractometer with 32 detectors; incident wavelengths of 0.208 nm, 0.154 nm, and 0.120 nm, with resolution up to $\Delta d/d \approx 8 \times 10^{-4}$.

[5] BT-9 Multi Axis Crystal Spectrometer (MACS II), a cold neutron spectrometer for ultra high sensitivity access to dynamic correlations in condensed matter on length scales from 0.1 nm to 50 nm and energy scales from 2.2 meV to 20 meV.

[6] BT-8 Engineering Diffractometer optimized for depth profiling of residual stresses in large components.

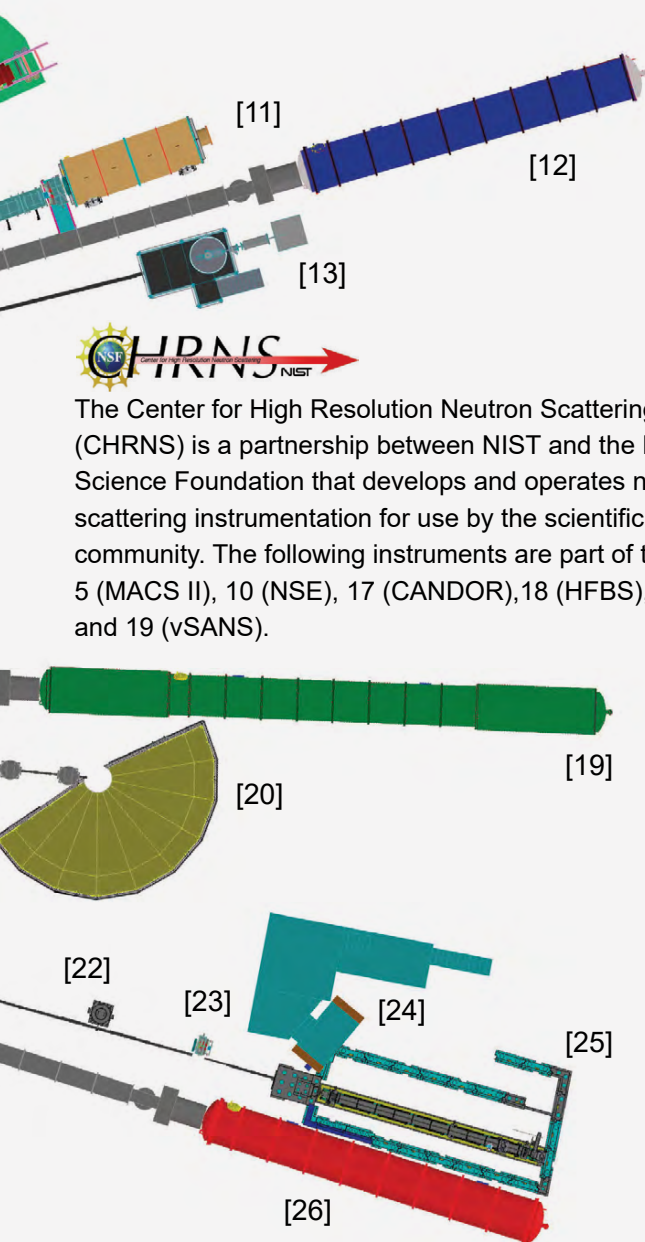
[7] BT-7 Thermal Triple Axis Spectrometer with large double focusing monochromator and interchangeable analyzer/detectors systems.

[8] VT-5 Thermal Neutron Capture Prompt Gamma-ray Activation Analysis Instrument used for quantitative elemental analysis of bulk materials including highly hydrogenous materials ($\approx 1\%$ H) such as foods, oils, and biological materials.


[9] NG-A' Cold Neutron Depth Profiling for profiling of subsurface elemental composition.


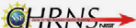

[10] NG-A Neutron Spin-Echo Spectrometer (NSE) for measuring dynamics from 5 ps to 100 ns.





The Center for High Resolution Neutron Scattering (CHRNS) is a partnership between NIST and the National Science Foundation that develops and operates neutron scattering instrumentation for use by the scientific community. The following instruments are part of the Center: 5 (MACS II), 10 (NSE), 17 (CANDOR), 18 (HFBS), and 19 (vSANS).

- [11] NG-B 10 m SANS for macromolecular structure measurements. 
- [12] NG-B 30 m SANS for microstructure measurements.
- [13] NG-C Neutron lifetime experiment.
- [14] NG-D Cold neutron capture Prompt Gamma Activation Analysis, for quantitative elemental analysis of bulk materials
- [15] NG-D MAGIK off-specular reflectometer for studies of thin-film samples with in-plane structure.

- [16] NG-D Polarized Beam Reflectometer (PBR) for measuring reflectivities as low as 10^{-8} to determine subsurface structure.
- [17] NG-1 CANDOR Chromatic Analysis Diffractometer or Reflectometer, capable of high throughput measurements. 
- [18] NG-2 Backscattering Spectrometer (HFBS), high intensity inelastic scattering instrument with energy resolution $< 1 \mu\text{eV}$ for studies of motion in molecular and biological systems. 
- [19] NG-3 VSANS for single measurement investigation of lengths from 1 nm to 2 micron. 
- [20] NG-4 Disk Chopper Time-of-Flight Spectrometer for diffusive motions and low energy dynamics. Wavelengths from $\approx 0.18 \text{ nm}$ to 2.0 nm and energy resolutions from $\approx 2 \text{ meV}$ to $< 10 \mu\text{eV}$.
- [21] NG-5 Spin-Polarized Triple Axis Spectrometer (SPINS) using cold neutrons with position sensitive detector capability for high-resolution studies.
- [22] NG-6 Precision measurement of the magnetic dipole moment of the neutron.
- [23] NG-6 Precision measurement of neutron flux.
- [24] NG-6 LAND detector development, neutron source calibration, and neutron cross section measurement
- [25] NG-6 Cold Neutron Imaging Facility for imaging hydrogenous matter in large components such as water in fuel cells and lubricants in engines.
- [26] NG-7 30 m SANS for microstructure measurements, in partnership with ExxonMobil and University of Minnesota's IPrime.
- [27] NG-7 PHADES Cold neutron test station.
- [28] NG-7 Neutron Interferometry and Optics Station with perfect crystal silicon interferometer. A vibration isolation system provides exceptional phase stability and fringe visibility.
- [29] NG-7 Neutron Physics Interferometry Test Bed for quantum information science.
- [30] NG-7 Horizontal Sample Reflectometer allows reflectivity measurements of free surfaces, liquid/vapor interfaces, as well as polymer coatings.

Molecular origins of two-dimensional membrane viscosity measured by neutron and X-ray spectroscopies

M. Nagao,^{1,2,3} E. G. Kelley,¹ A. Faraone,¹ M. Saito,⁴ and P. D. Butler^{1,3,5}



Our body is composed of trillions of cells, and each cell is delimited by a border that distinguishes its inner and outer regions. This boundary is a molecular membrane that is only two molecules thick and is known as the cell membrane. The variety of lipids and proteins that form these fluid membrane boundaries facilitates interactions between individual lipids and proteins as well as reorganization of the components to form a variety of internal membrane structures and multimeric signaling complexes. Understanding the transport properties in two-dimensional lipid membranes is, thus, both fundamentally interesting and biologically relevant.

Although viscosity is an intrinsic material property that characterizes the transport of momentum in a material, there have been both experimental and computational challenges in measuring the viscosity of two-dimensional fluid membranes. Estimates for the membrane viscosity from a variety of experimental and computational techniques vary by orders of magnitude depending on the method used [1]. Moreover, most of the experimental techniques use optical methods to access the membrane viscosity as a macroscopic property on length scales much larger than the individual lipids. As such, there is a growing need for a more detailed understanding of the molecular origins of membrane viscosity. This is why we sought to expand on the power of quasielastic neutron and X-ray scattering techniques by extending the length and time resolutions of previous measurements to study the structural dynamics at the molecular level and open new avenues to understanding the molecular origins of membrane viscosity [2].

It is not straightforward to realize a molecular understanding of membrane viscosity without good theoretical frameworks. In three-dimensional liquid systems, the relaxation time of molecular motions measured at the structural correlation peak follows the same temperature dependence as the liquid viscosity [3]. This relation suggests a universal feature in that the friction within liquids likely originates from structural rearrangements of the constituent molecules. Accordingly, here we extended these studies to two-dimensional membrane systems and measured structural relaxation times of the lipid acyl tails. We then used these relaxation times to estimate the membrane viscosity of a lipid bilayer [2].

We employed both neutron spin echo (NSE) spectroscopy and Mössbauer time-domain interferometry (MTDI) [4]. As a model cell membrane, we used multilamellar vesicles composed of dimyristoyl phosphatidylcholine (DMPC) bilayers in water. Tail-deuterated DMPC dissolved in D₂O was used for the NSE experiments, and protiated DMPC was dissolved in H₂O for the MTDI experiments. The experiments were performed above and below the lipid molecular melting transition temperature T_m ($T_m = 24^\circ\text{C}$ and 20.5°C for protiated and tail-deuterated DMPC, respectively) to see the lipid acyl tail dynamics both in the fluid ($T > T_m$) and gel ($T < T_m$) phases.

A prior neutron scattering experiment on TAIKAN at J-PARC showed a structural correlation peak from the lipid acyl tails at a scattering vector transfer of $q \approx 1.5 \text{ \AA}^{-1}$, where $q = 4\pi \sin(\theta/2)/\lambda$ with θ and λ being the scattering angle and the wavelength of the incident neutrons, respectively. The orientational order of the lipids in the gel phase is higher than that in the fluid phase, and a sharper correlation peak was observed in the gel phase [2]. Quasielastic scattering measurements then were performed at q values corresponding to the structural correlation peak to measure the acyl tail correlation dynamics at length scales of about 5 \AA . The NGA-NSE at NIST was used to measure the structural relaxations both in the fluid and gel phases at time scales from 5 ps up to 16 ns. To further extend the time resolution, synchrotron radiation from SPring-8 on BL09XU was used to record MTDI signals from $\approx 10 \text{ ns}$ up to $\approx 300 \text{ ns}$ at temperatures mainly in the gel phase. Both techniques measured the normalized intermediate scattering function, $I(q,t)/I(q,0)$, of the lipid acyl tail correlations.

We observed fast relaxation dynamics in the fluid phase ($T > T_m$) compared to those in the gel phase ($T < T_m$) as shown in Figure 1. In the fluid phase, two relaxation processes were identified, where the majority component had a faster relaxation time of $\approx 0.03 \text{ ns}$, and the second minor component had a slower relaxation time of $\approx 0.5 \text{ ns}$. The faster relaxation time that relates to the structural rearrangements of the individual DMPC lipid acyl tails was about an order of magnitude slower than the structural relaxation dynamics of the analogous linear alkane (tetradecane, C₁₄H₃₀), where computer simulation results showed a relaxation time of about 0.003 ns in the liquid at $T = 25^\circ\text{C}$ [5]. As tetradecane does not

¹ NIST Center for Neutron Research, National Institute of Standards and Technology, Gaithersburg MD 20899

² University of Maryland, College Park, MD 20742

³ University of Delaware, Newark, DE 19716

⁴ Department of Physics, Tohoku University, Sendai, Miyagi 980-8578, Japan

⁵ University of Tennessee, Knoxville, TN 37996

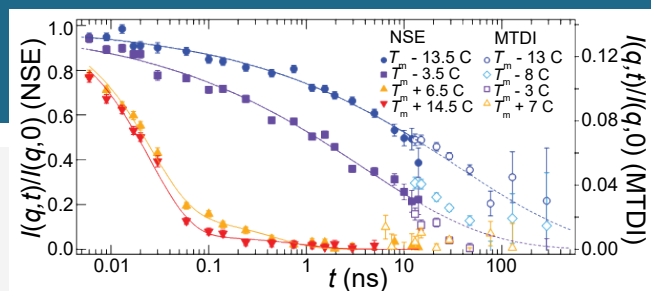


FIGURE 1: Normalized intermediate scattering functions measured with NSE and MTDI. The NSE data are shown as full symbols on the left axis, and the MTDI data are shown as open symbols on the right axis. The scale of the MTDI data is shifted to match the NSE data. The error bars represent ± 1 standard deviation.

form any internal structures in the bulk liquid, we deduce that two-dimensional confinement and orientational ordering of the C_{14} lipid tails as well as the restricted motions due to the binding of one end of the tail to the headgroup significantly slows the chain relaxations. The slower relaxation time originates from the entire lipid molecule escaping from its cage and rearranging with the neighboring lipid molecules, and its origins were confirmed by comparing the present results with nuclear magnetic resonance spectroscopy measurements of the lipid diffusion time [6].

Meanwhile, below T_m , the dynamics significantly slowed down with relaxation times of ≈ 10 ns to ≈ 100 ns depending on temperature. Interestingly, the data clearly show that molecular motions persist even as the temperature is lowered into the gel phase, and the membranes are increasingly solidified at the molecular level as the temperature decreases further. However, we were not able to resolve two independent relaxation modes that were seen in the fluid phase at low temperatures, indicating that the single relaxation dynamics in the lipid gel phase had a much broader distribution of the relaxation times.

Our estimates for the membrane viscosity, η_m , calculated from the structural relaxation times are summarized in Figure 2. In the fluid phase, the slower relaxation gives a membrane viscosity on the order of 1 nPa·s·m, which falls in the middle of broadly distributed η_m values for DMPC in literature [1]. This result indicates that the membrane viscosity has a clear relationship with the lipid molecular structural relaxations. In the present study, we also give the first estimates for the membrane viscosity in the gel phase based on the measured structural relaxations. The estimated membrane viscosity in the vicinity of T_m is about 10 times larger than that in the fluid phase and significantly increases with decreasing temperature.

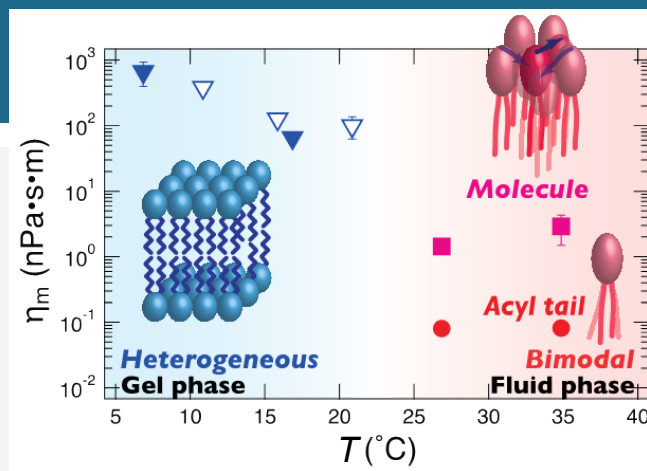


FIGURE 2: Estimated membrane viscosity, η_m , from the structural relaxation time measured by the NSE (full symbols) and MTDI (open symbols) experiments. Schematic illustrations show the molecular origins of the estimated η_m .

In summary, the combination of NSE and MTDI accessed the structural relaxation dynamics of the lipid acyl tails over more than 4 orders of magnitude in time. This is a unique opportunity afforded by the combination of neutron and X-ray spectroscopic techniques and provided new insights into the collective acyl tail dynamics. The slower of the two modes in the fluid phase relates to the structural relaxation of the lipid molecules, and the time required for a lipid molecule to escape from its molecular cage is related to the macroscopic membrane viscosity. The present results provide new insights into how the motions of individual lipid molecules can influence the membrane viscosity and may one day lead to future applications in drug discovery and control over membrane functions.

References

- [1] H. A. Faizi, R. Dimova, P. M. Vlahovska, *Biophys. J.* **121**, 910 (2022).
- [2] M. Nagao, E. G. Kelley, A. Faraone, M. Saito, Y. Yoda, M. Kurokuzu, S. Takata, M. Seto, P.D. Butler, *Phys. Rev. Lett.* **127**, 078102 (2021).
- [3] F. Mezei, W. Knaak, B. Farago, *Phys. Rev. Lett.* **58**, 571 (1987).
- [4] M. Saito, R. Masuda, Y. Yoda, M. Seto, *Sci. Rep.* **7**, 12558 (2017).
- [5] T. Yamaguchi, *J. Chem. Phys.* **146**, 094511 (2017).
- [6] A. Filippov, G. Orädd, G. Lindblom, *Biophys. J.* **64**, 3079 (2003).

In-situ monitoring of protein unfolding/structural states under cold high-pressure stress

D. C. Gomes,^{1,2} S. C. M. Teixeira,^{2,3} and C. J. Roberts²



Therapeutic protein solutions are commonly stored under cold conditions to increase product shelf-life, but freezing and low temperatures can impact protein native conformation and formulation efficiency. Degradation mechanisms are not fully understood and measuring conformational changes can help to elucidate non-native protein aggregation. Through an international collaboration between researchers from the Universities of Lisbon and Delaware, Amgen Inc. and the NCNR, high pressure (HP) small angle neutron scattering (SANS) and intrinsic fluorescence (FL) techniques were used to study the solutions of three model proteins *in situ*, at temperatures down to -15 °C [1]. Self-association events and the reversibility of each condition were determined to assess folding transitions and aggregation propensity. This approach has the potential to overcome limitations of *ex situ* methods—often based on extrapolations from high temperature conditions—by providing new insights into protein stability.

Protein unfolding and aggregation may increase the risk of immunogenic responses in food and pharmaceutical formulations. Although difficult to predict, the change in the Gibbs free energy upon protein unfolding can be on the order of only a few kcal/mol, and the midpoint temperature of cold denaturation (T_{CD}) is not far below 0 °C for some cases [2]. Cold induced denaturation is often extrapolated from heat denaturation conditions (T_{HD}) with unreliable results, due to the broad temperature range (T_{CD} often differs from T_{HD} by more than 50 °C) as well as the over-simplistic assumption of a 2-state folded-unfolded protein structure. Transient states have been measured for many solution structures, and the assumption also ignores potential differences between unfolded protein states triggered by heat vs cold denaturation [3]. Protein folding transitions at low temperatures were monitored while bypassing freezing, using HP environments to keep the solutions in the liquid state. Freezing generally limits measurements for most analytical techniques and has the potential to induce other stresses that may impact protein structure (e.g., ice-liquid interfacial stress, cryo-concentration). HP-SANS was chosen to investigate cold induced denaturation states of three protein solutions using the LIPPS system [4]: two relatively small globular proteins (alpha Chymotrypsinogen A, aCgn, and Ovalbumin, Ova) and the monoclonal antibody Anti-Streptavidin IgG1 (AS-IgG1). Changes in each protein

molecular size were obtained for a series of pressure and temperature conditions by determination of the radius of gyration (R_g) from SANS scattering profiles. Figure 1 shows the average protein size increase measured as the ratio $R_g/R_{g,N}$, where $R_{g,N}$ is the reference radius of gyration for the native protein structure obtained at 20 °C. While the aCgn monomer size is relatively constant over all conditions tested, a significant increase in protein size is observed for both Ova (below -10 °C at any pressure condition tested) and AS-IgG1 (below -5 °C and above 35 °C, above 200 MPa). Normalized Kratky plots (NKP) were used to provide additional information on the structures of Ova and AS-IgG1 at temperature and pressure conditions where an increase in $R_g/R_{g,N}$ was observed (Fig. 2). Conformational changes were observed for Ova detected as a shift of the NKP peak(s) typical of increased structural flexibility. For AS-IgG1, denaturing conditions caused the appearance of a plateau at higher qR_g values. Reversibility of conformational changes was evaluated by setting the conditions back to 20 °C and atmospheric pressure for the three model proteins, but only Ova and aCgn structure was observed to refold.

Additional FL measurements under both atmospheric and pressure environments (data not shown) suggest that, at temperatures below and above 0 °C, pressure effects on the structures of aCgn and Ova were negligible, consistent with the SANS data. In contrast, for AS-IgG1, HP low temperature environments seem to induce the formation of unfolding intermediates (or “molten globule” states), whereas HP and high temperature conditions appears to trigger the formation of a more disordered structure. T_{CD} of ca. -19 °C and -17 °C were estimated for aCgn and Ova solutions, respectively via isothermal chemical denaturation measurements (ICD; data not shown). *In situ* SANS measurements are however able to capture minor structural changes starting at -5 °C. Pairwise distribution functions, $p(r)$, were also calculated from the SANS data to detect the presence of aggregates in solution (see example shown in Fig. 3). A broadening of the $p(r)$ peaks was observed at -10 °C for Ova at all pressure conditions tested, consistent with the presence of oligomeric states (we refer the interested reader to reference [1] for further details).

¹ Centro de Química Estrutural, Dep. Engenharia Química, Instituto Superior Técnico, Universidade de Lisboa, Av. Rovisco Pais, 1049-001 Lisboa, Portugal.

² Department of Chemical and Biomolecular Engineering, University of Delaware, Newark, DE 19713

³ NIST Center for Neutron Research, National Institute of Standards and Technology, Gaithersburg, MD 20899

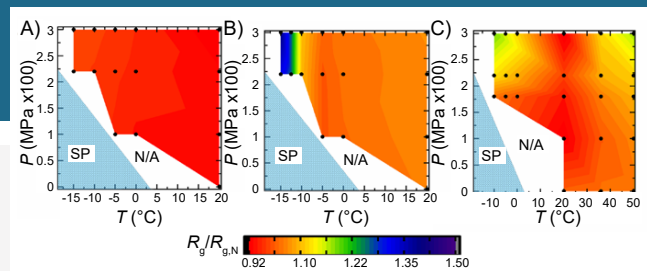


FIGURE 1: Surface plot representation of $R_g/R_{g,N}$ (normalized to a 1.5-fold increase of the ratio) obtained from the Guinier approximation to HP-SANS data at various temperatures, for D_2O solutions of: A) 10 mg/mL aCgn in 10 mmol/L acetate buffer pH 4.5; B) 10 mg/mL Ova in 10 mmol/L histidine buffer pH 7; C) 5 mg/mL AS-IgG1 in 5 mmol/L citrate buffer pH 4. Black circles represent data points measured. The blue SP area represents the solid phase conditions where a pure D_2O solution is expected to be frozen (not drawn to scale), and the N/A white area represents for non-acquired measurements.

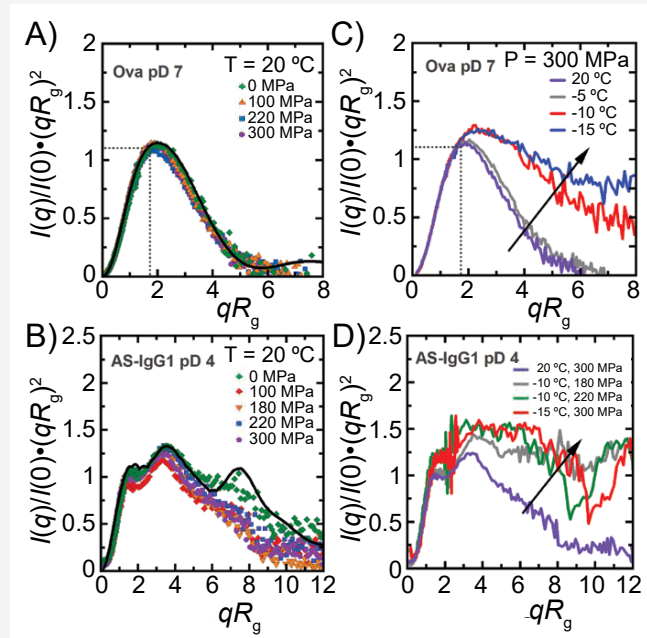


FIGURE 2: Normalized Kratky plots for SANS data collected for D_2O solutions of: 10 mg/mL Ova in 10 mmol/L histidine buffer pH 7 (A, C); and 5 mg/mL AS-IgG1 in 5 mmol/L citrate buffer pH 4 (B, D). The pressure and temperature conditions tested are labeled for each protein solution. Arrows on NKP plots C and D highlight the unfolding effects of low temperature under high-pressure. The black solid lines in plots A and B represent fit curves to the data, calculated using available crystal structure files for the respective proteins.

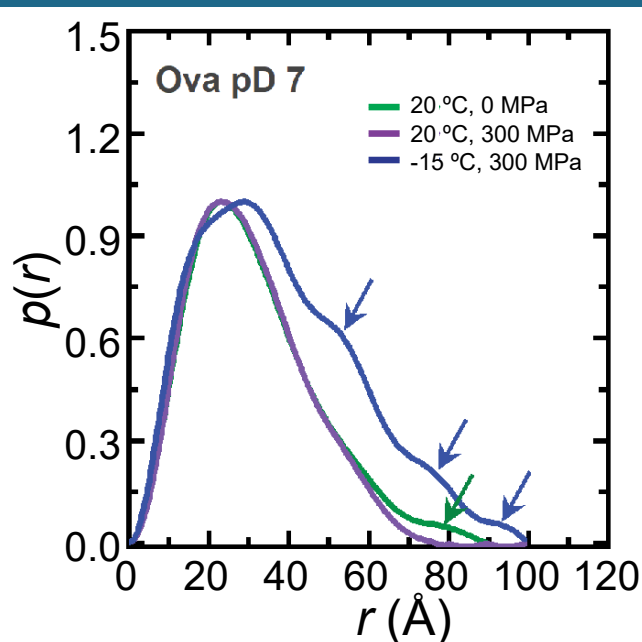


FIGURE 3: Pair distance distribution function calculated for D_2O solutions of 10 mg/mL Ova in 10 mmol/L histidine buffer pH 7. The conditions tested are labeled in the main panel; arrows indicate the presence of oligomeric state peaks.

A successful *in situ* approach was used to access the sub-0 °C regime under HP environments using SANS and FL. Three model proteins, differing in size, structure and conformational stability, were studied: aCgn was found to be quite resistant to all conditions tested, while alterations were detected for Ova and AS-IgG1 solution structures at a broad range of conditions. Although *ex-situ* methods anticipate an increase in Ova unfolded population as temperature approaches -17 °C, the *in situ* approach was able to capture significant conformational changes ~12 °C above T_{CD} (pressure alone was shown to have negligible effects in the range measured). The formation of reversible Ova oligomeric states (*i.e.*, aggregation) was also detected. For AS-IgG1 solutions, structural perturbation is likely to occur as both high/low temperature and pressure increase. Intermediate denatured states were readily identified for AS-IgG1 at ≈ 200 MPa from -5 °C to -10 °C. Overall, this work questions the practical utility of *ex situ* methods to estimate folding states at low temperatures via extrapolation, shown to be limited and often imprecise. Instead, the *in situ* approach provides a means to directly detect conformational states and improve classical textbook analysis on protein stability.

References

- [1] D. Gomes, S. Teixeira, J. Leão, V. Razinkov, W. Qi, M. Rodrigues, C. Roberts, *Mol. Pharmaceutics* **18**, 4415 (2021).
- [2] D. Sanfelice, P.A. Temussi, *Biophys. Chem.* **208**, 4 (2016).
- [3] J. Roche, C. A. Royer, C. Roumestand, *Progress in Nuclear Magnetic Resonance Spectroscopy* **102**, 15 (2017).
- [4] S. Teixeira, J. Leão, C. Gagnon, M. McHugh, J. Neutron Research **20**, 13 (2018).

Small-angle neutron scattering provides insight into the self-association of lactate dehydrogenase during freeze-thaw in buffered solutions

J. Sonje,¹ S. Thakral,^{1,2} S. Krueger,³ and R. Suryanarayanan¹



Commercial biologic drug products have revolutionized the field of therapeutics in recent years. These drug products consist of proteins that have a unique three-dimensional structure that is responsible for its therapeutic activity. This structure is known as the native state of the protein. Proteins (the drug substance) are regularly stored in the frozen state, often for long periods of time, before they are prepared in solution or freeze-dried as the final drug product. The stresses that the protein undergoes during freezing and thawing can have a detrimental effect by destabilizing the native structure, causing a loss of activity and making the drug less effective. One of the major types of destabilization is irreversible protein aggregation in which the native state is not recovered upon thawing. To lessen these detrimental effects, excipients such as sugars, buffers and surfactants are used to stabilize the protein so that it remains in the native state during freezing.

In order to be effective cryoprotectants, the excipients and protein must remain together in the amorphous phase as the solution freezes. This is illustrated in Figure 1, which shows a temperature bar on the left and the corresponding state of a protein formulation consisting of a drug substance and excipients to the right of the temperature bar. The solution becomes supercooled as the temperature is lowered below 0 °C and ice crystallization begins around -10 °C, at which time ice nuclei form as illustrated on the far right. As the temperature continues to fall to -70 °C and below, the ice nuclei continue to grow into crystals, leading to the concentration of the protein and excipients. At this point, two phases exist: ice crystals and an amorphous phase called the freeze concentrate that ideally contains protein, excipients and water. Figure 1 also lists the events that can cause stresses on the protein during the freezing process, *i.e.*, adsorption at ice-air and ice-freeze concentrate interfaces as well as freeze concentration leading to excipient crystallization. The latter removes the excipient from the amorphous phase, which can result in a loss in cryoprotection. In some cases, buffer crystallization results in pH shifts that can also be detrimental to protein stability.

In this work, the aggregation behavior of a model protein, lactate dehydrogenase (LDH), was observed during freezing and thawing [2]. LDH is a globular protein (molar mass 144 kDa; isoelectric point (pI) of ≈ 7.2) with a tetrameric native state that is known to be sensitive to freezing stresses,

especially at pH < 5 [3, 4]. When prepared in sodium phosphate (NaP) buffered solutions, LDH experiences pH shifts up to ≈ 4 units during cooling due to selective crystallization of the disodium hydrogen phosphate buffer component [5], which causes protein aggregation [6]. LDH was also found to aggregate due to adsorption at the ice-air interface [7, 8]. Most of these studies were conducted at protein concentrations at or below 100 $\mu\text{g/mL}$, whereas protein formulations are often at concentrations of 1 mg/mL and above.

The SANS experiments, performed using a technique known as contrast variation, proved essential in constructing a model of the LDH structure in both the liquid and frozen states. By changing the H/D composition of the buffer, the scattering from the air-water (or air-ice) interface contributes to the scattering in 100 % D₂O buffer, but not in a buffer with a D₂O mole fraction of 8 %. This allowed for the measurement of only protein aggregates by using a buffer with a D₂O mole fraction of 8 %, providing key information for understanding the aggregation state of LDH during freezing.

Initial SANS studies were performed in 10 mM histidine buffer to determine the structure of LDH in the liquid and frozen states. Figure 2A shows the scattering intensity, $I(q)$, as a function of the momentum transfer, q , from 1 mg/mL LDH in 10 mM (M = mol/L) histidine buffer at room temperature before freezing. The red curve was obtained from LDH in 100 % D₂O buffer and the black curve from LDH in buffer with a D₂O mole fraction of 8 %. The lack of an upturn at q values below 0.025 \AA^{-1} shows that there are no initial LDH aggregates in buffer with a D₂O mole fraction of 8 %, as opposed to a small amount of aggregation in 100 % D₂O buffer. Thus, the scattering curves at both contrasts give a complete picture of the structure of LDH before freezing. The solid black curve is the calculated scattering curve from the LDH tetramer (structure shown in the inset). It agrees well with the data, including the shoulder at $q = 0.15 \text{ \AA}^{-1}$, which results from the symmetry in the native tetrameric LDH structure. Thus, it can be concluded that LDH is in its native tetrameric state prior to freezing.

To determine if the increase in scattering below $q = 0.25 \text{ \AA}^{-1}$ after thawing is indeed due to protein aggregation, a freeze-thaw study was also conducted of 1 mg/mL LDH in 10 mM histidine in buffer with a D₂O mole fraction of 8 %, where the scattering from air bubbles that could form during thawing

¹ Department of Pharmaceutics, College of Pharmacy, University of Minnesota, Minneapolis, MN 55455

² Characterization Facility, University of Minnesota, Minneapolis, MN 55455

³ NIST Center for Neutron Research, National Institute of Standards and Technology, Gaithersburg, MD 20899

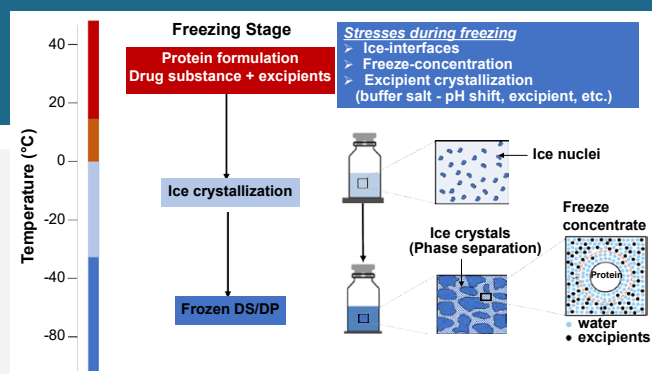


FIGURE 1: Illustration of phase separation of protein and excipient in the freeze concentrate as ice crystals form during freezing of a protein formulation. Adapted from [1].

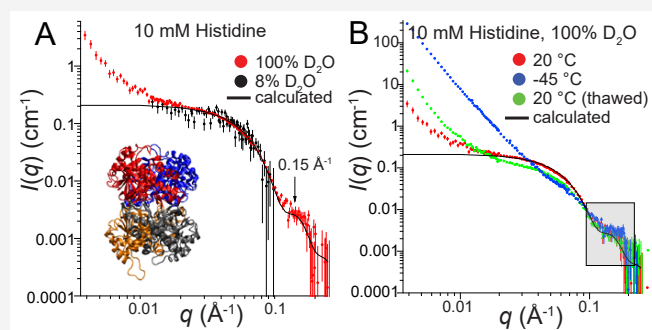


FIGURE 2: SANS curves from LDH (1 mg/mL) in histidine (10 mM) buffer A) in 8 % D₂O and 100 % D₂O at 20 °C prior to freezing compared with the calculated SANS curve for a LDH tetramer (inset), B) in 100 % D₂O before freezing, frozen at -45 °C and after thawing. 8 % D₂O denotes a buffer with a D₂O mole fraction of 8 %. Adapted from [2].

does not contribute to $I(q)$. The resultant scattering curves in Figure 3A showed large aggregates formed upon freezing (blue curve) and evidence for some protein aggregation after thawing (green curve compared to red curve), but it is less pronounced than in 100 % D₂O buffer (Figure 2B). Thus, it can be concluded from the SANS contrast variation experiment that 1 mg/mL LDH in 10 mM histidine buffer self-assembles into large aggregates comprised of native LDH tetramers during freezing, resulting in retention of the native state upon thawing.

Measurements were also made from 1 mg/mL LDH in buffer with a D₂O mole fraction of 8 % consisting of 10 mM NaP and 100 mM NaP to assess the effect of pH shift on the LDH structure during freezing. The resultant SANS curves are shown in Figure 3B and 3C, respectively. It is apparent from the data that LDH forms large aggregates upon freezing (blue curves), similar to those formed in 10 mM histidine buffer. There is also evidence of irreversible aggregation upon thawing (green curves), but the scattering intensities below $q = 0.25 \text{ \AA}^{-1}$ are lower than that for LDH in 10 mM histidine buffer, suggesting even less irreversible aggregation after thawing. This result was unexpected since it was hypothesized that the pH shift experienced by LDH in NaP buffer during freezing would be more detrimental to LDH stability than the freezing stresses experienced by LDH in the non-crystallizing histidine buffer.

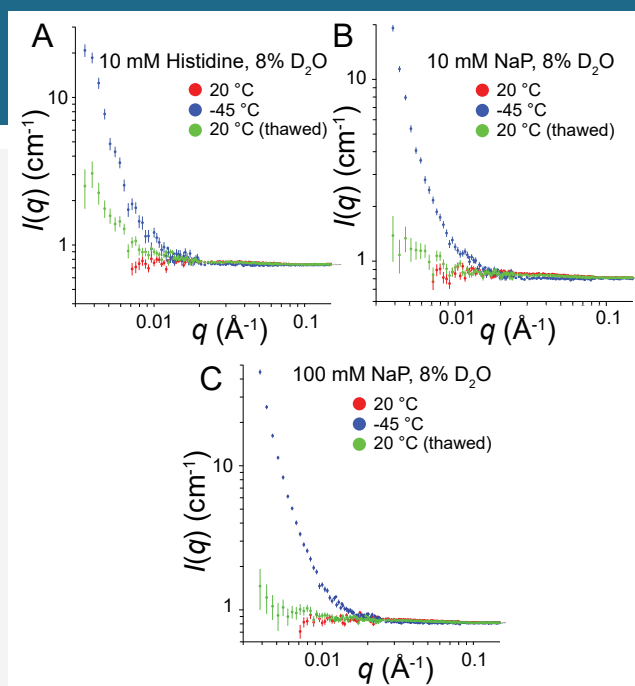


FIGURE 3: SANS curves from 1 mg/mL LDH before freezing, frozen at -45 °C and after thawing in histidine and NaP 8 % D₂O buffers. 8 % D₂O denotes a buffer with a D₂O mole fraction of 8 %. Adapted from [2].

This discrepancy was resolved by performing freeze-thaw DLS experiments on LDH in the same buffers at 10 µg/mL, 100 µg/mL and 1 mg/mL. After five freeze-thaw cycles, significant aggregation was observed for 10 µg/mL LDH in all three buffers. At 100 µg/mL, aggregation was only observed in the two NaP buffers. At 1 mg/mL, aggregation was only observed in the 100 mM NaP buffer. The combined results from the SANS and DLS studies showed that concentration and number of freeze-thaw cycles play an important role in protein stability. In addition, the effect of the pH shift in NaP buffer is more pronounced at concentrations lower than 1 mg/mL. Since the bulk drug substances are stored at protein concentrations $\geq 1 \text{ mg/mL}$, it may be perfectly feasible to use NaP buffers without fear of loss of protein stability upon freezing.

References

- [1] S. Thakral, J. Sonje, B. Munjal, R. Suryanarayanan, *Advanced Drug Delivery Reviews* **173**, 1 (2021).
- [2] J. Sonje, S. Thakral, S. Krueger, R. Suryanarayanan, *Mol. Pharmaceutics* **18**, 4459 (2021).
- [3] O. P. Chilson, G. B. Kitto, N. O. Kaplan, *Proc. Natl. Acad. Sci. USA* **53**, 1006 (1965).
- [4] E. S. Vesell, K. L. Yielding, *Proc. Natl. Acad. Sci. USA* **56**, 1317 (1966).
- [5] G. Gómez, M. J. Pikal, N. Rodríguez-Hornedo, *Pharm Res* **18**, 90 (2001).
- [6] T. J. Anchordoquy, J. F. Carpenter, *Arch Biochem Biophys* **332**, 231 (1996).
- [7] B. S. Bhatnagar, M. J. Pikal, R. H. Bogner, *Journal of Pharmaceutical Sciences* **97**, 798 (2008).
- [8] J. J. Schwegman, J. F. Carpenter, S. L. Nail, *J Pharm Sci* **98**, 3239 (2009).

Probing protein-protein interactions in monoclonal antibody formulations with neutrons

A. Y. Xu,^{1,2} N. J. Clark,^{1,3} J. Pollastrini,³ S. Krueger,¹ A. McAuley,³ and J. E. Curtis¹

Monoclonal antibodies (mAbs) represent a major class of biopharmaceuticals for treating a wide range of medical conditions, including cancer, infections, auto-immune diseases, and metabolic disorders. Owing to gastric degradation and their inherent high molecular weights, the preferred administration route for mAb therapeutics is subcutaneous (SC) injections. Limited by the administration volume of SC injection, mAb concentration greater than 50 mg/mL can be required to meet the desired therapeutic dosage. When prepared at high concentrations, mAb molecules have an increased tendency to self-associate into large-scale structures, resulting in severe adverse effects and difficulties in administration. Therefore, to improve the stability and reduce the viscosity of concentrated mAb formulations, excipients have been developed and added into the formulation to modulate the protein-protein interactions (PPI) among crowded mAb molecules. Commonly used excipients include salts, sugars, amino acids, and non-ionic surfactants. Although there are many excipients to choose from, the formulation process still involves lengthy empirical screening and represents a critical barrier to the development of mAb products.

The most straightforward method to determine the optimal formulation condition for a particular mAb candidate is to measure the viscosity and long-term stability of concentrated mAb samples prepared in various excipient formulations and then choose the one with the best stability and viscosity profile. However, such an approach is time-consuming and resource intensive. Therefore, high-throughput biophysical characterization methods have been developed to accelerate the formulation development of mAb products. These measurements extract experimental parameters containing information on the net PPI, with the underlying assumption that mAbs are stable if the net PPIs are repulsive and unstable if the net PPIs are attractive [1].

Dynamic light scattering (DLS) and static light scattering (SLS) are the most widely used methods in the pharmaceutical industry for determining optimized excipient formulations. These techniques measure the diffusion interaction parameter k_D and the second virial coefficient B_{22} , respectively. Although k_D and B_{22} are used to characterize PPI, they are only accessible at low mAb concentrations, whereas the nature of PPI at high protein concentrations can be significantly different compared to that in dilute samples. The effective structure factor $S(q)_{\text{eff}}$ measured

from small-angle X-ray and neutron scattering (SAXS/SANS) also provides information on spatial arrangements and PPI of mAbs in solution. One of the major differences between k_D/B_{22} and $S(q)_{\text{eff}}$ is that the latter can be measured directly from concentrated mAb solutions up to hundreds of mg/mL [2]. Therefore, $S(q)_{\text{eff}}$ provides a direct measure of PPI present in pharmaceutically relevant formulations.

In this study, the thermodynamic, hydrodynamic and structural properties of a human anti-streptavidin monoclonal antibody (ASA-IgG2) were determined with various amounts of NaCl in solution, ranging from 0 mmol/L up to 1200 mmol/L [3]. High NaCl concentrations were included to extensively modulate the PPI and monomer-oligomer equilibrium of ASA-IgG2. This approach allowed us to thoroughly characterize the effects of NaCl on interactions among concentrated mAb molecules. To characterize PPI, k_D values were measured by DLS from dilute mAb samples, whereas $S(q)_{\text{eff}}$ profiles were obtained from SAS measurements from a series of mAb samples with varying mAb concentrations. Knowing changes in PPI with an increasing amount of salt will allow a fundamental understanding of the physics of PPI as probed by the various scalar and derived scattering parameters determined in this study.

SAS measurements of $S(q)_{\text{eff}}$ were performed on ASA-IgG2 solutions as a function of both mAb and NaCl concentration (C_{mAb} and C_{NaCl}). The value of $S(q)_{\text{eff}}$ as the momentum transfer q approaches zero, $S(0)_{\text{eff}}$ was obtained by fitting the profiles using appropriate models (Figure 1). This quantity can then be used to infer the nature of net PPI: a value greater than 1 indicates the net PPI are attractive, whereas a value less than 1 suggests the net PPI are repulsive. Different from $S(q)_{\text{eff}}$, k_D can only be obtained from dilute mAb samples, therefore one k_D value was measured per NaCl concentration. As shown in Figure 2, k_D values measured from all samples were greater than the cut-off value of -8 mL/g [4], suggesting the net PPI were repulsive among all examined NaCl concentrations.

The $S(0)_{\text{eff}}$ results shown in Figure 2 demonstrate that the net PPI was not only dependent on C_{NaCl} but it also varied with C_{mAb} . Comparing PPI characterized by k_D and $S(0)_{\text{eff}}$ values, it is found that the correlations between the two datasets are only valid for samples prepared with low to intermediate C_{NaCl} , i.e., up to 150 mM for the current study. At higher C_{NaCl} the correlations between $S(0)_{\text{eff}}$ and k_D also demonstrated

¹ NIST Center for Neutron Research, National Institute of Standards and Technology, Gaithersburg, MD 20899

² Institute for Bioscience and Biotechnology Research, University of Maryland, Rockville, MD 20850

³ Amgen Inc., Thousand Oaks, CA 91320

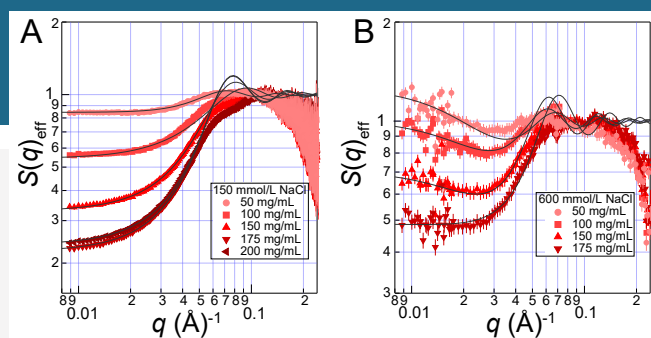


FIGURE 1: $S(q)_{\text{eff}}$ profiles measured from ASA-IgG2 samples prepared in 150 mmol/L (A) and 600 mmol/L (B) NaCl solutions. $S(q)_{\text{eff}}$ profiles are fitted with either Hayter-Penfold (A) or Two-Yukawa (B) models to extrapolate $S(0)_{\text{eff}}$ values. Error bars in the scattering profiles represent the relative uncertainties in the scattering intensity measurements based on counting statistics.

dependence on C_{mAb} presumably due to variations in non-specific PPI when mAb molecules become crowded. As a result, parameters measured from dilute and concentrated mAb samples could lead to different predictions on the stability of mAb formulations.

It is commonly accepted that solution viscosity is expected to increase under conditions where net PPI are attractive, and the viscosity should remain low where net PPI are repulsive [5]. Therefore, we also evaluated whether an empirical relationship exists between the experimentally determined viscosity results and those predicted from interaction parameters measured from both dilute and concentrated mAb formulations. To do this, we compared experimentally determined viscosity results with those predicted from k_D and $S(q)_{\text{eff}}$. Our results show that the viscosity predicted by k_D values does not agree with experimental data. This is not surprising since k_D is measured from dilute samples, whereas increases in viscosity largely occur at much higher concentrations. The comparison between measured viscosity with that predicted from $S(q)_{\text{eff}}$ implies that the overall attractive PPI do not necessarily lead to increased solution viscosity, and the overall repulsive PPI can be observed in solutions with elevated viscosity. Thus, the observed relationship between the measured and predicted viscosity in this study contradicts the commonly accepted relationship between net PPI and the viscosity of concentrated mAb formulations. It is anticipated that the nature and significance of various PPI can change dramatically when mAb molecules are at higher concentrations, with concomitant reduced intermolecular distances and, therefore, an increased propensity of intermolecular association. To obtain reliable viscosity predictions, further studies are needed to establish the relationship between the measured viscosity and PPI measured from concentrated mAb formulations.

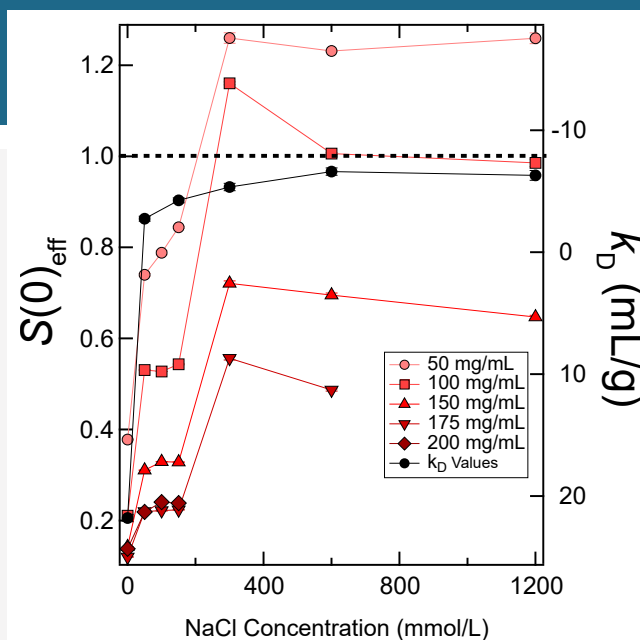


FIGURE 2: Changes in $S(0)_{\text{eff}}$ (left axis) and k_D (right axis) values as a function of C_{NaCl} . The dotted line represents cut-off values of $S(0)_{\text{eff}}$ of 1 and k_D of -8 mL/g . Divided by the dotted line, the top and bottom panels of the figure highlight samples with $S(0)_{\text{eff}}$ and k_D values that are indicative of attractive and repulsive PPI, respectively.

On the fundamental level, the formulation challenges of mAb therapeutics come from the limited knowledge of the impacts of various PPI on the collective behavior of mAb molecules and the lack of analytical methods for characterizing PPI directly from concentrated formulations. The complete mechanism of the self-association propensity of mAbs to improve the prediction of bulk viscosity in concentrated formulations will rely on measurements carried out at high concentrations to account for the correct physics at the phase points of interest. The unique capability of SANS for characterizing PPI directly from pharmaceutically relevant concentrations will help lay the groundwork for a more comprehensive understanding of the impacts of various PPI on the collective behavior of mAb molecules that is needed for more efficient formulation development for mAb products.

References

- [1] E. Y. Chi, S. Krishnan, B. S. Kendrick, B. S. Chang, J. F. Carpenter, T. W. Randolph. *Protein Sci.* **12**, 903 (2003).
- [2] A. Y. Xu, M. M. Castellanos, K. Mattison, S. Krueger, J. E. Curtis. *Mol. Pharm.* **16**, 4319 (2019).
- [3] A. Y. Xu, N. J. Clark, J. Pollastrini, M. Espinoza, H. J. Kim, S. Kanapuram, B. Kerwin, M. J. Treuheit, S. Krueger, A. McAuley, J. E. Curtis. *Antibodies*. **11**, 24 (2022).
- [4] J. Jayaraman, J. M. Wu, M. C. Brunelle, A. M. M. Cruz, D. S. Goldberg, B. Lobo, A. Shah, P. M. Tessier. *Biotechnol. Bioeng.* **111**, 1513 (2014).
- [5] B. D. Connolly, C. Petry, S. Yadav, B. Demeule, N. Ciaccio, J. M. R. Moore, S. J. Shire, Y. R. Gokarn. *Biophys. J.* **103**, 69 (2012).

Dynamics of molecular associates in methanol water mixtures

Y. Zhai,^{1,2} P. Luo,² J. Waller,³ J. L. Self,⁴ L. W. Harriger,⁵ Y. Z.,^{1,2,6} and A. Faraone⁵



Molecular association, the formation of chains of molecules temporarily linked by some kind of interaction, e.g. hydrogen bonding, and microsegregation, the existence of domains rich in a molecular specie or moiety in otherwise macroscopically homogeneous liquids, are topics of intense research. Such phenomena impact relevant macroscopic properties such as viscosity and ionic conductivity in, among others, novel green solvents such as ionic liquids (IL) and deep eutectic solvents (DES), or superconcentrated electrolytes, which hold great promise for the development of the next safe and sustainable electrochemical devices. An archetypical system to investigate these phenomena are methanol/water solutions. Methanol with a hydroxyl head and a methyl tail could be considered the simplest amphiphile. The behavior of the excess entropy of the mixture as a function of methanol concentration has long been considered a strong indication of molecular association. More recently the idea that cluster of methanol molecules could be present in the mixture and be the origin of the anomalous behavior of its thermodynamic and transport parameters has been put forward [1].

An understanding of the nature of association and structuring in methanol/water necessitates information on the mutual motion of all atomic pairs. A possible experimental technique to gain such information is QuasiElastic Neutron Scattering (QENS), with measurements focusing on the coherent component of the spectra. Coherent QENS spectra provide information on the relaxation time of the spatial correlation of couples of atoms in the system at the nanometer length scale on a time scale ranging from few picoseconds up to several nanoseconds.

QENS measurements were carried out using the time-of-flight Disk Chopper Spectrometer (DCS) and the Neutron Spin Echo (NSE) spectrometer on four methanol/water samples at a mole fraction $x = 0.54$, $\text{CD}_3\text{OD}/\text{D}_2\text{O}$ (S1), $\text{CH}_3\text{OD}/\text{D}_2\text{O}$ (S2), $\text{CD}_3\text{OH}/\text{H}_2\text{O}$ (S3), and $\text{CH}_3\text{OH}/\text{H}_2\text{O}$ (S4), differing only by their isotopic composition. Combining the signal from the four samples to obtain $S^c(Q, E)$ as detailed below, the incoherent scattering of the samples can be eliminated completely, obtaining spectra originating from the coherent mutual dynamics of hydrogens atoms in the hydroxyl group with respect to those in the methyl groups, only:

$$S^c(Q, E) = S^{\text{S1}}(Q, E) + S^{\text{S2}}(Q, E) - S^{\text{S3}}(Q, E) - S^{\text{S4}}(Q, E) \quad (1)$$

The investigation of the static structure factor, $S^c(Q) = \int_{-\infty}^{\infty} S^c(Q, E) dE$, was carried out first. The static structure factor $S^c(Q)$ is reported in Fig. 1. Static structure factor results were validated using the Small Angle Neutron Scattering (SANS) instrument on NG7, the cold triple axis spectrometer (SPINS) and polarized diffraction measurements on NSE. In a two components mixture, the thermodynamic limit of the cross terms partial structure factor is known to be mostly determined by the concentration fluctuations. In the thermodynamic limit ($Q = 0$), the comparison with the prediction for $S^c(Q)$ from the Kirkwood-Buff parameters (cyan stars) validate the interpretation of the obtained data in terms of the mutual correlation between water and methanol molecules. A flat negative region extends from low- Q up to almost 1.5 \AA^{-1} ; after that, $S^c(Q)$ increases, becoming positive, reaching a maximum at $\approx 1.75 \text{ \AA}^{-1}$, at a similar Q value as the maximum in $S^{\text{S1}}(Q)$. In Fig. 1, the continuous lines represent the distinct term of the structure factor for binary hard spheres; the agreement at low Q between the collected data and this simple modeling puts in evidence the absence of anomalous concentration fluctuations.

The line shape of $S^c(Q, E)$ was analyzed as a function of Q with a Lorentzian function. The low Q ($< 1 \text{ \AA}^{-1}$) data provide a nanoscopic mutual diffusion coefficient between water and methanol. When the obtained results are compared with those for the self-diffusion coefficients of both methanol and water, as in Fig. 2 panel a), a significant slowing down of the nanoscopic mutual dynamics is apparent which is attributed to the presence of molecular associates of methanol and water.

The analysis of $S^c(Q, E)$ at the maximum of the structure factor, $Q = 1.8 \text{ \AA}^{-1}$ provides the structural relaxation time, τ_R . Fig. 2 panel b) is an Arrhenius plot of structural relaxation time in water, methanol, and methanol/water mixtures compared with the macroscopic shear viscosity, η . The viscosity of water does not follow an Arrhenius law; however, considering a relatively small temperature range around room temperature, an activation energy value can be extracted. The activation energy, E_A , for the microscopic mutual diffusion process and for the structural relaxation of the associates are the same, indicating that the same microscopic process activates both observed motions, i.e. the lifetime of the associates. The values obtained for E_A lays in the range of hydrogen bond energy. However, in the sample investigated here the activation energy

¹ Department of Nuclear, Plasma, and Radiological Engineering, University of Illinois at Urbana-Champaign, Urbana, IL 61801

² Beckman Institute for Advanced Science and Technology, University of Illinois at Urbana-Champaign, Urbana, IL 61801

³ Department of Physics and Mathematics, North Carolina State University, Raleigh, NC 27695

⁴ McKetta Department of Chemical Engineering, University of Texas at Austin, Austin, TX 78712

⁵ NIST Center for Neutron Research, National Institute of Standards and Technology, Gaithersburg, MD 20899

⁶ Department of Electrical and Computer Engineering, University of Illinois at Urbana-Champaign, Urbana, IL 61801

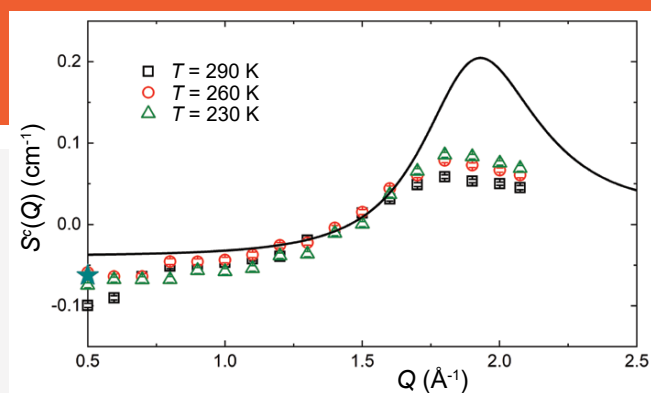


FIGURE 1: Static structure factor $S^c(Q)$. The cyan stars indicate the value of $S^c(Q=0)$ calculated from the Kirkwood-Buff integrals. The continuous lines represent the distinct term of the structure factor for binary hard spheres.

is much larger than for methanol, roughly by a factor of two, and close to the one of water. It is known that methanol has a significant fraction of molecular associates, likely in the form of chains, however, also in water the H-bond network is ubiquitous with tetrameric and pentameric associates. Thus, in water more than one hydrogen bond must be broken for the transport process to be triggered. The obtained results indicate that this is the case also for methanol/water mixtures. The presence of methanol does not seem to enforce a chain like structuring in the system. In fact, structural X-ray investigations found evidence that methanol chains coordinate with water trimers and tetramers. The existence of these associates has a significant weight in determining the viscosity, even though other correlations play a role as well. Using viscosity data, the structural relaxation times were also used to estimate the shear modulus at infinite frequency, G_∞ , through the Maxwell relation: $G_\infty = \eta/\tau_R$. Although, the viscosity of the methanol/water mixture at $x = 0.54$ is higher than that of the pure components, G_∞ at the investigated concentration matches what is obtained by a molar weighted sum of the methanol and water values.

In summary, neutron scattering measurements employing a novel isotopic substitution technique provide new evidence of nanoscopic association in methanol/water mixtures. The relative motion of the water to methanol molecules, *i.e.* their mutual dynamics, was measured at the nanoscale. The thus obtained diffusion coefficient is significantly slower than the single particle diffusion of either methanol or water in the system as well as than their macroscopic mutual diffusion. These results indicate the existence of long lived but dynamic molecular associates of water and methanol molecules. Analysis of the structural relaxation indicates that molecular association plays a role in determining the viscosity of the mixtures and explain how it leads to the fact that the viscosity of the methanol/water mixtures at certain concentrations is higher than that of both pure components [2].

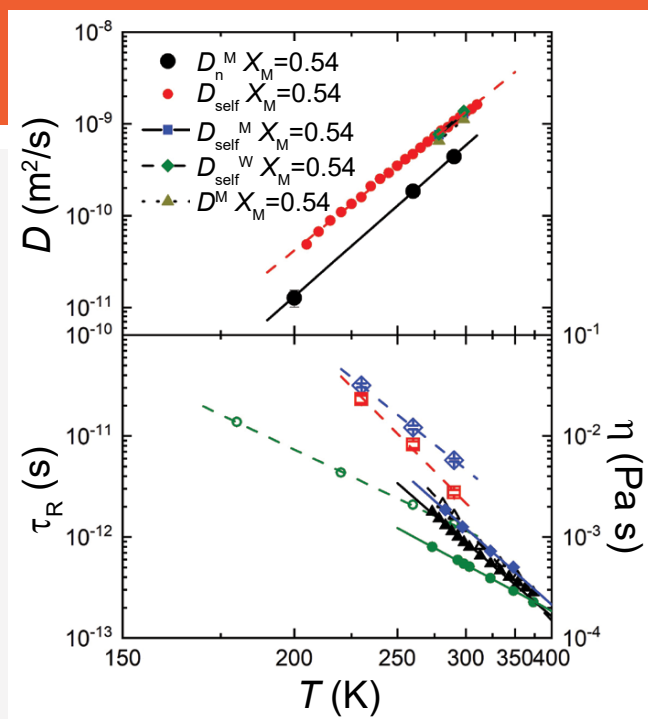


FIGURE 2: a) Arrhenius plot of the nanoscopic mutual diffusion coefficient, D_n^M , compared with previous reports of the self-diffusion coefficient of methanol/water mixtures at $x_M = 0.5$ by NMR, (red circles) and of the self-diffusion coefficients of methanol (blue squares) and water (green diamonds) in the mixture, as well as of the mutual diffusion coefficient (dark triangles) obtained by tracer diffusion. b) Arrhenius plot of the relaxation time (hollow) and viscosity (solid). Black triangles represent values for water; green circles represent values for methanol; blue diamonds represent values for $x_M = 0.54$ methanol–water mixture; red squares represent values for calculated S^c [2].

References

- [1] S. Dixit, J. Crain, W. C. K. Poon, J. L. Finney, A. K. Soper, *Nature* **416**, 829 (2002).
- [2] Y. Q. Zhai, P. Luo, J. Waller, J. L. Self, L. W. Harriger, A. Faraone, *Physical Chemistry Chemical Physics* **24**, 2287 (2022).

Aluminium formate, $\text{Al}(\text{HCOO})_3$: an Earth-abundant, scalable and highly-selective material for CO_2 capture

H. A. Evans,¹ D. Mullangi,² Z. Deng,² Y. Wang,³ S. B. Peh,³ F. Wei,⁴ J. Wang,² C. M. Brown,^{1,5} D. Zhao,³ P. Canepa,^{2,3} and A. K. Cheetham^{2,6}

Efficient CO_2 capture and storage technologies can reduce the environmental impact of fossil fuel use. Conventional chemical sorbents based on aqueous amine solutions have a considerable capacity for post-combustion CO_2 capture but suffer the disadvantages of thermal degradation, corrosion, oxidative reactions, and usually energy-intensive regeneration processes. Porous solid sorbents that capture CO_2 through physisorption require less energy for regeneration and have great potential for cost-effective CO_2 capture. However, traditional solid sorbents, such as zeolites and porous carbon-based materials, also have considerable limitations. In particular, aluminosilicate zeolites have inadequate CO_2 uptake capacity in humid gas streams, and porous polymer and carbonaceous materials have low adsorption capacities and poor CO_2/N_2 selectivities.

Metal-organic frameworks (MOFs), with their high surface areas, tunable pore sizes, surface functionality, and structural diversity, offer several advantages as the next-generation solid adsorbent materials for CO_2 capture but possess limitations of their own. These usually include sensitivity to humidity, poor mechanical properties, and, for many high-performing MOF materials, complex ligand precursors that may be too costly for large-scale applications. Here, we describe how the cost and scalability issues could be addressed by exploring the adsorption properties of one of the simplest of all MOFs, aluminum formate, $\text{Al}(\text{HCOO})_3$ (ALF) [1]. ALF is a mechanically robust material that can be made from the inexpensive and widely available starting reagents aluminum hydroxide and formic acid. It exhibits excellent CO_2 adsorption properties and CO_2/N_2 selectivities for dried CO_2 -containing gas streams.

The remarkable CO_2 adsorption performance of ALF is rooted in its crystal structure [2], where two types of cavities exist. The most important of these cavities, denoted as the small cavity (SC), has inward-pointing formate hydrogens that hydrogen bond with adsorbed CO_2 molecules (Figure 1A). The second cavity in ALF, denoted as the large cavity (LC), also adsorbs CO_2 molecules, but in this case the molecules do not strongly associate with any atoms of the crystal structure framework (Figure 1B). *In situ* CO_2 -dosed neutron powder diffraction data of ALF taken at the NIST Center for Neutron Research were instrumental to understanding how the cavities of ALF fill preferentially with CO_2 . Figure 1C and 1D illustrate

some of these results. The top panel of Figure 1C shows the Rietveld refinement of the diffraction pattern of the empty ALF structure, and the bottom panel shows a representative Rietveld refinement of ALF filled with CO_2 . The bottom panel refinement was how the model structures shown in Figure 1A and 1B were resolved. Figure 1D displays results from multiple refinements of filling ALF with increasing amounts of CO_2 . The graphs illustrate two main conclusions: that the unit cell of ALF contracts with increasing CO_2 adsorption, and that there is preferential filling of the small cavity with CO_2 relative to the large cavity. This understanding of cavity preferential filling is only available through crystallographic probes like diffraction, as crystallography provides the atomic positions of constituent atoms of a given sample.

The gas adsorption properties of ALF were also measured and are shown in Figures 1E and 1F. Figure 1E shows the gas adsorption isotherms of ALF at various temperatures with dry CO_2 gas. As can be seen, ALF's peak CO_2 adsorption above 1 bar is near 323 K (50 °C). If heated to just 360 K (not shown) with 1 bar of CO_2 atmosphere, ALF will release any adsorbed CO_2 . This gentle temperature swing for adsorption/desorption is attractive for functionality, as limited energy is needed to regenerate the material to its porous state. Figure 1F illustrates the other captivating feature of ALF, which is its ability to discriminate against N_2 and instead adsorb CO_2 at all pressures. As flue gas is predominantly N_2 (roughly 85 %, with CO_2 making up most of the remainder), being able to adsorb CO_2 preferentially instead of N_2 is a prerequisite for CO_2 capture materials. The isotherms shown in Figure 1F were taken at 298 K, but the same performance exists at the operating temperature near 323 K.

Although ALF is remarkable in its ability to adsorb CO_2 preferentially instead of N_2 at elevated temperatures and with high quantities per weight/volume, ALF is not without flaws. Under high humidity (50 % relative humidity or greater) and elevated temperatures (310 K or above), ALF will slowly degrade. This degradation can be reduced by having CO_2 adsorbed within ALF's cavities, but for a real-world application with high humidity flue gas, ALF needs to be robust enough to withstand years of continued use. Therefore, the industrial use of ALF would require dried flue streams.

¹ NIST Center for Neutron Research, National Institute of Standards and Technology, Gaithersburg, MD 20899

² Department of Materials Science and Engineering, National University of Singapore, 9 Engineering Drive 1, 117575 Singapore

³ Department of Chemical and Biomolecular Engineering, National University of Singapore, 4 Engineering Drive 4, 117585 Singapore

⁴ Institute of Materials Research and Engineering, Agency for Science Technology and Research, 2 Fusionopolis Way, Innovis, Singapore, 138634

⁵ Department of Chemical and Biomolecular Engineering, University of Delaware, Newark DE 19716

⁶ Materials Research Laboratory, University of California, Santa Barbara, CA 93106

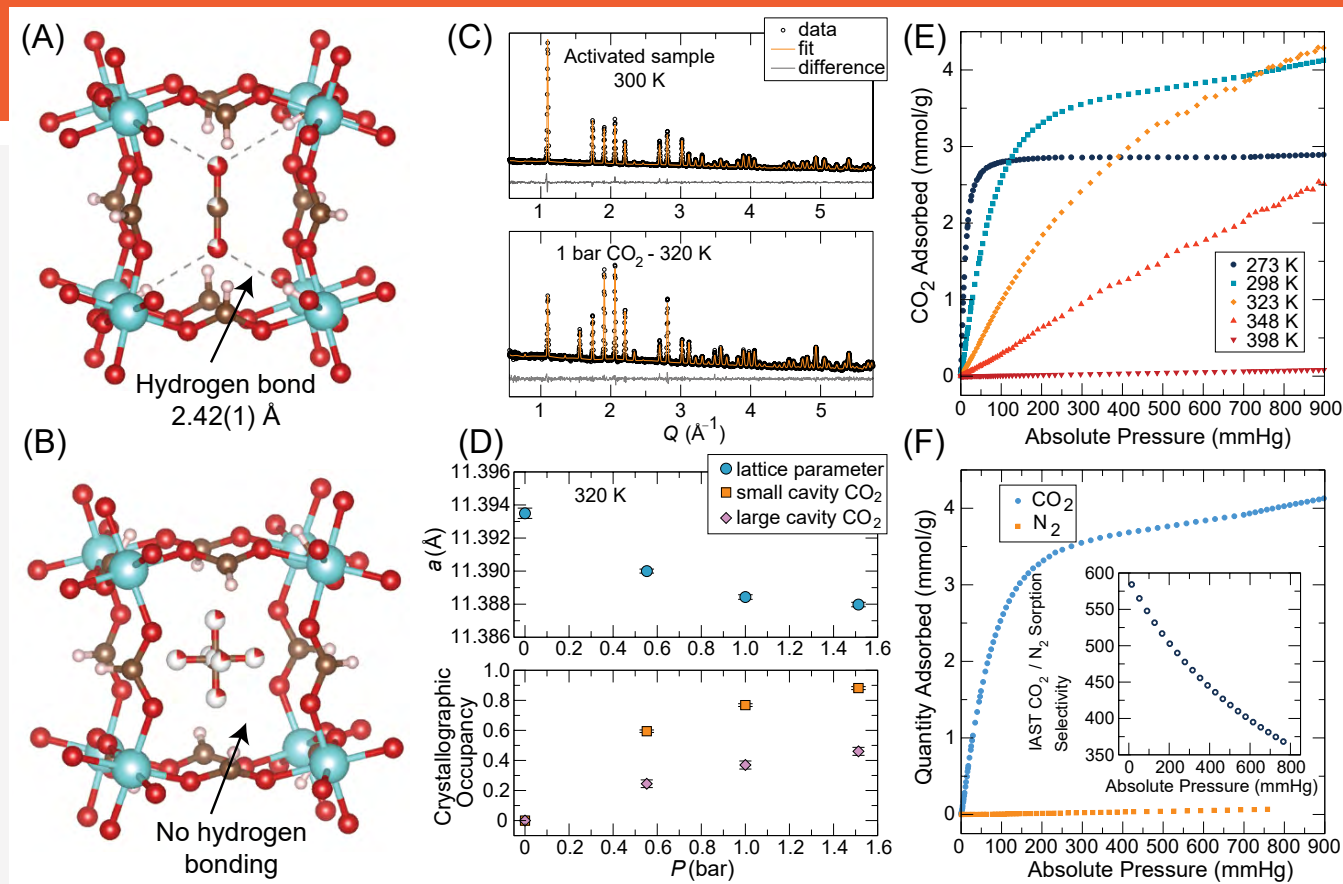


FIGURE 1: Summary of ALF crystal structure and neutron powder diffraction data taken at NIST. Error bars represent 1σ . (A) SC (small cavity), illustrating hydrogen bonding with formate ligands and CO_2 . (B) LC (large cavity), illustrating lack of hydrogen bonding between formate ligands and disordered CO_2 . (C) Top panel: [NCNR, BT1, $\lambda = 2.079 \text{ \AA}$] Rietveld refinement fit of activated ALF at 300 K; $a = 11.39051(12)$, $R_{\text{wp}} = 2.74\%$, $R_p = 2.19\%$. Bottom panel: Rietveld refinement fit of ALF exposed to 1 bar of CO_2 at 320 K; $R_{\text{wp}} = 3.35\%$, $R_p = 3.43\%$. The scan time for the activated sample data was twice that of the CO_2 exposed data. (D) Top panel: Lattice parameters obtained from Rietveld refinements as a function of CO_2 dosing pressure for ALF at 320 K. Bottom panel: CO_2 crystallographic occupancies obtained from Rietveld refinements as a function of the CO_2 dosing pressure for ALF at 320 K. (E) CO_2 adsorption isotherms at various temperatures. (F) Comparison of the CO_2 and N_2 adsorption isotherms at 298 K. The inset shows the CO_2/N_2 sorption selectivity based on ideal adsorbed solution theory (IAST) for a 15/85 mixture of CO_2/N_2 at 298 K.

For many materials, the cost of using this engineering addition is financially impractical. However, as ALF is prepared simply from commodity chemicals, the material offers an alternative option for CO_2 capture. The estimated cost of ALF on the metric ton scale from two commodity chemicals, aluminum hydroxide and formic acid, is only $\approx \$1000$ per ton, making it substantially cheaper than any of the other MOF alternatives, which currently range between $\$25,000$ and $\$100,000$ per ton. Furthermore, if ALF does degrade, this Al containing degradation product can be reused in future synthesis of ALF, which is another cost saving attribute. We propose that this extensive cost reduction afforded by ALF may well enable the inclusion of a drying step in the flue gas treatment process, costing as little as $\$2$ per ton of CO_2 captured in certain embodiments [3].

Lastly, ALF offers a remarkably efficient vehicle for long-term CO_2 storage in the future if the selective reduction of CO_2 to formic acid with solar hydrogen becomes more effective. CO_2 could then be stored in the stable ALF framework itself,

according to the overall reaction $\text{Al}_2\text{O}_3 + 6 \text{CO}_2 + 3 \text{H}_2 \rightarrow 2 \text{Al}(\text{HCOO})_3$. This reaction would yield a storage capacity for CO_2 of 81 wt % (not including additional CO_2 that could be further stored in the channels). If ALF is filled completely with CO_2 , and formic acid is sourced from captured CO_2 , ALF represents a CO_2 packing efficiency that is 96.35 % of that of dry ice.

References

- [1] H. A. Evans *et al.*, *submitted* (2022).
- [2] H. A. Evans *et al.*, *Nat. Rev. Mater.* **5**, 196 (2020).
- [3] M. M. F. Hasan *et al.*, *Ind. Eng. Chem. Res.*, **51**, 15665 (2012).

Weyl-mediated helical magnetism in NdAlSi

J. Gaudet,^{1,2,3} H.-Y. Yang,⁴ S. Baidya,⁵ B. Lu,⁶ G. Xu,² Y. Zhao,^{2,3} J. A.-Rodriguez-Rivera,^{2,3} C. M. Hoffmann,⁷ D. E. Graf,⁸ D. H. Torchinsky,⁶ P. Nikolić,^{9,1} D. Vanderbilt,⁵ F. Tafti,⁴ and C. L. Broholm^{1,2}



Topological materials have changed our way to think about the electronic band structure of materials and consequently, their electronic transport properties. This led to the discovery of novel transport properties including symmetry-protected surface states, anomalous Hall and Nernst effect, and photogalvanic effects [1]. Less explored, however, is how non-trivial topology of electrons can affect the collective electronic behavior of materials. To address this question, we studied the collective magnetism of the non-centrosymmetric tetragonal Weyl semimetal NdAlSi [2]. In this material, the interactions between the strongly localized magnetic Nd³⁺ *f*-orbitals are mediated by conductive electrons, which consist of Weyl electrons. Using neutron diffraction, we found these interactions mediate a long-wavelength modulated spin density wave (SDW) whose periodicity can be linked to the nesting wave vector between two topologically non-trivial Fermi pockets. We then show this SDW harbors a small helical chiral spin canting that is favored by bond-oriented Dzyaloshinskii-Moriya (DM) interactions predicted to arise in recent theories of Weyl-mediated RKKY magnetism [3].

We first introduce the crystal structure of NdAlSi (I4_{md}) in Fig. 1A. As the lack of inversion symmetry is crucial to stabilizing electronic Weyl nodes in NdAlSi, we have confirmed the validity of its nuclear structure using single crystal neutron diffraction and second harmonic generation measurements [2]. Confirming the presence of conductive electrons in NdAlSi, its electrical resistivity (Fig. 1B) shows semi-metallic behavior with low temperatures anomalies that are associated with the magnetism. These anomalies are also observed in the temperature dependence of the magnetic heat capacity (*C_p*) of NdAlSi (Fig. 1C). *C_p* shows one broad Schottky-like anomaly centered around 18 K as well as two sharp anomalies at *T_{inc}* = 7.2 K and *T_{com}* = 3.3 K that both arise from collective magnetism. The high-temperature anomaly can be modeled by the crystal-field induced symmetry breaking of the (2*J*+1) = 10 spin-orbital ground state of the Nd³⁺ ions (*J* = 9/2). The magnetic susceptibility data (Fig. 1D) reveals isotropic Curie-Weiss paramagnetic spins at high temperatures.

We have found complex magnetism for NdAlSi indexed by three temperature dependent magnetic ordering vectors

including *k*₁=(2/3+δ, 2/3+δ, 0), *k*₂=(1/3-δ, 1/3-δ, 0), and *k*₃=(3δ, 3δ, 0). The order parameter curves (Fig. 2A) and the temperature dependence of the incommensurability δ (Fig. 2B) were determined by tracking the temperature evolution of the magnetic Bragg peaks near both the *Q* = (2/3, 2/3, 0) and the *Q* = (1, 1, 2) positions. From Fig. 2B, we see that the incommensurate magnetism arises below *T_{inc}* and slightly diminishes upon cooling. The incommensurability of the (3δ, 3δ, 0) peaks are exactly three times the incommensurability of the (2/3+δ, 2/3+δ, 0) peaks indicating that they are the third harmonics of the main spin density wave. Their presence shows a “squaring” of the sine wave arising upon equilibrating the local magnetization on every Nd³⁺ sites. Below *T_{com}*, the system transits into a commensurate (δ = 0) ferrimagnetic state.

We performed magnetic refinement of the commensurate spin structure of NdAlSi. To do so, we measured the integrated intensities of several magnetic Bragg peaks indexed by all three different ordering vectors. The magnetic *k* = (0, 0, 0) peaks were found to originate from a ferromagnetic spin component pointing along the *c*-axis as they are observed only at nuclear-allowed positions and are absent at *Q* = (0, 0, *L*) positions [2]. The observation of the *k* = (2/3, 2/3, 0) and *k* = (1/3, 1/3, 0) peaks indicate the magnetic unit cell of NdAlSi is 3*3 times bigger than the nuclear unit cell. The (2/3, 2/3, 0) and (1/3, 1/3, 0) components are respectively sensitive to a spin component that is anti-parallel and parallel relative to the two Nd³⁺ ions sitting at the primitive site position *r*₁ = (0, 0, 0) and *r*₂ = (0, 1/2, 1/4). The spin polarization associated to each spin components can be deduced by their *L*-dependence, which are reported in Fig. 2C. The (2/3, 2/3, 0) Bragg peaks refine well assuming an Ising spin component, while the (1/3, 1/3, 0) peaks are well described by a helical in-plane spin component. The intensity of the (2/3, 2/3, 0) magnetic peaks are about two orders of magnitude greater than the (1/3, 1/3, 0) peaks so the Ising component of NdAlSi is prominent. We determined the spin structure of NdAlSi by adding up all its spin components and by assuming equal magnetization on every Nd³⁺ sites (2.9(1)μ_B). The result consists of an Ising ferrimagnetic up-down spin density wave propagating along the [1, 1, 0] (or [1, -1, 0]) direction with a small helical in-plane spin canting perpendicular to that direction (Fig. 2D).

¹ Department of Physics and Astronomy and Institute for Quantum Matter, The Johns Hopkins University, Baltimore, MD 21218

² NIST Center for Neutron Research, National Institute of Standards and Technology, Gaithersburg, MD 20899

³ Department of Materials Science and Engineering, University of Maryland, College Park, MD 20742

⁴ Department of Physics, Boston College, Chestnut Hill, MA 02467

⁵ Department of Physics and Astronomy, Rutgers University, Piscataway, NJ 08854

⁶ Department of Physics, Temple University, Philadelphia, PA 19122

⁷ Neutron Scattering Division, Oak Ridge National Laboratory, Oak Ridge, TN 37831

⁸ National High Magnetic Field Laboratory, Tallahassee, FL 32310

⁹ Department of Physics and Astronomy, George Mason University, Fairfax, VA 22030

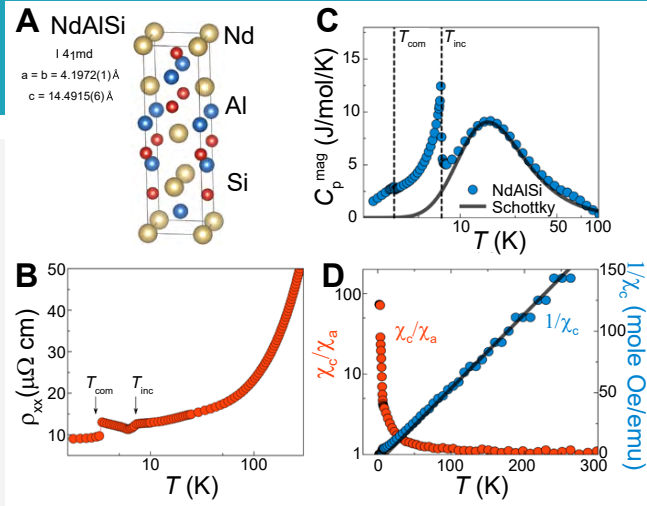


FIGURE 1: A) Non-centrosymmetric tetragonal crystal structure of NdAlSi (I4₁md, no.109). B) Temperature dependence of the electrical resistivity of NdAlSi. C) Temperature dependence of the magnetic heat capacity of NdAlSi, which was obtained by subtracting the heat capacity measured for the isostructural non-magnetic LaAlSi. D) Temperature dependence of the inverse susceptibility ($1/\chi_c$) for field along the c-axis (blue) and the ratio of the out-of-plane (χ_c) and in-plane (χ_a) magnetic susceptibility (red).

We have performed DFT calculations to determine the electronic band structure of NdAlSi (Fig. 3A), which consists of several linearly dispersive Weyl bands. We reported the exact momentum space location of the Weyl nodes in Fig. 3B. The resulting Fermi surface of NdAlSi is reported in Fig. 3C. We note that the observed magnetic order with $k = (2/3 + \delta, 2/3 + \delta, 0)$ can be favored through Fermi surface nesting between Fermi pockets lying close to $Q = (\pm 1/3, \pm 1/3, L)$ with both $L = 0$ and $L \neq 0$ (see q_m on Fig. 3C). Interestingly, the Fermi pockets involved in these nesting processes contain several Weyl nodes (see Fig. 3B), which allude to the possibility of Weyl-mediated magnetism. To further analyze this possibility, it has been shown that Weyl-mediated RKKY coupling induces DM interactions whose DM vector is constrained to lie parallel to the displacement vector between two nearest-neighbor (n.n.) spins [3]. Thus, using a 1st and 2nd n.n. exchange interactions, strong Ising crystal field anisotropy, and weaker bond-oriented DM interactions, we were able to energetically stabilize the observed spin structure of NdAlSi. In this case, the observed helical chiral spin canting is a direct consequence of the Weyl-mediated DM interactions.

In conclusion, we have performed bulk thermodynamic measurements, second harmonic generation measurements, electrical transport, neutron diffraction, and DFT calculations to study the collective magnetism of the non-centrosymmetric Weyl semi-metal NdAlSi. We found an incommensurate long-wavelength Ising modulated SDW, which transits to a ferrimagnetic commensurate up-down-down spin structure at low temperatures. The periodicity of this SDW can be linked to the nesting processes between topologically non-trivial Fermi pockets thus providing evidence for Weyl-mediated magnetism. We further show the presence of a small spin

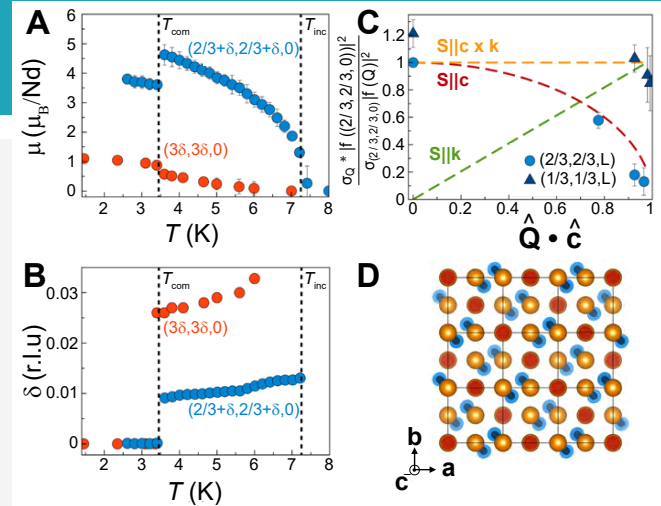


FIGURE 2: A) Order parameter for the $k_1 = (2/3 + \delta, 2/3 + \delta, 0)$ and $k_3 = (3\delta, 3\delta, 0)$ ordering vectors of NdAlSi. B) Temperature dependence of the magnetic incommensurability δ . C) L -dependence of the magnetic Bragg scattering of the $Q = (2/3, 2/3, L)$ and $Q = (1/3, 1/3, L)$ peaks. The Bragg intensity was divided by the Bragg intensity at $L = 0$ and normalized by the ratio of the form factors $f(Q)$. D) Spin structure of the ferrimagnetic state of NdAlSi. The red spins are pointing along the c-axis, while the blue spins are pointing down and have a small helical spin canting of $4(2)^\circ$. The tilt of the blue spins has been amplified by a factor 6 for viewing purposes.

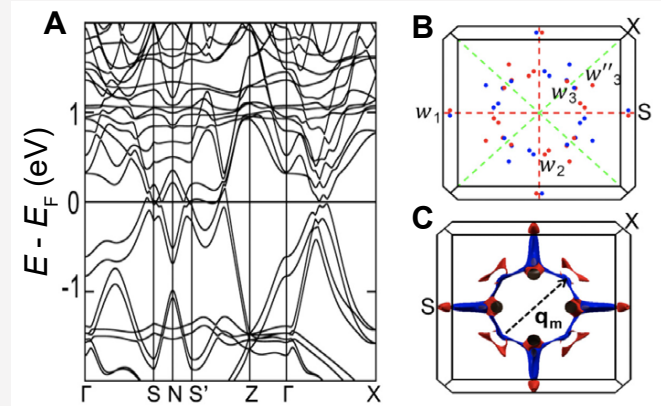


FIGURE 3: A) Electronic band structure of NdAlSi obtained by DFT calculations and benchmarked by quantum oscillations measurements. B) Location of the electronic Weyl nodes in momentum space of NdAlSi. C) Fermi surface of NdAlSi. The vector q_m shows the nesting vector that linked non-trivial Fermi pockets by the magnetic ordering vector $k = (2/3 + \delta, 2/3 + \delta, 0)$.

canting whose chirality is a direct consequence of the spin-momentum locking of the Weyl fermions. We hope our work will inspire further theoretical and experimental studies to investigate novel magnetic phenomena mediated by topological non-trivial electrons.

References

- [1] N. P. Armitage, E. J. Mele, Ashvin, Rev. Mod. Phys. **90**, 015001 (2018).
- [2] J. Gaudet *et al.*, Nat. Mat. **20**, 1650 (2021).
- [3] P. Nikolić, Phys. Rev. B **103**, 155151 (2021).

Magnetic fields induce a topological electronic transition leading to a new geometry for thermoelectric conversion in the itinerant ferromagnet $\text{Fe}_{3-x}\text{GeTe}_2$

P. P. Balakrishnan,¹ J. Macy,^{2,3} D. Ratkovski,² M. Strungaru,⁴ Y.-C. Chiu,^{2,3} A. F. Savvidou,^{2,3} A. Moon,^{2,3} W. Zheng,^{2,3} A. Weiland,⁵ G. T. McCandless,⁵ J. Y. Chan,⁵ G. S. Kumar,⁶ M. Shatruk,⁶ A. J. Grutter,¹ J. A. Borchers,¹ W. D. Ratcliff,¹ E. S. Choi,^{2,3} E. J. G. Santos,^{4,7} and L. Balicas^{2,3}

Topologically non-trivial compounds hold great promise for technological applications due to their fascinating coupled magnetic, optical, and electronic properties. In particular, the large anomalous Nernst-effect, in which heat flow is converted to a transverse electric voltage, is a possible candidate for efficient thermoelectric energy conversion. $\text{Fe}_{3-x}\text{GeTe}_2$ has a layered, van der Waals structure and is a metallic ferromagnet in which the magnetic moments align parallel to the c-axis. In addition to other novel magnetoelectronic phenomena, this material exhibits large anomalous Hall and Nernst coefficients that are claimed to originate from the non-trivial electronic topology. In this work, our combined neutron diffraction, transport measurements, and simulations clearly demonstrate that these anomalies are consistent with a topological electronic transition that is associated with magnetic field-induced spin textures.

The net magnetization of a bulk $\text{Fe}_{3.05}\text{GeTe}_2$ crystal (Fig. 1A), with a ferromagnetic ordering temperature $T_C \approx 203$ K, differs starkly when cooled with or without a magnetic field (field-cool FC and zero-field-cool ZFC, respectively). The ZFC ground state has a much lower magnetization, and the trajectory to this state exhibits anomalies near 37 K and 153 K. The electrical resistivity shows only a change in slope at T_C , while broad anomalies in the thermopower (Fig. 1B) and thermal conductivity are evident near all three temperatures. This behavior suggests that variations in the spin-spin scattering mechanism has a clear effect on the charge carriers.

In contrast to magnetometry, neutron diffraction is a direct probe of the ordered iron moments. Specifically, all domains with moments in the plane perpendicular to the scattering vector Q contribute equally to the magnetic scattering, whereas the bulk magnetization of domains pointing along opposite directions cancels out. Zero field diffraction measurements made on the BT-4 triple-axis spectrometer reveal a continuous ferromagnetic transition in which the Fe moments order ferromagnetically along the c-axis (brown markers in Fig. 1A). This is consistent with previous observations and our simulations of a labyrinthine domain ground state (Fig. 2D) with moments aligned along the c-axis but domains anti-aligned relative to each other and moments tilting at the

domain walls. To reconcile the smooth neutron diffraction data with the field-cooled magnetization data, we speculate that the magnetization anomalies arise from small variations in the tilt angle of the moments with respect to the inter-planar c-axis.

Large anomalous in-plane transport is observed for magnetic fields along the c-axis, with a change in sign of the Nernst signal corresponding to a topological transition (Fig. 1C). Remarkably, large anomalous transport is also observed when $\mu_0 H_{\parallel}$ lies in-plane and is aligned along the gradient of the chemical potential generated by thermal gradients or electrical currents, a configuration that should not lead to their observation. These anomalous planar transport quantities (Fig. 2A) do not scale with the component of the planar magnetization (M_{\parallel}), showing instead a sharp decrease beyond $\mu_0 H_{\parallel} \cong 4$ T or the field required to align the magnetic moments along $\mu_0 H_{\parallel}$. We argue that chiral spin structures associated with domain walls, or the very same magnetic domains, lead to a field-dependent spin chirality that produces a novel type of topological transport in the absence of interactions between the magnetic field and electrical or thermal currents.

These transport anomalies suggest that current and heat may be transported by different carriers; however, we tested this idea using the Wiedemann–Franz law and found no evidence for this. Thus, the electrical and thermoelectric transport can only be understood in terms of a gauge field intrinsic to the electronic band structure of $\text{Fe}_{3-x}\text{GeTe}_2$. This gauge field acts as an effective “band magnetic field” that bends the electronic orbits as in a magnetic field, but it produces an anomalous Hall-like signal, even in the paramagnetic state, in the absence of interactions between the electrical currents and the external magnetic field. At lower temperatures within the ferromagnetic state, we observed for the first time that this anomalous and antisymmetric planar Hall signal is accompanied by anomalous planar Nernst and thermal Hall effects. We propose that the local Dzyaloshinskii–Moriya (DM) interaction, a special type of magnetic interaction that favors non-collinear alignment, generates a magnetic-field-dependent canted and non-coplanar spin structure that scatters the charge carriers, thereby affecting their Berry phase and leading to these novel effects.

¹ NIST Center for Neutron Research, National Institute of Standards and Technology, Gaithersburg, MD 20899

² National High Magnetic Field Laboratory, Florida State University, Tallahassee, FL 32310

³ Department of Physics, Florida State University, Tallahassee, FL 32306

⁴ Institute for Condensed Matter Physics and Complex Systems, School of Physics and Astronomy, The University of Edinburgh, Edinburgh EH9 3FD, United Kingdom

⁵ Department of Chemistry and Biochemistry, The University of Texas at Dallas, Richardson, TX 75080

⁶ Department of Chemistry and Biochemistry, Florida State University, 95 Chieftain Way, Tallahassee, FL 32306

⁷ Higgs Centre for Theoretical Physics, The University of Edinburgh, Edinburgh EH9 3FD, United Kingdom

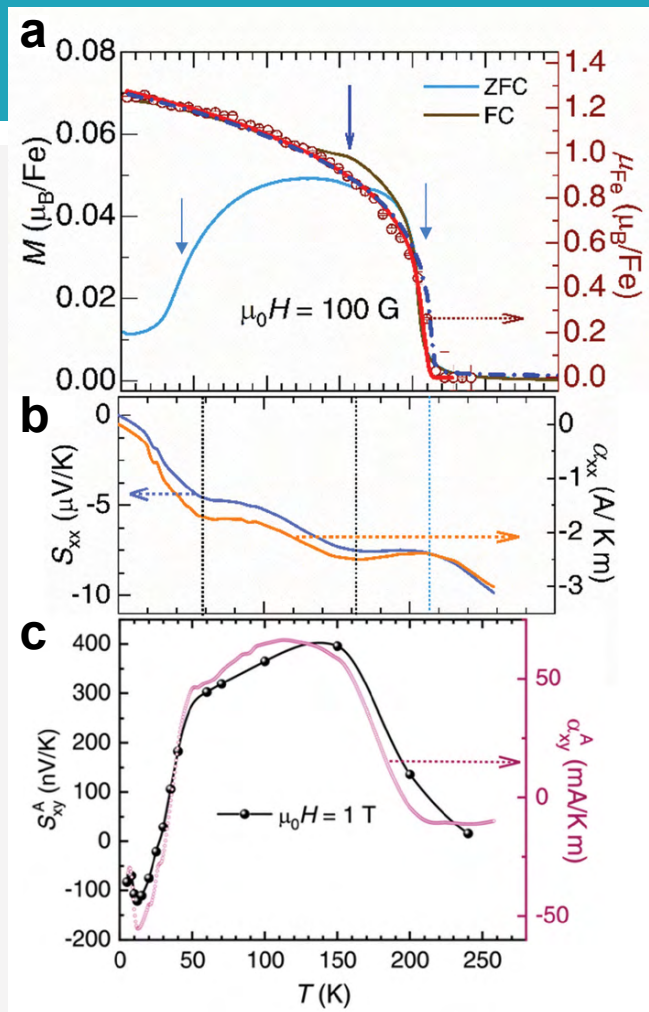


FIGURE 1: Anomalies in thermal transport correspond to anomalies in magnetization with temperature. (a) Magnetization M for a single crystal with a magnetic field of $\mu_0 H \approx 100 \text{ G}$ applied along the inter-layer direction; light blue and brown curves correspond to zero-field and field-cooled conditions, respectively. Brown markers represent the normalized magnetic moment per Fe atom as measured by zero-field neutron diffraction. Red line is a phenomenological model fit to the data while the dashed dark blue line represents the calculated $\mu_{Fe}(T)$ according to a spin Hamiltonian that includes biquadratic exchange interactions. Arrows indicate the maximal derivatives near 150 K and 50 K as well as the Curie temperature $T_c \approx 203 \text{ K}$. (b) Thermoelectric power S_{xx} (left) and Peltier conductivity $\alpha_{xx} = \sigma_{xx} S_{xx}$ (right) of a different sample have broad anomalies centered around $T_c \approx 212 \text{ K}$ and 160 K and 60 K, matching the anomalies in magnetization. (c) Anomalous Nernst coefficient S_{xy}^A with the field applied along the c-axis exhibits these same anomalies and changes sign.

These observations are supported by field-dependent neutron diffraction measurements (Fig. 2B, c). At $T = 50 \text{ K}$, there is a pronounced hysteresis in the neutron data between the increasing and decreasing field sweeps accompanied by a change in the anisotropy direction near 4.5 T that is coincident with the dips in the anomalous planar transport parameters [1]. These results are suggestive of changes in the magnetic domain structure and spin texture. A spin texture with local regions of chiral spin ordering is supported by our Monte Carlo simulations including DM and biquadratic exchange interactions, which correctly capture the formation

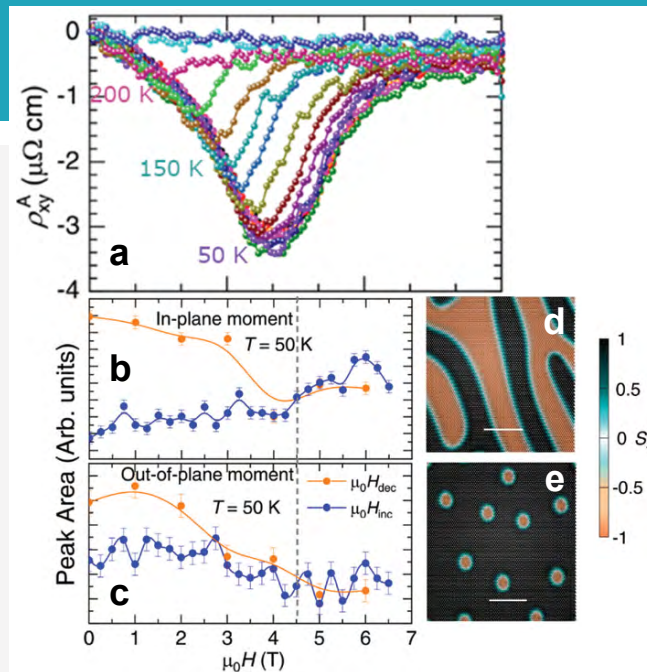


FIGURE 2: Large anomalous planar transport correlates with changes in magnetic spin texture in an applied magnetic field. (a) Anomalous Hall resistivity ρ_{xy}^A for a single crystal as a function of $\mu_0 H$ applied along the a-axis. All thermoelectric transport coefficients follow similar behavior, exhibiting an anomalous peak as a function of $\mu_0 H$ that shifts with temperature rather than scaling with magnetization. (b,c) Neutron diffraction intensities corresponding to in-plane and out-of-plane orientation of Fe moments as $\mu_0 H$ is increased (blue) and then decreased (orange), resulting in an irreversible hysteretic magnetic transition at the same field as the anomalous transport peak. (d,e) Atomistic simulations of the limiting 0 K state when cooling in (d) zero field (e) or 2 T. Different preparations of the sample result in (d) the experimentally observed striped domains with chiral domain walls or in (e) the predicted skyrmion or chiral bubble state. The white scale bar is 70 nm wide, and each pixel corresponds to one Fe moment.

of the labyrinthine domains previously observed under zero magnetic field (Fig. 2D) as well as the development of Néel skyrmions upon field application (Fig. 2E). Most importantly, upon application of magnetic fields within the plane, the biquadratic exchange interaction stabilizes labyrinthine domains characterized by a chiral spin texture, thus providing the necessary ingredient of spin chirality for the topological transport we have found.

Finally, the Nernst effect is often used as a probe of topological excitations in quantum materials, which provide a means to convert heat into electricity. Our study suggests not only a new way to detect such excitations but also a new geometry for heat conversion that expands the horizon of thermoelectric technology.

References

- [1] J. Macy *et al.*, Appl. Phys. Rev. **8**, 041401 (2021).

Magnetic excitations: a window into the electronic interactions in a spin-triplet superconductor

N. P. Butch,^{1,2} S. Ran,^{1,2,3} S. R. Saha,^{1,2} P. M. Neves,^{1,2} M. P. Zic,^{1,2} J. Paglione,^{1,2} S. Gladchenko,¹ Q. Ye,^{1,4} and J. A. Rodríguez-Rivera^{1,4}



UTe₂ has captured the world's attention because it may be an exotic spin-triplet topological superconductor [1]. Evidence for such a configuration was identified in a combined study of optical Kerr rotation, sensitive to a spontaneous magnetic moment, and calorimetry, which found that there are two superconducting phase transitions [2]. The ancillary existence of chiral, or directionally oriented, surface states was determined by scanning tunneling spectroscopy [3]. An outstanding question is, what kind of electronic states and presumably magnetic interactions can give rise to such superconductivity?

Inelastic neutron scattering is a useful tool to study electronic interactions. Although it is typically used to study magnetic structures and their excitations, in certain materials, it can indirectly probe aspects of the electronic structure. Recent neutron studies of UTe₂ have explained their observations in terms of magnetic interactions reflective of a magnetic ordered state [4, 5]. In contrast, this study leads to the conclusion that the dominant magnetic excitations in UTe₂ are not due to incipient magnetic order, but rather to a hybridized electronic band structure [6]. In particular, our results reveal excitations that have a peak intensity at an energy transfer of 4 meV, a momentum distribution along the Brillouin zone edges, and a temperature dependence that all agree with the characteristics of *f*-electron hybridization, and thus the heavy renormalized electronic band structure. This shows that the superconductivity involves heavy quasiparticles but cannot determine whether electron interactions are predominantly ferromagnetic or antiferromagnetic [6].

For this experiment, single crystals of UTe₂ were synthesized by the chemical vapor transport method at the Quantum Materials Center of the University of Maryland in College Park. Crystals were shipped to the NCNR, where Laue X-ray diffraction was used to determine the crystalline orientation. This was a challenging process, as neutron scattering demands an appreciable mass of material, but UTe₂ crystals tend to be small, and are air-sensitive. In total, 1.2 g of single crystals, ranging in mass from 0.01 g to 0.1 g, were coaligned and affixed to a copper assembly that was designed for measurements at low temperatures in a dilution refrigerator. The DCS spectrometer was used for initial work and the data discussed here were measured on the MACS spectrometer.

The magnetic excitations in UTe₂ were studied in the H-K plane, corresponding to the a-b plane of the orthorhombic crystal structure. The main results, presented in Figure 1, are bands of intense magnetic scattering, plotted here as the dynamic magnetic susceptibility, at energy 4 meV. Note that these bands are periodic along the K direction and coincide with the overlaid Brillouin zone boundaries, offering an important clue that these excitations derive from the electronic structure of the material, rather than from excitations associated with magnetic order, which is absent in UTe₂ at ambient conditions. Calculations of the neutron scattering in models of materials in which localized *f*-electrons hybridize with conduction electrons, also known as Kondo lattices, show this kind of Brillouin zone boundary scattering [7].

The momentum and energy dependence of the magnetic excitations in UTe₂ is shown in Figure 2. Along the K direction, the excitations sharply disperse, with minima at 4 meV, at the momenta indicated in Figure 1. In fact, the 4meV energy scale of these magnetic excitations is the same as that of the hybridization gap detected in scanning tunneling spectroscopy, showing that these phenomena are consistent. Upon close inspection, it is apparent that the V-shaped dispersion is asymmetric and is steeper towards the Z point. In contrast, the dispersion is horizontal, or independent of momentum, in the H direction. This behavior may arise from the directional, chain-like crystal structure, but properly understanding the asymmetry, as well as the detailed intensity variation, requires further study.

The temperature dependence of the magnetic excitations corresponds closely to the temperature evolution of the Kondo lattice in UTe₂. One of the defining features of such materials is their relatively small energy scale compared to that of typical metals. This can lead to dramatic changes in the magnetic and electrical behavior of Kondo lattices as they are cooled below room temperature and approach absolute zero. At high temperatures, say near 300 K, the electrons are weakly correlated, or in other words, behave as if they only weakly interact with each other. However, once cold, the *f*-electrons act in concert as a hybridized metal. This is apparent in the bulk magnetic susceptibility, for example, where a maximum occurs as the electrons cross over from their individual to collective behavior.

¹ NIST Center for Neutron Research, National Institute of Standards and Technology, Gaithersburg, MD 20899

² Maryland Quantum Materials Center, Department of Physics, University of Maryland, College Park, MD 20742

³ Department of Physics, Washington University in St. Louis, St. Louis, MO 63130

⁴ Department of Materials Science and Engineering, University of Maryland, College Park, MD 20742

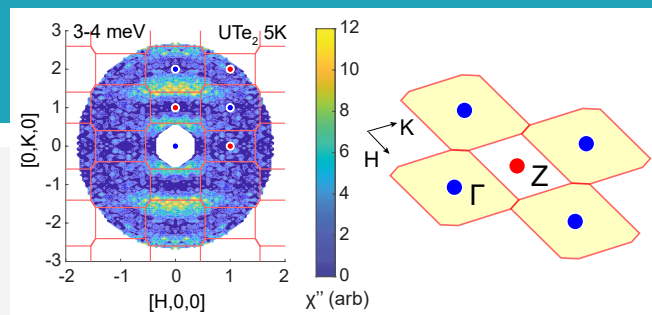


FIGURE 1: Magnetic excitations in UTe_2 at a temperature of 5 K. The excitations in the H-K plane are most intense in the energy range 3 meV to 4 meV, shown here on a reciprocal lattice map with an overlay of the repeating Brillouin zones. The excitations clearly fall on the boundaries between adjacent Brillouin zones, which is a feature of magnetic excitations arising from heavy electron bands. The alternating pattern of Gamma and Z points of this cut of the body-centered orthorhombic structure is illustrated in the schematic.

The intensity of the magnetic excitations in UTe_2 closely follows this trend. As seen in Figure 3, the intensity of the excitations is strongest at low temperatures and decreases with increasing temperature. The main features are still discernable at 20 K, but they are gone by 60 K. The hybridization gap energy of 4 meV corresponds to a temperature of approximately 40 K, which is where the maximum in the bulk magnetic susceptibility is measured. The fact that the magnetic excitations in UTe_2 develop below 40 K points once again to their origin in Kondo lattice physics. Note also that the data at 0.2 K were collected at temperatures for which UTe_2 is superconducting. No dramatic changes were detected. There are subtle, but measurable, changes from the data at 5 K that suggest that the electronic structure may respond to the onset of superconductivity, even at low temperatures. An important final point regards the goal of identifying whether the electrons in UTe_2 tend towards ferromagnetism or antiferromagnetism, which could inform understanding of the superconductivity. Unfortunately, these magnetic excitations due to electron hybridization do not provide information about potential magnetic order. Thus, additional neutron studies will be required to search for other signatures of magnetic interactions.

To summarize, this study has demonstrated that the magnetic excitations in UTe_2 measured by inelastic neutron scattering are signatures of Kondo lattice physics. The excitations have the appropriate energy, momentum, and temperature dependence for such interactions. This result shows that the unusual spin-triplet superconductivity in this material emerges from a background of strongly-interacting, hybridized electrons, further highlighting the exotic nature of this interesting material.

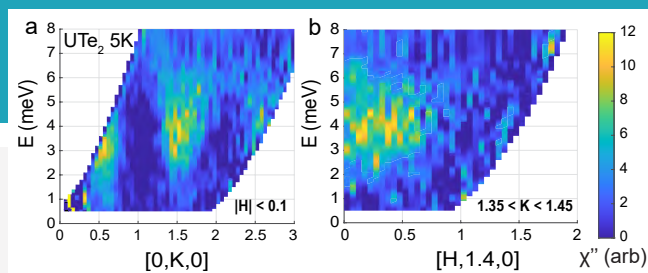


FIGURE 2: Momentum dependence of magnetic excitations in UTe_2 . a) The dispersion is V-shaped along the K direction, with a minimum energy of 4 meV at the Brillouin zone edge. b) The excitation energy is constant parallel to the Brillouin zone edge.

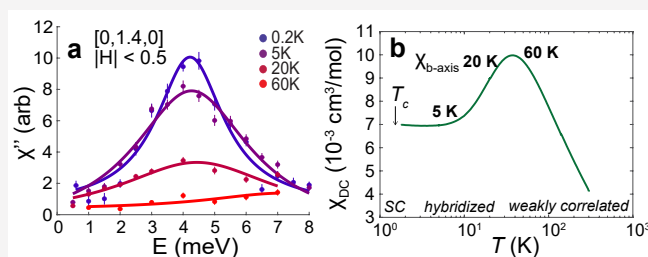


FIGURE 3: Temperature dependence of the magnetic excitations in UTe_2 . a) The energy dependence of the excitations at the zone edge decreases as temperature increases. b) This temperature dependence follows closely the development of the Kondo lattice hybridization, which is also reflected in the bulk magnetic susceptibility.

References

- [1] S. Ran *et al.*, *Science* **365**, 6454 (2019).
- [2] I. M. Hayes *et al.*, *Science* **373**, 797 (2021).
- [3] L. Jiao *et al.*, *Nature* **579**, 523 (2020).
- [4] C. Duan *et al.*, *Phys. Rev. Lett.* **125**, 237003 (2020).
- [5] W. Knafo *et al.*, *Phys. Rev. B* **104**, L100409 (2021).
- [6] N. P. Butch *et al.*, *npj Quantum Materials* **7**, 39 (2022).
- [7] B. H. Brandow *Phys. Rev. B* **37**, 250 (1988).

Chemical origin of magnetic dead shells in Ni nanoparticles deduced from polarized small-angle neutron scattering

B. Das,¹ J. T. Batley,¹ K. L. Krycka,² J. A. Borchers,² P. Quarterman,² C. Korostynski,¹ M. Nguyen,¹ I. Kamboj,¹ E. S. Aydil,³ and C. Leighton¹



Magnetic nanoparticles (NPs) can be chemically synthesized with impressive precision and now underpin several existing and developing applications in the biomedical arena and beyond [1]. Superparamagnetism dominates the magnetic behavior of such NPs. In essence, as the size of ferromagnetic NPs is decreased, the energy required to reverse the magnetization also decreases, at some point reaching thermal energies. At a given size and time scale, as temperature increases there is thus a superparamagnetic blocking point where thermal fluctuations of the magnetization become spontaneous, averaging the net magnetization to zero. While this superparamagnetism is relatively simple in principle, quantitative understanding has proven challenging due to myriad complicating factors. These include complex magnetic anisotropies, the common occurrence of dead shells with suppressed magnetization, statistical distributions in NP characteristics, *etc.* Recent work [2] was thus significant in that it achieved *quantitative* understanding of the relation between blocking temperature and NP size in ensembles of elemental Ni NPs. However, this assumed (a) a surface dead shell of unknown origin, and (b) bulk-like magnetism in the Ni NP cores, even at diameters down to 4 nm. In the current work [3] these assumptions have been rigorously tested using polarized small-angle neutron scattering (SANS), generating critical new insight.

The Ni NP ensembles studied in this work were synthesized by chemical means and then characterized by X-ray diffraction (XRD), transmission electron microscopy (TEM), Raman and Fourier transform infrared spectroscopies, magnetometry, and unpolarized and polarized SANS [2,3]. The NPs have an average diameter between 4 nm to 22 nm and are coated with trioctylphosphine and oleylamine ligands. As is often the case, the NPs exhibit suppressed magnetization relative to bulk, which can be accounted for quantitatively by assuming non-ferromagnetic surface shells. The estimated thickness of these shells (t^*) was found to depend on synthesis temperature T_s : $t^* \approx 1$ nm at $T_s = 200$ °C [2]. Fig. 1 provides the first clue to the origin of these dead shells through experiments performed at various T_s . At 170 °C and 200 °C, typical Ni NPs are observed in TEM (Figs. 1(D, E)); XRD patterns (Figs. 1(A, B)) are consistent with Ni, and there is clear evidence of ferromagnetism (Fig. 1(G)). Data analysis suggests $t^* = 0.6$ nm and 1.2 nm, respectively. Increasing T_s to just 250 °C,

however, eradicates all XRD signatures of Ni (Fig. 1(C)), generates a clear core-shell morphology (Fig. 1(F)), and destroys the ferromagnetism (Fig. 1(G)). Instead of Ni, the 250 °C XRD pattern in Fig. 1(C) is that of Ni_{12}P_5 , a line compound in the Ni-P equilibrium phase diagram. Trioctylphosphine, the reducing agent, solvent, and ligand used in this, and many other NP syntheses [1], is the only viable source of this P. We thus deduce that diffusion-limited surface reactions generate Ni_{12}P_5 at high T_s , leading to the hypothesis that the dead shells at lower T_s , while very thin, may also be of chemical origin and due to surface phosphide formation.

This hypothesis was tested in a series of unpolarized and polarized SANS measurements on the NG-7 SANS instrument at the NIST Center for Neutron Research. SANS is ideally suited to this task, as it can determine the average internal structures of magnetic NPs, both chemical and magnetic, with sub-nm resolution. Unpolarized SANS data taken at 300 K revealed isotropic scattering in the Q_x - Q_y detector plane (Q_x , Q_y are components of the scattering wave vector Q) and were thus circularly averaged to obtain the scattering cross-section ($d\Sigma/d\Omega$) vs Q profiles in Fig. 2(A). The latter reveal a drop-off at low Q , followed by a peak/shoulder feature, all aspects of which are captured by SasView fits (solid red lines). These fits employ a hard-sphere structure factor, a core-shell form factor, the expected size dispersity, and a generalized-Porod background. Most importantly, the fits are based on cores of pure Ni surrounded by shells of Ni_{12}P_5 . (Since the nuclear scattering length densities of Ni and P differ substantially, SANS sensitivity to the exact Ni-P composition of the shell is high). Moreover, the fitted NP diameters agree with TEM while, remarkably, the shell thicknesses also agree with estimates from magnetometry, *both to within ≈ 0.1 nm*. The Ni_{12}P_5 shell thickness deduced from SANS increases from 0.6 nm at $T_s = 170$ °C, to 1.1 nm at 200 °C, to 5.3 nm at 250 °C. This progression directly confirms the hypothesized Ni_{12}P_5 shell, which eventually consumes all Ni at high T_s , generating *hollow* cores (Fig. 1(F)).

Significantly, the fits in Fig. 2(A) are insensitive to the Ni core magnetization, *i.e.*, these unpolarized SANS data are chemically-dominated. Full-polarization SANS measurements were therefore also performed, using a supermirror cavity and spin flipper to control the incoming neutron polarization (spin up or spin down) and a ^3He analyzer to select the outgoing

¹ Department of Chemical Engineering and Materials Science, University of Minnesota, Minneapolis, MN 55455

² NIST Center for Neutron Research, National Institute of Standards and Technology, Gaithersburg, MD 20899

³ Department of Chemical and Biomolecular Engineering, New York University Tandon School of Engineering, Brooklyn, NY 11201

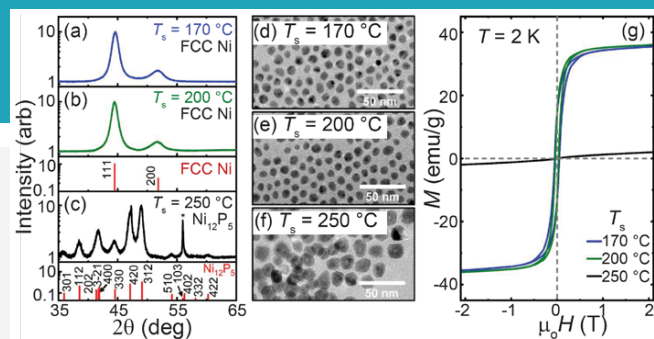


FIGURE 1: XRD patterns (a-c), TEM images (d-f), and magnetization hysteresis loops (g) of Ni NP ensembles synthesized at $T_s = 170^\circ\text{C}$, 200°C , and 250°C .

polarization. In this way, non-spin-flip (unchanged polarization) and spin-flip (reversed polarization) scattering profiles were measured at 5 K, at the coercive magnetic field (*i.e.*, where the *net* magnetization is zero). For NPs synthesized at $T_s = 200^\circ\text{C}$, for example, the non-spin-flip profile is isotropic and in quantitative agreement with the unpolarized data, as expected. However, the spin-flip cross-section shown in Fig. 2(B) is stretched along Q_x (parallel to the applied field). Due to neutron scattering selection rules, the sector cut illustrated in this figure enables the isolation of a purely magnetic cross-section, sensitive only to the magnetization perpendicular to the field. This cross-section is shown in Fig. 2(C) and is strikingly reminiscent of single-particle spherical form factors. This observation is reinforced by the solid red line fits, which are based on the Ni core/ Ni_{12}P_5 shell model, but with fitted magnetizations of the core and shell. Assuming an isotropically-distributed magnetization at the coercive field (which we have verified [3]), these magnetizations refined to zero for the shell, in all cases, and to 52 emu g^{-1} to 58 emu g^{-1} for the Ni cores at $T_s = 170^\circ\text{C}$ and 200°C ($1\text{ emu} = 10^{-3}\text{ A m}^2$). Complementary measurements made in *saturating* fields generated non-spin-flip magnetic cross-sections sensitive to the net magnetization *parallel* to the field and led to similar conclusions: a non-magnetic shell and Ni core magnetizations of 50 emu g^{-1} to 55 emu g^{-1} . These measurements thus not only further validate the Ni core/ Ni_{12}P_5 shell morphology, but they also confirm the nonmagnetic nature of the shell, the bulk-like magnetism in the core despite the nanoscale dimensions (bulk Ni has 58 emu g^{-1}), and the insignificance of inter-particle magnetic interactions at low fields (the fits in Fig. 2(C) ignore such interactions). Finally, half-polarization SANS measurements showed that these findings persist at all measured temperatures (5 K to 300 K), particularly the bulk-like Ni core ferromagnetism.

Our SANS measurements thus directly confirm the prior assumptions of a non-ferromagnetic dead shell for these Ni NPs, a ferromagnetic core with bulk-like magnetic characteristics, and negligible inter-particle magnetic interactions. The non-ferromagnetic dead shell is found to be of chemical origin, occurring due to diffusion-limited (and thus synthesis-temperature-dependent) reactions with the

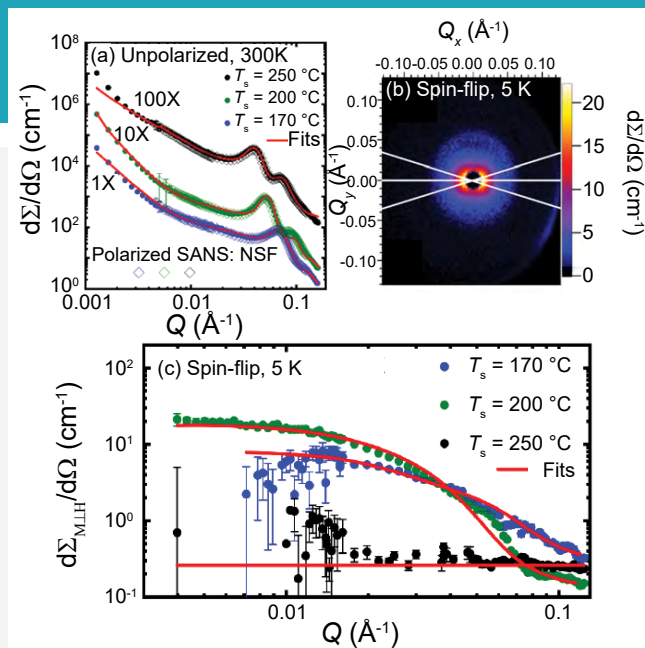


FIGURE 2: (a) 300-K unpolarized $d\Sigma/d\Omega(Q)$ for Ni NP ensembles synthesized at $T_s = 170^\circ\text{C}$ to 250°C . (b) 5-K polarized Q_x - Q_y map of the spin-flip scattering for Ni NPs synthesized at $T_s = 200^\circ\text{C}$. (c) Magnetic (spin-flip) $d\Sigma/d\Omega(Q)$ for $T_s = 170^\circ\text{C}$ to 250°C . All polarized data are at the coercive field.

trioctylphosphine commonly used in chemical synthesis of NPs, forming paramagnetic Ni_{12}P_5 . The prior claim of fully quantitative understanding of the superparamagnetic blocking temperature-particle size relation in ferromagnetic NPs [2] is thus directly supported by SANS determinations of the chemical and magnetic structure of Ni NP ensembles [3]. These results also point to a potential route to ligand-free stabilization of magnetic NPs (if the Ni-P shell formation can be appropriately controlled) and serve to further highlight the power of SANS in the study of magnetic NP systems for both fundamental and applied purposes.

References

- [1] M. Colombo, S. Carregal-Romero, M. F. Casula, L. Gutiérrez, M. P. Morales, I. B. Böhm, J. T. Heverhagen, D. Prosperi, W. J. Parak, *Chem. Soc. Rev.* **41**, 4306 (2012).
- [2] J. T. Batley, M. Nguyen, I. Kamboj, C. Korostynski, E. S. Aydil, C. Leighton, *Chem. Mater.* **32**, 6494 (2020).
- [3] B. Das, J. T. Batley, K. L. Krycka, J. A. Borchers, P. Quarterman, C. Korostynski, M. Nguyen, I. Kamboj, E. S. Aydil, C. Leighton, in press, *ACS Appl. Mater. & Interf.*

Characteristic rotation of principal stress axes after friction stir welding

T. Gnäupel-Herold,¹ M. Bhattacharyya,² K. Raja,³ J. Darsell,⁴ S. Jana,⁵ and I. Charit^{2,4,5}

Chloride-induced stress corrosion cracking (CISCC) in spent nuclear fuel dry storage canisters (SNF-DSC) is an area of great concern for the long-term storage of radioactive waste in salt caverns. Generally, austenitic stainless-steel plates of 13 mm to 16 mm thickness are arc-welded to fabricate overpack drums that host SNF for long-term storage in salt caverns. While the SNF cools, a convective airflow sets in the annular area between the canister and overpack, which draws in salt-containing dust. The decay heat from the SNF deliquesces the salt in the form of deposits. These deposits are detrimental to the canisters, as they initiate various forms of corrosion cracks that are not easily repaired by conventional arc welding because of the SNF radioactivity.

Friction stir welding (FSW), a solid state joining method with lower heat input, is being considered as an effective way to repair cracks in stainless steel DSCs. The damage repair can be accomplished by passing a rotating tool along a pre-existing crack. The process produces a characteristic residual stress state which may improve resistance to environmental degradation through the creation of a compressive stress profile on or near the plate surface. It is surmised that a suitable combination of the tool shape, tool rotation rate, tool travel speed and down force can produce the desired compressive stresses and thus suppress crack formation. To test this hypothesis, simulated cracks were produced in hot-rolled, annealed stainless steel plates (304L, 12.7 mm thick) using electrical discharge machining to create narrow slits 0.4 mm wide and 5 mm deep. These simulated cracks were healed using isothermal FSW at different temperatures (725 °C, 825 °C, 900 °C). The resulting residual stresses were evaluated through a combination of neutron diffraction and surface X-ray diffraction in combination with chemical layer removal, thus allowing both detailed mapping of bulk and shallow near-surface residual stresses [1].

For comparable materials, stresses generated by FSW share common aspects because of process similarities. However, large differences in stresses may also arise depending on factors such as power input, thickness, and, crucially, whether the process was used on a monolithic plate or to join two plates. Research has overwhelmingly focused on stresses in directions suggested by the weld geometry: the weld direction, the transverse direction (the in-plane direction perpendicular to the weld direction), and the direction normal to the surface.

The stress measurements were performed using the BT-8 Diffractometer for Stress and Texture at the NIST Center for Neutron Research. The neutron results show that near-surface compressive stresses were indeed generated in the transverse direction (see contour maps in Fig. 2) for all weld temperatures; however, a tensile-stress-distribution broadening in the weld direction arises on heating. The depth range from 0 mm to 1 mm below the surface was not included in the neutron measurements due to the difficulties of neutron diffraction stemming from minimum gauge volume requirements; therefore, additional measurements were done using X-ray diffraction together with chemical layer removal.

Surface and layer-removed data proved crucial for assessing the true depth distribution of the stress (Fig. 2). Strong compressive stress gradients were found at depths between 0 mm and 1 mm, which, in the case of the transverse stresses, exhibit a stronger dependence on the weld temperature. The region of interest is the stir zone and its immediate vicinity, which is where the original crack was 'healed.' Prior to the FSW procedure, the crack originated in an area with high tensile stress.

Post FSW, the original stresses have been replaced by those shown in Fig. 2. Given that FSW produces crack-suppressing stresses only in the transverse direction, it can be surmised that the weld direction should follow the direction of the crack—not just to erase the crack, but also to induce stresses that suppress the formation of new cracks. Additional insights from X-ray data far beyond standard spatial scanning (Fig. 2) are possible by including in-plane shear measurements. Shear strain measurements are required to obtain shear stresses, and they are almost never done with neutron diffraction due to assumptions made about their negligible magnitudes. It was found that such assumptions are misplaced, as the shear stresses are substantial and form a characteristic anti-symmetric distribution (σ_{shear} in Fig. 3).

An added benefit of measuring the shear stresses shown in Fig. 3 is that one can then determine the magnitude and orientation of the principal stresses (σ_1 and σ_2 in Figure 3). Principal stresses are defined as the diagonal elements of the principal-axes-transformed stress tensor. In simpler terms, a stress tensor with shear (off-diagonal elements) can be rotated such that all off-diagonal elements become zero by

¹ NIST Center for Neutron Research, National Institute of Standards and Technology, Gaithersburg, MD 20899

² Materials Science and Engineering Program, University of Idaho, Moscow, ID 83844

³ Pacific Northwest National Laboratory, Richland, WA 99352

⁴ Department of Nuclear Engineering and Industrial Management, Idaho Falls, ID 83402

⁵ Center for Advanced Energy Studies, Idaho Falls, ID 83401

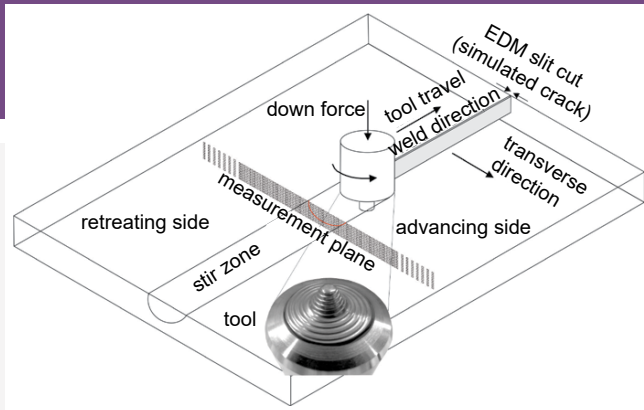


FIGURE 1: Schematic of the friction-stir-welding process and measurement locations.

reapportioning. The angle of rotation denotes how the principal stresses are oriented with respect to the original sample directions. By convention, σ_1 and σ_2 are the major and minor principal stresses.

The takeaway from Fig. 3 is that the principal stresses σ_1 and σ_2 are substantially larger in the vicinity of the stir zone (SZ)—not just along the weld and transverse directions. Instead, maximum tensile stresses occur near the stir zone oriented $\approx -45^\circ$ on the advancing side (AS) and $\approx 45^\circ$ on the retreating side. Note that the discontinuous transitions of the rotation angle are caused by the change in sign of the shear stress at ± 30 mm from the center of the stir zone.

In summary, the complementary use of neutron and X-ray diffraction confirmed that the friction-stir-weld crack repair does indeed serve the intended purpose of inducing near-surface compressive stresses, but only in the direction perpendicular to the weld tool travel. In terms of principal stresses, the magnitudes are even larger, but at angles $\pm 45^\circ$ on both sides of the stir zone. In other words, to take advantage of crack-suppressing compressive stresses produced by FSW, the weld direction must be angled to the crack direction such that the maximum benefit occurs. An important finding is the presence of significant post-weld shear stresses, which lead to characteristic rotations of the principal stress axes that are intrinsically linked to the rotation of the FSW tool and the tool travel direction. Stress distributions, together with the range in which the axes rotations occur, become broader with increasing weld temperature.

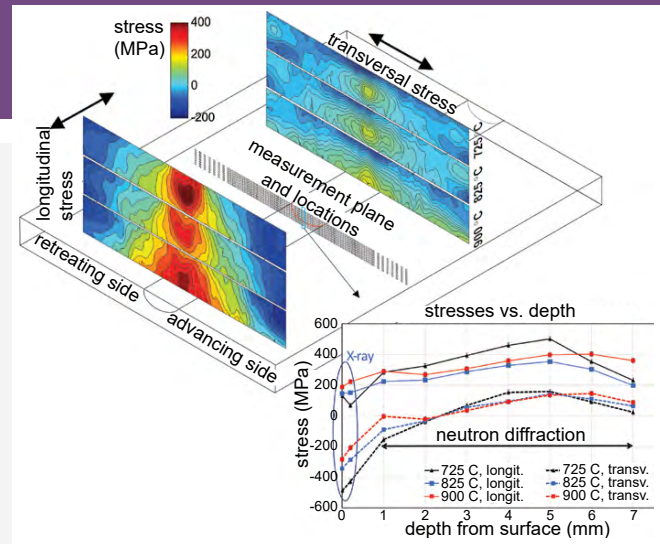


FIGURE 2: Stresses from neutron diffraction (contour maps) showing compressive stresses along the transverse direction for all three weld temperatures. Stresses in the normal direction are negligible.

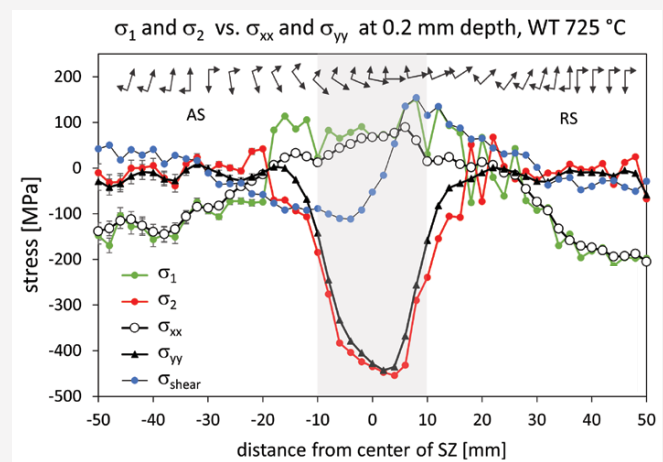


FIGURE 3: Stresses along the principal directions and sample direction with rotation of the principal axes shown in the inset on top of the graph for greater clarity.

Reference

- [1] M. Bhattacharyya *et al.*, Materials Science and Engineering: A **826**, 141982 (2021).

Exploring microstructure development of tricalcium silicate for additive manufacturing in construction using rheoSANS

A. J. Allen,¹ S. Z. Jones,¹ J. B. Hipp,^{1*} and C. V. Gagnon¹



Portland cement-based concrete remains one of the primary materials for manufacturing components of the physical infrastructure such as roadways, bridges, and dams. Thus, the hydration reactions between cement clinker and water remain an essential topic of research. New additive manufacturing concrete construction methods such as extrusion-based 3-D concrete printing (3DCP) and automated slipform casting require precise control over the transition of the material from one exhibiting properties of a flowing material to a hardened solid able to withstand design load forces. In this context, rheology is becoming a powerful diagnostic materials research tool. It is increasingly used to interrogate the physical properties of concentrated viscous colloidal suspensions and slurries of technological interest. Using capillary-based, parallel-plate or rotating-drum geometries, an oscillatory shear stress is applied to the slurry or suspension fluid, and measurements are made of the real and imaginary parts of the shear modulus, and the associated frequency-dependent complex viscosity as a function of oscillatory frequency. However, for many systems including cement, the frequency variation can be subtle over a wide range and so time-dependent measurements suffice even if they are carried out at a single representative frequency. By combining rheological measurements with simultaneous small-angle neutron scattering (SANS) measurements (= rheoSANS) the microstructural underpinnings of the rheological properties can be probed. Such studies can be rendered even more powerful through the addition of simultaneous dielectric measurements of the complex electrical impedance across the fluid (dielectric rheoSANS), although this is often simply extrapolated to zero electrical frequency to provide the electrical conductivity, σ .

Cement and concrete hydration is complex, encompassing multiple heterogeneous processes that occur simultaneously. So, in order to elucidate key aspects of cement hydration, dielectric rheoSANS studies were conducted in real time on hydrating pure tricalcium silicate (C_3S in cement notation), the most basic active ingredient in hydrating cement, which hydrates to form amorphous/nanocrystalline calcium-silicate-hydrate (C-S-H), the primary strength-giving phase that binds set cement (and concrete) together. Both polymorphs of C_3S were studied: monoclinic and triclinic, and the effects of sucrose addition were also investigated, this being one of the main methods of slowing the cement setting process in a controlled manner to allow time for precision product placement, as needed for 3DCP [1].

Figure 1 presents absolute-intensity-calibrated SANS data, intensity, $I(q)$ versus q (where $q = (4\pi/\lambda)\sin\theta$ and θ is half of the scattering angle) obtained on the NG7 30m SANS instrument using a neutron wavelength, $\lambda = 6 \text{ \AA}$. Changes in the scattering profile are shown with increasing hydration time following addition of water (H_2O) to monoclinic C_3S with a water-to-solids ratio, $w/s = 0.4$. Figures are shown both for "standard" hydration and for "retarded" hydration resulting from the addition of a small amount of sucrose (1.33 \mu L/g). Throughout the SANS measurements, each sample was mounted in the NCNR ARES-G2 strain-controlled rheometer equipped with a custom-built titanium Couette geometry (ID = 25 mm, OD = 24 mm, truncation gap = 1 mm) in the flow-vorticity (1–3) plane [2], and subjected to small amplitude oscillatory shear (SAOS). The SANS datasets were subjected to a composite Porod scattering (for total surface area), volume- and surface-fractal model analysis, formulated previously to quantify the developing hydrated C-S-H product microstructure [3].

Figure 2 summarizes real-time rheological data for monoclinic C_3S , as a function of hydration time. Again, figures are shown both for "standard" hydration and for "retarded" hydration resulting from addition of sucrose. In each case the variation with hydration time is shown for the ratio of the imaginary to real parts of the complex shear modulus, G''/G' (equates to $\tan\delta$ where $\delta =$ angular phase lag of G'' with respect to G') using an oscillatory strain amplitude, $\gamma = 0.10 \%$ (*i.e.*, $\pm 0.05 \%$) and frequency 1 Hz (6.28 rad/s angular frequency), together with the corresponding variation with hydration of the electrical conductivity, σ , extrapolated to zero electrical frequency. A Generalized Additive Model (GAM) was fit to the stochastic G''/G' data to provide an unbiased smooth curve for its variation with hydration time.

Based on Figures 1 and 2 for monoclinic C_3S , and corresponding plots for triclinic C_3S , together with the quantitative fractal analysis of the SANS data, a key finding emerges. The ratio, G''/G' drops to a low equilibrium value after a hydration time, t_{eqbm} , that corresponds to when the electrical conductivity also starts to decrease significantly. The value of t_{eqbm} indicates this point occurs at some time after the end of the well-known cement induction period (the time delay before any significant hydration reaction). Essentially, at t_{eqbm} , sufficient cement hydration has occurred both for the slurry to have an elastic, rather than plastic, response to SAOS, and for the loss of conducting water paths that percolate across the sample. Furthermore, on connecting this information with the SANS

¹ NIST Center for Neutron Research, National Institute of Standards and Technology, Gaithersburg, MD 20899

* Present address: Formulated Products and Processes, The Procter & Gamble Company, West Chester Township, OH 45069

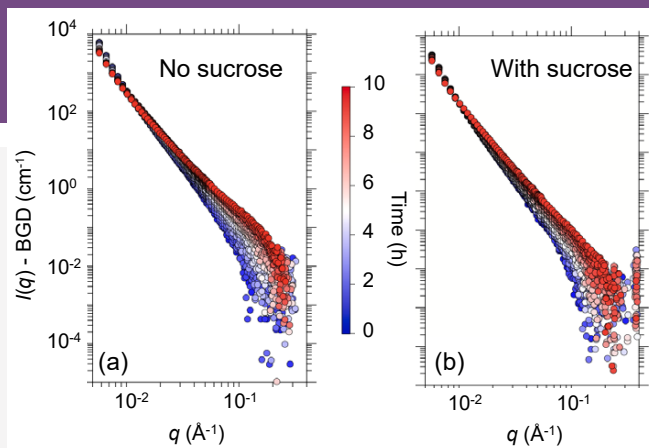


FIGURE 1: SANS data for hydrating monoclinic C_3S : (a) no sucrose, (b) with sucrose.

fractal microstructure analysis, it is found that t_{eqbm} corresponds in all 4 cases studied (monoclinic and triclinic C_3S , with both "standard" and "retarded" hydration) to a total surface area of C-S-H hydration product so far generated of $\approx 17 \text{ m}^2/\text{cm}^3$.

A major advantage of working with pure C_3S material in this study is that thermal calorimetry measurements of hydrating C_3S (either polymorph) measure only the main hydration reaction kinetics. The heat output from the primary hydration reaction is not masked by other coexisting reaction processes, such as occur in Portland and other common cements due to the presence of non- C_3S phases in the clinker grains. Thus, the integrated heat output versus hydration time can be calibrated against that expected for 100 % conversion of C_3S to C-S-H, to obtain the degree of hydration reaction at any point in the process. With the hydration times recalibrated in terms of the degree of hydration in each case, Figure 3 can be derived, which plots the volume fraction of the solid volume-fractal C-S-H phase versus degree of hydration for all 4 systems studied. Two important conclusions can be made. First, the time delay effect of the sucrose addition collapses out, revealing (from this and other microstructure model variations, not shown here) that sucrose addition does not affect the hydrated morphology that is ultimately formed. Second, as Figure 3 shows, the different C_3S polymorphs hydrate differently, potentially producing different final hydrated morphologies. This suggests that different cements can be designed for 3DCP, with hydration time dependences adjustable through sucrose addition without compromising the final hydrated cement morphology.

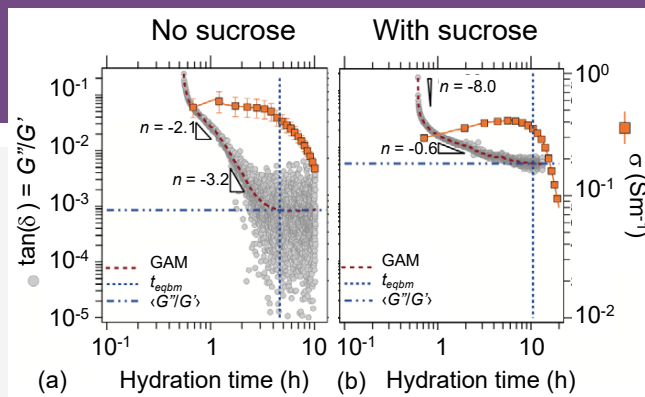


FIGURE 2: Rheological data for hydrating monoclinic C_3S : (a) no sucrose, (b) with sucrose.

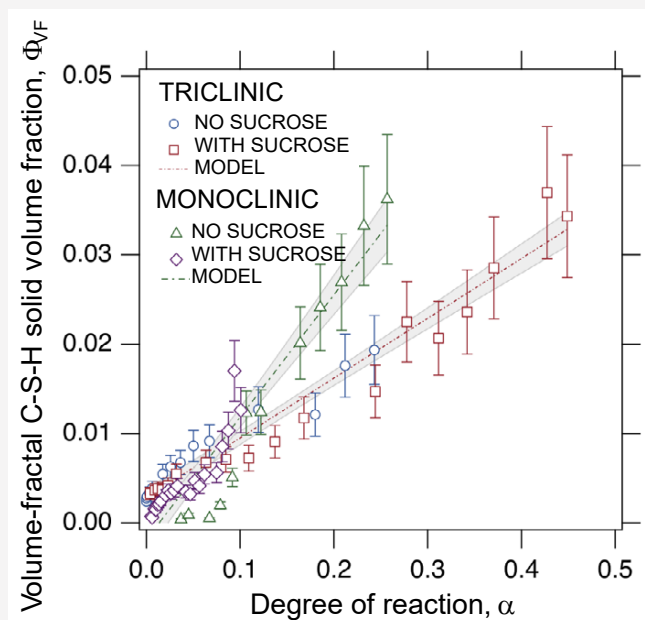


FIGURE 3: Volume-fractal C-S-H FFV versus degree of reaction.

References

- [1] S. Z. Jones, J. B. Hipp, A. J. Allen, C. V. Gagnon, *Cem. Concr. Res.* **152**, 106651 (2022).
- [2] J. J. Richards, C. V. L. Gagnon, J. R. Krzywon, N. J. Wagner, P. D. Butler, *J. Vis. Exp.* **122**, e55318 (2017).
- [3] A. J. Allen, *J. Appl. Cryst.* **24**, 624 (1991).

NeXT provides insight on the durability of concrete structures

L. E. Dalton,¹ J. M. LaManna,² S. Jones,³ and M. Pour-Ghaz'

Durability of concrete infrastructure is directly related to the ability of concrete to impede mass transport (*i.e.*, penetration of water and ions). In 1953, Farran first observed the transition zone between the interface of cement paste and aggregates where the properties of the paste are reported to differ from those of the “bulk” paste [1]; over time this region has become known as the ITZ. The ITZ is believed to develop from the “wall” effect of the relatively small cement grains packing against the much larger aggregate inclusions [2]. The packing is reported to lead to a disproportionate increase in smaller cement particles near the aggregate which leads to a local increase in porosity directly adjacent to the aggregate. The thickness of ITZ is reported as low as 15 μm and as high as 100 μm depending on the size of the cement grains with the most widely accepted thickness falling between 30 μm to 50 μm [2-4]. However, most, if not all the evidence of ITZ has been determined using qualitative methods.

Since its discovery, ITZ has been identified as a contributor to many phenomena in concrete materials such as deviations of concrete from linear elastic behavior during compression loading that has been attributed to the lower strength and cracking at ITZ and influence of ITZ on the rate of fluid and ion transport in concrete [2-4]. In the 1980s and into the past decade, Diamond presented evidence that questioned the contributions of the ITZ since its discovery [3-4]. These papers have mainly been refuted, perhaps because, by this time, the “evidence” for the existence of ITZ was overwhelming and ITZ was credited for qualitative explanations for many observed phenomena; notwithstanding the fact that by this time ITZ was extensively studied by the scientific community. However, to experimentally study ITZ, one needs to artificially promote formation of ITZ; or to simulate ITZ, one needs to program its existence.

It has been proposed that the interfacial transition zone (ITZ) is a major contributor to mass transport in concrete, but its role remains ambiguous and disputed [1-4]. In this study, the Neutron and X-Ray Tomography (NeXT) system [5] is used to image water absorption in the ITZ and to develop advanced and novel techniques for reconstructing images. Because neutrons and X-rays “see” materials differently, due to differences in their interactions with nuclei and atomic electrons, combining the two imaging techniques can assist in elucidating whether transport properties change in the

presence of ITZ relative to the “bulk” paste. X-ray computed tomography (CT) can be used to capture internal details while neutron tomography can capture where the water moves. Combined results are achieved by collecting time-resolved neutron and X-ray scans in one-hour increments during water absorption in a concrete cylinder containing a single coarse aggregate.

We hypothesize that ITZ is not a complete ring of continuous phase around each and every aggregate and it is at best, a statistically-distributed, discontinuous phase around aggregates. In the present paper [6], we ask if ITZ indeed influences the rate of moisture ingress in concrete by performing a simple experiment using one concrete cylinder containing a single coarse aggregate using the NeXT system during water absorption. The equipment is used to capture the internal concrete structure at high resolutions before water is added and sparse projection tomography is then used to capture the temporal evolution of water through the concrete specimen. These methods are used to determine if an increased rate of transport is found in the ITZ relative to the “bulk” paste during water absorption.

High resolution scans were obtained by collecting 708 evenly spaced projections from 0° to 360° simultaneously for both modalities and reconstructed using the Filtered-Back Projection (FBP) algorithm included in the Livermore Tomography Toolbox (LTT) [7]. The reconstructions (Figures 1a-b) were aligned for proper registration, and both were used to improve the segmentation of phases (Figures 1C-D).

After the simultaneous scans of the dry specimen, the concrete cylinder was removed from the beamline, a plastic reservoir was secured to the top surface, placed back in the beamline, and a fixed height of water was placed in the reservoir to initiate absorption. To obtain a temporal resolution of 1 hour, the projections were reduced from 708 to 60. Nine dynamic scans were completed in sequence to give temporal information of water absorption. The first iterative scan from each data set, neutron and X-ray, was reconstructed using the Adaptive Steepest Descent-Projection Onto Convex Subsets (ASD-POCS) algorithm [7] and reconstructed using the aligned FBP reconstruction as a seed for each iterative neutron and X-ray scan. The 4D X-ray and neutron seeded reconstructions are shown in Figure 2. The advancing water

¹ Department of Civil, Construction and Environmental Engineering, North Carolina State University, Raleigh, NC 27695

² Physical Measurement Laboratory, National Institute of Standards and Technology, Gaithersburg, MD 20899

³ Engineering Laboratory, National Institute of Standards and Technology, Gaithersburg, MD 20899

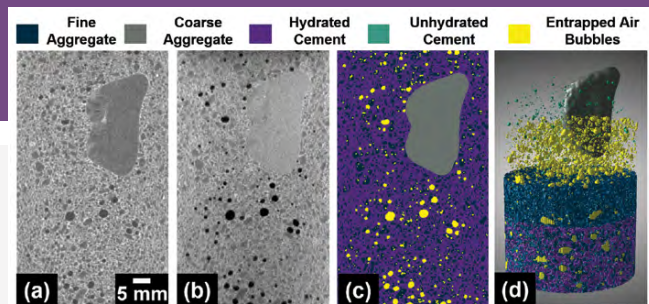


FIGURE 1: FBP reconstructions: (a) neutron, (b) X-ray, (c) segmented, and (d) 3D.

front is clearly observed in the neutron reconstructions where the saturated cement paste is higher attenuating (brighter) relative to the dry paste in Figures 2D–F.

Because segmentation methods inherently have some uncertainty, the subtractions were completed using the original seeded reconstructions with no image processing, and the water was segmented using an automatic threshold. The 4D results around the coarse aggregate are shown in Figure 3. The water plume moves downward within the first hour (Figure 3A) and then outward to the cylinder boundary (Figure 3B). Some residual water movement is observed in the top right corner of the aggregate in the third hour (Figure 3C). A small gap between the water front and aggregate is observed at hour six in Figure 3F becoming most apparent in Figure 3H highlighted by the red circle. The lack of change in water content to one side of the aggregate further suggests that if an ITZ region does have any effect, the ITZ is not a uniform, interconnected layer.

With the ITZ reported to contain higher porosity relative to the “bulk” paste, we anticipate water to percolate in the ITZ (*i.e.*, a flow path directly around the single coarse aggregate) during water absorption. If the porosity is increased around the aggregate, capillary action should take over and a slightly faster flow path directly around the coarse aggregate should be observed; however, the results from this study show no indications of water preferentially migrating around the coarse aggregate during water absorption. The findings in this study support prior findings by Diamond and Huang [4] that “The structure of the ITZ in ordinary concretes is not different enough from the bulk cement paste to provide any basis for large effects on permeance.” The ITZ may not facilitate preferential percolation of water transport and additional research is likely needed to explain some of the phenomena that have been attributed to the presence of the ITZ.

The purpose of this study was to develop imaging and reconstruction techniques to study mass transport in concrete materials and use these methods to determine if the rate of transport increases in the ITZ relative to the “bulk” paste during water absorption in a concrete cylinder containing a single coarse aggregate using the NeXT system. The voxel resolution achieved was approximately 30 μm for both modalities.

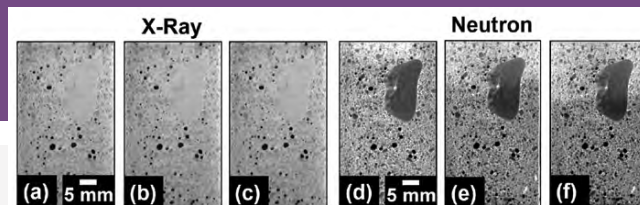


FIGURE 2: X-ray seeded reconstructions: (a) hour 1, (b) hour 5, (c) hour 9; neutron seeded reconstructions: (d) hour 1, (e) hour 5, (f) hour 9.

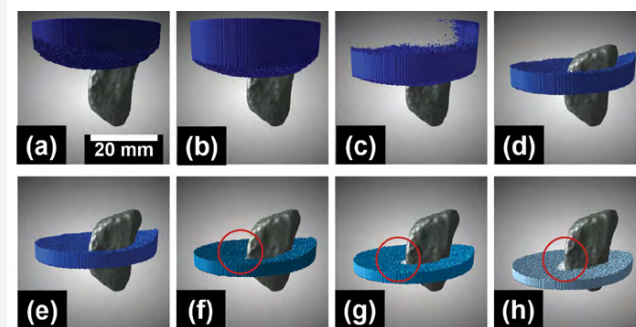


FIGURE 3: 4D renderings of water volume subtractions: (a) hour 2 subtract hour 1 volume difference, (b) hour 3 subtract hour 2 volume difference, (c) hour 4 subtract hour 3 volume difference, (d) hour 5 subtract hour 4 volume difference, (e) hour 6 subtract hour 5 volume difference, (f) hour 7 subtract hour 6 volume difference, (g) hour 8 subtract hour 7 volume difference, (h) hour 9 subtract hour 8 volume difference.

Combining the complementary information enhanced phase segmentation and using the high-resolution scans of the dry cylinder as a seed for scans during water absorption enhanced the moisture transport detection at the temporal resolution of one hour. During absorption, water advanced uniformly throughout the cement paste. No indications of water preferentially migrating faster around the coarse aggregate in the ITZ region during water absorption was captured at the resolutions of the dual neutron and X-ray scans.

References

- [1] J. C. Maso, CRC Press, (1996).
- [2] K. L. Scrivener, A. K. Crumbie, P. Laugesen, *Interface Science*, **12** (4), 411 (2004).
- [3] S. Diamond, *MRS Online Proceedings Library Archive* **85**, (1986).
- [4] S. Diamond, J. Huang, *Cement and Concrete Composites* **23** (2-3), 179 (2001).
- [5] J. M. LaManna, D. S. Hussey, E. Baltic, D. L. Jacobson, *Review of Scientific Instruments* **88** (11), 113702 (2017).
- [6] L. E. Dalton, J. M. LaManna, S. M. Jones, S. M. Pour-Ghaz, *Transp Porous Med*, **144**, 623 (2022).
- [7] K. M. Champley, T. M. Willey, H. Kim, K. Bond, S. M. Glenn, J. A. Smith, J. S. Kallman, W. D. Brown, I. M. Seetho, L. Keene, S. G. Azevedo, L. D. McMichael, G. Overturf, H. E. Martz, Jr., *NDT & E International* **126**, 102595 (2022).

Probing oil recovery in shale nanopores with small- and ultra-small-angle neutron scattering

C. W. Neil,¹ R. P. Hjelm,^{1,2} M. E. Hawley,¹ E. B. Watkins,¹ C. Cockreham,^{1,3} D. Wu,³ Y. Mao,^{3,5} M. Cheshire,⁶ J. Burger,⁶ T. B. Fischer,⁶ M. R. Stokes,^{6,†} and H. Xu¹



While shale oil/gas production in the US has increased exponentially from virtually nonexistent in late 1990s to about half of the domestic oil/gas production, the US still imports half of its oil to meet demands, and shale oil production is predicted to decline barring the discovery of new resources or improved recovery technology. Current hydrocarbon recovery rates are less than 10 % for oil and about 20 % for gas. These recovery rates are limited by diminishing returns with time due to slow diffusion of target hydrocarbons in the shale matrix, where transport is restricted by the small nanopore size and low permeability (10^{-16} m² to 10^{-20} m²) of tight shale formations. One proposed improvement is enhanced oil recovery (EOR), whereby a secondary substance is injected into an existing oil well to increase pressure and reduce oil viscosity, allowing for more efficient extraction of oil upon pressure drawdown. Maximizing recovery of hydrocarbons from these nanopores during EOR necessitates understanding the nature and extent of fluid interactions within small nanopores. To accomplish this research goal, we applied small-angle neutron scattering (SANS) and ultra-small-angle neutron scattering (uSANS) to probe the recoverability of hydrocarbons from a shale matrix.

Shale nanopores are intrinsically heterogeneous and occur in both organic (e.g., kerogen) and inorganic (e.g., clay) components of shale matrices. The proportion and size distribution of open/accessible and closed/inaccessible nanopores in each component largely determines the shale matrix permeability in the absence of fractures. Furthermore, these heterogeneous nanopores store the majority of hydrocarbons and constitute the majority of pore volume. Most current knowledge on fluid behavior in nanopores has been obtained via molecular simulations and phase equilibrium modeling, with little experimental data available due to a lack of suitable techniques for *in situ* real-time measurements at nanoscales. Experimental techniques, such as optical microscopy and X-ray/neutron micro-tomographic imaging, lack the necessary resolution to infer structures and properties of nanopores, while high resolution electron microscopic methods are difficult to combine with *in situ* environmental cells and fluids. Neutron scattering, on the other hand, is particularly well-suited for these measurements because

neutrons are sensitive to the lighter elements which constitute hydrocarbons (C, H/D) and because their neutral charge leads to greater penetration depths, making it possible to combine these techniques with high pressure environmental cells. SANS/uSANS have been used extensively to characterize the structure and connectivity of shale nanopores [1]. More recently, our team has used *in situ* experiments at high pressure to observe novel shale geophysical properties, including the changing accessibility of pore spaces to water [2] and methane trapping by kerogen deformation at high pressures [3].

As the neutron beam passes through a sample, compositional elements and isotopes scatter neutrons at characteristic lengths. The overall scattering length density (SLD), ρ , of a material can thus be calculated by summing the nuclear scattering lengths, b_i (cm), of atoms present in a given volume, V (cm³): $\rho = \frac{\sum b_i}{V}$ (cm⁻²). For shaly rock, scattering intensity is proportional to $\Delta\rho^2$ divided by the sample volume, where $\Delta\rho = \rho_p - \rho_m$ (ρ_p indicates the pore SLD and ρ_m refers to the shale SLD). Within air-filled pores, ρ_p is assumed to be zero, meaning that the strongest scattering comes from the difference between empty pores and the shale matrix. As accessible pores are filled with a fluid or gas that has an SLD greater than zero, $\Delta\rho$ decreases, decreasing the overall scattering intensity. This phenomenon allows for contrast matching, a technique whereby pores are filled with a solution that has the same SLD as the matrix. Thus, when pores are filled, their contribution to scattering is minimized, allowing for clear delineation of accessible vs. inaccessible pores.

In the current study, we harness this novel technique to probe the efficacy of methane injection for oil recovery in clay- and carbonate-rich shales [4]. SANS/uSANS analyses are used to measure both the accessibility of shale nanopores to decane, a corollary for target oil hydrocarbons, and the decane residual after pressurizing the system with methane and depressurizing to mimic recovery. Samples were first measured dry to determine the total scattering from empty pores. They were then saturated with a contrast-matched decane mixture under vacuum and remeasured to determine the initial distribution of decane in the pores. Decane-saturated samples were next pressurized with deuterated methane (CD₄) gas and SANS measurements were taken in 1500 psi increments up to

¹ Los Alamos National Laboratory, Los Alamos, NM 87545

² The New Mexico Consortium, Los Alamos, NM 87544

³ Washington State University, Pullman, WA 99164

⁴ University of Maryland, College Park, MD 20742

⁵ NIST Center for Neutron Research, National Institute of Standards and Technology, Gaithersburg, MD 20899

⁶ Chevron Technology Center, 3901 Briarpark Drive, Houston, TX 77042

[†] Current affiliation: Geology, Energy and Minerals Science Center, U.S. Geological Survey, Reston, VA 20192

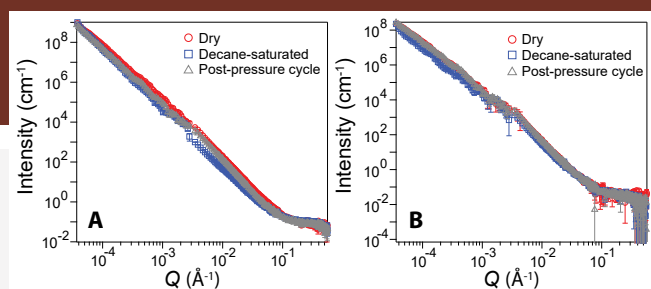


FIGURE 1: Combined USANS and SANS spectra for clay- and carbonate-rich shale under dry conditions, after initial decane saturation, and following the methane pressurization and depressurization cycle.

7500 psi (10.3 MPa to 51.7 MPa) and back down to ambient conditions. Due to the long measurement time of approximately 6 hours per pressure point, uSANS was conducted using a limited pressure cycle, with measurements taken at ambient dry conditions, ambient saturated conditions, then 1500 psi, 4500 psi, 7500 psi (10.3 MPa, 31.0 MPa, 51.7 MPa), and back down through the sequence of pressures to ambient. Changes in pore accessibility to contrast-matched decane were assessed by calculating the apparent pore size distribution function (PDF).

Figure 1 presents the combined uSANS and SANS spectra for clay- and carbonate-rich shale at ambient pressure taken under dry conditions, after initial decane saturation, and following the methane pressurization and depressurization cycle. The post-pressure cycle spectrum for the clay-rich shale remained decreased relative to the dry spectra, indicating that some contrast-matched decane remains in pore spaces (Figure 1A). For the carbonate-rich shale, there was both less initial decane uptake, as indicated by the smaller intensity decrease upon saturation, and most of this decane was removed (Figure 1B).

These trends become more obvious when SANS spectra are fitted for their pore size distribution (Figure 2). For both shale samples, upon decane imbibition, the size distribution shifted to a peak centered at a radius of 1 nm (10 Å). It is likely that due to the size of these pores, they are less accessible to decane, which has an end-to-end length of 9.97 ± 1.03 Å. After pressure cycling, the PDF for the carbonate-rich shale returned to nearly its initial dry state (Figure 2B), while for the clay-rich shale, the PDF remained decreased in the 2 nm to 10 nm region (Figure 2A). Previous analysis indicates that these pores are likely hosted by kerogen, which are expected to interact favorably with hydrocarbons such as decane and which are much more prevalent in clay-rich shale based on its composition analysis [2]. Porosities were also calculated for the two shale samples (Figure 2C). While the clay-rich shale had a much higher porosity and more of this porosity was accessible to decane, only about 20 % of the decane-filled porosity was removable, while for carbonate-rich shale more than 90 % of the decane-filled porosity was removable.

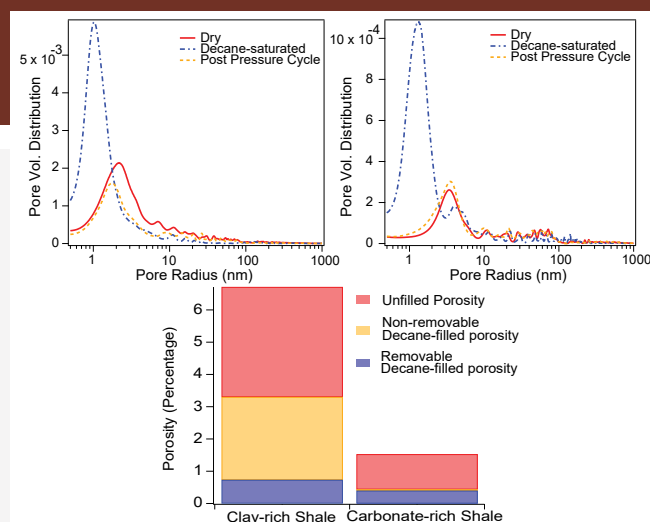


FIGURE 2: Fitted PDFs for clay- (A) and carbonate- (B) rich shales and calculated porosities (C).

In this study, we show that uSANS/SANS can be a powerful tool for probing fluid behavior during oil recovery. While preliminary results indicate that methane does not remove decane from kerogen pores during a single pressure cycle, there are many avenues through which we can expand this work, including measuring recovery over multiple pressure cycles and exploring other secondary injectant gases such as carbon dioxide. By furthering our understanding of shale response to pressure cycling, we can improve hydrocarbon recovery to achieve a more sustainable and economical harvesting of this valuable resource.

References

- [1] H. Xu, *Int. J. Coal Geol.* **217**, 103325 (2020).
- [2] C. W. Neil, R. P. Hjelm, M. E. Hawley, E. B. Watkins, C. B. Cockreham, D. Wu, Y. Mao, T. B. Fischer, M. R. Stokes, H. Xu, *Energy Fuels*. **34** (7), 8178 (2020).
- [3] C. W. Neil, M. Mehana, R. P. Hjelm, M. E. Hawley, E. B. Watkins, Y. Mao, H. Viswanathan, Q. Kang, H. Xu, *Commun. Earth Environ.* **1** (1), 1 (2020).
- [4] C. W. Neil, R. P. Hjelm, M. E. Hawley, E. B. Watkins, C. B. Cockreham, D. Wu, Y. Mao, M. Cheshire, T. B. Fischer, M. R. Stokes, H. Xu, *Int. J. Coal Geol.* **253**, 103950 (2022).

High-flux, high-resolution neutron reflectometry with CHRNS CANDOR

D. P. Hoogerheide, A. J. Grutter, B. B. Maranville, and C. F. Majkrzak



The new Chromatic Analysis Neutron Diffractometer or Reflectometer (CANDOR) is a one-of-a-kind instrument in the world of neutron reflectivity (NR). Produced in partnership with the National Science Foundation-funded Center for High Resolution Neutron Scattering (CHRNS) at the NCNR, CANDOR is an advanced neutron instrument based on an innovative “multiplexing” design that allows simultaneous measurement of neutrons from a continuous source over a wide spectral band, resulting in large increases in data collection rates. Extensive characterization of the instrument during and after its commissioning in 2020 has confirmed that CANDOR boasts world-class data rates and, due to its unique detector design, intrinsically low background. This article discusses these features and their implications for fast, high-resolution measurements with CANDOR.

In order to resolve fine features of NR patterns, reflectometers at reactor sources are conventionally configured to expose the sample to a relatively narrow, *i.e.* monochromatic, incident wavelength band (Fig. 1A). The detector is not generally wavelength-sensitive, but because of the monochromatic nature of the incident beam wavelength selection, the wavelength is still known to a high precision, typically about 1 %. A monochromatic reflectometer at a reactor source thus uses only a small fraction of the available neutrons, and measurements are quite slow, typically spanning hours or days.

By contrast, the novelty of CANDOR lies in its “energy-dispersive” detector, which permits a polychromatic beam to be reflected by the sample and then separated into constituent wavelengths on the detector end. Otherwise, the instrument geometry is identical to that of a monochromatic reflectometer (Fig. 1B). The detector analyzes the scattered beam using a linear series of 54 crystals, each oriented to diffract neutrons of one wavelength into a corresponding detection element, while neutrons of other wavelengths pass through to other crystals located downstream (Fig. 1C). Assuming specular elastic scattering, the wavelength and scattering vector Q are known for each neutron detected. The detection elements consist of thin plates of $^6\text{LiF/ZnS(Ag)}$ scintillation material with embedded wavelength-shifting fibers [1, 2]. Because each detector behaves as if it were viewing an independent source of neutrons with a unique wavelength, CANDOR can be viewed as a series of monochromatic reflectometers operating in parallel. This multiplexing scheme increases data rates into

a single CANDOR detector bank such as that shown in Figure 1C by about 20 times relative to the NCNR’s monochromatic MAGIK reflectometer.

The 20-fold improvement in data collection does more than speed up the type of investigation previously done with NR; it unlocks the ability to address entirely new types of scientific questions. Kinetic investigations become feasible at shorter time scales (seconds to minutes), particularly when researchers can focus on a limited Q -range corresponding to a single instrumental setting. Similarly, faster data rates also make feasible the complete characterization of samples that would otherwise be unstable or deteriorate during the many hours previously required to collect a full data set. The ability to perform more measurements on a single sample expands the scope of parametric studies that can be performed in a single experiment or beam time allocation, and for complex samples where reproducibility is not assured, replicates of nominally identical samples can be probed.

For magnetic materials, the increased data rates not only improve experimental throughput but also enable the detection of smaller splittings between spin-up and spin-down polarized neutron reflectivities (“spin-splitting”), which scale roughly linearly with the net magnetization. Many of the most exciting problems in modern magnetic materials and spintronics involve materials with weak or trace net magnetizations, an ideal use case for CANDOR where the increased flux will enable the resolution of magnetic details that would otherwise have required an unfeasibly large beamtime allocation to achieve.

With the increased data collection rate of CANDOR, the intrinsic neutron reflectivity will often be less of a limiting factor than the signal-to-background ratio at high scattering angles. The maximum scattering angle determines the spatial resolution that can be achieved in a measurement, and thus the ability to resolve the structures of thin films (those with thickness less than about 10 Å to 20 Å). This is particularly problematic for complex sample environments in which the beam unavoidably passes through thick materials; a notable example is the liquid-flow cell, in which the beam passes through dense, bulk materials on either side of a solid-liquid interface. Because the reflectivity of neutrons drops quickly with scattering angle, even a small amount of background scattering from these materials can degrade the reflectivity signal quality at scattering angles of experimental interest.

NIST Center for Neutron Research, National Institute of Standards and Technology, Gaithersburg, MD 20899

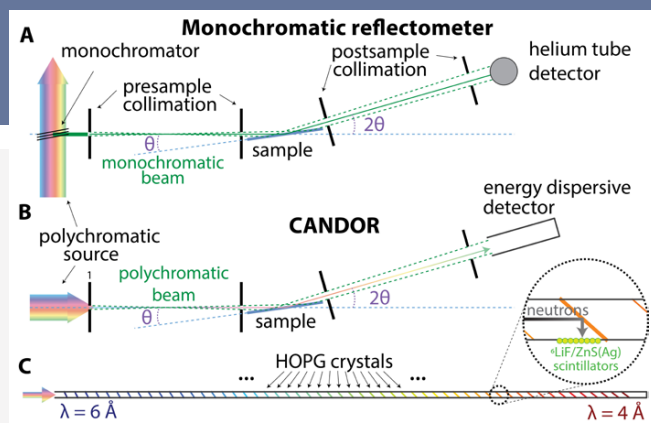


FIGURE 1: (A) Schematic of conventional reactor-based monochromatic reflectometers and (B) the CHRNS CANDOR polychromatic reflectometer. (C) The unique energy-dispersive detector bank design. A detector bank comprises 54 HOPG crystals, each of which diffracts a unique neutron wavelength between 4 Å and 6 Å into an individually addressed $^6\text{LiF/ZnS(Ag)}$ scintillation detector.

In the first manuscript published using scientific data from CANDOR [3], we have shown that much of the background scattering from common liquid-flow cell materials, such as silicon, air, D_2O , and (to a lesser extent) H_2O , is inelastic in nature. Thus, the neutrons detected as scattering background in a conventional monochromatic reflectometer have a different wavelength from that of the incident beam. Because the CANDOR detector is sensitive only to neutrons in the (4 to 6) Å wavelength band, neutrons arriving at the detector with wavelengths outside this band are not observed. In addition, incident neutrons outside this band are suppressed by the combination of an upstream X-deflector and cold beryllium filter. As a result, the CANDOR detector intrinsically rejects most of the inelastic background from common liquid cell materials, resulting in an intrinsic background level that is several times smaller than that observed at the MAGIK reflectometer for the same sample. After background subtraction, features in the NR pattern are observed at $1.5\times$ and $2\times$ the maximum scattering vector for $\text{Si/SiO}_2/\text{D}_2\text{O}$ and $\text{Si/SiO}_2/\text{H}_2\text{O}$ interfaces, respectively (Fig. 2).

References

- [1] N. C. Maliszewskyj, A. Osovizky, K. Pritchard, Y. Yehuda-Zada, E. Binkley, J. Ziegler, P. Tsai, N. Hadad, G. M. Baltic, M. Jackson, C. Hurlbut and C. F. Majkrzak, *Nuc. Instr. Meth. Phys. Res. A* **907**, 90 (2018).
- [2] K. Pritchard, A. Osovizky, J. Ziegler, E. Binkley, P. Tsai, N. Hadad, M. Jackson, C. Hurlbut, G. M. Baltic, C. F. Majkrzak, N. C. Maliszewskyj, *IEEE Trans. Nuc. Sci.* **67**, 414 (2020).
- [3] D. P. Hoogerheide, J. A. Dura, B. B. Maranville, C. F. Majkrzak *J. Appl. Cryst.* **55**, 58 (2022).

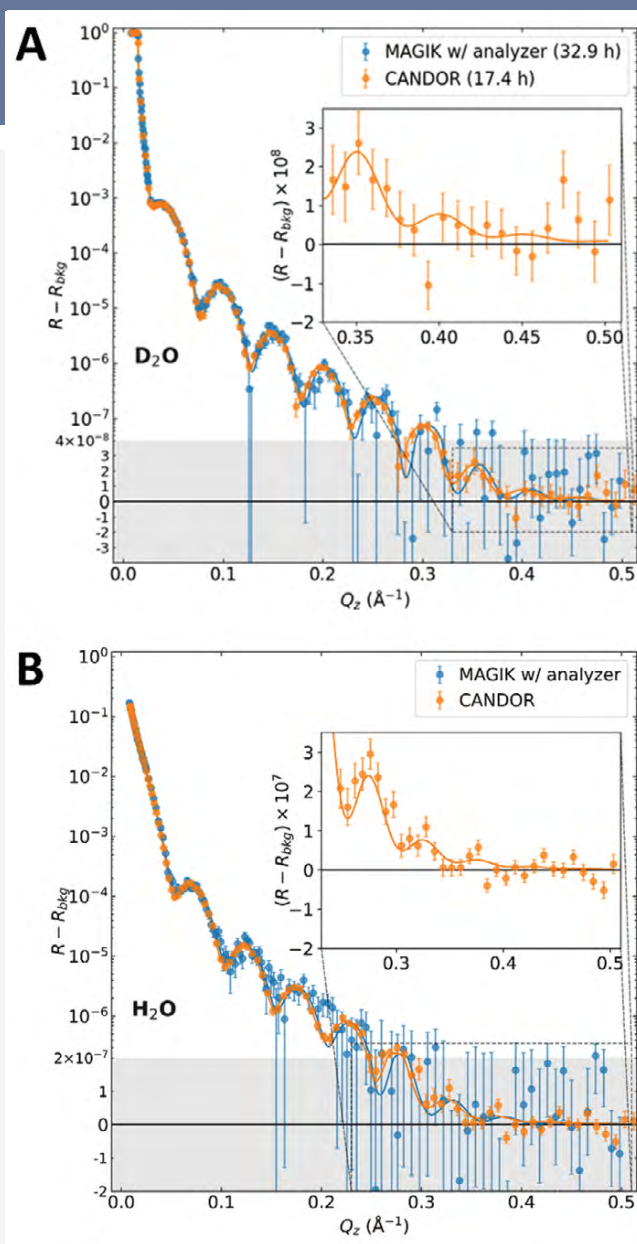


FIGURE 2: CANDOR's high data rate and intrinsic rejection of inelastic background combine to allow high- Q_z (*i.e.* high resolution) NR measurements. (A) For $\text{Si/SiO}_2/\text{D}_2\text{O}$ interfaces, features in the NR pattern are resolved out to $Q_z > 0.4 \text{ Å}^{-1}$, a $1.5\times$ improvement over the MAGIK reflectometer, even when the latter is equipped with an energy analyzer. (B) For $\text{Si/SiO}_2/\text{H}_2\text{O}$ interfaces, the improvement is even more dramatic. The high incoherent scattering background results in a lower maximum Q_z of about 0.33 Å^{-1} ; however, this is a 2-fold improvement in resolution over the conventional measurement.

Upgrade of the BT-8 diffractometer for stress and texture

T. Gnäupel-Herold, E. Binkley, D. Adler, K. Pritchard, and J. Milner

Since its first commissioning in 1995 the BT-8 diffractometer for stress and texture (DARTS) has served the NIST mission through a variety of measurements in collaboration with federal agencies, academic institutions, and industrial partners. As the range of applications has increased, and the overall field of diffractive analysis of stress and texture has grown, so have instrumentation performance needs. Therefore, a comprehensive instrument upgrade plan was devised with the stated goal to achieve a greater than tenfold gain in performance through simultaneous increases of detector coverage area, detection efficiency, detector position resolution, and neutron flux on the sample. This has been exceeded though the combination of narrower diffraction peaks through better position resolution, increased detection (30 % to 40 % higher count rate per unit of detector area) and an eightfold increase of the detection area. Additionally, neutron flux on the sample is increased by up to 70 % through deployment of a 3λ multi-wavelength monochromator. Secondary improvements aimed at reducing downtime are achieved through improved sample positioning and orientation, thus eliminating the need for sample re-mounting and allowing the use of sample changers. Thirdly, new sample environment options aimed at measurements under multi-axial applied stress were developed to address the need to study the behavior of structural materials under complex deformation paths typical for industrial forming operations.

Final assembly and installation of components for positioning and sample rotation (Figure 1) was completed recently. The detector now fully illuminated after installation of a new housing, therefore allowing for the first time the full benefit of both the improved flux on sample and the increased neutron detection capabilities shown in Figure 2. The 3λ -monochromator consists of elastically bent perfect silicon crystal packets in three orientations (Figure 2, top left) delivering three wavelengths and an integral flux that is up to 70 % larger than the comparable flux of the single wavelength monochromator (Figure 2, bottom left). Structural materials investigated at BT-8 have predominantly cubic crystal structures, which, when combined with the 3λ -monochromator, produce non-overlapping diffraction peaks in an angular window that is sufficiently narrow for stress analysis (Figure 2, top right). Note that the single

wavelength performance of the 1λ -monochromator is superior, thus presenting a trade-off where the 3λ -monochromator allows measurement of four (hkl) simultaneously but at lower intensity compared to one peak with superior intensity with the 1λ -device. Three wavelengths can map up to four reflections (hkl) into the detector window for simultaneous measurement, which improves the stress accuracy through better average of elastic and plastic anisotropy. The largest gains are achieved in texture analysis where the orientation distribution function can now be determined around ten times faster because all required pole figures are obtained in a single measurement.

For texture analysis the collection of scattered neutrons scales with the vertical detector dimension. In stress analysis the self-absorption of diffracted neutrons in the sample limits further gains from the vertical opening. Nonetheless, at greatest proximity of the detector to the sample the vertical opening amount to $\approx 35^\circ$ which is sufficient for simultaneously measuring shear stresses.

Triaxial stress measurements require measurements in three orthogonal sample directions which typically necessitates a manual remounting of the sample. In order to eliminate this time-consuming process sample positioning systems were designed to allow XYZ translations together with Euler angle rotations for all but the heaviest samples (>40 kg) for which only XYZ translation is available. The Euler angle goniometer allows stress measurements without the need for sample remounting and it serves as an efficient texture goniometer with integrated sample changer for high throughput measurements (Figure 3, top left).

Available sample environment options include innovative straining devices aimed at the investigation of yield functions in sheet metal forming. The first device (dubbed Octo-strain) is based on eight individually controlled 40 kN actuators for achieving large strain bi-axial deformation under a large variety of strain paths (Figure 3, bottom right). The second device has two independently controlled actuators for exploring materials behavior under a variety of shear modes (Figure 3, bottom left). Both devices can be rotated in order to allow the determination of the principal axis system. A uniaxial load frame (150 kN) is available as well (Figure 3, top right).

NIST Center for Neutron Research, National Institute of Standards and Technology, Gaithersburg, MD 20899

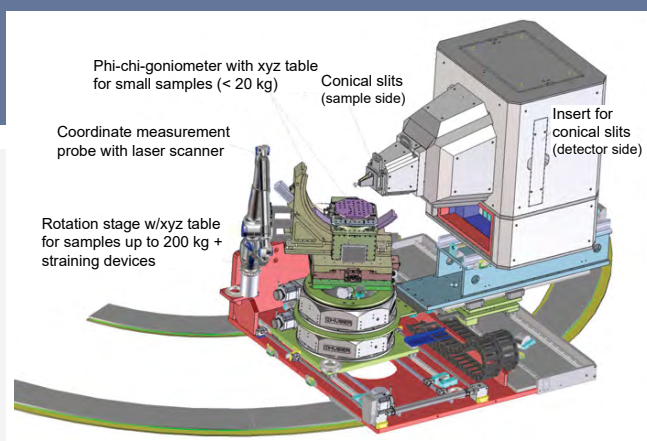


FIGURE 1: Final component assembly of the BT-8 diffractometer. Floor-mounted rails support adjustment of the take-off angle for wavelength changes.

In summary, the instrument upgrade addresses several needs: First, it provides options for higher neutron flux on the sample through multiple wavelengths. Second, vastly improved detection of scattered neutrons allows simultaneous measurement of both multiple peaks (hkl) and multiple sample directions benefitting measurements of both stress and texture. New devices for sample positioning and orientation save beam time through the elimination of sample remounting. Additionally, innovative straining devices aimed at the study of multi-axial deformation of advanced high strength steels have been developed. All new components work in conjunction, that is, the full potential of the straining devices actually requires both the multi-wavelength monochromator and the new area detector for optimal results.

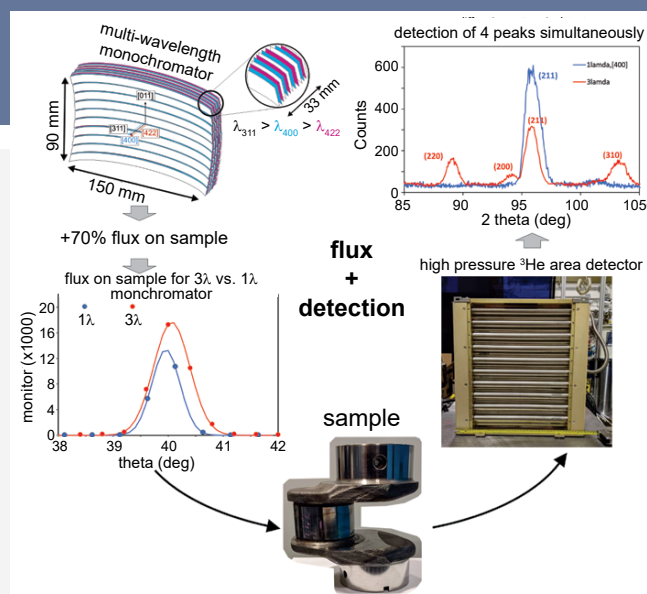


FIGURE 2: Improvements in monochromator and detector and the resulting gains.

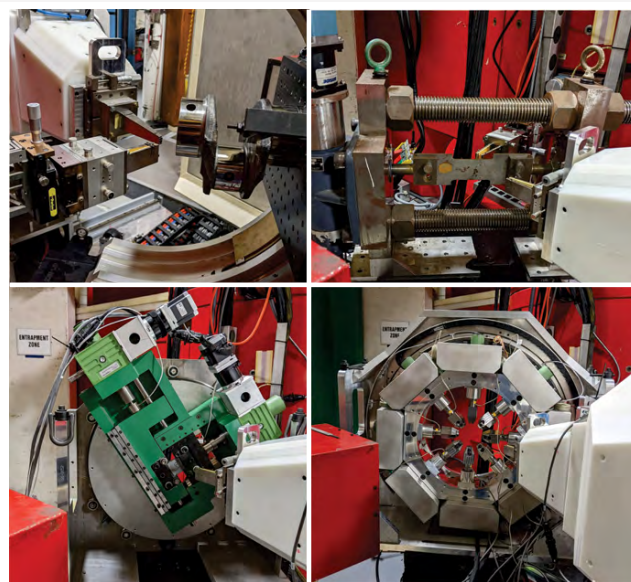


FIGURE 3: Examples for measurement set-ups. Clockwise, starting top left: crank shaft for residual stress measurement, uniaxial load frame, sample in shear loading, upgraded Octo-strain straining device.

Pendellösung interferometry probes the neutron charge radius, lattice dynamics, and fifth forces

B. Heacock,^{1,2,3} A. Henins,¹ M. G. Huber,¹ R. Valdillez,^{2,3} A. R. Young,^{2,3} T. Fujiie,^{4,5} M. Kitaguchi,⁴ H. Shimizu,⁴ K. Hirota,^{4,6} T. Hosobata,⁵ M. Takeda,⁵ Y. Yamagata,⁵ R. W. Haun,^{7,8} D. A. Pushin^{9,10}

There are four known fundamental forces of nature: electromagnetism, gravity, strong (nuclear), and weak. However, in an effort to solve several outstanding mysteries in modern physics, several theories predict a so-called 5th force of nature. A 5th force of nature could help to explain the incompatibility of general relativity and quantum mechanics, dark matter/energy, and the smallness of neutrino masses. Here we have used pendellösung interferometry to exclude the existence of a 5th force interacting at the 0.1 nm to 100 nm range [1]. This technique also gives insight into atomic bonds and how atoms thermally vibrate within the confines of a crystal lattice. Lastly, the neutron's internal electric structure is explored via its weak interaction with the electrons in a sample.

Bragg diffraction is a physical phenomenon familiar to most people who have taken an introductory physics class. During Bragg diffraction, a wave with a wavelength λ reflects from a lattice at a specified angle θ_B . This is often introduced as a geometric consequence of λ physically matching the crystal lattice spacing d . Specifically, Bragg's law is often written as $n\lambda = 2d \sin(\theta_B)$, where $n = 1, 2, 3, \dots$. This simple expression hides the complex and beautiful description of a wave interacting with a crystal lattice.

Described using quantum mechanics, a wave diffracting inside a crystal lattice is much more nuanced. In reality, a wave propagating through a crystal is in a quantum superposition of two wave states labeled Ψ_α and Ψ_β . One wave state propagates and interacts mostly with the atomic planes (β) while the other propagates and interacts mostly in the space between the planes (α). Both of the waves described by these states accumulate a phase shift (i.e. $\Psi_\alpha \rightarrow \Psi_\alpha \text{Exp}[-i\phi_1]$ and $\Psi_\beta \rightarrow \Psi_\beta \text{Exp}[-i\phi_2]$) as they traverse the crystal. The difference in phase $\Delta\phi = \phi_1 - \phi_2$ generates constructive and destructive interference at the exit of the crystal. By changing the crystal thickness or the incoming λ one can modulate $\Delta\phi$. This effect is called pendellösung interference. In this experiment, we changed the effective thickness of a crystal by tilting it. One should note that this technique requires a high degree of beam

collimation to resolve the interference and a uniform crystal to maintain coherence. These limitations contribute to why this method is not more widely used.

The crystal used in this work was a 1-cm-thick, perfect-crystal-silicon sample fabricated at RIKEN, Japan. Three angles were cut along its top surface, so that there were well-defined (220), (111), and (440) Bragg orientations. This corresponds to $d = 0.192$ nm, 0.34 nm, and 0.136 nm, respectively. To vary the effective thickness, we rotated the crystal a few degrees. Figure 1 shows the beam diffracting off the (220) lattice planes of the sample. An example of pendellösung oscillations for the (220) and (111) reflections is shown in right hand side of Fig. 1.

The phase of the pendellösung oscillation is related to the crystal's structure factor $F_{hkl} \propto e^{-W_{hkl}} [C^0 + C^1_{hkl} + C^2_{hkl}]$ where $\{h, k, l\} = \{2, 2, 0\}$, $\{1, 1, 1\}$, or $\{4, 0, 0\}$. The Debye-Waller factor, $e^{-W_{hkl}}$, describes the atomic thermal vibrations. The term C^0 corresponds to nuclear scattering and does not depend on the specific reflection studied. C^1_{hkl} , which is roughly $0.001 \times C^0$ in size, describes the neutron's interaction with the crystal electric field. Lastly, if a fifth force exists it would correspond to the term C^2_{hkl} . By measuring three different reflections, we can isolate each term in F_{hkl} .

Pendellösung measurements were performed at the neutron interferometer and optics facility auxiliary beamline (NIOFa) [2]. The NIOFa provides both 0.22 nm and 0.44 nm monochromatic neutrons. The (220) and (400) pendellösung interferograms were measured using 0.22 nm neutrons, and the (111) pendellösung interferograms were measured using 0.44 nm neutrons. To account for the reflection-independent C^0 term a separate measurement was made at the neutron interferometer and optics facility (NIOF). Using a Mach-Zehnder neutron interferometer, the pendellösung crystal was suspended in one of the two Mach-Zehnder beam paths (see Fig. 2). Care was taken so that the neutron beam passed through the same part of the crystal, which was slightly different for each reflection, as during the pendellösung measurements. The phase shift of the crystal was determined

¹ National Institute of Standards and Technology, Gaithersburg, MD 20899

² North Carolina State University, Raleigh, NC 27695

³ Triangle Universities Nuclear Laboratory, Durham, NC 27708

⁴ Nagoya University, Nagoya 464-8602, Japan

⁵ RIKEN Center for Advanced Photonics, Saitama 351-0198, Japan

⁶ High Energy Accelerator Research Organization, Tsukuba 305-0801, Japan

⁷ Institute for Physical Science and Technology University of Maryland, College Park, MD 20742

⁸ Tulane University, New Orleans, LA 70118

⁹ Institute for Quantum Computing, Waterloo, ON N2L3G1, Canada

¹⁰ University of Waterloo, Waterloo, ON N2L3G1, Canada

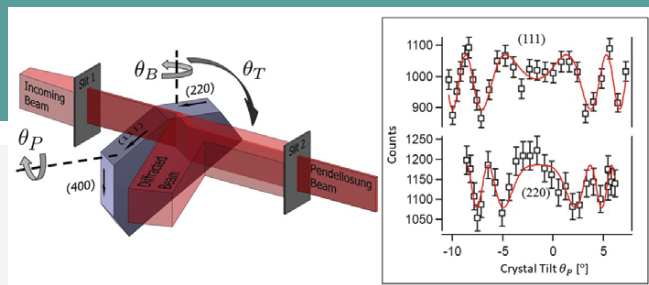


FIGURE 1: The experimental setup (left). Typical pendellösung oscillations for both the (111) and (220) reflection (right).

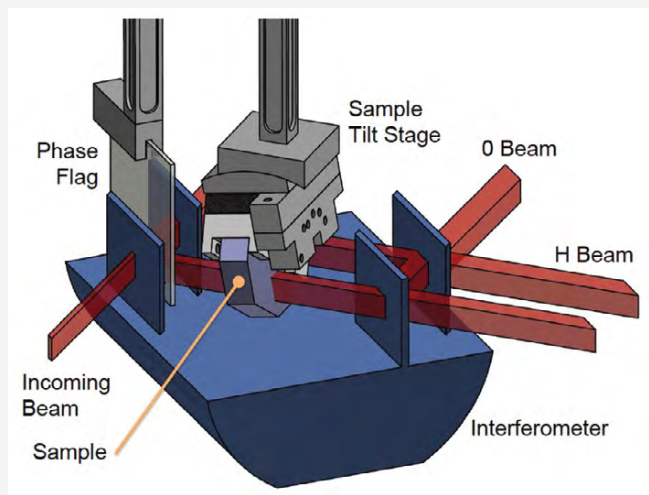


FIGURE 2: A Mach-Zehnder neutron interferometer is used to isolate the reflection-independent term.

by traditional neutron interferometric techniques. Inside a Mach-Zehnder neutron interferometer the measured phase shift is not sensitive to reflection dependent terms such as C_{hkl}^1 and C_{hkl}^2 . The measured pendellösung phase was normalized using the Mach-Zehnder data, which eliminated the need for a direct, precise measurement of C^0 .

A common parameterization for constraining Beyond-the-Standard-Model physics is a Yukawa modification to gravity: $V_G \rightarrow V_G [1 + \alpha_5 e^{-r/\lambda_5}]$. Here, V_G is given by Newton's law of universal gravitation. Figure 3 shows constraints (shaded region) on a possible fifth force in terms of α_5 and λ_5 determined by this work. Note that the range of α_5 and λ_5 extends many orders of magnitude beyond what is shown in Fig. 3. Limits are provided in those regions by various methods from collider physics, atomic physics, and geophysics.

The Debye-Waller factor accounts for the thermal motion of the atoms in the lattice. Lattice dynamical results can be found by fitting neutron inelastic scattering data to a Born-von Kármán (BvK) model. Our work is in slight contention with the BvK model when scaled to room temperature where this experiment took place. This may be due to the harmonic approximations used in the BvK model despite silicon's known

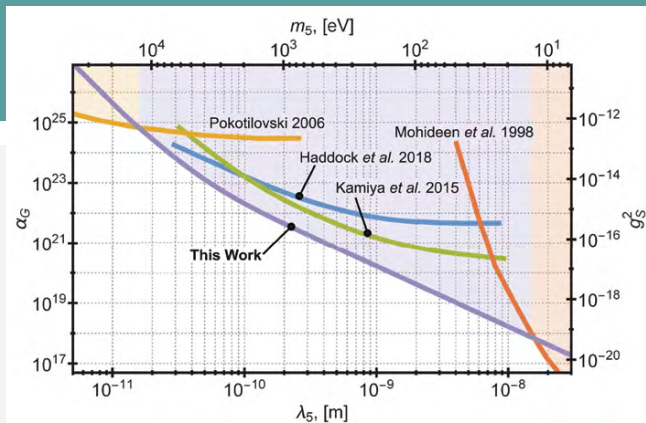


FIGURE 3: New limits on a fifth force at the nanometer scale. The force is parameterized by a strength α_5 (alternatively g_5^2) and length-scale λ_5 (or alternatively a mass m_5). Here one can see our results (purple) compared to other efforts.

strong anharmonicity. Future pendellösung measurements can probe silicon's anharmonicity directly by studying higher-order reflections at various temperatures.

The neutron charge radius, $\langle r_n^2 \rangle$, describes the spherically symmetric distribution of charge within a neutron. It is known from angular scattering and lead/bismuth transmission measurements that the neutron has a positively charged core surrounded by a negatively charged outer shell. This is due to the couplings between the three quarks inside the neutron. The radius $\langle r_n^2 \rangle \propto C_{hkl}^1$ through a series of known physical constants. Our determination of $\langle r_n^2 \rangle$ agrees with the Particle Data Group's computed world average and strongly matches with recent theoretical calculations. Previous $\langle r_n^2 \rangle$ measurements, using angular scattering and total transmission, may have reached their systematic limit. But the uncertainty in $\langle r_n^2 \rangle$ using pendellösung oscillations, while currently larger than the other methods, has several clear pathways for reduction.

We will continue our search for a fifth force and improve our knowledge of the neutron internal structure and crystal dynamics by making many more pendellösung oscillation measurements. These include measuring pendellösung oscillations in silicon at higher order reflections like (333), (444), and (555). In addition, there are other structure factors to consider in crystals such as germanium and titanium. This work is complementary to X-ray pendellösung data but subject to different forces.

References

- [1] B. Heacock *et al.*, *Science* **373**, 1239 (2021).
- [2] C. B. Shahi *et al.*, *Nucl. Instr. Meth. A* **813**, 111 (2016).

Structural and dynamical roles of bound polymer chains in rubber reinforcement

D. Salatto,¹ J.-M. Y. Carrillo,² M. K. Endoh,¹ T. Taniguchi,³ B. M. Yavitt,¹ T. Masui,⁴ H. Kishimoto,⁴ M. Tyagi,^{5,6} A. E. Ribbe,⁷ V. Garcia Sakai,⁸ M. Kruteva,⁹ B. G. Sumpter,² B. Farago,¹⁰ D. Richter,⁹ M. Nagao,^{5,6,11} and T. Koga^{1,12}



Automobiles are an integral part of our society today. According to Energy Technology Perspectives 2017, in 2050 the total number of cars globally will be three times greater than that in 2010. The substantial increase suggests that we will face a major challenge in the depletion of natural rubbers available to produce car tires. It is therefore critical to develop advanced reinforced synthetic elastomers with balanced and superior performance including durability and safety. To address this, we tackle the critical and unsolved problem in the field: a molecular understanding of the basic mechanisms behind rubber reinforcement (*i.e.*, mechanical property enhancement).

Carbon black (CB) filled elastomers are the most successful rubber nanocomposites. Twiss made the first observation in 1925 [1] of the improvement of the key mechanical properties upon the inclusion of CB fillers and bound rubber (BR) (*i.e.*, polymer chains that physically adsorb on the surfaces). Since then, there is general agreement that BR is critical for reinforcement in CB-filled rubber as it engages with the matrix as well as with adjacent CB fillers. However, a detailed understanding on the nano-scale has been impeded by the lack of experimental tools to directly probe the bound chains buried in a polymer matrix composed of the same polymer. Furthermore, there are indications that the bound chains are made up of different types of segment ("trains" (adsorbed segments), "loops" (sequences of free segments connecting successive trains), and "tails" (non-adsorbed chain ends) as shown in Figure 1), giving rise to a hierarchy of the structures and dynamics at the segment and chain levels. The resultant local heterogeneities thereby create additional complications for understanding the molecular mechanisms.

To directly provide insight into the structure and dynamics of the BR, we used a simplified CB-filled polybutadiene (PB) system. Based on previous experience [2] we prepared bound chains composed of hydrogenated PB and then embedded the "BR coated CB fillers" into a deuterated polybutadiene (dPB) matrix, thereby creating a strong contrast between the

matrix and the BR. Utilizing small-angle neutron scattering and neutron spectroscopy, the structures of the bound chains on the nanometer scale as well as the dynamics on time scales up to nearly 1 μ sec were probed. In this study, the filler concentration was set below the percolation threshold to reveal the structures and dynamics of the "isolated" bound chains. In addition, coarse-grained molecular dynamics (MD) simulations were performed to complement the experimental results and to unravel details that are not accessible experimentally. These results were then linked to macroscopic mechanical analysis to establish a correlation among the structure, dynamics, and resulting rheological properties.

Fig. 2(A) shows small-angle neutron scattering (SANS) from the BR-coated CB filler in dPB at 150 °C. This scattering originates from inhomogeneity within the BR layer. To analyze the excess scattering, the following three assumptions were made: (i) the CB filler is approximated as a "planar" geometry (see, the inset of Fig. 2B); (ii) the BR is modeled as two layers, an inner layer composed of strongly adsorbed chains and an outer layer composed of loosely adsorbed chains; (iii) the tails and loops of a BR chain can be approximated by a parabolic function. The details of the SANS experiments and data analysis have been described elsewhere [3]. Fig. 2B shows the concentration profile obtained from the best-fit (the solid line in Fig. 2A) to the data. The results indicate that the inner layer of $0.43 \text{ nm} \pm 0.03 \text{ nm}$ in thickness, which is commensurate with the segment length of a PB monomer ($= 0.67 \text{ nm}$ for PB), does not allow any penetration of matrix chains. As it was further confirmed by the MD, this inner region consists of the train segments of BR chains. Moreover, it was found that the outer layer, which is composed of loops and tails, extends well into the matrix.

We then utilized two neutron spectroscopies, *i.e.*, neutron backscattering (NBS) and neutron spin echo (NSE) that allow us to study the dynamics of BR chains from 10 ps to ≈ 500 ns and length scale from 0.1 nm to 10 nm. BR-coated CB in dPB as well as (free) hPB chains blended in the dPB melt (hereafter assigned as "hPB in dPB", as a control) were investigated. The total volume

¹ Department of Materials Science and Chemical Engineering, Stony Brook University, Stony Brook, NY 11794

² Center for Nanophase Materials Sciences, Oak Ridge National Laboratory, Oak Ridge, TN 37831

³ Graduate School of Engineering, Department of Chemical Engineering, Kyoto University, Katsura-Campus, Nishikyo-ku, Kyoto, 615-8510, Japan

⁴ Sumitomo Rubber Industries Ltd., 1-1, 2-chome, Tsutsui-cho, Chuo-ku, Kobe, 671-0027, Japan

⁵ NIST Center for Neutron Research, National Institute of Standards and Technology, Gaithersburg, MD 20899

⁶ Department of Materials Science and Engineering, University of Maryland, College Park, MD 20742

⁷ Department for Polymer Science & Engineering, University of Massachusetts, Amherst, MA 01003

⁸ ISIS Pulsed Neutron and Muon Facility, Science and Technology Facilities Council, Rutherford Appleton Laboratory, Harwell Campus, Didcot OX11 0QX, United Kingdom

⁹ Jülich Centre for Neutron Science (JCNS), Forschungszentrum Jülich GmbH, 52428 Jülich, Germany

¹⁰ Institut Laue-Langevin, 6 rue Jules Horowitz, BP 156-38042, Grenoble Cedex 9, France

¹¹ Department of Physics and Astronomy, University of Delaware, Newark, DE 19716

¹² Department of Chemistry, Stony Brook University, Stony Brook, NY 11794

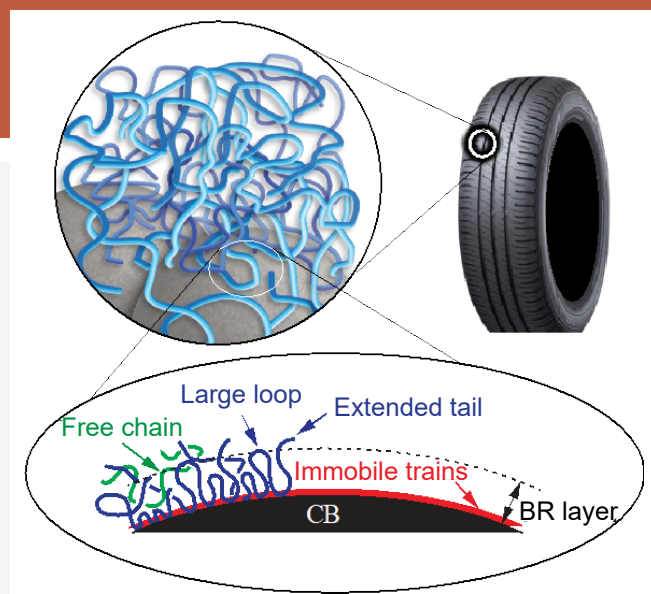


FIGURE 1: Bound rubber (BR) chains on CB filler surface are composed of loop, tail, and train sequences.

fraction of the free hPB in the dPB matrix was set equal to that for the BR-coated CB in dPB (a volume fraction of 3.1 %). Combined with the MD results, we concluded that the trains are immobile within the experimental time window, while the tails and loops are mobile and the segmental dynamics remain unchanged between the bound chains and free chains in the melts [3].

We further analyzed the NSE data which covers the dynamics of the BR chains at the larger length scale and slower time scale compared to the NBS windows. Based on the NBS results, we applied the same two-phase model composed of immobile and mobile (bulk-like) parts to the NSE data. At spatial and time windows beyond the Rouse regime (*i.e.*, the segmental dynamics) probed by NBS, long chains are confined by their mutual entanglements, leading to a retardation of the decay of a structure factor in the NSE spatial and time domains. In the reptation model, this lateral confinement is captured by the tube diameter [4]. Hence, the following equation was adopted to analyze the tube diameter of the BR chains:

$$\frac{S(q,t)}{S(q,0)} = \mu + (1-\mu) \times \left([1 - \exp(-\frac{Q^2 d^2 t}{36})] S_{\text{local}}(q,t) + \exp(-\frac{Q^2 d^2 t}{36}) S_{\text{esc}}(q,t) \right) \quad (1)$$

where $S(q,t)/S(q,0)$ is the normalized intermediate dynamic structure factor for the BR-coated CB in dPB, μ is the fraction of immobile polymer components, and $S_{\text{local}}(q,t)$ and $S_{\text{esc}}(q,t)$ are the contributions from local Rouse motion along the tube and escape from the tube, respectively [5]. We set $S_{\text{esc}}(q,t) = 1$ since the chains do not escape from the tube in the NSE time window [3]. The local reptation part is expressed as $S_{\text{local}}(q,t) = \exp[(t/\tau_0) \operatorname{erfc}(\sqrt{t/\tau_0})]$, where $\tau_0 = 36/(W^4 q^4)$ is the time scale for the Rouse motion along the tube. Figure 2C shows the best fits of eq. (1) to the NSE data at the four different q values, giving us an elastic fraction of $\mu \approx 0.3$, suggesting that the trains ($\approx 20\%$ in the BR chains extracted from the MD results [3]) and the short loops are immobile

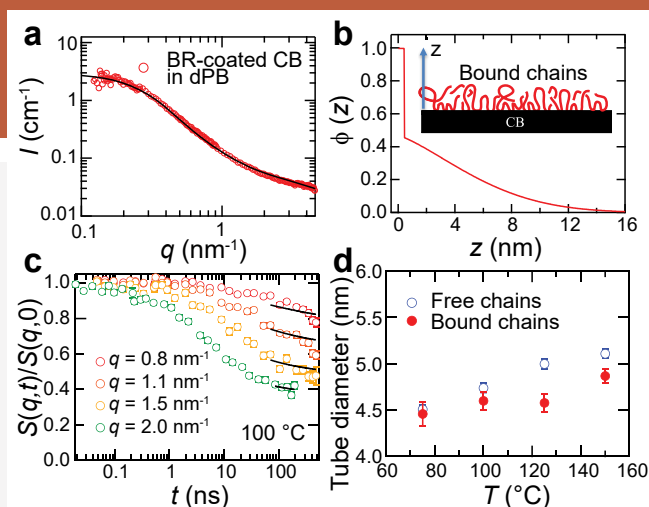


FIGURE 2: (a) Excess scattering from the BR at $T = 150$ °C. The solid line corresponds to the best-fit of the Fourier transform of the polymer concentration profile of the BR layer as a function of the distance from the filler surface (z) shown in (b). In the inset, the schematic view of the BR chains on the CB surface is shown. (c) shows $S(q,t)/S(q,0)_{\text{BR}}$ for the BR-coated CB in dPB at the given four q values and 100 °C. The solid lines correspond to the best-fits of eq. (1) to the data. Temperature dependence of the tube diameter of the BR chains obtained from the best-fits of eq. (1) to the data are shown in (d). The tube diameter of free chains measured by using the hPB in dPB sample is also plotted in (d).

within the NSE domains. The trains promote the strong formation of the BR chains on the filler surface, improving the stability of the BR during deformation.

Figure 2D summarizes the temperature dependences of the tube diameters of the free and bound chains. The results indicate that the temperature dependence of the tube diameter for the bound chains is similar to that of the bulk. Therefore, the results demonstrate that the BR chains entangle (for the tails) or interdigitate (for the loops) with the free chains in the matrix. The chain entanglement/interdigitation at the interface leads to a well-developed and adhesive interface between the filler and matrix polymer.

From an industrial point of view, the origins of reinforcement (such as impact fracture, wear performance, wet grip performance, fuel efficiency, fatigue fracture) are diverse depending on the structures and dynamics at different length scales (angstrom-scale to micron-scale) and time scales (fs to s). Hence the development of advanced filler reinforced synthetic rubbers relies on studies of polymer chains and fillers' hierarchical structure and dynamics, allowing us to establish a comprehensive structure-dynamics-property relationship for filler-reinforced rubbers.

References

- [1] D. F. Twiss, *J. Soc. Chem. Ind.*, **44**, 1067 (1925).
- [2] N. Jiang *et al.*, *ACS Macro Letters*, **4**, 838 (2015).
- [3] D. Salatto *et al.*, *Macromolecules*, **54**, 11032 (2021).
- [4] M. Doi, S. F. Edwards, *The Theory of Polymer Dynamics*. Clarendon Press: Oxford, 1986.
- [5] D. Richter *et al.*, *Adv. Polym. Sci.*, **174**, 1 (2005).

Neutron scattering techniques yield insight into the structure and dynamics of computationally designed coiled coil bundlemers and their supramolecular 1-D assemblies

N. J. Sinha,^{1,2±} G. V. Jensen,^{2,3#} and D. J. Pochan¹



New biomaterials research and discovery requires a fundamental understanding of the structure-property relationships of their building blocks [1]. An attractive class of building blocks is comprised of proteins and peptides that are ubiquitous as nature's structural biomaterials. Neutron scattering techniques *i.e.*, small-angle neutron scattering (SANS) combined with neutron spin echo (NSE) spectroscopy can give unique information about the structure and dynamics in peptides and proteins since the techniques are non-invasive, non-destructive and probe length scales (1 nm to 1000 nm) and time scales (0.1 ns to 100 ns) that are relevant to this class of biomaterials. We have exploited neutron scattering techniques for characterizing non-natural computationally informed peptide assembly. Specifically, we have shown that a novel building block called the *bundlemers* which is a computationally designed coiled coil assembly not only mimics the solution behavior of small globular proteins but can also be linked into 1-D supramolecular polymers that are either rod-like or flexible depending on the type of linker between bundlemers [2-4]. SANS and NSE have been employed to systematically investigate the structure and dynamics of the individual bundlemers as well as the 1-D supramolecular polymers of bundlemers [5, 6].

SANS measurements of a dilution series of bundlemers dispersed in solution was utilized to characterize their shape, size and interactions [5]. Under dilute solution conditions, the cylinder form factor ($P_{\text{cyl}}(Q)$) fit the data well yielding dimensions of 2 nm diameter and 4 nm length that are in close agreement with published literature [2]. A structure factor ($S(Q)$) peak was apparent at higher concentrations. The curves were fit using both Hayter Penfold (HP) $S(Q)$ or Effective Hard Sphere (EHS) $S(Q)$, where the former description yields an apparent net charge on the bundlemers of ca. 8 electronic charges. Thus, bundlemers locally interact as repulsive colloid-like particles in solution. Importantly, a low- Q upturn was recorded under all solution conditions which can be attributed to the presence of clusters of bundlemers due to short-range attraction between them, a consequence of their mixed charged surface. The results highlight the complexity of bundlemers interactions, which are similar to those of small globular protein-protein interactions.

The bundlemers were linked together using a hybrid physical covalent assembly pathway that results in 1-D supramolecular polymers of bundlemers [3]. When a short linear linker was used to link the bundlemers in an end-to-end fashion, rigid rod-like polymers were formed; the SANS curves were fit using a rod form factor as shown in Fig. 1 (bottom, blue) [6]. In contrast, when a small and flexible four-armed linker was utilized to link bundlemers, flexible polymeric chains were formed; SANS curves in this case fit well with a semiflexible cylinder model as shown in Fig. 1 (bottom, red) [6]. The cross-section of both supramolecular polymers was 2 nm which is expected for end-to-end linked bundlemers.

To investigate the impact of type of linker on the nanoscale dynamics of bundlemers within the supramolecular polymers, NSE spectroscopy measurements were performed [6]. In figure 2, we show the log-log plot of decay rate Γ versus scattering vector Q , which was extracted from a single or stretched exponential fit (β is the stretch exponent) to the intermediate scattering function. For rigid rod-like polymers, a single exponential fit was sufficient to describe the nanoscale dynamics. Two dynamical regimes were evident for the semiflexible chain like polymers. At high Q corresponding to intra-bundlemers length scales, the single exponential model yielded satisfactory fits, whereas at mid- Q corresponding to inter-bundlemers length scales, a stretched exponential fit with $\beta < 1$ were required to fit the data. In the latter regime, both Zilman-Granek model developed for thermal fluctuations in stiff rods ($\beta = 3/4$) and Zimm model for polymers ($\beta = 2/3$) gave satisfactory fits to the data. The NSE results prove that the linker type dictates inter-bundlemers dynamics in the supramolecular polymers.

Our studies show that bundlemers are diverse functional units for elucidating structure property relationships for proteins as well as polyelectrolytes and patchy colloids. Furthermore, bundlemers can be linked using bioconjugation and click chemistry methods to build assemblies of arbitrary shapes. Future studies of individual inter-bundlemers interactions and dynamics within new bundlemers assemblies will benefit from neutron scattering measurements that have been reported in this manuscript.

¹ Department of Material Science and Engineering, University of Delaware, Newark, DE 19716

² NIST Center for Neutron Research, National Institute of Standards and Technology, Gaithersburg, MD 20899

³ Department of Chemical and Biomolecular Engineering, University of Delaware, Newark, DE 19716

[±] Present address: Materials Research Laboratory, University of California Santa Barbara, Santa Barbara, CA 93106

[#] Present address: Danish Technological Institute, Taastrup, Denmark

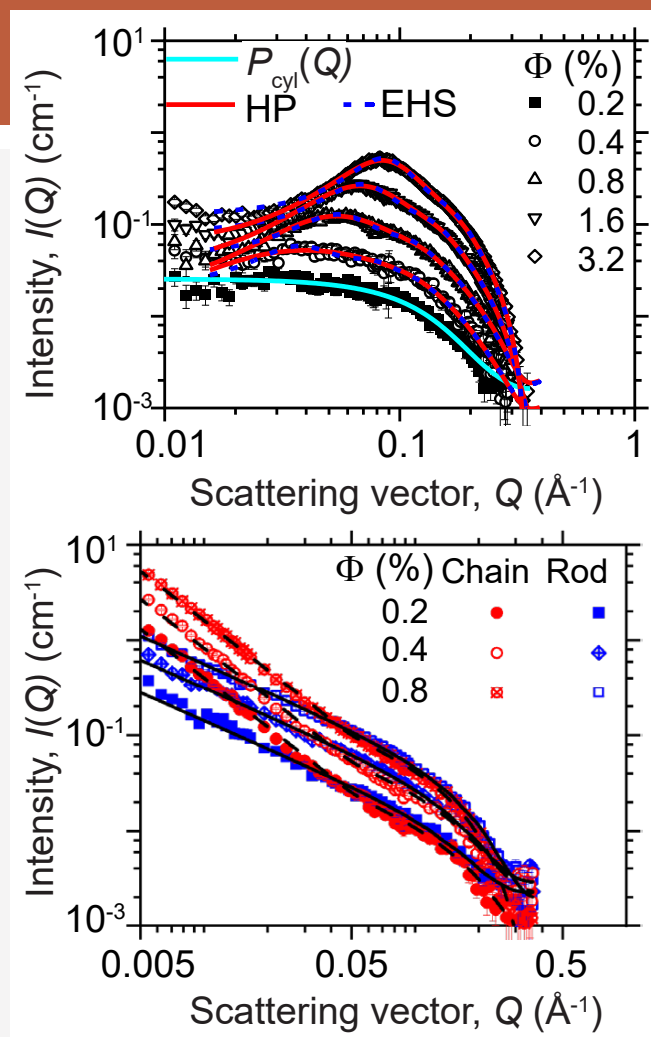


FIGURE 1: (Top) Fits to SANS data using cylinder form factor $P(Q)$ and either a Hayter-Penfold repulsive (HP, solid red line) or Effective Hard Sphere (EHS, blue dashed line) structure factor; (Bottom) SANS data for a concentration series of the semi-rigid polymers ("Chain", red circles) and rigid rod-like polymers ("Rod", blue squares). The concentration of polymer is reported in volume fraction, Φ . The solid and dashed black lines are the corresponding fits to a straight cylinder and flexible cylinder form factor models, respectively. Error bars represent $\pm 1\sigma$ (standard deviation).

References

- [1] N. J. Sinha, M. G. Langenstein, D. J. Pochan, C. J. Kloxin, J. G. Saven, *Chem. Rev.* **121**, 13915 (2021).
- [2] M. J. Haider, H. V. Zhang, N. Sinha, J. A. Fagan, K. L. Kiick, J. G. Saven, D. J. Pochan, *Soft Matter* **14**, 5488 (2018).
- [3] D. Wu, N. Sinha, J. Lee, B. P. Sutherland, N. I. Halaszynski, Y. Tian, J. Caplan, H. V. Zhang, J. G. Saven, C. J. Kloxin, D. J. Pochan, *Nature* **574**, 658 (2019).
- [4] N. J. Sinha, D. Wu, C. J. Kloxin, J. G. Saven, G. V. Jensen, D. J. Pochan, *Soft Matter* **15**, 9858 (2019).
- [5] N. J. Sinha, R. Guo, R. Misra, J. Fagan, A. Faraone, C. J. Kloxin, J. G. Saven, G. V. Jensen, D. J. Pochan, *J. Colloid Interface Sci.* **606**, 1974 (2022).
- [6] N. J. Sinha, Y. Shi, Y. Tang, C. J. Kloxin, J. G. Saven, A. Faraone, G. V. Jensen, D. J. Pochan, *Phys. Rev. Mater.* **5**, 95601 (2021).

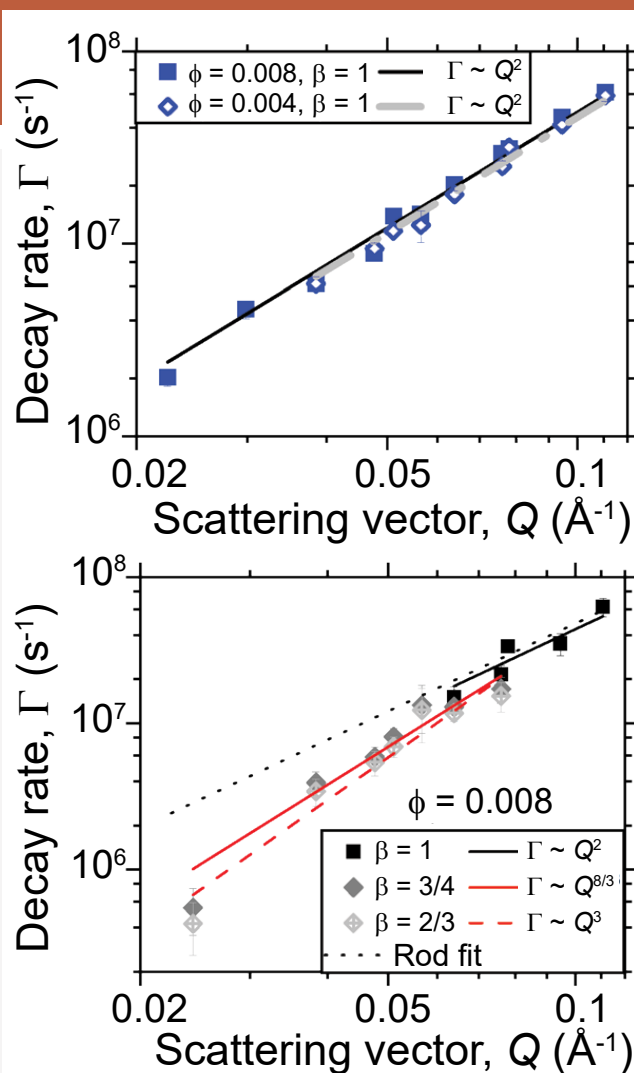


FIGURE 2: (Top) Neutron spin echo (NSE) data and scaling-law fits for rigid rod-like polymers. Measurements were performed on freshly prepared samples at two different volume fractions of polymers, Φ , in deuterium oxide with 50×10^{-3} mol/L sodium chloride at 22 °C. The black solid and grey dashed line are fits to free diffusion dynamics; (Bottom) Neutron spin echo (NSE) data and scaling-law fits for rigid rod-like polymers. Measurements were performed on freshly prepared samples at $\Phi = 0.008$ volume fraction of polymers in deuterium oxide with 50×10^{-3} mol/L sodium chloride at 22 °C. Error bars represent $\pm 1\sigma$ (standard deviation).

Predicting the plateau modulus from molecular parameters of conjugated polymers

A. M. Fenton,¹ R. Xie,¹ M. P. Aplan,¹ Y. Lee,² M. G. Gill,¹ R. Fair,³ F. Kempe,⁴ M. Sommer,⁴ C. R. Snyder,⁵ E. D. Gomez,^{1,3,6} and R. H. Colby^{3,6}

The relationship between Kuhn length l_k , Kuhn monomer volume v_0 , and plateau modulus G_N^0 , initially proposed by Graessley and Edwards for flexible polymers [1] and extended by Everaers [2] to include semiflexible polymers such as filamentous actin, has a large gap in experimental data between the flexible and stiff regimes. This gap prevents the prediction of mechanical properties from chain structure for any polymer in this region. Given their chain architecture, including a semiflexible backbone and side chains, conjugated polymers are an ideal class of material to study this cross-over region. Figure 1 shows the polymer structures considered in a recent study of such materials [3].

Using small angle neutron scattering (SANS), oscillatory shear rheology to determine the plateau modulus G_N^0 , and the freely rotating chain model, we have shown that twelve polymers with aromatic backbones populate a large part of this gap. Figure 2 shows that SANS data on the more soluble conjugated polymers yields a Kuhn length that is invariably in agreement with the estimation of Kuhn length from the freely rotating chain model. Hence, we conclude that we can use the freely rotating chain model to reliably estimate the Kuhn length of other conjugated polymers.

Figure 3 shows that conjugated polymers invariably lie in the crossover of the Graessley-Edwards-Everaers plot, between (and partially overlapping) flexible polymer melts (solid green symbols) and semiflexible solutions (open blue squares). Hence, the conjugated polymers allow us to study the crossover between these limits. That crossover is very nicely described by the curving line, given by the equation below.

$$N_e = \frac{k_B T}{G_N^0 v_0} = 400 \left(\frac{l_k^3}{v_0} \right)^{-2} + 7.77 \left(\frac{l_k^3}{v_0} \right)^{-2/5}$$

This form recognizes that the y-axis of Figure 3 is just the reciprocal of the number of Kuhn monomers in an entanglement strand N_e . This equation is a significant advance in the field, as it allows estimation of plateau modulus from knowledge of the Kuhn length, which for conjugated polymers at least seems to be calculable from the freely rotating chain model, with just knowing bond angles and bond lengths.

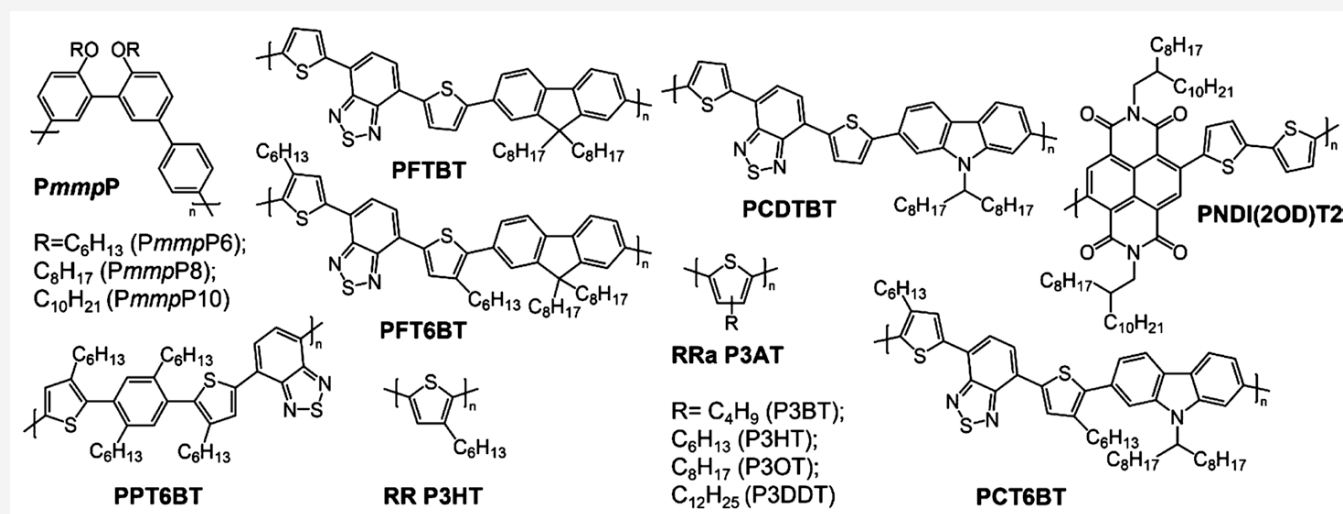


FIGURE 1: Chemical structures of conjugated polymers investigated in this study.

¹ Department of Chemical Engineering, The Pennsylvania State University, University Park, PA 16802

² Department of Chemical Engineering, The New Mexico Institute of Mining and Technology, Socorro, NM 87801

³ Department of Materials Science and Engineering, The Pennsylvania State University, University Park, PA 16802

⁴ Institute for Chemistry, Chemnitz University of Technology, Strasse der Nationen 62, 09111 Chemnitz, Germany

⁵ Materials Science and Engineering Division, National Institute of Standards and Technology, Gaithersburg, MD 20899

⁶ Materials Research Institute, The Pennsylvania State University, University Park, PA 16802

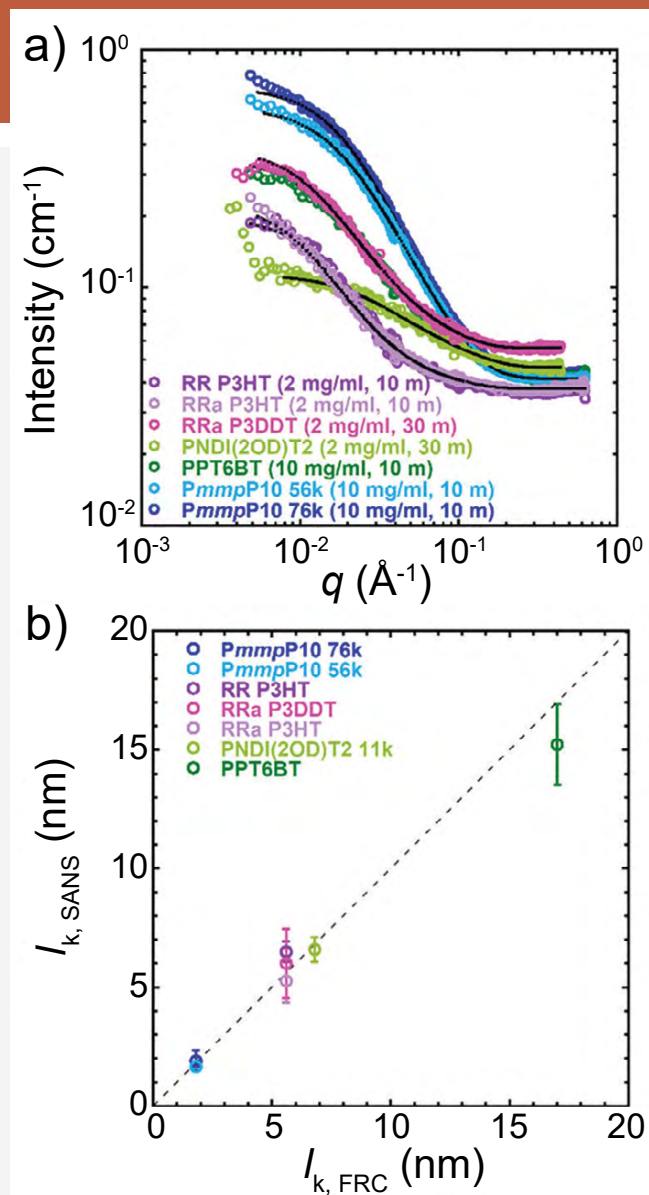


FIGURE 2: Kuhn lengths obtained from small angle neutron scattering (SANS) and the freely rotating chain model. a) Typical SANS data for 7 conjugated or aromatic polymers in d⁵-chlorobenzene. Intensity is normalized to the scattering cross section and plotted vs. scattering vector q . These data are fit to the flexible cylinder model using contour length and dispersity (\mathcal{D}) obtained from polystyrene-standard calibrated gel permeation chromatography (GPC) as upper bounds on parameters as well as a fixed scattering length density. Fits are shown as black lines. b) l_k 's predicted by the FRC model ($l_{k, \text{FRC}}$) are consistent with experimentally measured l_k 's from SANS ($l_{k, \text{SANS}}$) over a wide range of chain stiffnesses. Error bars are the best representation of one standard deviation in the experimental uncertainty.

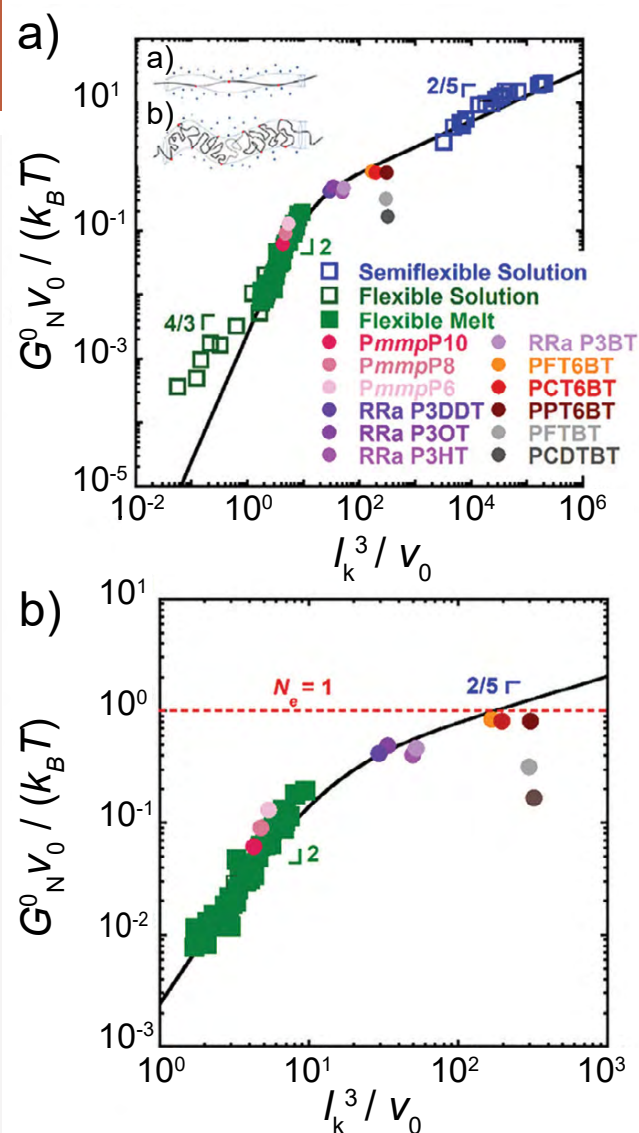


FIGURE 3: Conjugated polymer melts (circles) follow Everaers' scaling predictions with dimensionless plateau modulus G_N^0 vs dimensionless Kuhn monomer volume v_0 . a) The flexible melt data (solid green squares), the flexible solution data (open green squares), and the semiflexible solution data (open blue squares) were obtained from the literature as previously described [3]. The solid black line is the proposed crossover given by the equation in the text. The more flexible PmmpP polymers fit best with the flexible melt scaling argument $(l_k^3/v_0)^2$ while P3AT, PFT6BT and PCT6BT and PPT6BT fit best with the semiflexible scaling argument of $(l_k^3/v_0)^{2/5}$. The PFTBT and PCDTBT polymers lie well below the prediction, this is hypothesized to be due to lingering nematic domains slightly above their T_N . The tube model for a semiflexible and flexible polymer can be seen in insets a) and b), respectively. b) An expanded view of the crossover region. The dashed red line indicates $N_e = 1$.

References

- [1] W. W. Graessley, S. F. Edwards, *Polymer* **22**, 1329 (1981).
- [2] R. Everaers, S. K. Sukumaran, G. S. Grest, C. Svaneborg, A. Sivasubramanian, K. Kremer, *Science* **303**, 823 (2004).
- [3] A. M. Fenton, R. Xie, M. P. Aplan, Y. Lee, M. G. Gill, R. Fair, F. Kempe, M. Sommer, C. R. Snyder, E. D. Gomez, R. H. Colby, *ACS Central Science* **8**, 268 (2022).

Polymer architecture can change dynamics of polymer nanocomposites

S. Darvishi,¹ M. Tyagi,² and E. Senses¹



Dispersing rigid nanoparticles into soft polymer matrices creates a large interfacial area where polymer chains directly interact with the nanoparticles. The resulting nanometers-thick interfacial polymer can be dynamically altered compared to the nanoparticle-free polymer matrix. This brings along not only a unique opportunity to develop advanced polymer nanocomposites (PNC) with unprecedented properties (such as significantly improved mechanical reinforcement at a relatively low fraction of fillers) but also many fundamental physics questions yet to be answered. In our work [1], we show that the architecture of the polymers can be used for modulating the polymer-nanoparticle interfaces and serves as a powerful new parameter for the rational design of PNCs. We prepared nanocomposites of spherical silica nanoparticles of nominal diameter ≈ 50 nm and poly (ethylene oxide) (PEO) matrices with linear, 4-arm star, 8-arm star, and hyperbranched architectures (see Figure 1A for schematic representation). We kept NP loadings at 30 % (by volume) and the total molar mass of PEO at 20 kg/mol for each sample. The end groups of all polymers were hydroxyl (-OH). The only difference between the samples was the architecture of the polymer.

To quantitatively understand the architecture effect on conformation and size (radius of gyration) of the homopolymers, we employed small-angle neutron scattering (SANS) using NGB30SANS beamline at the NIST Center for Neutron Research. The polymers were dissolved in dilute regime (at 1 % by mass) in fully deuterated acetonitrile (C_2D_3N)—the same solvent used for the preparation of nanocomposite samples. In this system, the coherent intensity in SANS results from the scattering length-density difference between the hydrogenated monomers and the deuterated solvent and allows to obtain the spatial correlations of monomers along the isolated polymer chains (*i.e.* conformation) at high resolution. Figure 1B shows the intensity profiles in Kratky scaling (*i.e.* $I_{coh}Q^2$ vs. Q) as a function of wavevector, Q . For a random (Gaussian) coil of a linear flexible polymer, the Debye form factor predicts $I_{coh} \sim Q^{-2}$ scaling at intermediate and high Q . As seen from the profiles in Figure 1B, regardless of their macromolecular shape, all polymers display a plateau at sufficiently high Q (probing small length-scales), suggesting that the individual branches still obey the Gaussian statistics. However, at the intermediate Q values ($\approx 0.5 \text{ \AA}^{-1}$), the star polymers show intra-star peak due to the

correlation between the arms, which is a clear indication of their compact nature. As expected, the peak is most intense for 8-arm star (the most compact polymer) and it completely disappears for the linear and the hyperbranched PEO polymers as they retain their Gaussian coil conformation with no internal structure. Hyperbranched (3rd generation) PEO contains dendritic branches at both ends of a linear backbone, thus exhibiting more open structure compared to the linear one. Fitting the SANS data to the relevant form factors allowed us to estimate the radii of gyration of the polymers, which range from ≈ 3 nm (for 8-arm star, the most compact form) to ≈ 8 nm (hyperbranched, the least compact form).

We performed oscillatory shear rheology experiments on molten nanocomposites to see the effect of polymer topology on the bulk mechanical behavior. For meaningful comparison between the samples, we calculated the reinforcement factors, (G'_{PNC}/G'_{neat}) , defined as the ratio of composite elastic moduli (G'_{PNC}) to those of the neat polymers (G'_{neat}) at a fixed deformation frequency (we chose $\omega = 10$ rad/s, but the trend was similar for all frequencies). The results are shown in Figure 2. Remarkably, G'_{PNC}/G'_{neat} varies within a range exceeding one order of magnitude, even though the samples contain the same number of nanoparticles that are well dispersed and same total molar mass of PEO. Clearly, this variation is due to the shape/architecture of the polymer.

We used quasi-elastic neutron scattering (QENS) to further elucidate the underlying microscopic mechanism in our rheological observation. The experiments were performed on the same neat homopolymer PEO and the same nanocomposite samples used for the rheological tests at 400 K (well-above the melting temperature of PEO) using The High-Flux Backscattering Spectrometer (HFBS) at the NCNR. At low Q , the slow motion of H atoms follows the translational motion of the polymer backbone, thus, measures the segmental dynamics. Figure 3A–D shows the comparison of the normalized QENS spectra for the neat polymers and the respective nanocomposites at $Q = 3.6 \text{ nm}^{-1}$. The dynamic structure factors ($S(Q, \omega)$) were fit to the Fourier-transformed KWW function to obtain the average relaxation time, τ_{self} of the segmental motions and the stretching exponent, β . β was found to be close to 0.5 for all samples, confirming that the dominant process is the Rouse relaxation. The elementary Rouse relaxation rate (W^R) is given by $W^R = 9\pi/(Q^4\tau_{self})$.

¹ Department of Chemical and Biological Engineering, Koç University, Sariyer, Istanbul 34450, Turkey

² NIST Center for Neutron Research, National Institute of Standards and Technology, Gaithersburg, MD 20899

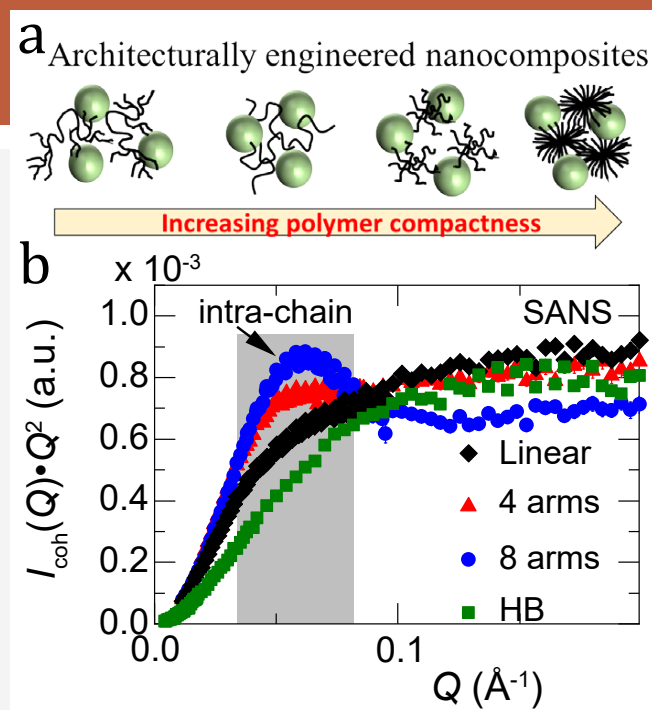


FIGURE 1: (a) Schematic representation of the nanocomposites prepared with different polymer architectures. (b) Kratky representation of the SANS profiles of 20 kg/mol PEO with varying architectures. In the intermediate Q -range, the compact star polymers exhibit peaks due to intra-star correlation.

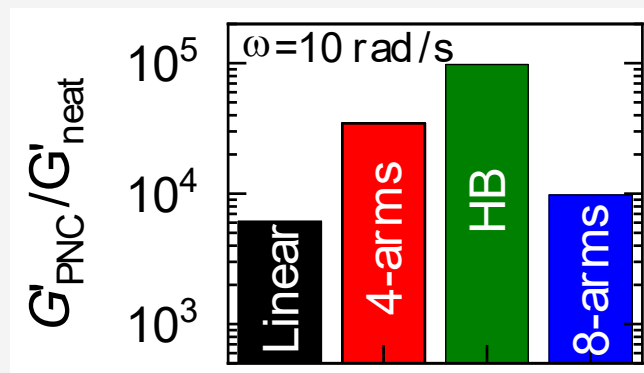


FIGURE 2: Reinforcement factor (G'/G'_{neat}) calculated at $\omega = 10$ rad/s for 30 vol % NP loadings.

The results reveal that the segmental relaxation rate in the nanocomposites decreases monotonically (with respect to their neat form) with the degree of branching. Specifically, compared to the neat polymers, $\approx 6\%$, $\approx 20\%$, $\approx 30\%$ and $\approx 40\%$ reduction in segmental relaxation were found for the nanocomposites prepared with linear, 4-arms, 8-arm and hyperbranched PEO, respectively. We attribute this to the increasing number of hydroxyl ($-\text{OH}$)-terminated end groups of the polymers that can form strong hydrogen bonding compared to the ether oxygen on the backbone. This results in stronger interfaces for the branched architectures (Figure 3E). The slow dynamics of the interfacial polymer can be further

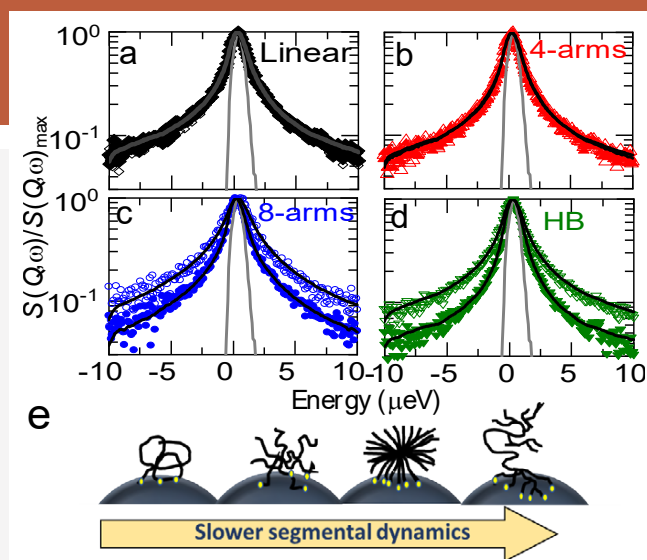


FIGURE 3: Normalized dynamic structure factors obtained from quasi-elastic neutron backscattering at $Q = 3.6 \text{ nm}^{-1}$ and $T = 400 \text{ K}$. The graphs compare the broadening of the spectra for the neat (open symbols) and PNCs (filled symbols) with 30 vol % loading for (a) linear, (b) four-arms, (c) eight-arms, and (d) hyperbranched PEO with the same molar mass of 20 kg/mol. (e) Schematic representation of the interfaces of NPs and the chains with different topologies. Yellow circles represent the H-bonding sites.

propagated into the bulk matrix with the help of entanglements between the interfacial and bulk chains, forming an interphase. This leads to the improved bulk mechanical reinforcement for 4-arm and hyperbranched PEO as they are penetrable and capable of forming entanglements. On the contrary, 8-arm PEO is very compact and contains short unentangling arms; thus, the formation of interphase is not favorable; therefore, we observe reduced reinforcement for the nanocomposite with this particular architecture despite forming strong interfaces.

In summary, our results showed that macromolecular architecture is a powerful new tool for tuning the bulk rheological properties. High-resolution neutron scattering and spectroscopy enabled us to explore the conformational differences in architecturally different polymers and to directly observe the reduction in segmental motions of the polymers at the nanoscale in presence of nanoparticles. These observations shed a light on complex underlying microscopic mechanisms governing the bulk rheological behavior of the nanocomposites with nonlinear polymer architectures.

References

- [1] S. Darvishi, M. A. Nazeer, M. Tyagi, Q. Zhang, S. Narayanan, S. Kizilel and E. Senses, *Macromolecules* **54** (21), 10118 (2021).

Understanding temperature dependent shear thinning of catalyst inks for fuel cells using small-angle neutron scattering

W. Yoshimune and M. Harada

nSoft

In a recent paper [1], we report neutron scattering data that reveals the molecular origins of a high temperature shear thinning transition in a model catalyst ink used in fuel cells. Catalyst inks are often nanoparticle/ionomer slurries, and the performance is strongly dependent on nanoparticle dispersion and slurry density. However, higher densities tend to lead to high viscosities and limiting the effectiveness of mixing technologies. Shear thinning, where viscosity drops with increased mixing, is a route to more economical and effective catalyst ink manufacturing. In addition to confirmation of the shear thinning transition at high temperature, we employ contrast variation small angle neutron scattering (CV-SANS), where a complex nanoscale structure is systematically revealed, to build a molecular model of the temperature dependent phenomena. These data for the first time highlight how manufacturing processes can use temperature to optimize the performance of a catalyst ink.

Polymer electrolyte fuel cells (PEFCs) are one of the primary alternative technologies to fossil fuel-based transportation, including automobiles. Within a PEFC, a catalyst is often a nanoparticle slurry, termed an “ink,” that drives the combination of hydrogen and oxygen to produce electricity and by-product water. To reach a necessary level of performance, catalyst inks must be designed to optimize catalyst dispersion and density while maintaining stability under temperature cycling. Shear thinning, where a fluid viscosity decreases with shear at a faster rate than in water, can either be a useful tool for, or a barrier to, economic control of dispersion and density during manufacturing. The amount of shear thinning with temperature is difficult to engineer as it can be the result of a balance of different attraction and repulsion potentials that can be screened or enhanced through small changes in structure. As a result, a vexing question within this field has been how the temperature dependent structure of nanoparticle ionomer slurries evolves during various stages of manufacturing. Reports of optimization include a range of approaches to achieve optimal performance while molecular level details are often missing.

As evidence, Figure 1 demonstrates a previously unreported shear thinning transition in three slurry formulations. Notably, in each, the zero-shear viscosity increases significantly as temperature is raised from 25 °C to 70 °C, while at the same time the high shear rate viscosity (achieved in mixing or slot-

die coating) decreases. The form of these curves is consistent with a fluid of rigid bodies interacting through hydrodynamic forces; however, the rheology cannot further probe the molecular structure of the fluid, which is necessary to aid formulation design. To probe the origins of the rheology, we employ CV-SANS.

Contrast variation is one of the foundational tools of neutron scattering, where the effects of individual components of a multicomponent structure can be isolated. The approach is to vary the neutron version of the index of refraction of a surrounding medium, termed the scattering length density (SLD), to systematically change the contribution of the individual components to the total measured scattering. With enough variations, each component has at times been highlighted with strong contrast and made transparent with diminishing contrast. Using an established function describing the contributions of each component to the total scattering, it is straightforward to determine a unique solution to the composition and length scales of each component and build a picture of the entire structure at the nanoscale.

Here, we employ CV-SANS on the carbon ionomer mixture used in the rheology measurements. Carbon particles are dispersed in a Nafion® ionomer and water-ethanol mixture. Contrast variation was achieved by varying the scattering length density of the water-ethanol mixture through deuterated analogs. The scattering data are modeled as rigid bodies (the nanoparticles) with a coating of distinct density from the surrounding medium. The ionomer adsorbs to coat the particles with a thickness that increases by a factor of 2 as temperature is increased. As seen in Figure 2, the density of the ionomer layer concurrently decreases. The increased thickness of the ionomeric coating is suggestive of a transition to hydrodynamic bridging, schematically illustrated in Figure 3, resulting in network formation and a dramatic rise in zero shear viscosity between 40 °C and 50 °C. However, the resulting decrease in density of the layer also mitigates electrostatic repulsion, reducing the capacity of the network to resist shear. The result is the shear thinning transition observed.

Using contrast variation neutron scattering, we have shown the high temperature shear thinning behavior of a catalyst ink formulation is derived from the thickness and density of the ionomer layer that surrounds the carbon supports.

Toyota Central R&D Labs, Inc, 41-1 Yokomichi, Nagakute, Aichi 480-1192, JAPAN

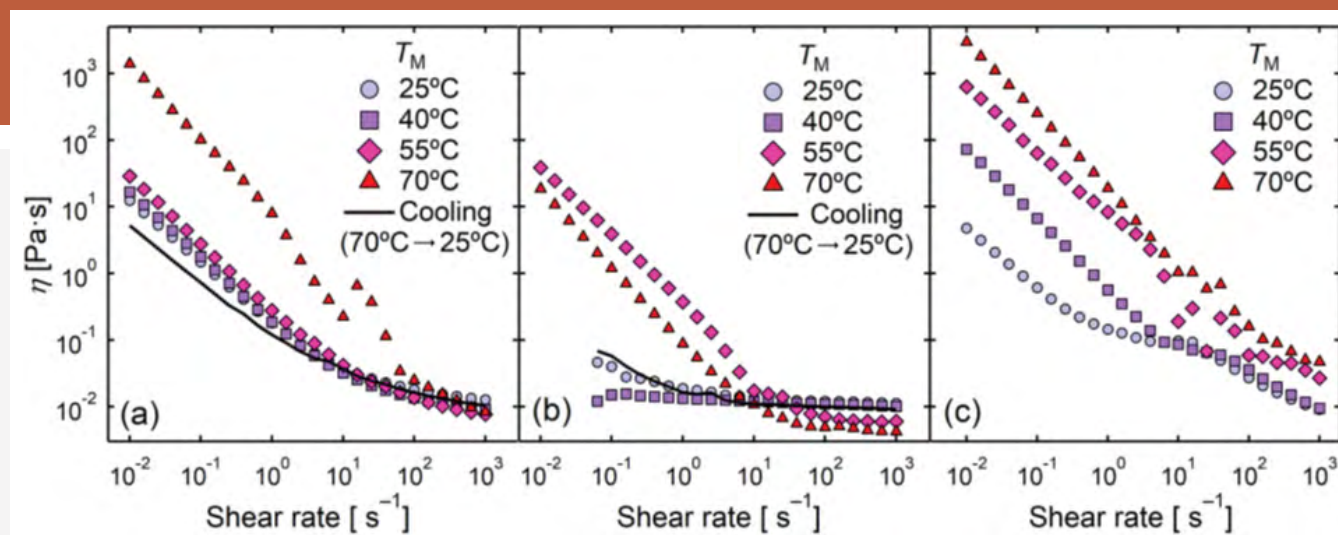


FIGURE 1: Steady shear viscosity η [Pa·s]: (a) Pt/C catalyst ink, (b) catalyst ink with surface-modified carbon supports, and (c) surface-modified carbon dispersion at various discrete temperatures T_M (25 °C, 40 °C, 55 °C, and 70 °C).

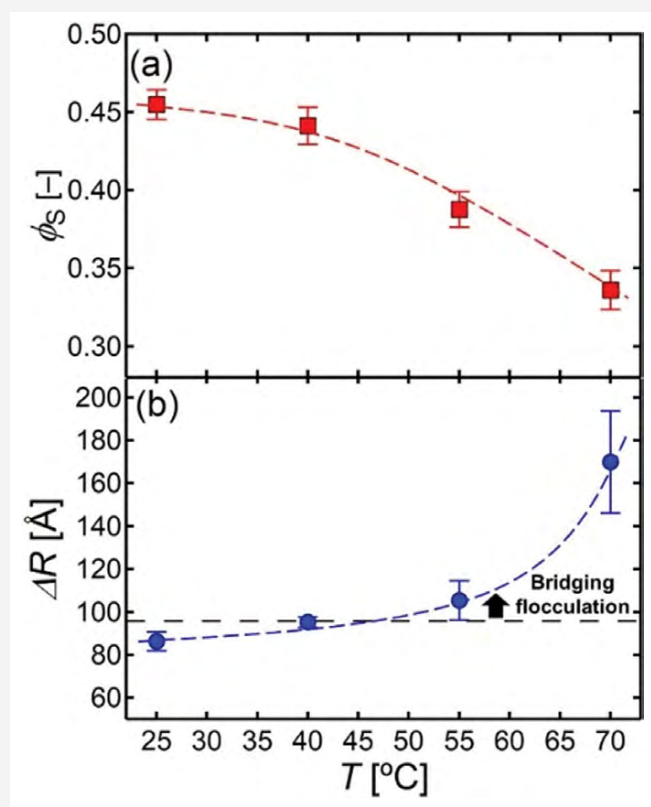


FIGURE 2: Structural evolution of the shell ionomer layer in the catalyst ink as a function of temperature. (a) ϕ_s [-] and (b) ΔR [Å] denote the ionomer concentration and thickness at the surface of the carbon supports, respectively. The dashed black line in (b) represents the boundary of the appearance of bridging flocculation due to hydrophobic interactions between the free end of adsorbed polymer chains.

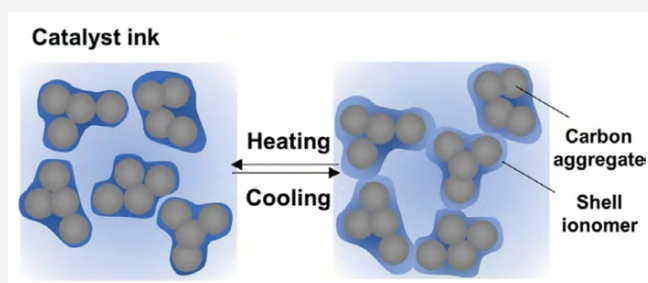


FIGURE 3: Schematic illustration of the structural evolution of a catalyst ink. The bridges between particles are indicated by the overlap of the adsorbed ionomers, not carbon aggregates, in the catalyst ink.

At elevated temperatures, the thickness of the shell increased by more than a factor of two while the density decreased. As this temperature-controlled shear thinning can be useful in temperature-controlled slot-die coating methods, this study provides key data to guide future formulation development of catalyst inks toward more efficient and stable PEFCs.

Reference

- [1] W. Yoshimune, M. Harada, *Electrochem. Comm.* **130**, 107099 (2021).

A versatile stopped-flow sample environment for time-resolved SANS studies

E. G. Kelley,¹ C. E. Stallard,² M. H. L. Nguyen,² D. Marquardt,^{2,3} B. B. Maranville,¹ and R. P. Murphy¹



Time-resolved small angle neutron scattering (TR-SANS) measurements provide unique insights into the time evolution of materials on nanometer length scales. From *in meso* membrane protein crystallization to growth of silica-based materials, cleverly designed experiments have shown how the local structure and composition of nanoscale materials change over time as molecules assemble, exchange, degrade, and react. While most TR-SANS studies to date have focused on time scales of minutes to hours, the newest very small angle neutron scattering (vSANS) instrument at the NCNR was designed with several features to push these measurement capabilities to even faster time scales. By providing high flux collimation options and a wide q range accessible in a single measurement, vSANS has the promise to achieve a tens of milliseconds time resolution for kinetic studies. These instrument advancements open new possibilities to study faster kinetic processes previously inaccessible in TR-SANS.

We have developed a versatile stopped-flow sample environment (Figure 1A) optimized for TR-SANS measurements on the second timescale to take full advantage of the high flux now accessible on vSANS [1]. The system uses multiple syringe pumps and valves to control the sample mixing and to automate cleaning of the quartz sample cells. By using a series of flow selector valves, two or more inlet sample streams can be repeatedly mixed and measured, and the cell can be rinsed with various solvents and dried prior to the next sample injection. The system is enclosed and insulated to control the temperature from 10 °C to 50 °C.

TR-SANS data are collected in 'event-mode', where the location and time of each detected neutron is recorded. Data are then post-processed and binned into the timescale of interest using recently developed scripts. Representative event mode data showing the total neutron counts over time are shown in Fig. 1B. as the quartz sample cell is rinsed with solvent multiple times, dried, and then the sample is injected. Proof of concept studies of a catalyzed lipid exchange process achieved a time-resolution of 3 s, as shown in Fig. 1C [1], where the measured intensity rapidly decays as the lipids in the outer membrane layer exchange between hydrogenated and deuterated vesicles.

Recent developments include an in-line UV-VIS detector and fluorescence cell to enable simultaneous measurement of light absorbance or fluorescence spectra as samples are mixed and injected into the neutron beam. A new graphical status indicator shows the current operating states of the pumps, valves, and sample cells (Fig. 1D). The status indicator will also display the

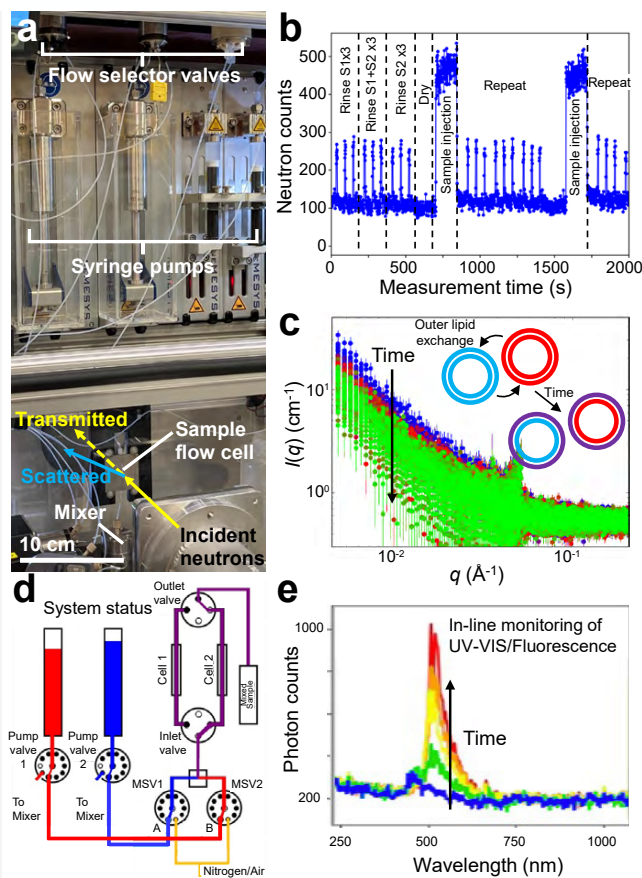


FIGURE 1: (a) The stopped-flow SANS sample environment combines various flow selector valves, syringe pumps, mixers, and flow cells to measure the structure of time-dependent processes. (b) Total neutron counts collected as a function of time throughout repeated solvent rinsing, drying, and sample injection. (c) Time-resolved vSANS measurements of mixed lipid vesicles that exchange hydrogenated and deuterated lipids predominantly in the outer-most leaflet in the presence of an exchange catalyst. (d) Graphical status indicator to display and monitor syringe levels, valve positions, pressure, and sample cell selection. (e) In-line measurements of UV-VIS and fluorescence spectra provide complementary kinetic measures and mixed sample quality control, as demonstrated using a test dye solution as a function of fill time.

measured UV-VIS spectra (Fig. 1E) and SANS intensity in real time during the stopped-flow experiment, which will enable remote operation, give faster feedback, verify mixing quality, and provide improved sample quality control for users. Ongoing developments to build a user-friendly software framework include implementing automatic overpressure shutdowns and integrating temperature control into the existing Python library.

Reference

- [1] E. G. Kelley, M. H. L. Nguyen, D. Marquardt, B. B. Maranville, R. P. Murphy, *J. Vis. Exp.* **174**, e62873 (2021).

¹ NIST Center for Neutron Research, National Institute of Standards and Technology, Gaithersburg, MD 20899

² Department of Chemistry, University of Windsor, Windsor, Ontario, Canada

³ Department of Physics, University of Windsor, Ontario, Canada

Large-area TKIDs for charged particle detection in neutron beta decay and beyond

E. M. Scott,¹ J. Caylor,² M. S. Dewey,¹ J. Gao,^{3,4} C. Heikes,⁵ S. F. Hoogerheide,¹ H. P. Mumm,¹ J. S. Nico,¹ J. Stevens,³ J. Ullom,^{3,4} and M. Vissers³

Precision measurements of fundamental symmetries are playing an increasingly important role in searches for Beyond Standard Model Physics (BSM). These small-scale, high-precision experiments have the potential to reach new physics scales that meet or exceed those that are directly accessible by the Large Hadron Collider (LHC). Neutron beta decay (the process by which a free neutron decays into a proton, electron, and anti-neutrino) is an excellent laboratory for BSM searches because it is understood to high precision. Any deviations from the Standard Model are unambiguous signs of new physics.

While ideal from a theoretical standpoint, precision neutron beta decay experiments face significant challenges. The energies of the decay particles are very low, less than 780 keV and 750 eV for the electron and proton respectively. This makes direct detection, especially of the decay proton, quite challenging. Even state of the art detectors require the proton to be accelerated by 15 kV to be detectable above a 6 keV noise threshold, with 3 keV energy resolution [1]. Additionally, the relatively long lifetime of the neutron (approximately 15 minutes) requires the use of large area detectors to achieve sufficient statistics from even the highest density neutron sources available. Enabling significant improvements in precision requires new detector paradigms to be developed. Quantum cryogenic sensors, particularly thermal kinetic inductance detectors (TKIDs), have been shown to have excellent energy resolution for photons—on the order of tens of eV—and can be multiplexed to very large areas [2] but have never been used for the detection of charged particles from external sources. To support orders of magnitude improvements in precision beta decay experiments we are developing a large area TKID that is optimized for the detection of low energy charged particles [3].

A TKID is a resonant circuit (Figure 1) that is made by lithographing thin layers of superconducting material on a wafer of some absorbing material. Since superconductors exhibit a temperature-dependent inductance when an alternating current is applied, the resonant frequency of this circuit will also shift as a function of temperature. The absorbing material stops the incident radiation, the deposited energy heats the substrate, and the subsequent temperature shift is measured as a shift in the resonant frequency.

The design requirements of our charged particle TKID, or CP-TKID, are very different than those of previous devices which

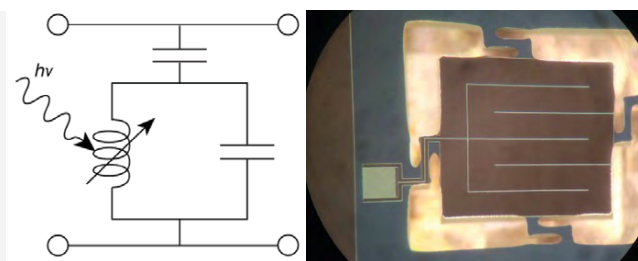


FIGURE 1: Left: Circuit diagram showing the resonant circuit of the TKID. Right: photograph of a functioning 5 mm x 5 mm early prototype CP-TKID.

have thicknesses on the order of μm and surface areas of order mm^2 . The detector thickness must be large enough to fully stop beta decay electron, and the detector active area must scale to large areas due to the statistical requirements of typical neutron beta decay experiments. In practice this introduces a strong tradeoff between performance and channel multiplicity. Geometrical parameters must be optimized while maintaining excellent energy resolution. These requirements suggest a design goal of 2 mm Si absorber thickness and a pixel size of 1 cm^2 , which enables a total active area of 1 m^2 assuming a well demonstrated multiplexing factor of 10^4 . Simple models suggest an energy resolution below 200 eV for such a detector, more than a factor of ten better than existing technologies. Our initial prototype, shown in Figure 1, is 1.5 mm thick and has a 5 mm x 5 mm active area. As this prototype has an absorber volume over 10^4 larger than traditional TKIDs, the absorber dominates the thermal behavior, and the detector response is fundamentally different than smaller devices.

The initial results of our first prototypes are promising, suggesting that a functional CP-TKID is possible at this scale. However, our characterizations are only just beginning and more work needs to be done to understand the thermal behavior of these large scale devices so that we can in turn optimize designs for experimental needs. If successful, CP-TKIDs would greatly improve charged particle detection across a range of disciplines, and in particular, could open the door to next-generation neutron beta decay experiments that would run on the world-class NG-C fundamental neutron physics beamline at the NCNR.

References

- [1] L. J. Broussard *et al.*, Nucl. Instrum. Methods Phys. Res. A **849**, 83 (2017).
- [2] G. Ulbricht *et al.*, Appl. Phys. Lett. **106**, 251103 (2015).
- [3] E. M. Scott *et al.*, J. Low Temp. Phys., (2022) accepted for publication.

¹ National Institute of Standards and Technology, Gaithersburg, MD 20899

² University of Tennessee, Knoxville, TN 37996

³ National Institute of Standards and Technology, Boulder, CO 80305

⁴ University of Colorado, Boulder, CO 80309

⁵ University of Maryland, College Park, MD 20742

ANDiE the autonomous neutron diffraction explorer

A. McDannald,¹ M. Frontzek,² A. T. Savici,² M. Doucet,² E. E. Rodriguez,^{3,4} K. Meuse,⁵ J. Opsahl-Ong,⁶ D. Samarov,⁷ I. Takeuchi,^{4,8} W. Ratcliff,^{8,9} and A. G. Kusne^{1,8}

Neutron diffraction is one of the few characterization techniques that can study the microscopic arrangement of magnetic moments in a material. The ordering of the moments and how the transition from ordered to disordered occurs can determine the usefulness of a material for many applications. Traditionally these measurements are scheduled *ad hoc*, requiring a lot of beamtime. In this work we implement and demonstrate ANDiE, the Autonomous Neutron Diffraction Explorer, to guide the experiment to acquire data at the most informative temperatures.

There are several physics-based constraints that are built into ANDiE. For example, because the magnetic transitions in a material could be hysteretic, ANDiE is constrained to only increase the temperature. ANDiE first infers the most likely parameters of a model describing the temperature dependence of the powder neutron diffraction intensities from the data then extrapolates behavior to higher temperatures with uncertainty. From the predicted intensity ANDiE can also estimate the measurement uncertainty. ANDiE compares extrapolated model uncertainty to the estimated measurement uncertainty. Where that ratio exceeds a user-defined threshold, ANDiE chooses that as the next temperature to measure. We call this threshold the Bravery Factor since it sets how ambitiously ANDiE explores the space—how uncertain the user is willing to let the extrapolation become before another measurement is acquired. Figure 1 illustrates this decision-making process.

ANDiE autonomously drives the powder neutron diffraction experiments until the magnetic transition behavior of the material is well characterized. When ANDiE acquires a powder neutron diffraction pattern at a temperature, it uses a statistical inference method to determine the most likely characteristics of the diffraction peaks from both the magnetic and nuclear ordering. Then, as described in Figure 1, ANDiE extrapolates and chooses the next temperature. This method naturally acquires more data in the temperature regions of interest (e.g., where the intensity changes quickly with temperature near the transition). Once the data has been collected, ANDiE then uses the whole data set to determine the most likely model to describe the magnetic transition behavior and transition temperature of the material being studied.

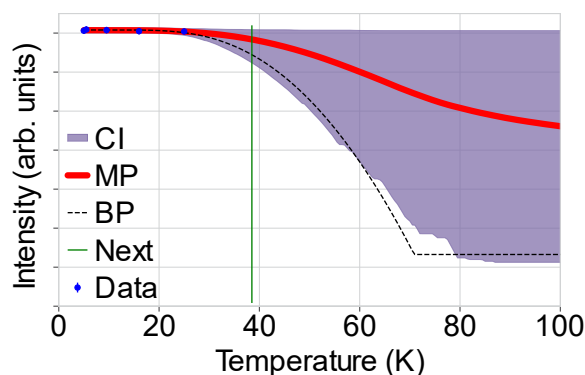


FIGURE 1: The temperature dependence of the magnetic component of the neutron diffraction intensity, for Fe₁₀₉Te measured during an autonomous run using the WAND² instrument. The blue dots show the measured values with error bars. Additionally plotted: the confidence interval (CI) of the model, mean of the posterior (MP) distribution of the model, the model using the best (*i.e.*, most likely) parameters (BP). The green vertical line shows the next measurement temperature, where the model uncertainty relative to the estimated measurement uncertainty exceeds the Bravery Factor.

We implemented ANDiE both on the National Institute of Standards and Technology (NIST) Center of Neutron Research (NCNR) BT-4 Triple-Axis Spectrometer and on the Wide-Angle Neutron Diffractometer (WAND²) at the HB-2C beamline at the Oak Ridge National Laboratory (ORNL) High Flux Isotope Reactor (HFIR). On WAND² we autonomously discover the magnetic transition behavior and transition temperature for two case studies. Firstly, we investigated the well-studied material MnO to ensure that ANDiE could reproduce well known results. ANDiE successfully discovered the Ising-type behavior with a transition temperature at 120.81(56) K in this material using only 16 measurements. Autonomously discovering the transition of Fe₁₀₉Te is a more challenging case study since the abrupt transitions in Fe-Te system occur over a wide range of temperatures depending on the composition. Yet ANDiE was able to autonomously discover the first-order transition behavior at 69.436(55) K. In both cases, ANDiE accelerated the experiment, reducing the number of measurements by a factor of about 5.

For more details see: <https://doi.org/10.1063/5.0082956>. The notebooks and data acquired during the autonomous experiments with ANDiE are available at https://github.com/usnistgov/ANDiE-v1_0, and <https://data.nist.gov/od/id/mds2-2449>.

¹ Materials Measurement Laboratory, National Institute of Standards and Technology, Gaithersburg, MD 20899

² Neutron Sciences Directorate, ORNL, Oak Ridge, TN 37831

³ Department of Chemistry and Biochemistry, University of Maryland, College Park, MD 20742

⁴ Maryland Quantum Materials Center, College Park, MD 20742

⁵ Department of Computer Science, Cornell University, Ithaca, NY 14850

⁶ Department of Computer Science, Rice University, Houston, TX 77005

⁷ Information Technology Laboratory, National Institute of Standards and Technology, Gaithersburg, MD 20899

⁸ Department of Materials Science and Engineering, University of Maryland, College Park, MD 20742

⁹ NIST Center for Neutron Research, National Institute of Standards and Technology, Gaithersburg, MD 20899

Streamlining small-angle neutron scattering data collection under extreme conditions

C. V. L. Gagnon,^{1,2} J. B. Leão,¹ Q. Ye,^{1,3} and S. C. M. Teixeira^{1,3}

The well-known sensitivity of biomolecules to their chemical and physical surroundings challenges measurement precision. The same functional polydispersity enables life in extreme conditions such as the prevalent microbiome on Earth that lives in high-pressure (HP) environments. HP technology is increasingly used in food, biomedical and pharmaceutical applications. Understanding adaptation mechanisms is key to harness molecules that perform under harsh conditions, from robust biocatalysts to stable vaccines [1]. SANS is well suited for *in-situ* non-destructive measurements, yet most HP instrumentation available worldwide—typically designed for Mechanics, Material Sciences and Physics—is inadequate for biomolecule solutions. Dedicated capabilities were therefore developed to increase throughput and broaden the scope of HP-SANS measurements at the NCNR.

Biomolecules are often stored at low temperature to extend their shelf-life but, when aqueous solutions are frozen, exposure to cold temperatures and ice can trigger sample degradation. Freeze-thaw cycles create aggressive microenvironments, including pressures ≥ 200 MPa (≈ 1974 bar) [2]. Biomolecule solutions are typically wasted after a single thaw over safety concerns, lacking experimental data to support stability studies for quality assurance. Low temperature HP-SANS measurements require extended time for thermal equilibration of the bulky pressure vessel and are further limited by deadtime for operation of the system between sample changes. The NCNR provides neutron users access to a liquid insertion pressure system (LIPSS) [3-4] that enables data collection *in-situ* up to 350 MPa and allows for sub-0 °C studies, a capability that no other synchrotron or neutron research center provides for this type of measurements. Recent developments allow for LIPSS to be installed at any of the NCNR suite of SANS instruments (Fig. 1) with or without pre-loaded samples. A plug-and-play port and a mounting frame streamlines sample changes and assists with alignment while keeping the external pressurizing system primed. The control of the external pressurizing system is integrated with the NCNR data collection software, for a more uniform experience for new and experienced neutron users alike. While LIPSS remains available for Soft-Matter and Polymer Science studies, the increased throughput increases accessibility for HP-SANS measurements at low temperature ([5]; see also Soft Matter highlights in this report) and supports a more sustainable use of biomolecules.

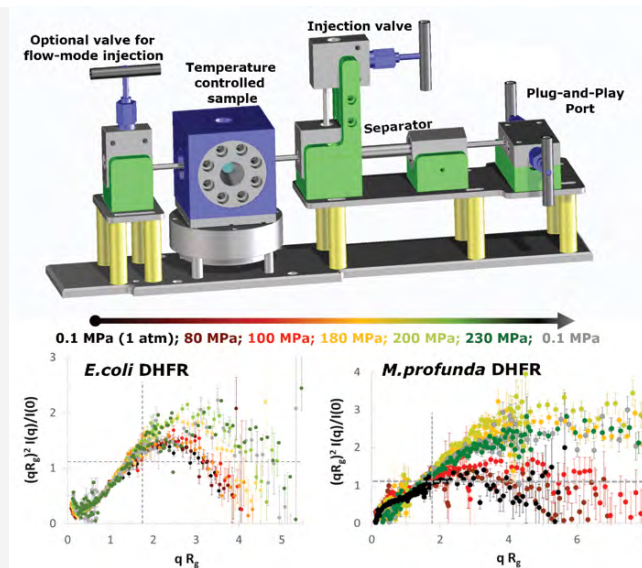


FIGURE 1: TOP: Schematic representation of the LIPSS assembly in the platform mount that now assists operation. BOTTOM: Kratky plots from HP-SANS data collected at the NCNR, where R_g is the radius of gyration of the enzyme dihydrofolate reductase (DHFR), and $I(q)$ are intensities measured at the momentum transfer q . Error bars represent one standard deviation of the mean. The data were measured at 6 °C for DHFR from bacteria adapted to atmospheric (*E.coli*) vs HP environments (*M. profunda*; optimal growth at 220 MPa), revealing how the higher flexibility of the deep-sea enzyme enables function [6].

References

- [1] M. Uddin, M. Roni, *Vaccines* **9**, 1033 (2021).
- [2] J. Authelin, M. Rodrigues, S. Tchessalov, S. Singh, T. McCoy, S. Wang, E. Shalae, *J. Pharm. Sci.* **109**, 44 (2020).
- [3] S. Teixeira, J. Leão, C. Gagnon, M. McHugh, *J. Neutron Research* **20**, 13 (2018).
- [4] S. Teixeira, *Current Opinion in Colloid & Interface Science* **42**, 99 (2019).
- [5] D. Gomes, S. Teixeira, J. Leão, V. Razinkov, W. Qi, M. Rodrigues, C. Roberts, *Mol. Pharmaceutics* **18**, 4415 (2021).
- [6] S. Teixeira, R. Penhallurick, J. Hoopes, R. Hemley, T. Ichiye, *Biophys. J.* **116**, 336a (2019).

¹ NIST Center for Neutron Research, National Institute of Standards and Technology, Gaithersburg, MD 20899

² Department of Materials Science and Engineering, University of Maryland, College Park, MD 20742

³ Department of Chemical and Biomolecular Engineering, University of Delaware, Newark, DE 19716

Neutron Source Operations

At the NCNR, neutrons are produced by a 20 MW reactor. The core consists of 30 fuel elements, four of which are replaced after each 38-day run cycle. On February 3, 2021, while in the process of restarting the reactor after refueling, a radiation monitor exceeded its set point which triggered an automatic shutdown of the reactor. During this incident all reactor safety systems functioned as designed and at no point was there any danger to either NCNR workers or the public.

It was quickly established that one of the fuel elements had not been latched securely in place which allowed it to escape from its hole in the lower grid plate through which cooling water is supplied. This led to significant overheating of the affected fuel element causing damage that resulted contamination of the entire primary coolant loop of the reactor. No damage to other reactor core components such as the lower grid plate was observed.

Cleaning the primary cooling system to a point where the reactor can safely operate has required multiple procedures, involving large debris removal, primary filtering, and reactor component removal. First, a contractor worked with NCNR staff to manually remove the larger fragments of debris from the core (Figure 1). This step was followed by thorough vacuuming of the area. After cleaning the most easily accessible parts of the primary system, custom designed filters, which have the same exterior dimensions as a fuel element, were placed in the core. The primary pumps were then run under numerous conditions to filter the primary water. A notable such condition was the use of ultrasound to dislodge radioactive particulates in regions exhibiting elevated radiation levels. To reduce contamination further, carbon dioxide was introduced into the cooling water causing agitation that helps removes debris from low-flow regions of the system. Finally, a drain valve was removed which allowed the complete removal of some particularly troublesome contamination. Through all these efforts, the primary cooling loop is now cleaned to the point that the reactor can safely operate.

Another issue was the potential contamination of the 29 other fuel elements that were in the core when the incident occurred. To ensure that they could be used again, each was backflushed and then inspected. Unfortunately, it wasn't possible to confirm that all contamination had been removed and in the interest of safety, it was decided not to reuse any of these fuel elements. This necessitated developing alternative fuel configurations for reactor start-up. While these configurations will have a small effect on the length of the first several cycles after restart of the reactor, they provide a means to safely operate the reactor without the need to procure a novel start-up core.

Review groups formed shortly after the incident reviewed all aspects of the event and found that the root causes of

the event included inadequacies in training, procedure compliance, refueling equipment, and management oversight. In response to these findings, teams were formed to develop and implement corrective actions and program improvements. In addition, NIST invited four outside experts to review the NIST analyses and planned corrective actions, as well as the organizational response, and to provide recommendations. Their individual reports can be found on the NIST website.

In March, the Nuclear Regulatory Commission (NRC) released a special inspection report that identified seven apparent violations, five of which NIST had already reported. Then in August, The NRC released a Confirmatory Order that noted that NIST has already completed many corrective actions and enhancements that would preclude recurrence of this type of incident. These actions include improvements to the NCNR safety culture; changes to how reactor operations are managed, and staff members are trained; and updated procedures, including a new requirement for fuel element latch verification through both mechanical and visual methods, which was recently approved by the NRC.

Corrective actions are ongoing with the goal to restart the reactor when the NRC is satisfied that sufficient progress has been made so that the incident will not recur, convinced that the reactor can and will operate safely, and grants permission to restart.



FIGURE 1: Workers from Framatome cleaning debris from the reactor core.

Facility Development

PROGRESS ON D₂ COLD SOURCE AND GUIDE UPGRADES

The NCNR is continuing to work towards major upgrades of the source moderator that serves all of the guide hall instruments. This work was slated for 2023, but it has now been delayed to facilitate reactor operation following the unplanned 2021–2022 outage.

The existing large liquid hydrogen cold source will be replaced with a liquid deuterium cold source that will boost the data

rate by a factor of 2 for most instruments in the guide hall. As shown in Figure 1, the D₂ cryostat is comprised of custom aluminum components that must be welded together into a leak-tight final assembly. This difficult machining and welding work is nearing completion. The middle image of Fig. 1 shows completed pieces of the cryostat that have passed X-ray radiography inspections for weld quality. Following assembly of all completed components, the cryostat will be cold-shock tested at NCNR as a final quality assurance demonstration.

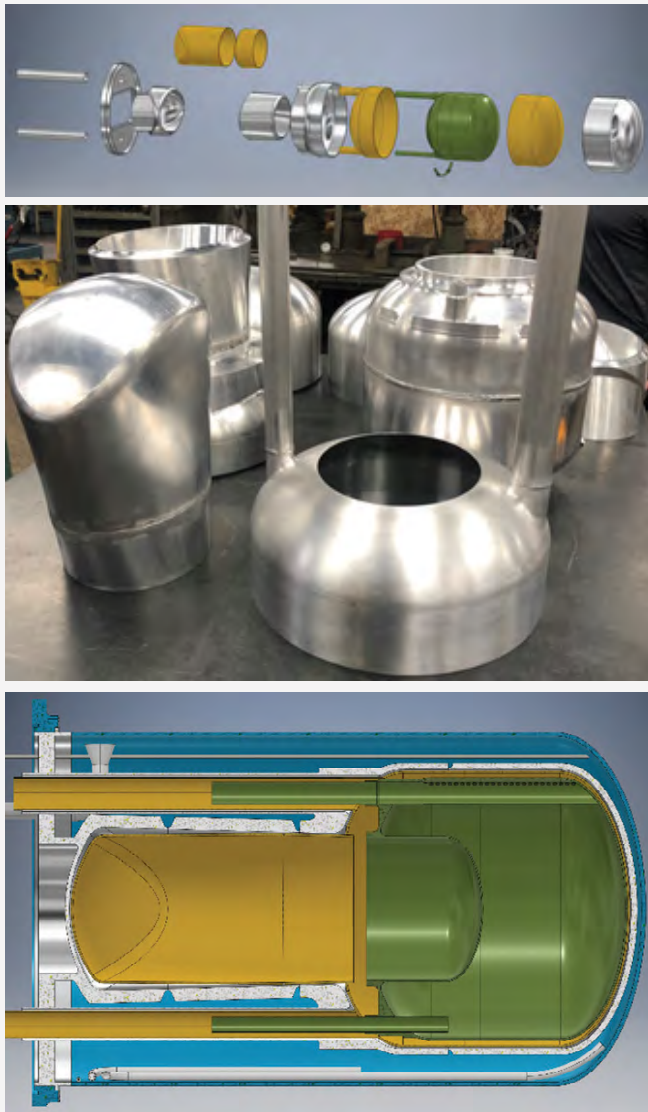


FIGURE 1: D₂ cold source cryostat components. Top: Exploded view of the downstream end of the cryostat; Middle: completed downstream components; Bottom: cryostat as-assembled. Green corresponds to the moderator, gold to vacuum, silver to helium, and blue to the heavy water jacket.

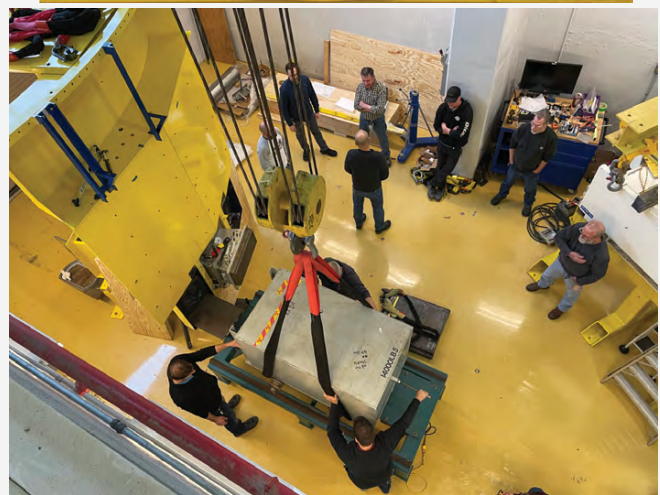


FIGURE 2: Work with the reactor face mock-up. Top: Raphael Erfe from the perspective of the mock reactor core. Bottom: Staff practicing removal of an in-pile guide casing.

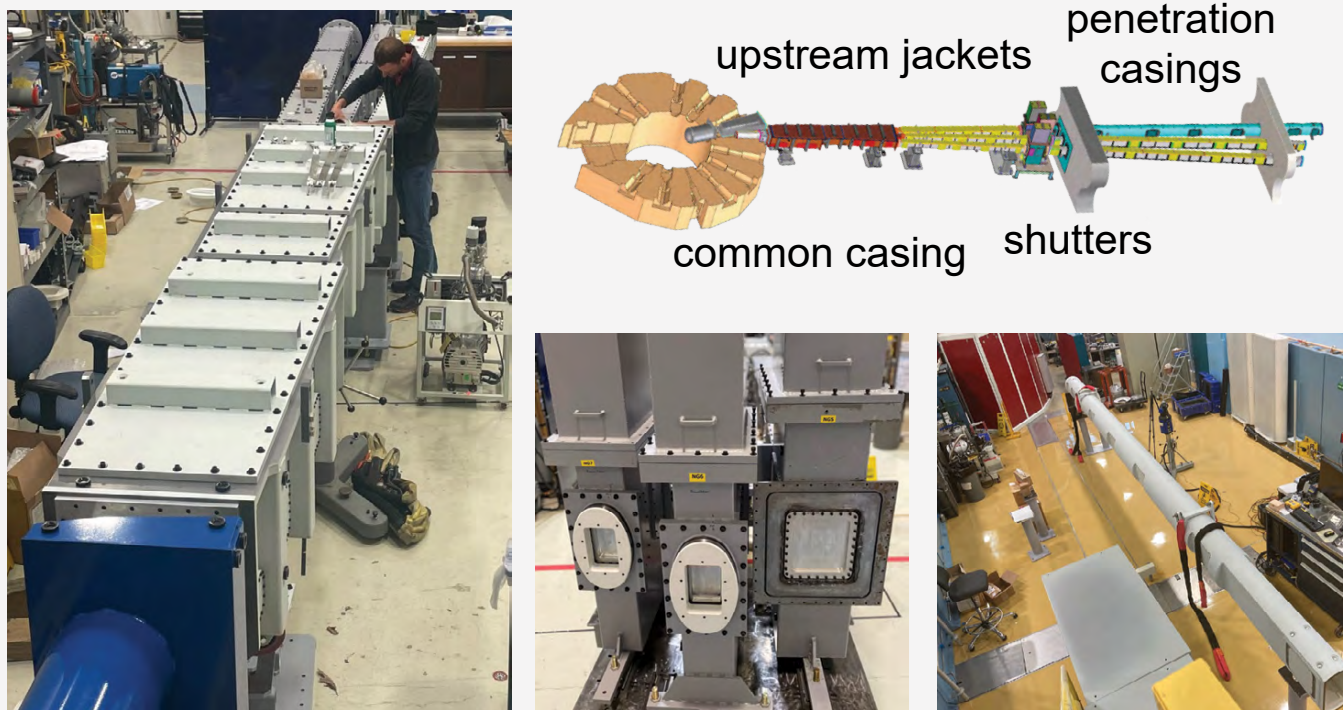


FIGURE 3: Counterclockwise from top right: Diagram of new NG5-NG7 guide sections extending from the reactor face, through the confinement wall, and into the guide hall. Doug Ogg in the high bay assembling the upstream jackets to the common casing. Shutter housings at the downstream end of the pre-assembled upstream guide network. NG5 wall penetration casing positioned for alignment work in the guide hall.

Installation of the new cold source will involve handling highly radioactive components. This work is complicated by the fact that engineering drawings of the reactor face area are not completely reliable. Therefore, we have constructed a mockup of the reactor face for procedure development and practice (Figure 2). The mock sessions conducted thus far have already paid valuable dividends—identifying gaps in procedure efficiency as well as mechanical interferences among components.

Replacing the cold source will require an extended reactor outage. NCNR will take advantage of this down time to upgrade neutron guides NG5-NG7 with modern supermirror guides and replace the in-pile optics serving NG1-NG4. All new guides, guide casings, and shutter assemblies required to re-establish confinement during the outage are now on-site. The new NG5-NG7 guide network from the reactor face to the reactor wall has been pre-assembled and the guides have been aligned in the high bay. The downstream wall penetration casings will be similarly pre-aligned using a mockup of the reactor wall.

NEUTRON SPIN ECHO

Funded by the National Science Foundation, the University of Delaware's Center for Neutron Science is collaborating with NIST and the Jülich Center for Neutron Science to develop a new neutron spin echo (NSE) spectrometer at the NCNR. This new instrument will replace the previous NSE at the end of NGA, and it will provide access to larger Fourier times and an

order of magnitude improvement in data rate. At the heart of the new NSE are the Optimized Superconducting Precession Coils (OSPCs), which drive the instrument's increased sensitivity. The OSCPCs (Figure 4) recently passed factory acceptance testing and are enroute to NCNR. Additionally, all other major components of the new NSE including the neutron velocity selectors, Pythagoras correction coils, power supplies, neutron polarizer, air pads, position sensitive detector, and shielding are complete, with parts received or pending shipment. Demolition of the old NSE has begun, and installation of the new instrument is scheduled to commence in late 2022, with a goal of commissioning with neutrons sometime in early 2023.

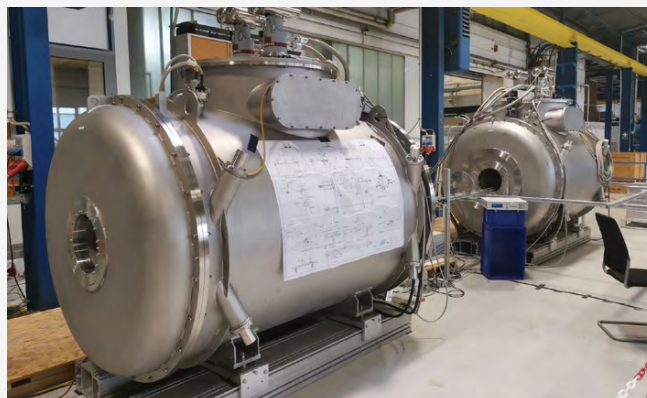


FIGURE 4: Superconducting coils for the new NSE during factory acceptance at Bilfinger in Würzburg, Germany.

DOUBLE FOCUSING MONOCHROMATOR CONTROL

Double focusing monochromators (DFM) are a common component of modern triple-axis spectrometers. DFMs are comprised of a tiled array of monochromating crystals that can be manipulated to tailor the resolution function and optimize flux. Two of the NCNR's two triple-axis instruments—MACS and BT7—utilize such a monochromator. These devices were fabricated nearly twenty years ago, and the associated control architecture were no longer state of the art. As a result, motor moves could take several seconds, adding substantial overhead to scans. In addition, the motor controllers were obsolete, making it impossible to obtain spare parts. The DFM control system was recently adapted to use the NCNR VIPER motor control standard, for which ample spares are on hand. The original Labview control software has also been discarded in favor of the refactored QViper control program, built around the cross-platform Qt toolkit (<http://www.qt.io>). The new system is substantially faster than the legacy electronics, boasting a benchmarked improvement of a sixfold increase in the speed of system moves. It has been tested with the NCNR's NICE instrument control software and is being used for both BT7 and MACS.



FIGURE 5: Double focusing monochromator in use at MACS.

Serving the Science and Technology Community

The mission of the NIST Center for Neutron Research is to assure the availability of neutron measurement capabilities to meet the needs of U.S. researchers from industry, academia and other U.S. government agencies. To carry out this mission, the NCNR uses several different mechanisms to work with participants from outside NIST, including a competitive proposal process, instrument partnerships, and collaborative research with NIST.

PROPOSAL SYSTEM

Most of the beam time on NCNR instruments is made available through a competitive, peer-review CHRNS proposal process. The NCNR typically issues calls for proposals approximately twice a year. Proposals are reviewed at several different levels. First, expert external referees evaluate each proposal on merit and provide us with written comments and ratings. This is a very thorough process where several different referees review each proposal. Second, the proposals are evaluated on technical feasibility and safety by NCNR staff. Third, we convene our Beam Time Allocation Committee (BTAC) to assess the reviews and to allocate the available instrument time. Using the results of the external peer review and their own judgment, the BTAC makes recommendations to the NCNR Director on the amount of beam time to allocate to each approved experiment. Approved experiments are scheduled by NCNR staff members in consultation with the experimenters.

The BTAC members for the Call for Proposals issued in November 2020 are:

- Pinar Akcora (Stevens Institute of Technology)
- Andrew Allen (NIST Materials Measurement Laboratory)
- Jeffrey Allen (Michigan Technological University)
- Collin Broholm (The Johns Hopkins University)
- Leslie Butler (Louisiana State University)
- Sara Callori (California State University San Bernardino)
- Mark Dadmun (University of Tennessee)
- Kendra Elk (Purdue University)
- Kushol Gupta (University of Pennsylvania)
- John Heron (University of Michigan)
- Michael Hore (Case Western Reserve University)
- Hubert King (ExxonMobil—Retired)
- Valery Kiryukhin (Rutgers University)
- Kai Liu (Georgetown University)
- Martin Mourigal (Georgia Institute of Technology)
- James Neilson (Colorado State University)
- Olivier Soubias (National Institute of Health)
- Stephen Wilson (University of California Santa Barbara)

PARTNERSHIPS

The NCNR may form partnerships with other institutions to fund the development and operation of selected instruments. Partnerships are negotiated for a fixed period and may be renewed if there is mutual interest and a continued need. These partnerships have proven to be an important and effective way to expand the research community's access to NCNR capabilities.

COLLABORATION WITH NIST

Some time on all instruments is available to NIST staff in support of our mission. This time is used to work on NIST research needs, instrument development, and promoting the widespread use of neutron measurements in important research areas, particularly by new users. As a result of these objectives, a significant fraction of the time available to NIST staff is used collaboratively by external users, who often take the lead in the research. Access through such collaborations is managed through written beam time requests. In contrast to proposals, beam time requests are reviewed and approved internally by NCNR staff. We encourage users interested in exploring collaborative research opportunities to contact an appropriate NCNR staff member.

RESEARCH PARTICIPATION AND PRODUCTIVITY

The NCNR continued its strong record of serving the U.S. research community this year. Over the 2021 reporting year, the NCNR served 1857 researchers. (Research participants include users who come to the NCNR to use the facility as well as active collaborators, including co-proposers of approved experiments, and co-authors of publications resulting from work performed at the NCNR.) As the number of participants has grown, the number of publications per year has also increased.

NCNR PROPOSAL PROGRAM

In response to the last two calls for proposals (calls 40 and 41) for instrument time, we received more than 723 proposals, of which 396 were approved and received beam time. The following table shows the statistics for several instrument classes. The oversubscription, *i.e.*, the ratio of days requested on all proposals to the days available, was 2.3 on average. Proposal demand has grown substantially since the NCNR first began accepting proposals in 1991. Note that the experiments for call 41 will be run immediately following the current outage. (Note that Imaging results from call 41 are not included in the totals.)

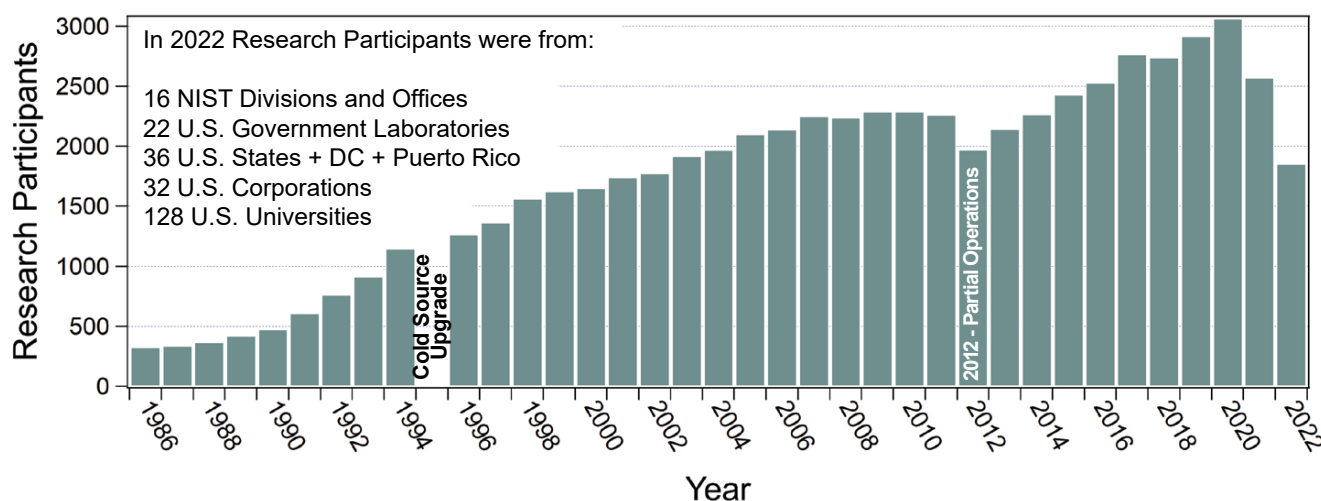


FIGURE 1: Research participants at the NCNR from 1986 to 2022. Fewer operational days in 2020, 2021, and 2022 due to COVID-19 closures and an unplanned shutdown resulted in reduced numbers of research participants.

Instrument class	Proposals	Days requested	Days allocated
SANS	274	999	487
Reflectometers	100	648	288
Spectrometers	297	1938	757
Diffraction	32	104	57
Imaging	20	92	38
Total	723	3781	1627

USERS GROUP

The NCNR Users Group (NUG) provides an independent forum for all facility users to raise issues to NCNR management, working through its executive officers to carry out this function. All members of the Executive Committee (EC) are elected by NCNR users. The current members of the NUG Executive Committee are Claire White (Chair, Princeton University), Michael Hore (Vice Chair, Case Western University), John Riley (The Dow Chemical Company), Malin Zackrisson Oskolkova (Novo Nordisk), Nairiti Sinha (Student/Postdoc Member, University of California Santa Barbara), Dustin Gilbert (University of Tennessee), and Stephen Wilson (CHRNA Liaison, University of California Santa Barbara).

The EC regularly solicits user feedback via a variety of means. The User Group held a well-attended meeting at the virtual American Conference on Neutron Scattering (ACNS) at the University of Colorado Boulder in June 2022 and plans to have another meeting at the ACNS in 2024. The EC also administers a brief email survey that is sent to users approximately one week after the completion of their experiment. Issues identified by the EC are regularly discussed with the NCNR and CHRNA.

management teams with a focus on resolving those requiring immediate action. The EC also conducted a comprehensive user survey in the winter of 2020. There were more than 160 responses, the majority of whom are CHRNA users. The results from the 2020 survey are posted on the NUG website (<https://nug.umd.edu/index.html>). Working closely with NUG, the NCNR and CHRNA management teams prepared an overview of the response/action plan to the 2020 survey designed to make the user experience more productive and enjoyable (Refer to [https://nug.umd.edu/NCNRResponse to 2020survey_Preamble%20final.pdf](https://nug.umd.edu/NCNRResponse%20to%20survey_Preamble%20final.pdf)).

PANEL OF ASSESSMENT

The major organizational components of NIST are evaluated annually for quality and effectiveness by the National Research Council (NRC), the principal operating agency of both the National Academy of Sciences and the National Academy of Engineering. A panel appointed by the NRC convened virtually on July 20–22, 2021. The panel members included Cherry Murray (University of Arizona, Harvard University—emerita, chair), Simon Billinge (Columbia University, Brookhaven National Laboratory), Olivia Graeve (University of California San Diego), Andrew Harrison (Diamond Light Source), Andrew Jackson (European Spallation Source), Dale Klein (University of Texas at Austin), Tonya Kuhl (University of California, Davis), Emilia Morosan (Rice University), Andrew Stephen (Frederick National Laboratory for Cancer Research), and Michael Tsapatsis (Johns Hopkins University). The report from the 2018 Panel of Assessment entitled “An Assessment of the National Institute of Standards and Technology Center for Neutron Research: Fiscal Year 2021” is available at https://www.nist.gov/system/files/documents/2022/02/25/NIST_NCNR_2021_2_24%20final%20report.v2.pdf.

THE CENTER FOR HIGH RESOLUTION NEUTRON SCATTERING (CHRS)

CHRS is a national user facility that is jointly funded by the National Science Foundation and the NCNR. Its primary goal is to maximize access to state-of-the-art neutron scattering instrumentation for the research community. It operates five neutron scattering instruments at the NCNR, enabling users from around the nation to observe dynamical phenomena involving energies from ≈ 30 neV to ≈ 10 meV, and to obtain structural information on length scales from ≈ 0.1 nm to ≈ 10 μ m. A more detailed account of CHRS activities may be found on pp 61 of this report.

PARTNERSHIPS FOR SPECIFIC INSTRUMENTS

NG-7 SANS CONSORTIUM

A consortium that includes NIST, the ExxonMobil Research and Engineering Company, and the Industrial Partnership for Research in Interfacial and Materials Engineering (IPRIME) led by the University of Minnesota, operates, maintains, and conducts research at the 30m SANS instrument located on NG7. Twenty-five percent of the beam time on this instrument is allocated to the general scientific community through the NCNR's proposal system. Consortium members conduct independent research programs primarily in the area of large-scale structure in soft matter. For example, ExxonMobil has used this instrument to deepen their understanding of the underlying nature of ExxonMobil's products and processes, especially in the fields of polymers, complex fluids, and petroleum mixtures.

THE NSOFT CONSORTIUM

Formed in August 2012, the nSoft Consortium allows member companies to participate with NIST in the development of advanced measurements of materials and manufacturing processes and develop their own expertise in state-of-the-art measurement technologies to include in their analytical research programs. nSoft develops new neutron-based measurement science for manufacturers of soft materials including plastics, composites, protein solutions, surfactants, and colloidal fluids. Members receive access to leading expertise and training support in neutron technology and soft materials science at NIST. Contact: Ron Jones, nSoft Director, rljones@nist.gov, 301-975-4624.

NIST / GENERAL MOTORS—NEUTRON IMAGING

An ongoing partnership and collaboration between General Motors and NIST, which also includes Honda Motors through GM's partnership with Honda, continues to yield

exciting results using neutron imaging. Neutron imaging has been employed to visualize the operation of fuel cells for automotive vehicle applications. Neutron imaging is an ideal method for visualizing hydrogen, the fuel of electric vehicle engines. These unique, fundamental measurements provide valuable material characterizations that will help improve the performance, increase the reliability, and reduce the time to market introduction of the next generation electric car engines. 25 % of the time on the BT-2 Neutron Imaging Facility is made available to the general scientific community through peer-reviewed proposals.

INTERAGENCY COLLABORATIONS

The Smithsonian Institution's Nuclear Laboratory for Archaeological Research is part of the Anthropology Department at the National Museum of Natural History. It has had a longstanding and productive partnership with the NCNR, during which time it has chemically analyzed over 43,100 archaeological artifacts by Instrumental Neutron Activation Analysis (INAA), drawing extensively on the collections of the Smithsonian, as well as on those of many other institutions in this country and abroad. Such chemical analyses provide a means of linking these diverse collections together in order to study continuity and change involved in the production of ceramic and other artifacts.

The Center for Food Safety and Applied Nutrition, U.S. Food and Drug Administration (FDA), maintains laboratory facilities at the NCNR providing agency-wide analytical support for food safety and food defense programs. Neutron activation and low-level gamma-ray detection techniques yield multi-element and radiological information about foods and related materials and provide a metrological foundation for FDA's field investigations and for radiological emergency response planning.

The Center for High Resolution Neutron Scattering (CHRNS)



The Center for High Resolution Neutron Scattering (<https://www.nist.gov/ncnr/chrns>) is a national user facility jointly funded by the National Science Foundation through its Division of Materials Research (grant number DMR-2010792) and by NIST. The CHRNS agreement was renewed for five years beginning on September 1, 2020. The mission of CHRNS is fourfold: (i) to develop and operate neutron scattering instrumentation, with broad application in materials research, for use by the general scientific community; (ii) to promote the effective use of the CHRNS instruments by having an identifiable staff whose primary function is to assist users; (iii) to conduct research that advances the capabilities and utilization of CHRNS facilities; and (iv) to contribute to the development of human resources through educational and outreach efforts. Simply put, CHRNS primary aim is “Maximizing access for the scientific community to transformative neutron scattering instrumentation.” A 2½ minute video, *Getting Great Data with CHRNS* (https://ncnr.nist.gov/dimeo/CHRNS_Animation_Final.mp4), highlights and summarizes CHRNS’ focus on advancing neutron scattering measurement capabilities and its prominent role in expanding, educating, and diversifying the community of researchers who use neutron methods.

The scientific community provides essential input through a variety of mechanisms including post-experiment feedback and user surveys, the most recent of which was administered by the NCNR User Group Executive Committee (EC) in the winter of 2021. The EC also led a well-attended discussion for neutron users at the recent American Conference on Neutron Scattering (ACNS) held on June 5–9, 2022 at the University of Colorado Boulder. Another meeting of the User Group is anticipated to be held during the next ACNS meeting in 2024. Users are also encouraged to provide input by directly contacting the CHRNS Director, Associate Director, NCNR Director, and/or members of the EC.

SCATTERING INSTRUMENTS

CHRNS provides robust user operations on the following premier neutron scattering instruments: a backscattering spectrometer (HFBS), the Multi-Axis Crystal Spectrometer (MACS), a neutron spin echo (NSE) spectrometer, and a very small angle neutron scattering instrument (vSANS). In addition, CHRNS is supporting the launch of an innovative white beam neutron reflectometer (CANDOR) with a unique multiplexing detector bank. Combined, CHRNS instruments can provide structural information on a length scale of 0.1 nm to ≈ 3 microns, and dynamical information on energy scales from ≈ 30 neV to ≈ 10 meV.

The unique strengths of these premier instruments are complementary by design. Specifically, HFBS can resolve motions with characteristic times of order a few nanoseconds. Since it offers the highest count rate with sub- μ eV resolution in the US, it is an ideal choice for high resolution, quasi-elastic scattering studies of low-energy dynamics in polymers and biomolecules.

MACS boasts the world’s highest monochromatic cold-neutron flux and routinely is featured in transformative investigations of quantum magnetism. With its 20-detector analyzer array, MACS is well suited for surveys of large regions of reciprocal space, leveraging its exceptional polarized beam capabilities that incorporate a unique toroidal ^3He spin filter.

The NSE instrument provides the highest energy resolution of any neutron spectrometer in North America. It relies upon the Larmor precession of neutrons’ magnetic moments as an internal “clock” attached to each neutron allowing measurements of the final polarization of the neutrons to be directly correlated with the speed of the neutron. This modality results in data being obtained in the time domain rather than in the frequency domain. Fourier times as long as 300 ns (roughly corresponding to an energy resolution of 0.01 μ eV) have been achieved for investigations of slow diffusive processes in a range of soft materials notably including polymer nanocomposites, biomembranes, and biopharmaceuticals. A complete upgrade of the NSE is underway with funding received by the University of Delaware, in collaboration with NIST, from the NSF Mid-Scale Research Infrastructure program (DMR-1935956). The new primary coils and detector will increase the maximum Fourier time achievable at a given wavelength by $> 2.5\times$ and reduce count times by as much as a factor of 10 for a given Fourier time.

For soft matter and magnetic structure characterization, the innovative vSANS instrument is meeting the emerging needs of the CHRNS user community. vSANS has a variety of front-end optics choices including three choices of wavelength resolution in addition to the traditional velocity selector and slit collimation as well as the standard pinhole geometry. Three separate, adjustable detectors yield an extended Q range from 0.002 nm^{-1} to 7 nm^{-1} in a single instrument setting. The flexible sample area opens possibilities for sophisticated sample environments ranging from capillary rheometers to Peltier temperature blocks to high-field magnets. The 45m instrument can also be readily configured for GISANS (Grazing Incidence Small Angle Neutron Scattering) experiments. All these features can be used with full polarization analysis. These elements together provide unprecedented possibilities not only for structural characterization of materials, but also for time-dependent studies of complex hierarchical structures.

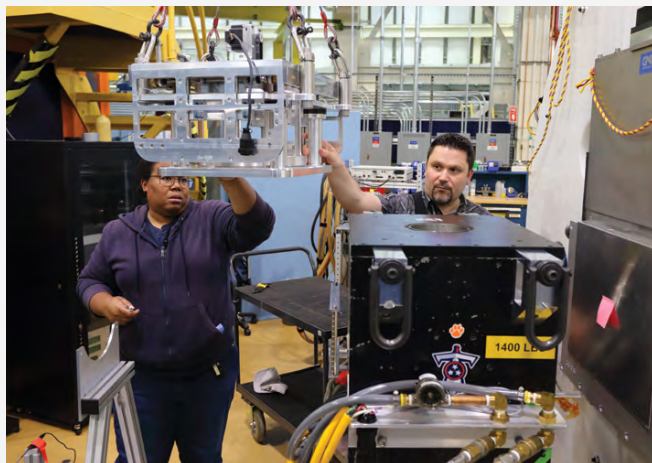


FIGURE 1: Shannon Watson (Neutron Polarization Scientist) and Cedric Gagnon (vSANS Instrument Staff) install a sample elevator on the Titan magnet mounted on vSANS.

A significant addition to the CHRNS instrument suite is CANDOR, which was included for the first time in the Call for Proposals in November of 2020. The novelty of CANDOR lies in its use of a bank of state-of-the-art “energy-dispersive” detectors, which permits a polychromatic beam to impinge on the sample for measurements of either specular and non-specular reflectivity with or without polarized beams. A gain of ≈ 20 compared to the previous generation of neutron reflectometers in service at the NCNR has been realized, and reflectivities as low as 10^{-8} have been measured. Data reduction is provided by *Reductus* which allows users to access and reduce their data anywhere they have a web connection. This exceptional performance will enable unprecedented structural and kinetic characterization of complex materials from the nanoscale to the mesoscale.

RESEARCH

The wide range of instrument capabilities available in CHRNS support a very diverse scientific program, allowing researchers in materials science, chemistry, chemical engineering, biosciences, geosciences, and condensed matter physics to investigate materials such as polymers, metals, ceramics, magnetic materials, colloids, fluids and gels, rocks, and biomaterials. The research community can obtain access to the state-of-the-art CHRNS instrumentation using the CHRNS proposal system. Proposals to use the CHRNS instruments are reviewed on the basis of scientific merit and/or technological importance and broader impacts. In the most recent Call for Proposals in November 2020, 311 instrument-days were awarded of the 887 days requested on the CHRNS instruments. These experiments will be run immediately following the current unplanned outage. More than $\frac{1}{3}$ of NCNR publications (see the “Publications” section on p. 74), are based at least in part on research performed using these instruments. This report contains several highlights of CHRNS publications. See the labeled highlights in the table of contents.

SCIENTIFIC SUPPORT SERVICES

CHRNS provides scientific support in the critical areas of sample environment and chemical laboratories. Specifically, CHRNS offers eight well-equipped and well-supplied user laboratories, including a Guide Hall Laboratory which provides a safe environment for CHRNS users to handle activated samples. The laboratory staff continues to ensure that the required equipment and/or supplies are available for users for their experiments.

The sample environment staff ensures that users have the equipment and training needed to make neutron measurements under external conditions of temperature, pressure, magnetic field, humidity, and fluid flow. From mK dilution refrigeration systems to a 1600 °C furnace, the equipment spans a large temperature range. Beyond precise temperature control, CHRNS provides access to a variety of flow systems, rheometers, gas-loading systems, superconducting magnets with fields of up to 11 Tesla, and other complex equipment to control parameters such as pressure, humidity, and electric fields. During the unplanned outage the user services team has focused on not only revising and updating documentation but also proactively testing and improving the equipment. Ensuring that the available equipment is working and that our staff can support the users in different research areas is critical to ensuring continuity of support when we return to service.

The procurement, development, and commissioning of sample environment is an essential part of the duties of the sample environment staff. We have recently developed a new 9-position Peltier block cell for use on the vSANS instrument. This unique design uses borated aluminum, improving the shielding, temperature, calibration, and even the cleanup of the block. The vSANS instrument also benefits from improvements to the rheometer systems. The MCR 301/501 rheometers have new NICE (NCNR-wide instrument control software) drivers, and new tubing management was installed making it easier for installation in the beamline. The ARES Rheometer has new NICE drivers, a new temperature control system allowing for temperatures from -100 °C to 200 °C a new safety shut-off switch, and a dry air tubing management system. The 1–2 shear cell also has new NICE-controlled modes of operation and a LabVIEW interface that operates via a Compact Rio controller. We have also improved the user interface and stability of the LabVIEW program for the LIPSS (Liquid Injection Pressure System for SANS) system. In addition, we have made changes resulting in improved usability which along with an increase in the number of available cells will allow for faster sample changes and improve neutron duty cycles.

Along with routine maintenance of the gas-dosing suite, we upgraded the syringe pump system that will minimize time wasted during certain shale-related experiments and allow for new kinds of experiments through the addition of a large-volume syringe pump with a redesigned computer-controlled

gas manifold to manage the three syringe pumps that can be in different configurations. We are working on new software to take advantage of the improvements.

The performance of the top-loading closed cycle refrigerator (CCR) for the backscattering instrument (HFBS) was improved by purchasing a new carbon fiber stick, implementing a thinner, easier-to-mount heat shield, and performing various vacuum tests with different kinds of pumps and procedures. These improvements resulted in a significant reduction of the temperature of the sample well while at high temperature, a more rapid initial sample cool down, and reductions in temperature cycling times. These improvements directly contribute to more efficient uses of neutron experimental time.

A new version of the low-temperature single crystal goniometer was designed for attachment to the sample plate of ^3He dilution refrigerator inserts and to the top-loading CCR sticks. The key engineering challenge over the initial model was the reduced diameter in these cryogenic systems, which required a much smaller device. These inserts can be used by themselves or with superconducting magnets (which have a small bore) during neutron scattering experiments to facilitate on-the-fly, controllable crystal orientation at ultralow temperatures for samples in a magnetic field. This version of the goniometer can operate under a 10 T maximum magnetic field. Initial thermalization issues have been solved by incorporating a new vacuum can with feedthroughs that allows the entire goniometer with the sample to be sealed under helium.

A new power supply for CANDOR was purchased that will allow the 3 T magnet to run smoothly with a fully reversible field. It is remote controlled even for flipping the field, a task that previously had to be performed manually. More importantly for data reliability, it eliminates a problem of sudden field jumps, which limited the users' ability to accurately characterize the field reversal process. The new power supply is more precise and stable than existing power supplies for CHRNS instruments, and it allows for fine field control and oscillation of the field that is required for the rapid data collection rates associated with the soon-to-be implemented time-resolved capabilities. It also has a higher current capacity, allowing it to expand to a more powerful magnet in the future. CANDOR also received a new liquid handling robot that was purchased in 2021 and will soon be incorporated into the available sample environments for CANDOR where it will be used to change fluid compositions on-the-fly and in certain cases be coupled with an on-going effort in automated experimental control that optimizes how CANDOR measures successive Q -ranges to maximize the information content in an experimental reflectivity curve.

A new electrochemical workstation was purchased and commissioned to provide features like high-frequency electrochemical impedance spectroscopy (EIS) capabilities, control of multiple channels and samples for optimization of neutron beamtime, and LabVIEW control. The LabVIEW control

allows the workstation to be integrated into measurements associated with the CHRNS Initiative for the Non-Equilibrium Structure of Materials that require specialized remote control of the workstation and time-stamping of the data.

INITIATIVE FOR NON-EQUILIBRIUM STRUCTURE OF MATERIALS

Efforts to optimize materials design and processing require a fundamental understanding of how the physical properties of a system evolve in time when forced out of equilibrium by external stimuli. As part of the current agreement, CHRNS is pursuing a [new initiative](#) that aims to provide the scientific community powerful new tools for probing materials out of equilibrium. The goals of the program are to enhance the nation's capabilities for using neutrons to study the time evolution of materials *in operando*, under processing conditions, *etc.*, such as the charge and discharge cycles of batteries, the non-equilibrium structures of complex fluids under shear, the kinetics of reactions, and the formation of biomolecular complexes. With the advent of vSANS, CANDOR, and MACS, which provide accelerated data rates, and the deployment of new, more flexible, data acquisition system at NIST, coupled with the rise of machine learning and AI, CHRNS is well-positioned to supply the advanced capabilities required to characterize materials out of equilibrium using neutron methods.

Specifically, CHRNS is in the process of implementing a systematic methodology for the absolute time-stamping of instrument and sample environment data. The aim is to couple the event-mode scattering data, which is collected with the NICE data acquisition software, with new sample environment capabilities (such as stopped-flow mixing) that are integrated with the same master clock. Since this initiative will also produce complex data sets that can be explored during and after the experiments, CHRNS is developing the data structures, hardware, and software required for facile manipulation and analysis of the data.

During the unplanned reactor outage, CHRNS staff has made significant progress on advancing this project toward its goals. Most hardware procurements have been received and prototypes designed to allow retro-fitting existing neutron detection systems to conform to the absolute timing requirements. The communication standard of the absolute-timed data transmission system is based-upon the Accelerating Data Acquisition, Reduction, and Analysis (ADARA) specification of the Spallation Neutron Source and has been extended to incorporate real-time neutron detections, instrument parameters (motors, monitors), and sample environment events into instrument networks where the events are ordered in time and stored. We have designed LabView-based absolute-time based broadcasting for slowly responding sample environments (magnets and temperature devices) and are working towards having devices as plug-and-play as possible for in house capabilities. This work is

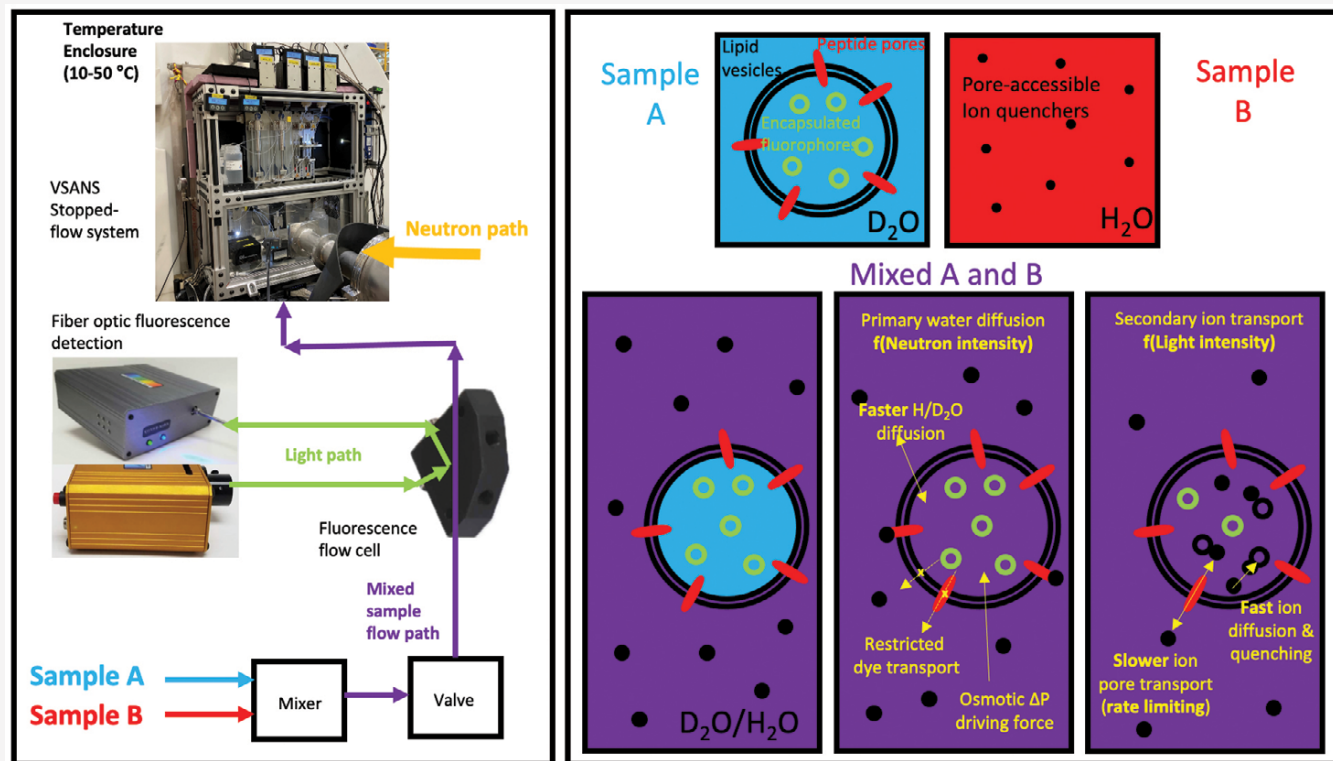


FIGURE 2: A multi-modal experimental configuration for combining stopped flow mixing, fluorescence detection, and small angle scattering measurements at the vSANS beamline. This setup builds upon kinetic neutron measurement capabilities to combine sensitivity of neutron scattering to the sample scattering contrast change as H_2O diffuses through lipid membrane walls into vesicles filled with D_2O (and vice versa), while also monitoring ion transport.

informing us how to reduce the barriers for users to bring their own equipment into the facility and quickly incorporating it into the neutron experimental workflow.

Engineering design and procurement orders were placed for an accurate sample rotation device to allow MACS to optimally double its count rate by constantly rotating the sample rather than stopping and starting motors. An electrochemical workstation was received and is being tested with a newly designed and 3D-printable battery 'cell' compatible for reflectometry measurements on CANDOR. A new fluids delivery robot for CANDOR was received and will be incorporated into CANDOR operations over the next year.

While we have procured a *commercial* stopped-flow apparatus with ≈ 30 ms time resolution that is suitable for materials with aqueous-like viscosities, further development of the *in-house* stopped-flow apparatus ("[Measuring the Time-evolution of Nanoscale Materials with Stopped-flow and Small-angle Neutron Scattering](#)") will allow us to achieve ≈ 400 ms deadtime, with fluids up to ≈ 100 times larger viscosities. The *commercial* system will have a standard temperature range of -10 °C to 80 °C and an attachment to allow for heating up to 180 °C. This year we built an enclosure for the *in-house* system that operates from 10 °C to 50 °C and has rapid temperature equilibration as well as considerations for neutron beam transmission and user access. The multi-modal capabilities

are being extended for the *in-house* system with the addition of in-line fluorescence measurements to allow for probing ion transport rates based upon the quenching of fluorescence dyes as compared to water transport through complex interfaces in vesicles (Fig. 2).

ADDITIONAL CHRS EFFORTS DURING THE UNEXPECTED REACTOR OUTAGE

During the past year a proof-of-principle Monte Carlo simulations have shown that the data rate on CANDOR could be doubled through the application of Bayesian statistics and Information Theory for autonomous data collection. This relies on improvements in data acquisition, optimization of codes for model building and Bayesian analysis, and automated data reduction and fitting of reflectivity curves. Over the next year we will work on making this concept a reality for CANDOR.

The NCNR has a demonstrated commitment to open data, for example with [a long-standing policy](#) that maintains, and backs-up most raw data taken during experiments on the neutron instruments, and it is immediately (within a few minutes) open and available for download by all, without a login. An exception exists for an 18-month opt-out period if the research team elects it, and we do not publish or maintain any proprietary data. Over the past year CHRS has greatly improved the overall FAIR stance of CHRS and the NCNR.



FIGURE 3: Jeff Lynn, Yang Zhao, William Ratcliff, and Rebecca Dally teaching a small group during a triple axis experiment. Parts of the GatherTown virtual room are seen in the lower part of the screenshot.

There is recognition amongst scientific agencies, funding bodies, and researchers that universal use of permanent identifiers (DOI) should be employed to make experimental data findable and citable. This DOI concept extends from the individual researchers that perform the experiment through to the raw data which includes instrument and sample environment data and meta-data. Users can now use a standard identifier (ORCID) when registering for an experiment that acts as a personal DOI in the metadata of the experiments allowing for attribution for those data. In addition to the context of the neutron measurement itself, many users arrive for an experiment with detailed information about preparation and previously measured properties of samples to be studied, and we previously provided no easy way to link that metadata with the CHRNS neutron measurements. We have implemented a system for users to enter this metadata according to predefined taxonomies while also supplying necessary flexibility for ad-hoc metadata entry. This metadata will be linked to the data files and form the basis of a public metadata-search system for finding relevant data files and experiments, resulting in great improvements to the findable and reusable aspects of FAIR data.

The raw experimental data and meta-data are automatically published to a public data/metadata repository (<https://data.nist.gov/sdp/#/>) on a schedule consistent with previous policy allowing for the deferral on an 18-month schedule. We have additionally vastly improved the search facility with a user-friendly front-end and an interoperable machine-accessible interface (API) to facilitate future large-scale AI and machine learning research using NCNR data outputs. The contents of this database results from harvesting both process and user-

supplied sample metadata from the datafiles as they are added to the raw data repository, along with historical data from current databases and further mining of metadata from many of the existing data files.

To support reproducibility and traceability, we are implementing data reduction processes (post-processing raw data to meaningful scientific units) that record all the necessary parameters and steps taken in the processing. For some instruments we embed this record in the output files, and for others it is available as a separate file for the user to add to their records. To further help users with this, the CHRNS spectrometers MACS, HFBS and NSE and instruments operating with NCNR's NICE instrument control software, have standard workflows that automatically tag datafiles with process metadata, e.g. identifying background scans and supplying sample identifiers that allow automatic grouping and sorting of data for further reduction and analysis. This auto-tagging renders the data Reusable with other systems, as it applies a standardized set of metadata. The NCNR will provide documentation and training on how users can easily publish this reduced data, the method file(s), and any additional post-processed, analyzed, plotted, or published data to a public data repository, and link back to the automatically created DOI for raw experimental data and meta-data.

Users will directly benefit by being able to cite their data (a requirement for an increasing number of journals) as well as keeping track of their data/metadata with a small set of links that is easily tracked in the PI's group and provides the necessary information to easily revisit that experiment. Any reuse of the data by the broader scientific community provides

FAIR access and can result in an additional citation for the users. The ORCID system provides yet another possible route for discovery and re-use of the data through searches for data by researcher.

EDUCATION AND OUTREACH

CHRS sponsors a variety of educational programs and activities tailored to specific student groups and professions. One of the premier outreach activities is the annual neutron school. During the past few years, the school has continued to attract graduate students, post-docs, and junior professors with a wide range of expertise in areas such as chemistry, engineering, physics, materials science, and biosciences. Recently we have adapted to the travel restrictions imposed by COVID 19 and developed a successful virtual school. Following the success of the previous virtual school in 2021, the 27th Center for High Resolution Neutron Scattering (CHRS) "School on Methods and Applications of Neutron Spectroscopy," was held virtually January 28–February 11, 2022. This school was attended by 51 students affiliated with North American universities and US industry located in 21 US states, the District of Columbia, and Canada. Students came from a diverse set of backgrounds including Physics, Chemistry, Chemical, Biomolecular, and Molecular Engineering, Materials Science and Engineering, Astronomy, Nuclear Science and Engineering, Polymer Science, Plant & Soil Sciences, and Structural and Materials Engineering.

The school content is tailored to those with little or no previous experience with neutron scattering methods. It included introductory lectures along with hands-on data analysis which simulated the work of a researcher after collecting neutron reflectivity and SANS neutron data. This school had many special features optimized to its virtual venue. While the lectures were provided via a conventional video-conference platform, the students' poster sessions, coffee hours, and small-group tutorial sessions were held in GatherTown, an online platform that allows participants to move their avatars around a virtual conference center. Poster sessions held during the coffee hours for the first four days gave students the opportunity to present their research to the instructors and fellow students. As a final project, the students were asked to write a beam time proposal on a subject of their choice, either related to their own research or based on one of the school experiments that they did. The student beam time proposals were then submitted through the NCNR Information Management System and reviewed in the same manner as real ones, giving students the same experience as researchers. Lessons learned from this undertaking are currently being applied to other virtual events.

Throughout the year staff scientists participated in teaching courses on topics including scattering theory and techniques at nearby universities and at international and national schools. One of the highlights was the three-day "Fundamentals of



FIGURE 4: Elizabeth Kelley (CHRS vSANS Instrument Scientist) shows students the beamstop in the vSANS detector tank during the "Fundamentals of Neutron Spin Echo (NSE) Spectroscopy for Biology and Soft Matter" workshop in October 2021.

Neutron Spin Echo (NSE) Spectroscopy for Biology and Soft Matter" workshop held from October 27th–October 29th, 2021 in Gaithersburg, MD. The 20 attendees included graduate students, post-docs and a few young faculty. This event was designed to prepare scientists for the use of NSE techniques, with emphasis on applications to soft matter and biology. The workshop included lectures by four CHRS scientists (Elizabeth Kelley, Michihiro Nagao, Antonio Faraone, and Madhusudan Tyagi) and a tour of the NCNR that highlighted the NSE instrument. The NSE workshop was also supported by the NSE upgrade project under NSF grant (DMR-1935956).

William Ratcliff (NCNR Instrument Scientist) was one of the principal organizers and lecturers in the virtual [Neutron] Representational Analysis and Magnetic Structure School held from November 8–12, 2021, which hosted 109 graduate students and post-docs. The school covered representational analysis, magnetic space group approaches, and the theory of magnetic structures, which are important approaches for solving magnetic structures from neutron diffraction data.

On December 9, 2021, Paul Butler (NCNR Team Leader) organized a virtual Sasview workshop entitled "Writing Your Own Model from Scratch is Easy" with 20 attendees from around the world. Also, William Ratcliff (NCNR Instrument Scientist) was a co-organizer for the first Data Science Education Community of Practice (DSECOP) workshop held in-person on June 22–23, 2022 at the University of Maryland. The 38 participants engaged in activities focused on getting data science into the physics curriculum.

CHRS co-sponsored the fifth Fundamentals of Quantum Materials School and Workshop at the University of Maryland on June 20–23, 2022. The workshop brings together senior and junior scientists to address topics at the forefront of current research into quantum materials while also providing practical training for junior scientists. Jeff Lynn (NCNR Team

Leader) was a lecturer at the school, and Nick Butch (NCNR Instrument Scientist) co-organized the event which included 35 graduate student/post-doc participants and featured a tour of the NCNR.

Under the leadership of Wangchun Chen (Neutron Polarization Scientist), several NCNR staff members organized the International PNCMI (Polarized Neutrons for Condensed Matter Investigations) conference, which was held in Annapolis, MD from July 25–29, 2022. The conference brought all levels of scientific professionals together to discuss the latest condensed-matter investigations using polarized neutrons and state-of-the-art methods of polarized-neutron production and their use in novel instrumentation and experiments with an emphasis on prospects for new science and instrument concepts as well as combining neutrons with complementary techniques. The attendance included 62 participants from 30 institutions and 10 countries crossing Europe, Asia, and North America. The event was preceded by an in-person polarized neutron school with 12 student attendees held on July 24–25, 2022 at the NCNR that featured lectures and hands-on experiments. This biannual conference was originally scheduled for the summer of 2020 but was cancelled due to the COVID outbreak. To fill this unexpected gap, the same team of NCNR staff members coordinated a virtual version of the PNCMI conference that was held from July 27–31, 2021 and included 110 participants from 40 institutions and 15 countries crossing Europe, Asia, Australia, and North America.

In November 2021, Alex Grutter (CHRNS CANDOR Instrument Scientist) and Brian Maranville (CHRNS CANDOR Instrument Scientist) were featured speakers at the 23rd ISIS Virtual Reflectivity Training Course that included 35–50 graduate student and post-doc attendees. This school was focused on data analysis, error treatment, etc. in neutron reflectometry measurements. On December 9, 2021, Michihiro Nagao (CHRNS NSE Instrument Scientist) also gave a virtual lecture on quasi-elastic scattering as part of the 5th Neutron and Muon School sponsored by the J-PARC neutron facility in Japan. In more of an informal setting, Yun Liu (CHRNS vSANS Instrument Scientist) participated on November 1, 2021 in a virtual discussion of designs for small angle neutron scattering instruments as part of an undergraduate design class with five undergraduate students in the Nuclear Science and Engineering Department at MIT. Yun Liu returned on December 8, 2021 as a judge of the final student presentations. Yun Liu also was featured on May 18–19, 2022 as a keynote speaker and gave a tutorial on “Studying Soft Matter with Neutron Scattering” at the Annual Center for Soft Matter and Biological Physics Symposium at Virginia Tech with attendance of approximately 20 graduate students and faculty members from the Center for Soft Matter and Biological Physics. Chuck Majkrzak (NCNR Team Leader) and Thomas Gnaupel-Herold (NCNR Residual Stress Scientist) gave in-person lectures in late July 2022 on the fundamentals of reflectivity and on polarized

neutrons, respectively, at the virtual National School on Neutron and X-ray Scattering which is co-sponsored by Argonne National Laboratory and Oak Ridge National Laboratory. On August 1, 2022 Yimin Mao (NCNR Instrument Scientist) was an instructor in a Small Angle X-ray Scattering (SAXS) Workshop at the Denver X-ray Conference held in Bethesda, MD.

As part of its education and outreach effort, CHRNS allows university-based research groups with BTAC-approved experimental proposals to request travel support for an additional graduate student to participate in the experiment. This support is intended to enable new graduate students, for example, to acquire first-hand experience with a technique that they may later use in their own research. Announcements of this program are sent to all university groups whose experimental proposals receive beam time from the BTAC. Recipients of the announcement are encouraged to consider graduate students from under-represented groups for this opportunity. The program is also advertised on the NCNR's website at <https://www.nist.gov/ncnr/chrns/travel-support>. As a COVID travel restrictions continue to be reduced, this opportunity will be expanded to include a limited number of travel awards to enable graduate students or post-docs to attend NCNR workshops or related CHRNS-sponsored events.

CHRNS supports universities seeking an NSF INTERN supplemental grant which allows them to station graduate students at NIST for an extended period. This opportunity helps educate the student on neutron scattering to become successful facility users. There have been three recipients who recently sent students to work at the NCNR. Donghui Zhang from Louisiana State University obtained the supplemental grant for her research on structures in amphiphilic coil-comb block copolymers, and her student (Meng Zhang) was at NIST in 2020. Dario Arena from the University of South Florida sent a student (Jenae Shoup) from September 2021 to January 2022 to investigate magnetic coupled heterostructures. In addition, Carol Korzeniewski at Texas Tech and Shelly Minter from the University of Utah obtained support for a student to apply neutron reflectometry to polymer electrolytes. Their student (Miharu Koh) from the University of Utah, began her internship in August 2022 and will visit NIST periodically for experiments throughout 2023. Marcus Foston from Washington University in St Louis won an award to work on catalyzing lignin depolymerization and plans to send a student to the NCNR in 2023 when neutrons are available.

CHRNS is pleased to announce the launch in late June 2022 of the new CHRNS Outreach and Research Experience (CORE) program. CORE is a paid internship program that provides undergraduate students with hands-on research and engineering experience under the mentorship of one or more NCNR staff members. CORE has an emphasis on retaining underrepresented groups in STEM and is more versatile than a standard summer internship with flexible start and end dates throughout the academic year. CHRNS looks forward to hosting its first CORE interns during FY2023.



FIGURE 5: CHRS SURF students Kim Taylor (far left) and Amy Musser tour the NCNR with their mentors Susana Marujo Teixeira and Yimin Mao (far right) during their SURF internship in the summer of 2022.

For 11 weeks in the summer of 2022, CHRS participated in NIST's Summer Undergraduate Research Fellowship (SURF) program by remotely hosting eight SURF students, including one previous Summer High School Internship Program (SHIP) students and two returning NCNR SURF students. The students performed research on topics ranging from stabilizing chitin nanocrystals in surfactant-free oil-in-water emulsions, to automatic identification of regions of neutron diffraction patterns during phase transitions. The students gave virtual oral presentations describing their work at the virtual NIST SURF colloquium in early August 2022 moderated by Dr. Guebre Tessema, a program director for CHRS from the National Science Foundation. The colloquium featured a plenary talk by Jack Rooks from SUNY at Buffalo on modeling of particle orientation in soft materials for SANS measurements. It is also notable that several former SURF students have published papers based on their research done at the NCNR. SURF students Kate Meuse and Jessica Opsahl-Ong were co-authors on the paper: "[On-the-fly autonomous control of neutron diffraction via physics-informed Bayesian active learning](#)." Emily Blick was a co-author on the publication "[Interactions, Diffusion, and Membrane Fluctuations in Concentrated Unilamellar Lipid Vesicle Solutions](#)." Jeffrey Self was co-author on the publication "[Dynamics of Molecular Associates in Methanol/Water Mixtures](#)" which is also one of the featured highlights in this year's report.

CHRS initiated a Research Experiences for Teachers (RET) program in 2010. Unfortunately, CHRS was unable to host RET participants on-site during the summer of 2022 due to access restrictions.

The Summer High School Intern Program (SHIP) is a successful, competitive NIST-wide program for students who are interested in performing scientific research. In the summer of 2022 CHRS hosted five SHIP interns from local high schools in a virtual format. The students developed Python scripts to investigate interactions of proteins in solution, used machine learning to locate peaks in neutron diffraction

patterns, and authored a tool for reducing standard format scattering data in an internet browser. The results of the students' summer investigations were highlighted in a NIST-wide virtual poster session, as well as in a well-attended hybrid symposium at the NCNR in mid-August. It is notable that a returning SHIP student, Satvik Lolla, was the first author of a publication entitled "[A Semi-Supervised Deep-Learning Approach for Automatic Crystal Structure Classification](#)" in the *Journal of Applied Crystallography* that highlighted his research results from the summer of 2021. Another SHIP student, Anna Job, co-authored two papers with her mentor Jamie Weaver: "[Adjustment to the Light Element Areal Concentration Calculation for Neutron Depth Profiles](#)", appearing in *Microscopy and Microanalysis*, and "[Energy broadening of neutron depth profiles by thin polyamide films](#)", appearing in the *Journal of Radioanalytical and Nuclear Chemistry*.

As access restrictions due to COVID-19 eased during the past year, CHRS was able to provide specialized tours and activities for high school and university students, some of which were virtual (as noted). On November 4, 2021 Elizabeth Kelley (CHRS vSANS Instrument Scientist) participated in a virtual panel discussion with the topic of non-academic career paths. This event was attended by approximately 100 graduate students and post-docs from the University of Delaware MRSEC and other MRSECs around the country. Dr. Kelley was also a virtual panel member in December 2021 for a panel on careers in national laboratories that included approximately 30 chemical engineering graduate students from the University of Houston. On July 21, 2022, Dan Neumann (Condensed Matter Science Group Leader) and Katie Weigandt (nSOFT Instrument Scientist) led a tour of the facility for 14 members of the Society of Physics Students. Twenty-two summer students (19 REU and 3 high school) from the University of Delaware toured the NCNR on August 2, 2022 during an event co-organized by Elizabeth Kelley. The tour featured a brief lecture by Ryan Murphy (CHRS vSANS Instrument Scientist) with stops at instruments staffed by NCNR scientists.

CHRS staff members typically give science-based talks or led hands-on activities and demonstrations at, or virtually for, local K-12 schools. Chuck Majkrzak (NCNR Team Leader) and Przemek Klosowski (NCNR Staff Scientist) mentored the FIRST Robotics Club at St. Johns College High School, during the 2021-22 academic year.

BROADENING PARTICIPATION IN STEM

Since direct outreach has proven to be an effective means to attract users, CHRS pursues many avenues for engaging institutions that serve diverse groups. Specific activities include PREM and CREST partnerships. Specifically, a partnership with the Interdisciplinary Materials Research and Education Laboratory (IMREL) at Fayetteville State University (FSU) was established in August 2018 through the NSF PREM (Partnerships for Research and Education in Materials) program (Agreement No. DMR-1827731). The [PREM](#) supports



FIGURE 6: 2022 CHRNS SHIP students and their mentors

cutting-edge materials research as the context for producing motivated and skilled members of those groups most underrepresented in materials research as future professional leaders. This partnership is organized around a common theme of structure-processing-property correlations of nanomaterials to support student training in research using neutron scattering.

During the fall of 2021, Yimin Mao (NCNR SANS Instrument Scientist) visited IMREL to meet with the PREM students and give a seminar entitled "Preferred Orientation: A Powerful Maneuver for Structural Analysis and Material Design." Following this activity, two PREM students (Caressia Edwards and Hanna Paige) presented posters based on joint CHRNS/IMREL research at the MRS PREM Research Scholars Summit Poster Session at the Materials Research Society meeting in December 2021. In the July of 2021, post-doc Navadeep Shrivastava participated in the polarized beam school at the NCNR as part of the PNCMI conference. Finally, CHRNS again hosted Roxanne Ware as a SURF student in the summer of 2021, and Carissa Edwards was a SURF intern in the NIST Materials Measurement Laboratory.

In a similar vein, CHRNS is engaged in a partnership with California State University, San Bernardino within the NSF CREST (Centers of Research Excellence in Science and Technology) program as part of their Phase II Center for Advanced Functional Materials (HRD-1914777).

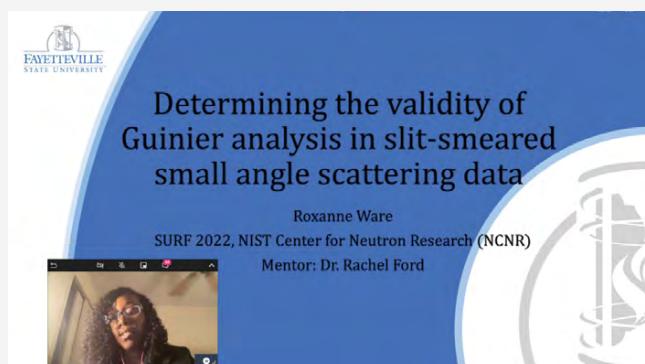


FIGURE 7: PREM student Roxanne Ware presents a summary of work at the virtual SURF symposium in August 2022.

2022 Awards



The NCNR's **Chuck Majkrzak** has been named a recipient of the **Presidential Rank Award of Distinguished Senior Professional**. He is recognized for his many contributions to the development and application of neutron reflectometry which have culminated in the creation of CANDOR, a groundbreaking reflectometer being commissioned on NG-1. This innovative instrument collects data more than 300 times faster than the first dedicated reflectometer that Chuck built at BT-7 thirty years ago. The Presidential Rank Award of Distinguished Senior Professional is the highest annual award for scientific career professionals.



The NCNR's own **Dan Neumann** is the recipient of the **2022 Clifford G. Shull Prize** "for outstanding contributions, leadership, and vision to the neutron scattering community as scientist, mentor, instrument developer, and facility steward." The Shull Prize, awarded by the Neutron Scattering Society of America, recognizes outstanding research in neutron science and leadership promoting the North American neutron scattering community in honor of Clifford G. Shull, who received the Nobel Prize in 1994 with Bert Brockhouse for seminal developments in the field of neutron science.



Peter Gehring of the NCNR was awarded the **2021 Department of Commerce Bronze Medal** as part of a NIST-wide group in recognition of "the development of an IT system to modernize and simplify NIST's publication processes."



The new **Fellows of the NSSA** were also announced and, included are NCNR's **Susan Krueger** and **Don Pierce**. The Neutron Scattering Society of America Fellowship Program "recognizes members who have made significant contributions to the neutron scattering community in North America in one or more of the following areas: advances in knowledge through original research and publication; innovative contributions in the application of neutron scattering; and/or contributions to the promotion or development of neutron scattering."



The NCNR's **Paul Kienzle**, **Brian Maranville**, and **William Ratcliff** received the **2021 Department of Commerce Bronze Medal** "for the development of cloud-based data reduction and visualization software benefiting the U.S. and international neutron scattering communities." The software, known as *Reductus*, is a graphical, easy-to-use tool that allows users of neutron and X-ray instrumentation to view and reduce their data from anywhere in the world with nothing more than an internet connection and a modern browser.



Paul Butler of the NCNR received a **2022 NSSA Service Award** from the Neutron Scattering Society of America (NSSA). Paul was recognized "for service to the neutron scattering community through his leadership in the development of scientific software for small-angle scattering."



William Ratcliff of the NCNR received a **2022 NSSA Service Award** from the Neutron Scattering Society of America (NSSA). William was recognized “for service to the neutron community by founding and organizing a national school on solving magnetic structures with neutron diffraction and developing new AI data collection and analysis methods.”



Wei Zhou of the NCNR was recognized as a **Clarivate Highly Cited Researcher** in the field of Chemistry. Clarivate recognizes researchers who produced multiple papers ranking in the top 1 % by citations for their chosen field or fields and year of publication, demonstrating significant influence among their peers. His research interests are in the areas of novel porous materials, computational materials design, neutron diffraction and spectroscopy.



Hui Wu of the NCNR has been recognized as a **Clarivate Highly Cited Researcher**, Cross-Field. Clarivate recognizes researchers who produced multiple papers ranking in the top 1 % by citations for their chosen field or fields and year of publication, demonstrating significant influence among their peers. Her research interests lie in the synthesis, structure, solid state chemistry, and properties of complex oxides/hydrides and porous framework materials.



Vivek Prabhu of NIST’s Material Measurement Laboratory has been named an **APS Physics Fellow** by the American Physical Society. Vivek, a long-time user of the NCNR, was recognized for fundamental insight into the chain conformation, structure, phase separation, and interfaces of polyelectrolytes enabled by light and neutron scattering methods.



The International Union of Crystallography has honored **Jill Trehwella** (University of Sydney, Australia) with the **2022 Guinier Prize**. The Guinier Prize is awarded in recognition of lifetime achievement, a major breakthrough or an outstanding contribution to the field of small-angle scattering (SAS). The prize citation, in part, reads: “Prof. Trehwella is a pioneer and acknowledged leader in the application of SAS to problems in structural biology as well as a tireless promoter of the technique in general. Throughout her stellar career, she has mentored generations of biomolecular SAS researchers. Prof. Trehwella’s achievements, positive influence and strong contributions clearly make her a most deserving recipient of the Guinier Prize.” Jill is a long-time user of the NCNR.



Sanat K Kumar, Professor of Chemical Engineering at Columbia University has been awarded the **2022 Polymer Physics Prize** from the American Physical Society. The award citation recognizes Sanat “For fundamental experimental, simulatory, and theoretical contributions to understanding structure, assembly, and dynamics in polymer nanocomposites and thin films.” Sanat is a long-time user of the NCNR facilities.



Greeshma Gadikota, Assistant Professor in the Department of Civil and Environmental Engineering at Cornell University was honored with a **Sigma Xi Young Investigator Award** for her outstanding contributions in advancing the science of carbon dioxide reactivity for developing innovative technologies for sustainable energy, resource recovery, and carbon sequestration. Greeshma is a former post-doctoral researcher at the NCNR.



Assistant Professor **Michelle Calabrese** of the Department of Chemical Engineering and Materials Science at the University of Minnesota has been selected for a **Faculty Early Career Development (CAREER) Award** from the National Science Foundation (NSF) to support her project "Beyond alignment: novel mechanisms for controlling block copolymer phase behavior using magnetic fields." This prestigious award provides support for junior faculty who exemplify the role of teacher-scholars through outstanding research, excellent education and the integration of education and research within the context of the mission of their organizations. Michelle used the NCNR facilities extensively during her graduate research.



Lilo Pozzo, Professor of Materials Science and Engineering at the University of Washington, has been honored by the Neutron Scattering Society of America as the first recipient of the **2022 NSSA Anne Mayes Award**. The NSSA recognizes the important contributions of women in neutron scattering, with Lilo's citation reading: "for her outstanding scholarship, exemplary service to the neutron community, and dedication to training and mentoring young scientists." Lilo's research makes extensive use of the NCNR's facilities.



Simon Rogers, Professor at University of Illinois, Urbana-Champaign, is the recipient of the **2022 Metzner Award** from the Society of Rheology, presented at their annual meeting in October. The citation reads, "for developing fundamentally new experimental and analytical methods for linear and nonlinear transient rheology that have provided an improved understanding of complex flow phenomena in yield stress fluids, polymer solutions, and colloidal suspensions." Simon's research has had extensive use of the NCNR's facilities.



Gordon Jones (of Hamilton College) and **Alexander Komives** (of DePauw University) won **NIST Distinguished Associate** awards this year for their work on the aCORN experiment. Gordon and Alexander were post-docs at NIST, and both have remained active in neutron programs at the NCNR.



Martin Mourigal, an associate professor in the School of Physics at Georgia Tech has been awarded the Neutron Scattering Society of America's **2022 NSSA Science Prize**. The prize recognizes major scientific contributions using neutron scattering techniques, specifically recognizing Martin "for significant and insightful use of neutron inelastic scattering in the study of quantum materials." Martin has been a long time collaborator and user of the NCNR facilities.



Mirjana Dimitrievska, a materials scientist at the École Polytechnique Fédérale de Lausanne (EPFL) has received the prestigious **Zonta Award** for her outstanding research on discovering and optimizing functional materials for solar cells and solid-state battery applications. Zonta Switzerland & Lichtenstein have been awarding an endowed prize to talented and aspiring young women scientists working at the forefront of research. Mirjana is a former post-doctoral researcher at the NCNR.



Erkan Şenses, Assistant Professor at Koç University, Turkey, was recognized by the Turkish Academy of Sciences with an **Outstanding Young Scientist Award**. This award from TÜBA-GEBİP is to foster young, outstanding scientists who are at the stage of establishing their own research programs in Turkey after finishing their post-doctoral research activities. Erkan is a former post-doctoral researcher at the NCNR.



Sylvia Lewin won the **Most Outstanding Poster** award in physics at the 29th Postdoctoral Poster Presentation sponsored by the NIST chapter of Sigma Xi. Her poster was entitled "Anisotropy of the Superconducting Upper Critical Field in UTe_2 ". Sylvia is a post-doc at the NCNR working with Nick Butch.



Ryan Klein of the NREL was awarded the Materials Chemical and Computational Science **Postdoctoral Researcher Publication and Technology Award**. Ryan was also a runner-up of the 2022 Hydrogen and Fuel Cell Technologies Office **Postdoctoral Recognition Award**. Ryan was recognized for his significant contributions to the Hydrogen Materials Advanced Research Consortium in characterizing hydrogen storage materials using neutron scattering techniques. Ryan is currently stationed at the NCNR working with Craig Brown.



UMD graduate student **Stephanie Gnewuch** was recognized by the American Crystallographic Association with a **Margaret C. Etter Student Lecturer Award**. Stephanie was invited to present her work "Centers of Spatial and Time Inversion Symmetry in Magnetoelectric Crystalline Materials" at the ACA Annual meeting held in August 2021. Stephanie is advised by Efrain Rodriguez of UMD.



Natalie Schwab, a graduate student in the Department of Materials Science at the University of Maryland won an **Outstanding Poster Award** at the ACNS 2022 for her poster "Analysis of Engineered Nafion Surfaces via Neutron Reflectometry." Natalie is advised by Rob Briber at the University of Maryland.

Publications: August 1, 2021 to July 31, 2022

- Akindele, O., Bowden, N., Carr, R., Conant, A., Diwan, M., Erickson, A., Foxe, M., Goldblum, B.L., Huber, P., Jovanovic, I., Link, J., Littlejohn, B., Mumm, P., Newby, J., "Nu Tools: Exploring Practical Roles for Neutrinos in Nuclear Energy and Security," Final Report of the Antineutrino Reactor Monitoring Scoping Study, Pacific Northwest Technical Report, **PNNL-31870**, 1 (2021).
- Al Hasan, M.A., Wang, J., Shin, S., Gilbert, D.A., Liaw, P.K., Tang, N., Liyanage, W.L.N.C., Santodonato, L., DeBeer-Schmitt, L., Butch, N.P., "Effects of Aluminum Content on Thermoelectric Performance of $\text{Al}_x\text{CoCrFeNi}$ High-Entropy Alloys," *J. Alloy Compd.* **883**, 160811 (2021).
- Alam, K., Ponce-Pérez, R., Sun, K., Foley, A., Takeuchi, N., Smith, A.R., "Investigating the Magnetic and Atomic Interface Configuration for a Model Fe/CrN Bilayer System," *J. Vac. Sci. Technol. A* **39**(6), 063209 (2021).
- Aleksenskii, A., Bleuel, M., Bosak, A., Chumakova, A., Dideikin, A., Dubois, M., Korobkina, E., Lychagin, E., Muzychka, A., Nekhaev, G., Nesvizhevsky, V., Nezvanov, A., Schweins, R., Shvidchenko, A., Strelkov, A., Turlybekuly, K., Vul', A., Zhernenkov, K., "Effect of Particle Sizes on the Efficiency of Fluorinated Nanodiamond Neutron Reflectors," *Nanomaterials-Basel* **11**(11), 3067 (2021).
- Ali, S., Mao, Y., Prabhu, V.M., "Pinhole Mirror-Based Ultra-Small Angle Light Scattering Setup for Simultaneous Measurement of Scattering and Transmission," *Rev. Sci. Instrum.* **93**(4), 044104 (2022).
- Almazán, H., Andriamirado, M., Balantekin, A.B., Band, H.R., Bass, C.D., Bergeron, D.E., Bernard, L., Blanchet, A., Bonhomme, A., Bowden, N.S., Bryan, C.D., Buck, C., Classen, T., Conant, A.J., Deichert, G., del Amo Sanchez, P., Delgado, A., Diwan, M.V., Dolinski, M.J., El Atmani, I., Erickson, A., Foust, B.T., Gaison, J.K., Galindo-Uribarri, A., Gilbert, C.E., Hans, S., Hansell, A.B., Heeger, K.M., Heffron, B., Jaffe, D.E., Jayakumar, S., Ji, X., Jones, D.C., Koblanski, J., Kyzlyova, O., Labit, L., Lamblin, J., Lane, C.E., Langford, T.J., LaRosa, J., Letourneau, A., Lhuillier, D., Licciardi, M., Lindner, M., Littlejohn, B.R., Lu, X., Maricic, J., Materna, T., Mendenhall, M.P., Meyer, A.M., Milincic, R., Mueller, P.E., Mumm, H.P., Napolitano, J., Neilson, R., Nikkel, J.A., Nour, S., Palomino, J.L., Pessard, H., Pushin, D.A., Qian, X., Réal, J.-S., Ricol, J.-S., Roca, C., Rogly, R., Rosero, R., Salagnac, T., Savu, V., Schoppmann, S., Searles, M., Sergeyeva, V., Soldner, T., Stutz, A., Surukuchi, P.T., Tyra, M.A., Varner, R.L., Venegas-Vargas, D., Vialat, M., Weatherly, P.B., White, C., Wilhelmi, J., Woolverton, A., Yeh, M., Zhang, C., Zhang, X., "Joint Measurement of the ^{235}U Antineutrino Spectrum by PROSPECT and STEREO," *Phys. Rev. Lett.* **128**(8), 081802 (2022).
- Ambika, D.V., Ding, Q.-P., Rana, K., Frank, C.E., Green, E.L., Ran, S., Butch, N.P., Furukawa, Y., "Possible Coexistence of Antiferromagnetic and Ferromagnetic Spin Fluctuations in the Spin-Triplet Superconductor UTe_2 Revealed by ^{125}Te NMR under Pressure," *Phys. Rev. B* **105**(22), L220403 (2022).
- An, F.P., Andriamirado, M., Balantekin, A.B., Band, H.R., Bass, C.D., Bergeron, D.E., Berish, D., Bishai, M., Blyth, S., Bowden, N.S., Bryan, C.D., Cao, G.F., Cao, J., Chang, J.F., Chang, Y., Chen, H.S., Chen, S.M., Chen, Y., Chen, Y.X., Cheng, J., Cheng, Z.K., Cherwinka, J.J., Chu, M.C., Classen, T., Conant, A.J., Cummings, J.P., Dalager, O., Deichert, G., Delgado, A., Deng, F.S., Ding, Y.Y., Diwan, M.V., Dohnal, T., Dolinski, M.J., Dolzhikov, D., Dove, J., Dvořák, M., Dwyer, D.A., Erickson, A., Foust, B.T., Gaison, J.K., Galindo-Uribarri, A., Gallo, J.P., Gilbert, C.E., Gonchar, M., Gong, G.H., Gong, H., Grassi, M., Gu, W.Q., Guo, J.Y., Guo, L., Guo, X.H., Guo, Y.H., Guo, Z., Hackenburg, R.W., Hans, S., Hansell, A.B., He, M., Heeger, K.M., Heffron, B., Heng, Y.K., Hor, Y.K., Hsiung, Y.B., Hu, B.Z., Hu, J.R., Hu, T., Hu, Z.J., Huang, H.X., Huang, J.H., Huang, X.T., Huang, Y.B., Huber, P., Koblanski, J., Jaffe, D.E., Jayakumar, S., Jen, K.L., Ji, X.L., Ji, X.P., Johnson, R.A., Jones, D.C., Kang, L., Kettell, S.H., Kohn, S., Kramer, M., Kyzlyova, O., Lane, C.E., Langford, T.J., LaRosa, J., Lee, J., Lee, J.H.C., Lei, R.T., Leitner, R., Leung, J.K.C., Li, F., Li, H.L., Li, J.J., Li, Q.J., Li, R.H., Li, S., Li, S.C., Li, W.D., Li, X.N., Li, X.Q., Li, Y.F., Li, Z.B., Liang, H., Lin, C.J., Lin, G.L., Lin, S., Ling, J.J., Link, J.M., Littenberg, L., Littlejohn, B.R., Liu, J.C., Liu, J.L., Liu, J.X., Lu, C., Lu, H.Q., Lu, X., Luk, K.B., Ma, B.Z., Ma, X.B., Ma, X.Y., Ma, Y.Q., Mandujano, R.C., Maricic, J., Marshall, C., McDonald, K.T., McKeown, R.D., Mendenhall, M.P., Meng, Y., Meyer, A.M., Milincic, R., Mueller, P.E., Mumm, H.P., Napolitano, J., Naumov, D., Naumova, E., Neilson, R., Nguyen, T.M.T., Nikkel, J.A., Nour, S., Ochoa-Ricoux, J.P., Olshevskiy, A., Palomino, J.L., Pan, H.-R., Park, J., Patton, S., Peng, J.C., Pun, C.S.J., Pushin, D.A., Qi, F.Z., Qi, M., Qian, X., Raper, N., Ren, J., Morales Revecio, C., Rosero, R., Roskovec, B., Ruan, X.C., Searles, M., Steiner, H., Sun, J.L., Surukuchi, P.T., Tmej, T., Treskov, K., Tse, W.-H., Tull, C.E., Tyra, M.A., Varner, R.L., Venegas-Vargas, D., Viren, B., Vorobel, V., Wang, C.H., Wang, J., Wang, M., Wang, N.Y., Wang, R.G., Wang, W., Wang, W., Wang, X., Wang, Y., Wang, Y.F., Wang, Z., Wang, Z., Wang, Z.M., Weatherly, P.B., Wei, H.Y., Wei, L.H., Wen, L.J., Whisnant, K., White, C., Wilhelmi, J., Wong, H.L.H., Woolverton, A., Worcester, E., Wu, D.R., Wu, F.L., Wu, Q., Wu, W.J., Xia, D.M., Xie, Z.Q., Xing, Z.Z., Xu, H.K., Xu, J.L., Xu, T., Xue, T., Yang, C.G., Yang, L., Yang, Y.Z., Yao, H.F., Ye, M., Yeh, M., Young, B.L., Yu, H.Z., Yu, Z.Y., Yue, B.B., Zavadskiy, V., Zeng, S., Zeng, Y., Zhan, L., Zhang, C., Zhang, F.Y., Zhang, H.H., Zhang, J.W., Zhang, Q.M., Zhang, S.Q., Zhang, X., Zhang, X.T., Zhang, Y.M., Zhang, Y.X., Zhang, Y.Y., Zhang, Z.J., Zhang, Z.P., Zhang, Z.Y., Zhao, J., Zhao, R.Z., Zhou, L., Zhuang, H.L., Zou, J.H., "Joint Determination of Reactor Antineutrino Spectra from ^{235}U and ^{239}Pu Fission by Daya Bay and Prospect," *Phys. Rev. Lett.* **128**(8), 081801 (2022).
- Andersson, M.S., Stavila, V., Skripov, A.V., Dimitrievska, M., Psurek, M.T., Leão, J.B., Babanova, O.A., Skoryunov, R.V., Soloninin, A.V., Karlsson, M., Udovic, T.J., "Promoting Persistent Superionic Conductivity in Sodium Monocarbide-Clathrate Dodecaborate $\text{NaCB}_{12}\text{H}_{12}$ via Confinement within Nanoporous Silica," *J. Phys. Chem. C* **125**(30), 16689 (2021). [CHRS]
- Andrade, P.L., Silva, V.A.J., Krycka, K.L., Leão, J.B., Liu, I.-L., Silva, M.P.C., Albino Aguiar, J., "The Effect of Organic Coatings in the Magnetization of CoFe_2O_4 Nanoparticles," *AIP Adv.*, in press.
- Andrejevic, N., Chen, Z., Nguyen, T., Fan, L., Heiberger, H., Zhou, L.-J., Zhao, Y.-F., Chang, C.-Z., Grutter, A., Li, M., "Elucidating Proximity Magnetism through Polarized Neutron Reflectometry and Machine Learning," *Appl. Phys. Rev.* **9**(1), 011421 (2022).

- Andriamirado, M., Balantekin, A.B., Band, H.R., Bass, C.D., Bergeron, D.E., Bowden, N.S., Bryan, C.D., Carr, R., Classen, T., Conant, A.J., Deichert, G., Delgado, A., Diwan, M.V., Dolinski, M.J., Erickson, A., Foust, B.T., Gaison, J.K., Galindo-Uribari, A., Gilbert, C.E., Grant, C., Hans, S., Hansell, A.B., Heeger, K.M., Heffron, B., Jaffe, D.E., Jayakumar, S., Ji, X., Jones, D.C., Koblanski, J., Kunkle, P., Kyzyllova, O., Lane, C.E., Langford, T.J., LaRosa, J., Littlejohn, B.R., Lu, X., Maricic, J., Mendenhall, M.P., Meyer, A.M., Milincic, R., Mueller, P.E., Mumm, H.P., Napolitano, J., Neilson, R., Nikkel, J.A., Nour, S., Palomino, J.L., Pushin, D.A., Qian, X., Rosero, R., Searles, M., Surukuchi, P.T., Tyra, M.A., Varner, R.L., Venegas-Vargas, D., Weatherly, P.B., White, C., Wilhelmi, J., Woolverton, A., Yeh, M., Zhang, C., Zhang, X., "PROSPECT-II Physics Opportunities," *J. Phys. G Nucl. Partic.* **49**(7), 070501 (2022).
- Anitas, E.M., "α-SAS: an Integrative Approach for Structural Modeling of Biological Macromolecules in Solution," *Acta Crystallogr. D*, in press. [CHNRNS]
- Anovitz, L.M., Huestis, P., Rampal, N., Stack, A.G., LaVerne, J.A., Zhang, X., Schenter, G.K., Chun, J., Legg, B.A., Liu, L., Bleuel, M., Gagnon, C., Mildner, D.F.R., "Frustrated Coulombic and Cation Size Effects on Nanoscale Boehmite Aggregation: A Tumbler Small- and Ultra-Small-Angle Neutron Scattering Study," *J. Phys. Chem. C* **126**(9), 4391 (2022). [CHNRNS]
- Armstrong, C.L., Mang, J.T., "Thermally-Driven Changes to Porosity in TATB-Based High Explosives," *Propell. Explos. Pyrot.* **46**(8), 1304 (2021). [CHNRNS]
- Barinov, V.V., Cleveland, B.T., Danshin, S.N., Ejiri, H., Elliott, S.R., Frekers, D., Gavrin, V.N., Gorbachev, V.V., Gorbunov, D.S., Haxton, W.C., Ibragimova, T.V., Kim, I., Kozlova, Y.P., Kravchuk, L.V., Kuzminov, V.V., Lubsandorzhiev, B.K., Malyshev, Y.M., Massarczyk, R., Matveev, V.A., Mirmov, I.N., Nico, J.S., Petelin, A.L., Robertson, R.G.H., Sinclair, D., Shikhin, A.A., Tarasov, V.A., Trubnikov, G.V., Veretenkin, E.P., Wilkerson, J.F., Zvir, A.I., "Results from the Baksan Experiment on Sterile Transitions (BEST)," *Phys. Rev. Lett.* **128**(23), 232501 (2022).
- Barker, J., Moyer, J., Kline, S., Jensen, G., Cook, J., Gagnon, C., Kelley, E., Chabot, J.P., Maliszewskyj, N., Parikh, C., Chen, W., Murphy, R.P., Glinka, C., "The Very Small Angle Neutron Scattering Instrument at the National Institute of Standards and Technology," *J. Appl. Crystallogr.* **55**(2), 271 (2022). [CHNRNS]
- Barker, J.G., Cook, J.C., Chabot, J.P., Kline, S.R., Zhang, Z., Gagnon, C.V., "Extraneous Scattering Background in SANS Instruments," *Neutron News* **33**(1), 4 (2022). [CHNRNS]
- Barnett, B.R., Evans, H.A., Su, G.M., Jiang, H.Z.H., Chakraborty, R., Banyeretse, D., Hartman, T.J., Martinez, M.B., Trump, B.A., Tarver, J.D., Dods, M.N., Funke, L.M., Börgel, J., Reimer, J.A., Drisdell, W.S., Hurst, K.E., Gennett, T., FitzGerald, S.A., Brown, C.M., Head-Gordon, M., Long, J.R., "Observation of an Intermediate to H₂ Binding in a Metal-Organic Framework," *J. Am. Chem. Soc.* **143**(36), 14884 (2021).
- Bauer, J.J., Quarterman, P., Grutter, A.J., Khurana, B., Kundu, S., Mkhoyan, K.A., Borchers, J.A., Ross, C.A., "Magnetic Proximity Effect in Magnetic-Insulator/Heavy-Metal Heterostructures across the Compensation Temperature," *Phys. Rev. B* **104**(9), 094403 (2021).
- Bellur, K., Medici, E.F., Hussey, D.S., Jacobson, D.L., LaManna, J., Leao, J.B., Scherschligt, J., Hermanson, J.C., Choi, C.K., Allen, J.S., "Data from Cryo-Neutron Phase Change Experiments with LH2 and LCH4," Data Brief, in press.
- Bellur, K., Médici, E.F., Hussey, D.S., Jacobson, D.L., LaManna, J., Leão, J.B., Scherschligt, J., Hermanson, J.C., Choi, C.K., Allen, J.S., "Results from Neutron Imaging Phase Change Experiments with LH2 and LCH4," *Cryogenics* **125**, 103517 (2022).
- Benedetto, A., Kelley, E.G., "Absorption of the [bmim][Cl] Ionic Liquid in DMPC Lipid Bilayers across Their Gel, Ripple, and Fluid Phases," *J. Phys. Chem. B* **126**(17), 3309 (2022). [CHNRNS]
- Berger, J.E., Teixeira, S.C.M., Reed, K., Razinkov, V.I., Sloey, C.J., Qi, W., Roberts, C.J., "High-Pressure, Low-Temperature Induced Unfolding and Aggregation of Monoclonal Antibodies: Role of the Fc and Fab Fragments," *J. Phys. Chem. B* **126**(24), 4431 (2022). [CHNRNS]
- Bhattacharjee, N., Mahalingam, K., Fedorko, A., Lauter, V., Matzelle, M., Singh, B., Grutter, A., Will-Cole, A., Page, M., McConney, M., Markiewicz, R., Bansil, A., Heiman, D., Sun, N.X., "Topological Antiferromagnetic Van der Waals Phase in Topological Insulator/Ferromagnet Heterostructures Synthesized by a CMOS-Compatible Sputtering Technique," *Adv. Mater.* **34**(15), 2108790 (2022).
- Bhattacharyya, M., Gnaupel-Herold, T., Raja, K.S., Darsell, J., Jana, S., Charit, I., "Evaluation of Residual Stresses in Isothermal Friction Stir Welded 304L Stainless Steel Plates," *Mater. Sci. Eng. A-Struct.* **826**, 141982 (2021).
- Bonini, M., Fratini, E., Faraone, A., "Dynamics of Water and Other Molecular Liquids Confined within Voids and on Surface of Lignin Aggregates in Aging Bio Crude Oils," *Front. Chem.* **9**(17), 753958 (2021). [CHNRNS]
- Bordelon, M.M., Wang, X., Pajeroski, D.M., Banerjee, A., Sherwin, M., Brown, C.M., Eldeeb, M.S., Petersen, T., Hozoi, L., Rößler, U.K., Mourigal, M., Wilson, S.D., "Magnetic Properties and Signatures of Moment Ordering in the Triangular Lattice Antiferromagnet KCeO₂," *Phys. Rev. B* **104**(9), 094421 (2021). [CHNRNS]
- Bosch-Santos, B., Cabrera-Pasca, G.A., Correa, E.L., Correa, B.S., Sales, T.N.S., Moon, K.-W., Dennis, C.L., Huang, Q., Leao, J.B., Lynn, J.W., Carbonari, A.W., "Magnetic and Structural Properties of the Intermetallic Ce_(1-x)La_xCrGe₃ Series of Compounds," *Phys. Rev. Mater.* **5**(11), 114406 (2021).
- Brooks, A.J., Hussey, D.S., Ham, K., Jacobson, D.L., Manke, I., Kardjilov, N., Butler, L.G., "Intact, Commercial Lithium-Polymer Batteries: Spatially Resolved Grating-Based Interferometry Imaging, Bragg Edge Imaging, and Neutron Diffraction," *Appl. Sci.-Basel* **12**(3), 1281 (2022).
- Budhani, R.C., Sharma, V., Negusse, E., Casey, J., Pathak, A.K., Sadowski, J.T., Kirby, B., "Magnetotransport and Magnetic Textures in Ho/FeCoGd/β-W Multilayers," *Phys. Rev. B* **105**(2), 024412 (2022).
- Butch, N.P., Ran, S., Saha, S.R., Neves, P.M., Zic, M.P., Paglione, J., Gladchenko, S., Ye, Q., Rodriguez-Rivera, J.A., "Symmetry of Magnetic Correlations in Spin-Triplet Superconductor UTe₂," *NPJ Quantum Mater.* **7**(1), 39 (2022). [CHNRNS]
- Byrne, J., Worcester, D.L., "The Neutron Lifetime Anomaly: Analysis of Charge Exchange and Molecular Reactions in a Proton Trap," *Eur. J. Phys. A*, in press.
- Cappelletti, R.L., Vinson, J., "Photons, Orbital Angular Momentum, and Neutrons," *Phys. Status Solidi B* **258**(9), 2000257 (2021).
- Carter, C.C., Klein, R.A., Zhou, W., Udovic, T.J., Brown, C.M., Wen, T.-B., Cundari, T.R., Yousufuddin, M., "Investigating the Non-Classical M-H₂ Bonding in OsClH₃(PPh₃)₃," *J. Alloy Compd.* **894**, 162445 (2022).
- Castillo, S.R., Rickeard, B.W., DiPasquale, M., Nguyen, M.H.L., Lewis-Laurent, A., Doktorova, M., Kav, B., Miettinen, M.S., Nagao, M., Kelley, E.G., Marquardt, D., "Probing the Link between Pancreatistatin and Mitochondrial Apoptosis through Changes in the Membrane Dynamics on the Nanoscale," *Mol. Pharmaceut.* **19**(6), 1839 (2022). [CHNRNS]
- Celikten, O.S., Sahin, D., "The Effects of Impurities in Down-Blending Highly Enriched Uranium on the Reactor Neutronics and Cycle Length," *T. Am. Nucl. Soc.* **125**(1), 165 (2021).

- Chen, S.H., Souana, A.J., Stranick, S.J., Jhalaria, M., Kumar, S.K., Soles, C.L., Chan, E.P., "Controlling Toughness of Polymer-Grafted Nanoparticle Composites for Impact Mitigation," *Soft Matter* **18**(2), 256 (2022). [CHNRNS]
- Chen, X., Wang, Y., Wang, Y., Dally, R.L., Wiaderek, K., Qiao, T., Liu, J., Hu, E., Burch, K., Lynn, J.W., Li, X., "Dynamically Preferred State with Strong Electronic Fluctuations from Electrochemical Synthesis of Sodium Manganate," *Matter* **5**(2), 735 (2022).
- Chen, Z., Mian, M.R., Lee, S.-J., Chen, H., Zhang, X., Kirlikovali, K.O., Shulda, S., Melix, P., Rosen, A.S., Parilla, P.A., Gennett, T., Snurr, R.Q., Islamoglu, T., Yildirim, T., Farha, O.K., "Fine-Tuning a Robust Metal-Organic Framework toward Enhanced Clean Energy Gas Storage," *J. Am. Chem. Soc.* **143**(45), 18838 (2021).
- Chen-Mayer, H.H., Tosh, R.E., Bateman, F.B., Bergstrom, P.M., Zimmerman, B.E., "Calorimetry in Computed Tomography Beams," *J. Res. Natl. Inst. Stan.* **126**, 126054 (2022).
- Cheng, D., Shimizu, R., Weaver, J., Meng, Y.S., "Unveiling the Stable Nature of LiPON-Associated Electrode/Electrolyte Interphases via Cryogenic Electron Microscopy," *Microsc. Microanal.* **27**(Suppl 1), 3324 (2021).
- Choudhary, K., Yildirim, T., Siderius, D.W., Kusne, A.G., McDannald, A., Ortiz-Montalvo, D.L., "Graph Neural Network Predictions of Metal Organic Framework CO₂ Adsorption Properties," *Comp. Mater. Sci.* **210**, 111388 (2022).
- Dalton, L.E., LaManna, J.M., Jones, S., Pour-Ghaz, M., "Does ITZ Influence Moisture Transport in Concrete?" *Transport Porous Med.*, in press.
- Danielsen, S.P.O., Bridges, C.R., Segalman, R.A., "Chain Stiffness of Donor-Acceptor Conjugated Polymers in Solution," *Macromolecules* **55**(2), 437 (2022). [CHNRNS]
- Darvishi, S., Nazeer, M.A., Tyagi, M., Zhang, Q., Narayanan, S., Kizilel, S., Senses, E., "Nonlinear Architectures Can Alter the Dynamics of Polymer-Nanoparticle Composites," *Macromolecules* **54**(21), 10118 (2021). [CHNRNS]
- Das, B., Batley, J.T., Krycka, K.L., Borchers, J.A., Quartermann, P., Korostynski, C., Nguyen, M., Kamboj, I., Aydil, E.S., Leighton, C., "Chemically Induced Magnetic Dead Shells in Superparamagnetic Ni Nanoparticles Deduced from Polarized Small-Angle Neutron Scattering," *ACS Appl. Mater. Interfaces* **14**(29), 33491 (2022). [CHNRNS]
- Daugherty, M.C., LaManna, J.M., Kim, Y., Baltic, E., Hussey, D.S., Jacobson, D.L., "Neural Networks for Dose Reduced Reconstruction Image Denoising in Neutron Tomography," *Microsc. Microanal.*, in press.
- Dawn, A., Pajoubpong, J., Mesmer, A., Mirzamani, M., He, L., Kumari, H., "Manipulating Assemblies in Metallosupramolecular Gels, Driven by Isomeric Ligands, Metal Coordination, and Adaptive Binary Gelator Systems," *Langmuir* **38**(5), 1705 (2022).
- De Mel, J.U., Gupta, S., Harmon, S., Stingaciu, L., Roth, E.W., Siebenbuerger, M., Bleuel, M., Schneider, G.J., "Acetaminophen Interactions with Phospholipid Vesicles Induced Changes in Morphology and Lipid Dynamics," *Langmuir* **37**(31), 9560 (2021). [CHNRNS]
- Del Maestro, A., Nichols, N.S., Prisk, T.R., Warren, G., Sokol, P.E., "Experimental Realization of One Dimensional Helium," *Nat. Commun.* **13**(1), 3168 (2022).
- Deng, P., Grutter, A., Han, Y., Holtz, M.E., Zhang, P., Quartermann, P., Pan, S., Qi, S., Qiao, Z., Wang, K.L., "Topological Surface State Annihilation and Creation in SnTe/Cr_x(BiSb)_{1-x}Te₃ Heterostructures," *Nano Lett.* **22**(14), 5735 (2022).
- Denlinger, J.D., Kang, J.-S., Dudy, L., Allen, J.W., Kim, K., Shim, J.-H., Haule, K., Sarrao, J.L., Butch, N.P., Maple, M.B., "Global Perspectives of the Bulk Electronic Structure of URu₂Si₂ from Angle-Resolved Photoemission," *Electron. Struct.* **4**(1), 013001 (2022).
- Dennis, C.L., "Introduction to Neutron Scattering as a Tool for Characterizing Magnetic Materials," in "Magnetic Measurement Techniques for Materials Characterization," edited by Franco, V., Dodrill, B. (Springer Nature Switzerland AG, Cham) Chap. **12**, 301 (2021). [CHNRNS]
- Dhital, C., Dally, R.L., Pham, D., Keen, T., Zhang, Q., Siwakoti, P., Nepal, R., Jin, R., Rai, R., "Magnetic Structure of Magnetoelectric Multiferroic HoFeWO₆," *J. Magn. Magn. Mater.* **544**, 168725 (2022).
- DiStefano, V.H., LaManna, J.M., Jacobson, D.L., Kienzie, P.A., Hussey, D.S., Bajcsy, P., "Assessment of Dose Reduction Strategies in Wavelength-Selective Neutron Tomography," in "Proceedings of the 2nd International Conference on Image Processing and Vision Engineering—IMPROVE," edited by Imai, F., Distanto, C., Battiato, S., in press.
- Dissanayake, S., Shi, Z., Rau, J.G., Bag, R., Steinhardt, W., Butch, N.P., Frontzek, M., Podlesnyak, A., Graf, D., Marjerrison, C., Liu, J., Gingras, M.J.P., Haravifard, S., "Towards Understanding the Magnetic Properties of the Breathing Pyrochlore Compound Ba₃Yb₂Zn₅O₁₁ through Single-Crystal Studies," *NPJ Quantum Mater.*, in press.
- Do, C., Ashkar, R., Boone, C., Chen, W.-R., Ehlers, G., Falus, P., Faraone, A., Gardner, J.S., Graves, V., Huegle, T., Katsumata, R., Kent, D., Lin, J.Y., McHargue, B., Olsen, B., Wang, Y., Wilson, D., Z. Y., "EXPANSE: A Time-of-Flight EXPanded Angle Neutron Spin Echo Spectrometer at the Second Target Station of the Spallation Neutron Source," *Rev. Sci. Instrum.* **93**(7), 075107 (2022). [CHNRNS]
- Do, S.-H., Zhang, H., Williams, T.J., Hong, T., Ovidiu Garlea, V., Rodriguez-Rivera, J.A., Jang, T.-H., Cheong, S.-W., Park, J.-H., Batista, C.D., Christianson, A.D., "Decay and Renormalization of a Longitudinal Mode in a Quasi-Two-Dimensional Antiferromagnet," *Nat. Commun.* **12**(1), 5331 (2021). [CHNRNS]
- Domhoff, A., Wang, X., Silva, M.S., Creager, S., Martin, T.B., Davis, E.M., "Role of Nanoparticle Size and Surface Chemistry on Ion Transport and Nanostructure of Perfluorosulfonic Acid Ionomer Nanocomposites," *Soft Matter* **18**(17), 3342 (2022).
- Dubackic, M., Idini, I., Lattanzi, V., Liu, Y., Martel, A., Terry, A., Haertlein, M., Devos, J.M., Jackson, A., Sparr, E., Linse, S., Olsson, U., "On the Cluster Formation of α -Synuclein Fibrils," *Front. Mol. Biosci.* **8**, 768004 (2021).
- Dubackic, M., Liu, Y., Kelley, E.G., Hetherington, C., Haertlein, M., Devos, J.M., Linse, S., Sparr, E., Olsson, U., " α -Synuclein Interaction with Lipid Bilayer Discs," *Langmuir*, in press. [CHNRNS]
- Dura, J.A., Rodriguez-Rivera, J., Ogg, R., "Virtual School on SANS and Neutron Reflectometry Held by NIST," *Neutron News* **32**(2), 10 (2021). [CHNRNS]
- Dura, J.A., Weigandt, K., Ogg, R., "Virtual School on Neutron Spectroscopy and Diffraction Held by NIST," *Neutron News*, in press. [CHNRNS]
- Elliott, J.P., Osti, N.C., Tyagi, M., Mamontov, E., Liu, L., Serrano, J.M., Cao, K., Liu, G., "Exceptionally Fast Ion Diffusion in Block Copolymer-Based Porous Carbon Fibers," *ACS Appl. Mater. Interfaces*, in press. [CHNRNS]
- Eufrazio, A.M., Pegg, I., Kafle, A., Wong-Ng, W., Huang, Q., Dutta, B., "Metal-Insulator Transition in Doped Barium Plumbates," *Electron. Mater.* **2**(3), 428 (2021).
- Fallarino, L., López Rojo, E., Quintana, M., Salcedo Gallo, J.S., Kirby, B.J., Berger, A., "Modifying Critical Exponents of Magnetic Phase Transitions via Nanoscale Materials Design," *Phys. Rev. Lett.* **127**(14), 147201 (2021).
- Fang, W., Tang, Y., Chen, J., Li, J., Fang, L., "Relationship between the Structure and Microwave Dielectric Properties of Garnet Ceramics Ca₃B₂GeV₂O₁₂ (B = Mg, Mn)," *Ceram. Int.* **48**(3), 4318 (2022).
- Feng, J., Mao, L., Yuan, G., Zhao, Y., Vidal, J., Liu, L., "Grain Size Effect on Corrosion Behavior of Inconel 625 Film Against Molten MgCl₂-NaCl-KCl Salt," *Corrosion Sci.* **197**, 110097 (2022).

- Fenton, A.M., Xie, R., Aplan, M.P., Lee, Y., Gill, M.G., Fair, R., Kempe, F., Sommer, M., Snyder, C.R., Gomez, E.D., Colby, R.H., "Predicting the Plateau Modulus from Molecular Parameters of Conjugated Polymers," *ACS Cent. Sci.* **8**(2), 268 (2022).
- Foglia, F., Berrod, Q., Clancy, A.J., Smith, K., Gebel, G., García Sakai, V., Appel, M., Zanotti, J.-M., Tyagi, M., Mahmoudi, N., Miller, T.S., Varcoe, J.R., Periasamy, A.P., Brett, D.J.L., Shearing, P.R., Lyonard, S., McMillan, P.F., "Disentangling Water, Ion and Polymer Dynamics in an Anion Exchange Membrane," *Nat. Mater.* **21**(5), 555 (2022). [CHNRNS]
- Fomin, N., Alarcon, R., Alonzi, L., Askanazi, E., Baeßler, S., Balascuta, S., Barrón-Palos, L., Barzilov, A., Blyth, D., Bowman, J.D., Birge, N., Calarco, J.R., Chupp, T.E., Cianciolo, V., Coppola, C.E., Crawford, C.B., Craycraft, K., Evans, D., Fieseler, C., Frlež, E., Fry, J., Garishvili, I., Gericke, M.T.W., Gillis, R.C., Grammer, K.B., Greene, G.L., Hall, J., Hamblen, J., Hayes, C., Iverson, E.B., Kabir, M.L., Kucuker, S., Lauss, B., Mahurin, R., McCrea, M., Maldonado-Velázquez, M., Masuda, Y., Mei, J., Milburn, R., Mueller, P.E., Musgrave, M., Nann, H., Novikov, I., Parsons, D., Penttilä, S.I., Počanić, D., Ramirez-Morales, A., Root, M., Salas-Bacci, A., Santra, S., Schröder, S., Scott, E., Seo, P.-N., Sharapov, E.I., Simmons, F., Snow, W.M., Sprow, A., Stewart, J., Tang, E., Tang, Z., Tong, X., Turkoglu, D.J., Whitehead, R., Wilburn, W.S., "Measurement of the Parity-Odd Angular Distribution of γ Rays from Polarized Neutron Capture on ^{35}Cl ," *Phys. Rev. C* **106**(1), 015504 (2022).
- Fuller, E.J., Strelcov, E., Weaver, J.L., Swift, M.W., Sugar, J.D., Kolmakov, A., Zhitenev, N., McClelland, J.J., Qi, Y., Dura, J.A., Talin, A.A., "Spatially Resolved Potential and Li-Ion Distributions Reveal Performance-Limiting Regions in Solid-State Batteries," *ACS Energy Lett.* **6**(11), 3944 (2021).
- Gao, J., Cai, Y., Qian, X., Liu, P., Wu, H., Zhou, W., Liu, D.-X., Li, L., Lin, R.-B., Chen, B., "A Microporous Hydrogen-Bonded Organic Framework for the Efficient Capture and Purification of Propylene," *Angew. Chem. Int. Edit.* **60**(37), 20400 (2021).
- Gao, Q., Sun, Q., Venier, A., Sanson, A., Huang, Q., Jia, Y., Liang, E., Chen, J., "The Role of Average Atomic Volume in Predicting Negative Thermal Expansion: The Case of $\text{REFe}(\text{CN})_6$," *Sci. China Mater.* **65**(2), 553 (2022).
- Gao, Y., Liu, H., Hu, F., Song, H., Zhang, H., Hao, J., Liu, X., Yu, Z., Shen, F., Wang, Y., Zhou, H., Wang, B., Tian, Z., Lin, Y., Zhang, C., Yin, Z., Wang, J., Chen, Y., Li, Y., Song, Y., Shi, Y., Zhao, T., Sun, J., Huang, Q., Shen, B., "Reversible Colossal Barocaloric Effect Dominated by Disorder of Organic Chains in $(\text{CH}_3-(\text{CH}_2)_{n-1}-\text{NH}_2)_2\text{MnCl}_4$ Single Crystals," *NPG Asia Mater.* **14**, 34 (2022).
- García Sakai, V., Neumann, D., "John R. D. Copley (1944-2022)," *Neutron News*, in press.
- Gaudet, J., Yang, H.-Y., Baidya, S., Lu, B., Xu, G., Zhao, Y., Rodriguez-Rivera, J.A., Hoffmann, C.M., Graf, D.E., Torchinsky, D.H., Nikolić, P., Vanderbilt, D., Tafti, F., Broholm, C.L., "Weyl-Mediated Helical Magnetism in NdAlSi ," *Nat. Mater.* **20**(12), 1650 (2021). [CHNRNS]
- Gilbert, J., Ermilova, I., Nagao, M., Swenson, J., Nylander, T., "Effect of Encapsulated Protein on the Dynamics of Lipid Sponge Phase: A Neutron Spin Echo and Molecular Dynamics Simulation Study," *Nanoscale* **14**(18), 6990 (2022). [CHNRNS]
- Gilbert, P.H., Zhang, Z., Qian, K.K., Allen, D.P., Ford, R., Wagner, N.J., Liu, Y., "Aggregation Kinetics of Polysorbate 80/*m*-Cresol Solutions: A Small-Angle Neutron Scattering Study," *Mol. Pharmaceut.* **19**(3), 862 (2022). [CHNRNS]
- Gomes, D.C., Teixeira, S.C.M., Leão, J.B., Razinkov, V.I., Qi, W., Rodrigues, M.A., Roberts, C.J., "In Situ Monitoring of Protein Unfolding/Structural States under Cold High-Pressure Stress," *Mol. Pharmaceut.* **18**(12), 4415 (2021).
- Gong, J., Li, J., Bao, X., Hou, R., Gao, X., "A Study of the Crystal Structure of a Tb-Dy-Fe Alloy during Annealing via Rietveld Analysis," *Intermetallics* **144**, 107506 (2022).
- Grutter, A.J., He, Q.L., "Magnetic Proximity Effects in Topological Insulator Heterostructures: Implementation and Characterization," *Phys. Rev. Mater.* **5**(9), 090301 (2021).
- Gu, X.-W., Wang, J.-X., Wu, E., Wu, H., Zhou, W., Qian, G., Chen, B., Li, B., "Immobilization of Lewis Basic Sites into a Stable Ethane-Selective MOF Enabling One-Step Separation of Ethylene from a Ternary Mixture," *J. Am. Chem. Soc.* **144**(6), 2614 (2022).
- Gu, X., Brantley, S.L., "How Particle Size Influences Oxidation of Ancient Organic Matter during Weathering of Black Shale," *ACS Earth Space Chem.* **6**(6), 1443 (2022). [CHNRNS]
- Gui, X., Marshall, M., Dissanayaka Mudiyanse, R.S., Klein, R.A., Chen, Q., Zhang, Q., Shelton, W., Zhou, H., Brown, C.M., Cao, H., Greenblatt, M., Xie, W., "Spin Reorientation in Antiferromagnetic Layered FePt_5P ," *ACS Appl. Electron. Mater.* **3**(8), 3501 (2021).
- Guo, R., Sinha, N.J., Misra, R., Tang, Y., Langenstein, M., Kim, K., Fagan, J.A., Kloxin, C.J., Jensen, G., Pochan, D.J., Saven, J.G., "Computational Design of Homotetrameric Peptide Bundle Variants Spanning a Wide Range of Charge States," *Biomacromolecules* **23**(4), 1652 (2022). [CHNRNS]
- Gurgen, A., Celikten, O.S., Sahin, D., "Development of Linear Nuclear Channel Noise Detection System," in "The New Outlook, Proceedings of the 2022 ANS Annual Meeting," edited by the American Nuclear Society, in press.
- Halloran, T., Wang, Y., Li, M., Rousochatzakis, I., Chauhan, P., Stone, M.B., Takayama, T., Takagi, H., Armitage, N.P., Perkins, N.B., Broholm, C., "Magnetic Excitations and Interactions in the Kitaev Hyperhoneycomb Iridate $\beta\text{-Li}_2\text{IrO}_3$," *Phys. Rev. B*, in press.
- Hameed, S., Joe, J., Thoutam, L.R., Garcia-Barriocanal, J., Yu, B., Yu, G., Chi, S., Hong, T., Williams, T.J., Freeland, J.W., Gehring, P.M., Xu, Z., Matsuda, M., Jalan, B., Greven, M., "Growth and Characterization of Large $(\text{YLa})\text{TiO}_3$ and $(\text{YCa})\text{TiO}_3$ Single Crystals," *Phys. Rev. Mater.* **5**(12), 125003 (2021).
- Han, B., Jin, Y., Chen, B., Zhou, W., Yu, B., Wei, C., Wang, H., Wang, K., Chen, Y., Chen, B., Jiang, J., "Maximizing Electroactive Sites in a Three-Dimensional Covalent Organic Framework for Significantly Improved Carbon Dioxide Reduction Electrocatalysis," *Angew. Chem. Int. Edit.* **61**(1), e202114244 (2022).
- Hansen, U.B., Syljuåsen, O.F., Jensen, J., Schäffer, T.K., Andersen, C.R., Boehm, M., Rodriguez-Rivera, J.A., Christensen, N.B., Lefmann, K., "Magnetic Bloch Oscillations and Domain Wall Dynamics in a Near-Ising Ferromagnetic Chain," *Nat. Commun.* **13**(1), 2547 (2022). [CHNRNS]
- Hayes, I.M., Wei, D.S., Metz, T., Zhang, J., Eo, Y.S., Ran, S., Saha, S.R., Collini, J., Butch, N.P., Agterberg, D.F., Kapitulnik, A., Paglione, J., "Multicomponent Superconducting Order Parameter in UTe_2 ," *Science* **373**(6556), 797 (2021).
- He, Z., Song, Y., Zhou, K., Guo, S., Wu, J., Yin, C., Guo, Z., He, L., Huang, Q., Li, L., Huang, R., Guo, J., Xing, X., Chen, J., "Correlation of Tunable CoSi_4 Tetrahedron with the Superconducting Properties of LaCoSi ," *Inorg. Chem.* **60**(15), 10880 (2021).
- Heacock, B., Fujie, T., Haun, R.W., Henins, A., Hirota, K., Hosobata, T., Huber, M.G., Kitaguchi, M., Pushin, D.A., Shimizu, H., Takeda, M., Valdillez, R., Yamagata, Y., Young, A.R., "Pendellösung Interferometry Probes the Neutron Charge Radius, Lattice Dynamics, and Fifth Forces," *Science* **373**(6560), 1239 (2021).
- Heil, C.M., Patil, A., Dhinojwala, A., Jayaraman, A., "Computational Reverse-Engineering Analysis for Scattering Experiments (CREASE) with Machine Learning Enhancement to Determine Structure of Nanoparticle Mixtures and Solutions," *ACS Cent. Sci.* **8**(7), 996 (2022). [CHNRNS]

- Heinrich, F., Van, Q.N., Jean-Francois, F., Stephen, A.G., Lösche, M., "Membrane-Bound KRAS Approximates an Entropic Ensemble of Configurations," *Biophys. J.* **120**(18), 4055 (2021).
- Henderson, M.E., Beare, J., Sharma, S., Bleuel, M., Clancy, P., Cory, D.G., Huber, M.G., Marjerrison, C.A., Pula, M., Sarenac, D., Smith, E.M., Zhernenkov, K., Luke, G.M., Pushin, D.A., "Characterization of a Disordered above Room Temperature Skyrmion Material $\text{Co}_5\text{Zn}_8\text{Mn}_4$," *Materials* **14**(16), 4689 (2021). [CHNRNS]
- Heroux, L., Moncada, J., Dadmun, M., "Controlling the Morphology of PEDOT:PSS Blend Films with Pre-Deposition Solution Composition and Deposition Technique," *ACS Appl. Polym. Mater.* **4**(1), 36 (2022). [CHNRNS]
- Hester, G., DeLazzer, T.N., Yahne, D.R., Sarkis, C.L., Zhao, H.D., Rodriguez Rivera, J.A., Calder, S., Ross, K.A., "Magnetic Properties of the Ising-like Rare Earth Pyrosilicate: D- $\text{Er}_2\text{Si}_2\text{O}_7$," *J. Phys. Condens. Matter* **33**(40), 405801 (2021). [CHNRNS]
- Higashi, K., Ochi, M., Nambu, Y., Yamamoto, T., Murakami, T., Yamashina, N., Tassel, C., Matsumoto, Y., Takatsu, H., Brown, C.M., Kageyama, H., "Enhanced Magnetic Interaction by Face-Shared Hydride Anions in $6\text{H-BaCrO}_2\text{H}$," *Inorg. Chem.* **60**(16), 11957 (2021).
- Himbert, S., D'Alessandro, A., Qadri, S.M., Majcher, M.J., Hoare, T., Sheffield, W.P., Nagao, M., Nagle, J.F., Rheinstädter, M.C., "The Bending Rigidity of the Red Blood Cell Cytoplasmic Membrane," *PLoS One*, in press. [CHNRNS]
- Hong, T., Ying, T., Huang, Q., Dissanayake, S.E., Qiu, Y., Turnbull, M.M., Podlesnyak, A.A., Wu, Y., Cao, H., Liu, Y., Umehara, I., Gouchi, J., Uwatoko, Y., Matsuda, M., Tennant, D.A., Chern, G.-W., Schmidt, K.P., Wessel, S., "Evidence for Pressure Induced Unconventional Quantum Criticality in the Coupled Spin Ladder Antiferromagnet $\text{C}_9\text{H}_8\text{N}_2\text{CuBr}_4$," *Nat. Commun.* **13**(1), 3073 (2022). [CHNRNS]
- Hoogerheide, D.P., Rostovtseva, T.K., Bezrukov, S.M., "Exploring Lipid-Dependent Conformations of Membrane-Bound α -Synuclein with the VDAC Nanopore," *BBA-Biomembranes* **1863**, 183643 (2021).
- Hoogerheide, D.P., Dura, J.A., Maranville, B.B., Majkrzak, C.F., "Low-Background Neutron Reflectometry from Solid/Liquid Interfaces," *J. Appl. Crystallogr.* **55**(Part 1), 58 (2022). [CHNRNS]
- Hoogerheide, D.P., Gurnev, P.A., Rostovtseva, T.K., Bezrukov, S.M., "Voltage-Activated Complexation of α -Synuclein with Three Diverse β -Barrel Channels: VDAC, MspA, and α -Hemolysin," *Proteomics* **22**(5-6), 2100060 (2022).
- Horkay, F., Douglas, J.F., "Evidence of Many-Body Interactions in the Virial Coefficients of Polyelectrolyte Gels," *Gels* **8**(2), 96 (2022). [CHNRNS]
- Horkay, F., Chremos, A., Douglas, J.F., Jones, R., Lou, J., Xia, Y., "Comparative Experimental and Computational Study of Synthetic and Natural Bottlebrush Polyelectrolyte Solutions," *J. Chem. Phys.* **155**(7), 074901 (2021).
- Horkay, F., Bassar, P.J., "Hydrogel Composite Mimics Biological Tissues," *Soft Matter* **18**(23), 4414 (2022). [CHNRNS]
- Huang, J., Yu, R., Xu, Z., Zhu, J.-X., Oh, J.S., Jiang, Q., Wang, M., Wu, H., Chen, T., Denlinger, J.D., Mo, S.-K., Hashimoto, M., Michiardi, M., Pedersen, T.M., Gorovikov, S., Zhdanovich, S., Damascelli, A., Gu, G., Dai, P., Chu, J.-H., Lu, D., Si, Q., Birgeneau, R.J., Yi, M., "Correlation-Driven Electronic Reconstruction in $\text{FeTe}_{1-x}\text{Se}_x$," *Commun. Phys.* **5**(1), 29 (2022).
- Huang, J., Xu, Q., Liu, Z., Jain, N., Tyagi, M., Wei, D.-Q., Hong, L., "Controlling the Substrate Specificity of an Enzyme through Structural Flexibility by Varying the Salt-Bridge Density," *Molecules* **26**(18), 5693 (2021). [CHNRNS]
- Huang, Q., Rawl, R., Xie, W.W., Chou, E.S., Zapf, V.S., Ding, X.X., Mauws, C., Wiebe, C.R., Feng, E.X., Cao, H.B., Tian, W., Ma, J., Qiu, Y., Butch, N., Zhou, H.D., "Non-Magnetic Ion Site Disorder Effects on the Quantum Magnetism of a Spin-1/2 Equilateral Triangular Lattice Antiferromagnet," *J. Phys. Condens. Matter* **34**(20), 205401 (2022). [CHNRNS]
- Huang, W., Yang, L., Chen, Z., Liu, T., Ren, G., Shan, P., Zhang, B.-W., Chen, S., Li, S., Li, J., Lin, C., Zhao, W., Qiu, J., Fang, J., Zhang, M., Dong, C., Li, F., Yang, Y., Sun, C.-J., Ren, Y., Huang, Q., Hou, G., Dou, S.-X., Lu, J., Amine, K., Pan, F., "Elastic Lattice Enabling Reversible Tetrahedral Li Storage Sites in High-Capacity Manganese Oxide Cathode," *Adv. Mater.* **34**(30), 2202745 (2022).
- Imel, A.E., Barth, B., Hayes, D.G., Dadmun, M., Zawodzinski, T., "Microemulsions as Emerging Electrolytes: The Correlation of Structure to Electrochemical Response," *ACS Appl. Mater. Interfaces* **14**(17), 20179 (2022).
- Jang, T.-H., Do, S.-H., Lee, M., Wu, H., Brown, C.M., Christianson, A.D., Cheong, S.-W., Park, J.-H., "Physical Properties of the Quasi-Two-Dimensional Square Lattice Antiferromagnet $\text{Ba}_2\text{FeSi}_2\text{O}_7$," *Phys. Rev. B* **104**(21), 214434 (2021).
- Jeong, C., Franklin, R., Edler, K.J., Vanommeslaeghe, K., Krueger, S., Curtis, J.E., "Styrene-Maleic Acid Copolymer Nanodiscs to Determine the Shape of Membrane Proteins," *J. Phys. Chem. B* **126**(5), 1034 (2022).
- Jeong, S., Yuan, G., Satija, S.K., Jeon, N., Lee, E., Kim, Y., Choi, S., Koo, J., "Polyamide Thin Films with Nanochannel Networks Synthesized at the Liquid-Gas Interface for Water Purification," *J. Membrane Sci.*, in press.
- Jiang, S., Peng, R.L., Máthias, K., Yan, H.-L., Farkas, G., Hegedues, Z., Lienert, U., Moverare, J., Zhao, X., Zuo, L., Jia, N., Wang, Y.-D., "Shear Banding-Induced $\langle c+a \rangle$ Slip Enables Unprecedented Strength-Ductility Combination of Laminated Metallic Composites," *J. Mater. Sci. Technol.* **110**, 260 (2022).
- Jiao, J., Zhang, S., Huang, Q., Zhang, M., Shu, M.F., Lin, G.T., dela Cruz, C.R., Garlea, V.O., Butch, N., Matsuda, M., Zhou, H., Ma, J., "Quantum Effect on the Ground State of the Triple-Perovskite $\text{Ba}_3\text{MnNb}_2\text{O}_9$ ($M = \text{Co}, \text{Ni}$, and Mn) with Triangular-Lattice," *Chem. Mater.* **34**(14), 6617 (2022).
- Jing, Z., Yuan, Q., Yu, Y., Kong, X., Tan, K.C., Wang, J., Pei, Q., Wang, X.-B., Zhou, W., Wu, H., Wu, A., He, T., Chen, P., "Developing Ideal Metalorganic Hydrides for Hydrogen Storage: From Theoretical Prediction to Rational Fabrication," *ACS Mater. Lett.* **3**(9), 1417 (2021).
- Jones, S.Z., Hipp, J.B., Allen, A.J., Gagnon, C.V., "Rheology and Microstructure Development of Hydrating Tricalcium Silicate-Implications for Additive Manufacturing in Construction," *Cement Concrete Res.* **152**, 106651 (2022).
- Jørgensen, M., Zhou, W., Wu, H., Udovic, T.J., Paskevicius, M., Černý, R., Jensen, T.R., "Polymorphism of Calcium Decahydrate-*Closo*-Decaborate and Characterization of Its Hydrates," *Inorg. Chem.* **60**(15), 10943 (2021).
- Kancharla, S., Jahan, R., Bedrov, D., Tsianou, M., Alexandridis, P., "Role of Chain Length and Electrolyte on the Micellization of Anionic Fluorinated Surfactants in Water," *Colloid Surface A* **628**, 127313 (2021). [CHNRNS]
- Kancharla, S., Dong, D., Bedrov, D., Alexandridis, P., Tsianou, M., "Binding of Perfluorooctanoate to Poly(Ethylene Oxide)," *Macromolecules* **55**(11), 4624 (2022). [CHNRNS]
- Kancharla, S., Bedrov, D., Tsianou, M., Alexandridis, P., "Structure and Composition of Mixed Micelles Formed by Nonionic Block Copolymers and Ionic Surfactants in Water Determined by Small-Angle Neutron Scattering with Contrast Variation," *J. Colloid Interf. Sci.* **609**, 456 (2022). [CHNRNS]
- Kancharla, S., Choudhary, A., Davis, R.T., Dong, D., Bedrov, D., Tsianou, M., Alexandridis, P., "GenX in Water: Interactions and Self-Assembly," *J. Hazard Mater.* **428**, 128137 (2022). [CHNRNS]

- Kasztovsky, Z., Stieghorst, C., Chen-Mayer, H.H., Livingston, R.A., Lindstrom, R.M., "Prompt-Gamma Activation Analysis and Its Application to Cultural Heritage," in "Handbook of Cultural Heritage Analysis," edited by D'Amico, S., Venuti, V. (Springer Nature Switzerland, Basel) Chap. **6**, 94 (2022).
- Kato, D., Tomita, O., Nelson, R., Kirsanova, M.A., Dronskowski, R., Suzuki, H., Zhong, C., Tassel, C., Ishida, K., Matsuzaki, Y., Brown, C.M., Fujita, K., Fujii, K., Yashima, M., Kobayashi, Y., Saeki, A., Oikawa, I., Takamura, H., Abe, R., Kageyama, H., Gorelik, T.E., Abakumov, A.M., "Bi₁₂O₁₇Cl₂ with a Sextuple Bi-O Layer Composed of Rock-Salt and Fluorite Units and its Structural Conversion through Fluorination to Enhance Photocatalytic Activity," *Adv. Funct. Mater.*, in press.
- Kelley, E.G., Nguyen, M.H.L., Marquardt, D., Maranville, B.B., Murphy, R.P., "Measuring the Time-Evolution of Nanoscale Materials with Stopped-Flow and Small-Angle Neutron Scattering," *JOVE-J. Vis. Exp.* **174**, e62873 (2021). [CHRSNS]
- Kelley, E.G., Blick, E.E., Prabhu, V.M., Butler, P.D., Nagao, M., "Interactions, Diffusion, and Membrane Fluctuations in Concentrated Unilamellar Lipid Vesicle Solutions," *Front. Phys.* **10**, 866024 (2022). [CHRSNS]
- Kelley, E.G., Heberle, F.A., "Sensing a Little Friction," *Biophys. J.*, in press. [CHRSNS]
- Kim, J., Yang, J., Won, C.J., Kim, K., Kim, B., Obeyseker, D., Lee, D.W., Cheong, S.-W., "Helical Versus Collinear Antiferromagnetic Order Turned by Magnetic Anisotropy in Polar and Chiral (Ni,Mn)₃TeO₆," *Phys. Rev. Mater.* **5**(9), 094405 (2021).
- Kim, Y., Kim, D., Hussey, D.S., Kim, J., Mirzaei, M., Pushin, D.A., Clark, C.W., Lee, S.W., "Analysis of a Silicon Comb Structure using an Inverse Talbot-Lau Neutron Grating Interferometer," *Sci. Rep.* **12**(1), 3461 (2022).
- Klein, R.A., Balderas-Xicohtencatl, R., Maehlen, J.P., Udovic, T.J., Brown, C.M., Delaplane, R., Cheng, Y., Denys, R.V., Ramirez-Cuesta, A.J., Yartys, V.A., "Neutron Vibrational Spectroscopic Evidence for Short H...H Contacts in the RNiInH_{1.4;1.6} (R = Ce, La) Metal Hydride," *J. Alloy Compd.* **894**, 162381 (2022).
- Klein, R.A., Balderas-Xicohtencatl, R., Maehlen, J.P., Udovic, T.J., Brown, C.M., Delaplane, R., Cheng, Y., Denys, R.V., Ramirez-Cuesta, A.J., Yartys, V.A., "Neutron Vibrational Spectroscopic Evidence for Short H...H Contacts in the RNiInH_{1.4;1.6} (R = Ce, La) Metal Hydride," *Neutron News* **33**(2), 7 (2022).
- Klein, R.A., Shulda, S., Parilla, P.A., Le Magueres, P., Richardson, R.K., Morris, W., Brown, C.M., McGuirk, C.M., "Structural Resolution and Mechanistic Insight into Hydrogen Adsorption in Flexible ZIF-7," *Chem. Sci.* **12**(47), 15620 (2021).
- Klein, R.A., Evans, H.A., Trump, B.A., Udovic, T.J., Brown, C.M., "Neutron Scattering Studies of Materials for Hydrogen Storage," in "Reference Module in Chemistry, Molecular Sciences and Chemical Engineering," edited by Reedijk, J., Poepelmeier, J. (Elsevier Ltd, Amsterdam) Chap. **1**, 1 (2021).
- Kline, S.R., "2021 NIST Center for Neutron Research Accomplishments and Opportunities," *NIST Spec. Publ.* **1274**, 1 (2021).
- Koegel, A.A., Mozur, E.M., Oswald, I.W.H., Jalarvo, N.H., Prisk, T.R., Tyagi, M., Neilson, J.R., "Correlating Broadband Photoluminescence with Structural Dynamics in Layered Hybrid Halide Perovskites," *J. Am. Chem. Soc.* **144**(3), 1313 (2022). [CHRSNS]
- Krause, K., Lee, J.K., Lee, C., Shafaque, H.W., Kim, P.J., Fahy, K.F., Shrestha, P., LaManna, J.M., Baltic, E., Jacobson, D.L., Hussey, D.S., Bazylak, A., "Electrolyte Layer Gas Triggers Cathode Potential Instability in CO₂ Electrolyzers," *J. Power Sources* **520**, 230879 (2022).
- Krueger, S., "Small-Angle Neutron Scattering Contrast Variation Studies of Biological Complexes: Challenges and Triumphs," *Curr. Opin. Struc. Biol.* **74**, 102375 (2022).
- Kumari, H., Dennis, C.L., Kline, S.R., Mossine, A.V., Deakyn, C.A., Atwood, J.L., "Solution-Phase Magnetic Mechanistic Study of Ni-Seamed Pyrogallol[4]arene Nanocapsules Reveal Presence of Novel Cylindrical and Spherical Species," *Angew. Chem. Int. Edit.* **134**(30), e202203010 (2022). [CHRSNS]
- Lane, H., Rodriguez, E.E., Walker, H.C., Niedermayer, C., Stühr, U., Bewley, R.I., Voneshen, D.J., Green, M.A., Rodriguez-Rivera, J.A., Fouquet, P., Cheong, S.-W., Attfield, J.P., Ewings, R.A., Stock, C., "Metastable Antiphase Boundary Ordering in CaFe₂O₄," *Phys. Rev. B* **104**(10), 104404 (2021).
- Lavén, R., Moraes, P.I.R., Targama, M.S., Karlsson, M., Leitão, A.A., Carvalho, P.H.B.B., Parker, S.F., Häussermann, U., Vekilova, O.Y., "Vibrational Properties of SrVO₂H with Large Spin-Phonon Coupling," *Phys. Rev. Mater.* **6**(2), 024409 (2022).
- Leão, J.B., "Minimizing Pressure Inhomogeneities across Large Samples under Helium Pressure Media at Low Temperatures," *J. Neutron Res.* **24**(1), 15 (2022). [CHRSNS]
- Lee, D.C., Guye, K.N., Paranjli, R.K., Lachowski, K., Pozzo, L.D., Ginger, D.S., Pun, S.H., "Dual-Stimuli Responsive Single-Chain Polymer Folding via Intrachain Complexation of Tetramethoxyazobenzene and β -Cyclodextrin," *Langmuir* **37**(33), 10126 (2021). [CHRSNS]
- Lee, Y.-F., Luo, Y., Bai, T., Brown, S.C., Wagner, N.J., "Microstructure of Continuous Shear Thickening Colloidal Suspensions Determined by Rheo-VSANS and Rheo-USANS," *Soft Matter* **18**(22), 4325 (2022). [CHRSNS]
- Li, Q., Ren, Y., Zhang, Q., Gu, L., Huang, Q., Wu, H., Sun, J., Cao, Y., Lin, K., Xing, X., "Chemical Order-Disorder Nanodomains in Fe₃Pt Bulk Alloy," *Natl. Sci. Rev.*, in press.
- Liang, X., Hu, Q., Wang, Q., Li, W., Zhang, T., Yang, S., Sun, M., Bleuel, M., Yao, G., "Changes in Nanoscale Pore Structures and Mesopore Connectivity as a Result of Artificial Maturation of a Source Rock from the Shanxi Formation, Ordos Basin," *Energ. Fuel*, in press. [CHRSNS]
- Lim, C., Ramsey, J.D., Hwang, D., Teixeira, S.C.M., Poon, C.-D., Strauss, J.D., Rosen, E.P., Sokolsky-Papkov, M., Kabanov, A.V., "Drug-Dependent Morphological Transitions in Spherical and Worm-Like Polymeric Micelles Define Stability and Pharmacological Performance of Micellar Drugs," *Small* **18**(4), 2103552 (2022). [CHRSNS]
- Liu, S., Li, R., Tyagi, M., Akcora, P., "Confinement Effects in Dynamics of Ionic Liquids with Polymer-Grafted Nanoparticles," *ChemPhysChem*, in press.
- Liu, Y., Zheng, X., Liang, F., Hu, F., Huang, Q., Li, Z., Liu, J., "Large Barocaloric Effect in Intermetallic La_{1.2}Ce_{0.8}Fe₁₁Si₂H₁₈₆ Materials Driven by Low Pressure," *NPG Asia Mater.* **14**, 30 (2022).
- Liu, Y., Wu, H., Guo, L., Zhou, W., Zhang, Z., Yang, Q., Yang, Y., Ren, Q., Bao, Z., "Hydrogen-Bonded Metal-Nucleobase Frameworks for Efficient Separation of Xenon and Krypton," *Angew. Chem. Int. Edit.* **61**(11), e202117609 (2022).
- Liu, Y., Baglioni, P., Choi, S.-M., "Sow-Hsin Chen (1935-2021)," *Neutron News* **32**(4), 34 (2021).
- Liu, Z., Ni, X.-S., Li, L., Sun, H., Liang, F., Frandsen, B.A., Christianson, A.D., dela Cruz, C., Xu, Z., Yao, D.-X., Lynn, J.W., Birgeneau, R.J., Cao, K., Wang, M., "Effect of Iron Vacancies on Magnetic Order and Spin Dynamics of the Spin Ladder BaFe_{2- δ} S₁₅Se_{1.5}," *Phys. Rev. B* **105**(21), 214303 (2022).
- Liu, Z., Liu, P., Li, M., He, T., Liu, T., Yu, L., Yuan, M., "Efficient and Stable FA-Rich Perovskite Photovoltaics: From Material Properties to Device Optimization," *Adv. Energy Mater.* **12**(18), 2200111 (2022).

- Loke, K., Zhang, Z.-Q., Narayanaswamy, S., Koh, P.K., Luzin, V., Gnaupel-Herold, T., Ang, A.S.M., "Residual Stress Analysis of Cold Spray Coatings Sprayed at Angles using Through-Thickness Neutron Diffraction Measurement," *J. Therm. Spray Technol.* **30**(7), 1810 (2021).
- Lolla, S., Liang, H., Kusne, A.G., Takeuchi, I., Ratcliff, W., "A Semi-Supervised Deep-Learning Approach for Automatic Crystal Structure Classification," *J. Appl. Crystallogr.*, in press. [CHNRNS]
- Lopez, C.G., Linders, J., Mayer, C., Richtering, W., "Diffusion and Viscosity of Unentangled Polyelectrolytes," *Macromolecules* **54**(17), 8088 (2021).
- Lopez, C.G., Horkay, F., Schweins, R., Richtering, W., "Solution Properties of Polyelectrolytes with Divalent Counterions," *Macromolecules* **54**(22), 10583 (2021). [CHNRNS]
- Louden, E.R., Manni, S., Van Zandt, J.E., Leishman, A.W.D., Taufour, V., Bud'ko, S.L., Debeer-Schmitt, L., Honecker, D., Dewhurst, C.D., Canfield, P.C., Eskildsen, M.R., "Effects of Magnetic and Non-Magnetic Doping on the Vortex Lattice in MgB_2 ," *J. Appl. Crystallogr.*, in press.
- Lu, Q., Liu, Z., Yang, Q., Cao, H., Balakrishnan, P., Wang, Q., Cheng, L., Lu, Y., Zuo, J.-M., Zhou, H., Quarterman, P., Muramoto, S., Grutter, A.J., Chen, H., Zhai, X., "Engineering Magnetic Anisotropy and Emergent Multidirectional Soft Ferromagnetism in Ultrathin Freestanding LaMnO_3 Films," *ACS Nano* **16**(5), 7580 (2022).
- Lubanska, D., Alrashed, S., Mason, G.T., Nadeem, F., Awada, A., DiPasquale, M., Sorge, A., Malik, A., Kojic, M., Soliman, M.A.R., deCarvalho, A.C., Shamisa, A., Kulkarni, S., Marquardt, D., Porter, L.A., Rondeau-Gagné, S., "Impairing Proliferation of Glioblastoma Multiforme with CD44+ Selective Conjugated Polymer Nanoparticles," *Sci. Rep.* **12**(1), 12078 (2022). [CHNRNS]
- Luo, P., Zhai, Y., Falus, P., García Sakai, V., Hartl, M., Kofu, M., Nakajima, K., Faraone, A., Z. Y., "Q-Dependent Collective Relaxation Dynamics of Glass-Forming Liquid $\text{Ca}_{0.4}\text{K}_{0.6}(\text{NO}_3)_{1.4}$ Investigated by Wide-Angle Neutron Spin-Echo," *Nat. Commun.* **13**(1), 2092 (2022). [CHNRNS]
- Lv, Y., Kally, J., Liu, T., Quarterman, P., Pillsbury, T., Kirby, B.J., Grutter, A.J., Sahu, P., Borchers, J.A., Wu, M., Samarth, N., Wang, J.-P., "Large Unidirectional Spin Hall and Rashba-Edelstein Magnetoresistance in Topological Insulator/Magnetic Insulator Heterostructures," *Appl. Phys. Rev.* **9**(1), 011406 (2022).
- Lyons, D.J., Weaver, J.L., Co, A.C., "Considerations in Applying Neutron Depth Profiling (NDP) to Li-Ion Battery Research," *J. Mater. Chem. A* **10**(5), 2336 (2022).
- Ma, C.T., Zhou, W., Kirby, B.J., Poon, S.J., "Interfacial Mixing Effect in a Promising Skyrmionic Material: Ferrimagnetic Mn_4N ," *AIP Adv.*, in press.
- Ma, L., Xie, Y., Khoo, R.S.H., Arman, H., Wang, B., Zhou, W., Zhang, J., Lin, R.-B., Chen, B., "An Adaptive Hydrogen-Bonded Organic Framework for the Exclusive Recognition of *p*-Xylene," *Chem.-Eur. J.* **28**(11), e202104269 (2022).
- Ma, L., Arman, H., Xie, Y., Zhou, W., Chen, B., "Solvent-Dependent Self-Assembly of Hydrogen-Bonded Organic Porphyrinic Frameworks," *Cryst. Growth Des.* **22**(6), 3808 (2022).
- Ma, Y., Ali, S., Prabhu, V.M., "Enhanced Concentration Fluctuations in Model Polyelectrolyte Coacervate Mixtures along a Salt Isopleth Phase Diagram," *Macromolecules* **54**(24), 11338 (2021). [CHNRNS]
- Macy, J., Ratkovski, D., Balakrishnan, P.P., Strungaru, M., Chiu, Y.-C., Savvidou, A.F., Moon, A., Zheng, W., Weiland, A., McCandless, G.T., Chan, J.Y., Kumar, G.S., Shatruck, M., Grutter, A.J., Borchers, J.A., Ratcliff, W.D., Choi, E.S., Santos, E.J.G., Balicas, L., "Magnetic Field-Induced Non-Trivial Electronic Topology in $\text{Fe}_{3-x}\text{GeTe}_2$," *Appl. Phys. Rev.* **8**(4), 041401 (2021).
- Majcher, M.J., Himbert, S., Vito, F., Campea, M.A., Dave, R., Jensen, G.V., Rheinstadter, M.C., Smeets, N.M.B., Hoare, T., "Investigating the Kinetics and Structure of Network Formation in Ultraviolet-Photopolymerizable Starch Nanogel Network Hydrogels via Very Small-Angle Neutron Scattering and Small-Amplitude Oscillatory Shear Rheology," *Macromolecules*, in press. [CHNRNS]
- Majkrzak, C.F., Berk, N.F., Maranville, B.B., Dura, J.A., Jach, T., "The Effect of Transverse Wavefront Width on Specular Neutron Reflection," *J. Appl. Crystallogr.*, in press.
- Malik, S., Kumar, V., Li, C.-H., Shih, K.-C., Krueger, S., Nieh, M.-P., Bahal, R., "Head on Comparison of Self- and Nano-Assemblies of Gamma Peptide Nucleic Acid Amphiphiles," *Adv. Funct. Mater.* **32**(7), 2109552 (2022). [CHNRNS]
- Mao, Y., Liu, T., Chu, B., "Scattering from Polymer Systems," in "Macromolecular Engineering: From Precise Synthesis to Macroscopic Materials and Applications, Second Edition," edited by Matyjaszewski, K., Gnanou, Y., Hadjichristidis, N., Muthukumar, M. (Wiley, Weinheim, Germany) **4**, Chap. 4, 1 (2022).
- Mao, Y., Hu, L., Ren, Z.J., "Engineered Wood for a Sustainable Future," *Matter* **5**(5), 1326 (2022).
- Martins, M.L., Sacchi, R.L., Lin, X., Matsumoto, R., Popov, I., Cui, J., Kobayashi, T., Tyagi, M., Guo, W., Dai, S., Pruski, M., Cummings, P.T., Sokolov, A.P., Mamontov, E., "Beyond Simple Dilution: Superior Conductivities from Cosolvation of Acetonitrile/LiTFSI Concentrated Solution with Acetone," *J. Phys. Chem. C* **126**(5), 2788 (2022). [CHNRNS]
- Masud, A., Wu, W., Singh, M., Tonny, W., Ammar, A., Sharma, K., Strzalka, J.W., Terlier, T., Douglas, J.F., Karim, A., "Solvent Processing and Ionic Liquid-Enabled Long-Range Vertical Ordering in Block Copolymer Films with Enhanced Film Stability," *Macromolecules* **54**(18), 8512 (2021).
- McCauley, P.J., Kumar, S., Calabrese, M.A., "Criteria Governing Rod Formation and Growth in Nonionic Polymer Micelles," *Langmuir* **37**(40), 11676 (2021). [CHNRNS]
- McColl, K., Griffith, K.J., Dally, R.L., Li, R., Douglas, J.E., Poeppelmeier, K.R., Corà, F., Levin, I., Butala, M.M., "Energy Storage Mechanisms in Vacancy-Ordered Wadsley-Roth Layered Niobates," *J. Mater. Chem. A* **9**(35), 20006 (2021).
- McDannald, A., Frontzek, M., Savici, A.T., Doucet, M., Rodriguez, E.E., Meuse, K., Opsahl-Ong, J., Samarov, D., Takeuchi, I., Ratcliff, W., Kusne, A.G., "On-The-Fly Autonomous Control of Neutron Diffraction via Physics-Informed Bayesian Active Learning," *Appl. Phys. Rev.* **9**(2), 021408 (2022). [CHNRNS]
- McFarlane, J., DiStefano, V.H., Bingham, P.R., Bilheux, H.Z., Cheshire, M.C., Hale, R.E., Hussey, D.S., Jacobson, D.L., Kolbus, L., LaManna, J.M., Perfect, E., Rivers, M., Santodonato, L.J., Anovitz, L.M., "Effect of Fluid Properties on Contact Angles in the Eagle Ford Shale Measured with Spontaneous Imbibition," *ACS Omega* **6**(48), 32618 (2021).
- Michalak, D.J., Unger, B., Lorimer, E., Grishaev, A., Williams, C.L., Heinrich, F., Lösche, M., "Structural and Biophysical Properties of Farnesylated KRas Interacting with the Chaperone SmgGDS-558," *Biophys. J.*, in press.
- Michelman-Ribeiro, A., Robinson, K.A., Silin, V., Kasianowicz, J.J., "Solution Structures of *Bacillus Anthracis* Protective Antigen Proteins using Small Angle Neutron Scattering and Protective Antigen 63 Ion Channel Formation Kinetics," *Toxins* **13**(12), 888 (2021).
- Mills, J., Mondal, P., Wagner, N., "Structure-Property Relationships and State Behavior of Alkali-Activated Aluminosilicate Gels," *Cement Concrete Res.* **151**, 106618 (2022). [CHNRNS]

- Mirzamani, M., Flickinger, M., Dawn, A., Aswal, V., Hammouda, B., Jones, R.L., Smith, E.D., Kumari, H., "Structural Alterations of Branched *versus* Linear Mixed-Surfactant Micellar Systems with the Addition of a Complex Perfume Mixture and Dipropylene Glycol as Cosolvent," *RSC Adv.* **12**(24), 14988 (2022).
- Mirzamani, M., Reeder, R.C., Jarus, C., Aswal, V., Hammouda, B., Jones, R.L., Smith, E.D., Kumari, H., "Effects of a Multicomponent Perfume Accord and Dilution on the Formation of ST2S/CAPB Mixed-Surfactant Microemulsions," *Langmuir* **38**(4), 1334 (2022).
- Mirzamani, M., Flickinger, M., Kharb, S., Jones, R.L., Ananthapadmanabhan, K., Smith, E., Kumari, H., "Investigating the Effect of Dipropylene Glycol and Mixed-Surfactant Concentrations on Perfume Release," *Colloid Surface A*, in press.
- Miyatsu, S., Kofu, M., Shigematsu, A., Yamada, T., Kitagawa, H., Lohstroh, W., Simeoni, G., Tyagi, M., Yamamuro, O., "Quasielastic Neutron Scattering Study on Proton Dynamics Assisted by Water and Ammonia Molecules Confined in MIL-53," *Struct. Dynam.-US* **8**(5), 054501 (2021). [CHNRS]
- Mkam Tsengam, I.K., Omarova, M., Kelley, E.G., McCormick, A., Bothun, G.D., Raghavan, S.R., John, V.T., "Transformation of Lipid Vesicles into Micelles by Adding Nonionic Surfactants: Elucidating the Structural Pathway and the Intermediate Structures," *J. Phys. Chem. B* **126**(11), 2208 (2022). [CHNRS]
- Moon, H.J., Carrillo, J.-M., Leisen, J., Sumpter, B.G., Osti, N.C., Tyagi, M., Jones, C.W., "Understanding the Impacts of Support-Polymer Interactions on the Dynamics of Poly(Ethyleneimine) Confined in Mesoporous SBA-15," *J. Am. Chem. Soc.* **144**(26), 11664 (2022). [CHNRS]
- Morgan, E.E., Evans, H.A., Pilar, K., Brown, C.M., Clément, R.J., Maezono, R., Seshadri, R., Monserrat, B., Cheetham, A.K., "Lattice Dynamics in the NASICON $\text{NaZr}_2(\text{PO}_4)_3$ Solid Electrolyte from Temperature-Dependent Neutron Diffraction, NMR, and Ab Initio Computational Studies," *Chem. Mater.* **34**(9), 4029 (2022).
- Moya, J.M., Lei, S., Clements, E.M., Kengle, C.S., Sun, S., Allen, K., Li, Q., Peng, Y.Y., Husain, A.A., Mitrano, M., Krogstad, M.J., Osborn, R., Puthirath, A.B., Chi, S., Debeer-Schmitt, L., Gaudet, J., Abbamonte, P., Lynn, J.W., Morosan, E., "Incommensurate Magnetic Orders and Topological Hall Effect in the Square-Net Centrosymmetric EuGa_2Al_2 System," *Phys. Rev. Mater.* **6**(7), 074201 (2022).
- Mundy, J.A., Grosso, B.F., Heikes, C.A., Segedin, D.F., Wang, Z., Shao, Y.-T., Dai, C., Goodge, B.H., Meier, Q.N., Nelson, C.T., Prasad, B., Xue, F., Ganschow, S., Muller, D.A., Kourkoutis, L.F., Chen, L.-Q., Ratcliff, W.D., Spaldin, N.A., Ramesh, R., Schlom, D.G., "Liberating a Hidden Antiferroelectric Phase with Interfacial Electrostatic Engineering," *Sci. Adv.* **8**(5), eabg5860 (2022).
- Murray, P.D., Jensen, C.J., Quintana, A., Zhang, J., Zhang, X., Grutter, A.J., Kirby, B.J., Liu, K., "Electrically Enhanced Exchange Bias via Solid-State Magneto-Ionics," *ACS Appl. Mater. Interfaces* **13**(32), 38916 (2021).
- Nagao, M., "Elucidation of the Origin of Two-Dimensional Membrane Viscosity by Mössbauer Time Domain Interferometry and Neutron Spin Echo," *SPring-8/SACLA Info.*, in press. [CHNRS]
- Nagao, M., Kelley, E.G., Faraone, A., Saito, M., Yoda, Y., Kurokuzu, M., Takata, S., Seto, M., Butler, P.D., "Relationship between Viscosity and Acyl Tail Dynamics in Lipid Bilayers," *Phys. Rev. Lett.* **127**(7), 078102 (2021). [CHNRS]
- Nahman-Lévesque, O., Sarenac, D., Cory, D.G., Heacock, B., Huber, M.G., Pushin, D.A., "Generalizing the Quantum Information Model for Dynamic Diffraction," *Phys. Rev. A* **105**(2), 022403 (2022).
- Nakagawa, H., Saio, T., Nagao, M., Inoue, R., Sugiyama, M., Ajito, S., Tominaga, T., Kawakita, Y., "Conformational Dynamics of a Multidomain Protein by Neutron Scattering and Computational Analysis," *Biophys. J.* **120**(16), 3341 (2021). [CHNRS]
- Neer, A.J., Milam-Guerrero, J., Fischer, V.A., Zheng, M., Spence, N.R., Cozzan, C., Gu, M., Rondinelli, J.M., Brown, C.M., Melot, B.C., "Magnetic-Field-Induced Dielectric Anomalies in Cobalt-Containing Garnets," *Inorg. Chem.* **61**(14), 5452 (2022).
- Neil, C.W., Hjelm, R.P., Hawley, M.E., Watkins, E.B., Cockreham, C., Wu, D., Mao, Y., Cheshire, M., Burger, J., Fischer, T.B., Stokes, M.R., Xu, H., "Probing Oil Recovery in Shale Nanopores with Small-Angle and Ultra-Small-Angle Neutron Scattering," *Int. J. Coal Geol.* **253**, 103950 (2022). [CHNRS]
- Neil, C.W., Boukhalfa, H., Xu, H., Ware, S.D., Ortiz, J., Avendaño, S., Harp, D., Broome, S., Hjelm, R.P., Mao, Y., Roback, R., Brug, W.P., Stauffer, P.H., "Gas Diffusion through Variably-Water-Saturated Zeolitic Tuff: Implications for Transport following a Subsurface Nuclear Event," *J. Environ. Radioactivity*, in press. [CHNRS]
- Ngo, V.A., Queralt-Martín, M., Khan, F., Bergdoll, L., Abramson, J., Bezrukov, S.M., Rostovtseva, T.K., Hoogerheide, D.P., Noskov, S.Y., "The Single Residue K12 Governs the Exceptional Voltage Sensitivity of Mitochondrial Voltage-Dependent Anion Channel Gating," *J. Am. Chem. Soc.*, in press.
- Novack, C.A., Anovitz, L.M., Hussey, D.S., LaManna, J.M., Labotka, T.C., "Experimental Limestone Dissolution and Changes in Multiscale Structure using Small- and Ultrasmall-Angle Neutron Scattering," *ACS Earth Space Chem.* **6**(4), 974 (2022). [CHNRS]
- Novak, E., Daemen, L., Ramirez-Cuesta, A.J., Cheng, Y., Smith, R., Egami, T., Jalarvo, N., "Uncovering the Hydride Ion Diffusion Pathway in Barium Hydride via Neutron Spectroscopy," *Sci. Rep.* **12**(1), 6194 (2022). [CHNRS]
- Oberdick, S.D., Borchers, J.A., Krycka, K.L., "Magnetic Correlations of Iron Oxide Nanoparticles as Probed by Polarized SANS in Stretched Magnetic Nanoparticle-Elastomer Composites," *Appl. Phys. Lett.* **120**(5), 052401 (2022). [CHNRS]
- Oh, O., Kim, Y., Kim, D., Hussey, D.S., Lee, S.W., "Phase Retrieval Based on Deep Learning in Grating Interferometer," *Sci. Rep.* **12**(1), 6739 (2022).
- Osti, N.C., Thapaliya, B.P., Matsumoto, R.A., Bansal, A., Lin, X., Cummings, P.T., Tyagi, M., Dai, S., Mamontov, E., "Direct Correlation of the Salt-Reduced Diffusivities of Organic Solvents with the Solvent's Mole Fraction," *J. Phys. Chem. Lett.* **13**(12), 2845 (2022).
- Paddison, J.A.M., Ehlers, G., Cairns, A.B., Gardner, J.S., Petrenko, O.A., Butch, N.P., Khalyavin, D.D., Manuel, P., Fischer, H.E., Zhou, H., Goodwin, A.L., Stewart, J.R., "Suppressed-Moment 2-k Order in the Canonical Frustrated Antiferromagnet $\text{Gd}_2\text{Ti}_2\text{O}_7$," *NPJ Quantum Mater.* **6**, 99 (2021).
- Pan, J., Lee, J., Li, M., Trump, B.A., Lobo, R.F., "Comparative Investigation of Ga- and In-CHA in the Non-Oxidative Ethane Dehydrogenation Reaction," *J. Catalysis*, in press.
- Pandey, S.A., Zhang, C., Ibrahim, D.H., Goldfine, E.A., Wenderott, J.K., dos Reis, R., Paul, R.L., Spanopoulos, I., Kanatzidis, M., Bedzyk, M.J., Dravid, V.P., González, G.B., Haile, S.M., "Hidden Complexity in the Chemistry of Ammonolysis-Derived ' γ - Mo_3N_4 ': An Overlooked Oxynitride Hydride," *Chem. Mater.* **33**(17), 6671 (2021).
- Pang, Y., Hao, L., Wang, Y., "Convolutional Neural Network Analysis of Radiography Images for Rapid Water Quantification in PEM Fuel Cell," *Appl. Energ.*, in press.
- Patil, A., Heil, C.M., Vanthournout, B., Bleuel, M., Singla, S., Hu, Z., Gianneschi, N.C., Shawkey, M.D., Sinha, S.K., Jayaraman, A., Dhinojwala, A., "Structural Color Production in Melanin-Based Disordered Colloidal Nanoparticle Assemblies in Spherical Confinement," *Adv. Opt. Mater.* **10**(5), 2102162 (2022). [CHNRS]

- Pena-Francesch, A., Jung, H., Tyagi, M., Demirel, M.C., "Diffusive Dynamic Modes of Recombinant Squid Ring Teeth Proteins by Neutron Spectroscopy," *Biomacromolecules*, in press. [CHNRNS]
- Peng, S., LaManna, J., Periwal, P., Shevchenko, P., "Water Imbibition and Oil Recovery in Shale: Dynamics and Mechanisms using Integrated Centimeter-to-Nanometer-Scale Imaging," in "Proceedings of the 10th Unconventional Resources Technology Conference," edited by SPE, (SPE Reservoir Evaluation & Engineering, June 2022, Houston, TX), **URTEC-3721559-MS** (2022).
- Perez-Salas, U., Porcar, L., Garg, S., Ayee, M.A.A., Levitan, I., "Effective Parameters Controlling Sterol Transfer: A Time-Resolved Small-Angle Neutron Scattering Study," *J. Membrane Biol.*, in press. [CHNRNS]
- Pickett, P.D., Ma, Y., Lueckheide, M., Mao, Y., Prabhu, V.M., "Temperature Dependent Single-Chain Structure of Poly[3-(Acrylamidopropyl-Dimethyl-Ammonium) Propyl-1-Sulfonate] via Small-Angle Neutron Scattering," *J. Chem. Phys.* **156**(21), 214904 (2022).
- Pokharel, G., Arachchige, H.S., Gao, S., Do, S.-H., Fishman, R.S., Ehlers, G., Qiu, Y., Rodriguez-Rivera, J.A., Stone, M.B., Zhang, H., Wilson, S.D., Mandrus, D., Christianson, A.D., "Spin Dynamics in the Skyrmion-Host Lacunar Spinel GaV_4S_8 ," *Phys. Rev. B* **104**(22), 224425 (2021). [CHNRNS]
- Posey, N.D., Ma, Y., Lueckheide, M., Danischewski, J., Fagan, J.A., Prabhu, V.M., "Tuning Net Charge in Aliphatic Polycarbonates Alters Solubility and Protein Complexation Behavior," *ACS Omega* **6**(35), 22589 (2021). [CHNRNS]
- Potashnikov, D., Caspi, E.N., Pesach, A., Tao, Q., Rosen, J., Sheptyakov, D., Evans, H.A., Ritter, C., Salman, Z., Bonfa, P., Ouisse, T., Barbier, M., Rivin, O., Keren, A., "Magnetic Structure Determination of High-Moment Rare-Earth-Based Laminates," *Phys. Rev. B* **104**(17), 174440 (2021).
- Qian, X., Han, D., Zheng, L., Chen, J., Tyagi, M., Li, Q., Du, F., Zheng, S., Huang, X., Zhang, S., Shi, J., Huang, H., Shi, X., Chen, J., Qin, H., Bernholc, J., Chen, X., Chen, L.-Q., Hong, L., Zhang, Q.M., "High-Entropy Polymer Produces a Giant Electrocaloric Effect at Low Fields," *Nature* **600**(7890), 664 (2021). [CHNRNS]
- Rajendran, M., Queral-Martín, M., Gurnev, P.A., Rosencrans, W.M., Rovini, A., Jacobs, D., Abrantes, K., Hoogerheide, D.P., Bezrukov, S.M., Rostovtseva, T.K., "Restricting α -Synuclein Transport into Mitochondria by Inhibition of α -Synuclein-VDAC Complexation as a Potential Therapeutic Target for Parkinson's Disease Treatment," *Cell. Mol. Life Sci.*, in press.
- Ran, S., Saha, S.R., Liu, I.-L., Graf, D., Paglione, J., Butch, N.P., "Expansion of the High Field-Boosted Superconductivity in UTe_2 under Pressure," *NPJ Quantum Mater.* **6**(1), 75 (2021).
- Ratcliff, W., "Revealing the Symmetry of Materials through Neutron Diffraction," *Symmetry* **14**(6), 1215 (2022).
- Riberolles, S.X.M., Zhang, Q., Gordon, E., Butch, N.P., Ke, L., Yan, J.-Q., McQueeney, R.J., "Evolution of Magnetic Interactions in Sb-Substituted MnBi_2Te_4 ," *Phys. Rev. B* **104**(6), 064401 (2021).
- Riddiford, L.J., Grutter, A.J., Pillsbury, T., Stanley, M., Reifsnnyder Hickey, D., Li, P., Alem, N., Samarth, N., Suzuki, Y., "Understanding Signatures of Emergent Magnetism in Topological Insulator/Ferrite Bilayers," *Phys. Rev. Lett.* **128**(12), 126802 (2022).
- Rios, J., Kabirajafi, M., Gameda, T., Mohammed, R., Xu, J., "Convective Heat Transfer of Ethanol/Polyalphaolefin Nanoemulsion in Mini- and Microchannel Heat Exchangers for High Heat Flux Electronics Cooling," in "Heat Transfer—Design, Experimentation and Applications," edited by Araiz, M. (IntechOpen, London UK) Chap. **9**, 1 (2021).
- Rivas-Barbosa, R., Ruiz-Franco, J., Lara-Peña, M.A., Cardellini, J., Licea-Claverie, A., Camerin, F., Zaccarelli, E., Laurati, M., "Link between Morphology, Structure, and Interactions of Composite Microgels," *Macromolecules* **55**(5), 1834 (2022).
- Romano, C., Bowden, N., Conant, A., Goldblum, B., Huber, P., Link, J., Littlejohn, B., Mumm, H.P., Ochoa-Ricoux, J.P., Prasad, S., Riddle, C., Sonzogno, A., Wieselquist, W., "Nuclear Data to Reduce Uncertainties in Reactor Antineutrino Measurements," Summary Report of the Workshop on Nuclear Data for Reactor Antineutrino Measurements (WoNDRAm), Lawrence Livermore National Laboratory Technical Report, **LLNL-TR-829851**, 1 (2021).
- Romanyukha, A., Consani, K., LaManna, J., Thompson, A., Mintz, J., "Determination of Energy Correction Coefficient for Neutron Albedo Dosimeter. Three Approaches," *Radiat. Meas.*, in press.
- Roos, M.J., Quarterman, P., Ding, J., Wu, M., Kirby, B.J., Zink, B.L., "Magnetization and Antiferromagnetic Coupling of the Interface between a 20 nm $\text{Y}_3\text{Fe}_5\text{O}_{12}$ Film and $\text{Gd}_3\text{Ga}_5\text{O}_{12}$ Substrate," *Phys. Rev. Mater.* **6**(3), 034401 (2022).
- Rubinson, K.A., "Measurement of Enthalpies and Entropies of Activation as a Function of Pairwise Distance for the Pairwise Relative Diffusion of SrI_2 in Water over Lengthscales from 6 Å to 40 Å," *New J. Chem.* **46**(13), 6174 (2022). [CHNRNS]
- Runčevski, T., Brown, C.M., "The Rietveld Refinement Method: Half of a Century Anniversary," *Cryst. Growth Des.* **21**(9), 4821 (2021).
- Ryu, B.K., Fenton, S.M., Nguyen, T.T.D., Helgeson, M.E., Zia, R.N., "Modeling Colloidal Interactions that Predict Equilibrium and Non-Equilibrium States," *J. Chem. Phys.* **156**(22), 224101 (2022). [CHNRNS]
- Sahin, D., Mattes, D., Turkoglu, D.J., "NBSR Power Regulating Control System Upgrade," *T. Am. Nucl. Soc.* **125**(1), 352 (2021).
- Saito, M., Tsuyoshi, Y., Nagao, M., "Synchrotron Mössbauer Time Domain Interferometry Sheds Lights on Dynamics of Atoms and Molecules on Nano to Micro Second Scales," *Butsuri*, in press.
- Sala, G., Mourigal, M., Boone, C., Butch, N.P., Christianson, A.D., Delaire, O., DeSantis, A.J., Hart, C.L., Hermann, R.P., Huegle, T., Kent, D.N., Lin, J.Y., Lumsden, M.D., Manley, M.E., Quirinale, D.G., Stone, M.B., Z, Y., "CHESS: The Future Direct Geometry Spectrometer at the Second Target Station," *Rev. Sci. Instrum.* **93**(6), 065109 (2022).
- Salatto, D., Carrillo, J.-M.Y., Endoh, M.K., Taniguchi, T., Yavitt, B.M., Masui, T., Kishimoto, H., Tyagi, M., Ribbe, A.E., Garcia Sakai, V., Kruteva, M., Sumpter, B.G., Farago, B., Richter, D., Nagao, M., Koga, T., "Structural and Dynamical Roles of Bound Polymer Chains in Rubber Reinforcement," *Macromolecules* **54**(23), 11032 (2021). [CHNRNS]
- Scheie, A., Sanders, M., Gui, X., Qiu, Y., Prisk, T.R., Cava, R.J., Broholm, C., "Beyond Magnons in $\text{Nd}_2\text{ScNbO}_7$: An Ising Pyrochlore Antiferromagnet with All-in-All-Out Order and Random Fields," *Phys. Rev. B* **104**(13), 134418 (2021). [CHNRNS]
- Schneeloch, J.A., Tao, Y., Cheng, Y., Daemen, L., Xu, G., Zhang, Q., Louca, D., "Gapless Dirac Magnons in CrCl_3 ," *NPJ Quantum Mater.* **7**(1), 66 (2022).
- Schneeloch, J.A., Tao, Y., Fernandez-Baca, J.A., Xu, G., Louca, D., "Large Change of Interlayer Vibrational Coupling with Stacking in $\text{Mo}_{1-x}\text{W}_x\text{Te}_2$," *Phys. Rev. B* **105**(1), 014102 (2022).
- Sebti, E., Evans, H.A., Chen, H., Richardson, P.M., White, K.M., Giovine, R., Koirala, K.P., Xu, Y., Gonzalez-Correa, E., Wang, C., Brown, C.M., Cheetham, A.K., Canepa, P., Clément, R.J., "Stacking Faults Assist Lithium-Ion Conduction in a Halide-Based Superionic Conductor," *J. Am. Chem. Soc.* **144**(13), 5795 (2022).

- Senses, E., Kitchens, C.L., Faraone, A., "Viscosity Reduction in Polymer Nanocomposites: Insights from Dynamic Neutron and X-ray Scattering," *J. Polym. Sci.* **60**(7), 1130 (2022). [CHRNS]
- Sharma, V.K., Mukhopadhyay, R., Mohanty, A., García Sakai, V., Tyagi, M., Sarma, D.D., "Influence of the Halide Ion on the A-Site Dynamics in FAPbX_3 ($X = \text{Br}$ and Cl)," *J. Phys. Chem. C* **126**(16), 7158 (2022). [CHRNS]
- Shi, Y., Xie, Y., Cui, H., Ye, Y., Wu, H., Zhou, W., Arman, H., Lin, R.-B., Chen, B., "Highly Selective Adsorption of Carbon Dioxide Over Acetylene in an Ultramicroporous Metal-Organic Framework," *Adv. Mater.* **33**(45), 2105880 (2021).
- Shimizu, R., Cheng, D., Weaver, J.L., Zhang, M., Lu, B., Wynn, T.A., Burger, R., Kim, M.-C., Zhu, G., Meng, Y.S., "Unraveling the Stable Cathode Electrolyte Interface in all Solid-State Thin-Film Battery Operating at 5 V," *Adv. Energy Mater.*, in press.
- Siebeneichler, S., Ovchinnikov, A., Bosch-Santos, B., Cabrera-Pasca, G.A., Flacau, R., Huang, Q., Carbonari, A.W., Ryan, D., Mudring, A.-V., "Magnetic Phase Diagram of the Solid Solution $\text{LaMn}_2(\text{Ge}_{1-x}\text{Si}_x)_2$ ($0 \leq x \leq 1$) Unraveled by Powder Neutron Diffraction," *Sci. Rep.* **12**(1), 9248 (2022).
- Siegfried, P.E., Bhandari, H., Jones, D.C., Ghimire, M.P., Dally, R.L., Poudel, L., Bleuel, M., Lynn, J.W., Mazin, I.I., Ghimire, N.J., "Magnetization-Driven Lifshitz Transition and Charge-Spin Coupling in the Kagome Metal YMn_6Sn_6 ," *Commun. Phys.* **5**, 58 (2022). [CHRNS]
- Singh, D.K., Ernst, A., Dugaev, V., Chen, Y., Gunasekera, J., "Quantum Magnetic Properties and Metal-to-Insulator Transition in Chemically Doped Calcium Ruthenate Perovskite," *Phys. Status Solidi B* **259**(4), 2100503 (2022). [CHRNS]
- Sinha, N.J., Shi, Y., Tang, Y., Kloxin, C.J., Saven, J.G., Faraone, A., Jensen, G.V., Pochan, D.J., "Intramolecular Structure and Dynamics in Computationally Designed Peptide-Based Polymers Displaying Tunable Chain Stiffness," *Phys. Rev. Mater.* **5**(9), 095601 (2021). [CHRNS]
- Sinha, N.J., Guo, R., Misra, R., Fagan, J., Faraone, A., Kloxin, C.J., Saven, J.G., Jensen, G.V., Pochan, D.J., "Colloid-Like Solution Behavior of Computationally Designed Coiled Coil Bundlers," *J. Colloid Interf. Sci.* **606**(Part 2), 1974 (2022). [CHRNS]
- Sjöblom, R., Hjärthner-Holdar, E., Pearce, C.I., Weaver, J.L., Ogenhall, E., McCloy, J.S., Marcial, J., Vicenzi, E.P., Schweiger, M.J., Kruger, A.A., "Assessment of the Reason for the Vitrification of a Wall at a Hillfort. The Example of Broborg in Sweden," *J. Archaeol. Sci. Rep.* **43**, 103459 (2022).
- Skaggs, C.M., Siegfried, P.E., Kang, C.-J., Brown, C.M., Chen, F., Ma, L., Ehrlich, S.N., Xin, Y., Croft, M., Xu, W., Lapidus, S.H., Ghimire, N.J., Tan, X., "Iridate Li_8IrO_6 : An Antiferromagnetic Insulator," *Inorg. Chem.* **60**(22), 17201 (2021).
- Skipov, A.V., Soloninin, A.V., Valeeva, A.A., Gusev, A.I., Rempel, A.A., Wu, H., Udovic, T.J., "Hydrogen in Nonstoichiometric Cubic Titanium Monoxides: X-ray and Neutron Diffraction, Neutron Vibrational Spectroscopy and NMR Studies," *J. Alloy Compd.* **887**, 161353 (2021).
- Skipov, A.V., Babanova, O.A., Skoryunov, R.V., Soloninin, A.V., Udovic, T.J., "Anion Reorientations and Cation Diffusion in a Carbon-Substituted Sodium *Nido*-Borate $\text{Na-79-C}_2\text{B}_9\text{H}_{12}$: ^1H and ^{23}Na NMR Studies," *Z. Phys. Chem.* **236**(6-8), 839 (2022).
- Slim, A.H., Shi, W.H., Samghabadi, F.S., Faraone, A., Marciel, A.B., Poling-Skutvik, R., Conrad, J.C., "Electrostatic Repulsion Slows Relaxations of Polyelectrolytes in Semidilute Solutions," *ACS Macro Lett.* **11**(7), 854 (2022). [CHRNS]
- Smith, E.M., Benton, O., Yahne, D.R., Placke, B., Schäfer, R., Gaudet, J., Dudemaine, J., Fitterman, A., Beare, J., Wildes, A.R., Bhattacharya, S., DeLazzer, T., Buhariwalla, C.R.C., Butch, N.P., Movshovich, R., Garrett, J.D., Marjerrison, C.A., Clancy, J.P., Kermarrec, E., Luke, G.M., Bianchi, A.D., Ross, K.A., Gaulin, B.D., "Case for a $\text{U}(1)_\pi$ Quantum Spin Liquid Ground State in the Dipole-Octupole Pyrochlore $\text{Ce}_2\text{Zr}_2\text{O}_7$," *Phys. Rev. X* **12**(2), 021015 (2022).
- Snow, W.M., Haddock, C., Heacock, B., "Searches for Exotic Interactions using Neutrons," *Symmetry* **14**(1), 10 (2022).
- Sonje, J., Thakral, S., Krueger, S., Suryanarayanan, R., "Reversible Self-Association in Lactate Dehydrogenase during Freeze-Thaw in Buffered Solutions using Neutron Scattering," *Mol. Pharmaceut.* **18**(12), 4459 (2021).
- Soto-Bustamante, F., Valadez-Pérez, N.E., Liu, Y., Castañeda-Priego, R., Laurati, M., "Clusters in Colloidal Dispersions with a Short-Range Depletion Attraction: Thermodynamic Identification and Morphology," *J. Colloid Interf. Sci.* **618**, 442 (2022).
- Spittle, S., Poe, D., Doherty, B., Kolodziej, C., Heroux, L., Haque, M.A., Squire, H., Cosby, T., Zhang, Y., Fraenza, C., Bhattacharyya, S., Tyagi, M., Peng, J., Elgammal, R.A., Zawodzinski, T., Tuckerman, M., Greenbaum, S., Gurkan, B., Burda, C., Dadmun, M., Maginn, E.J., Sangoro, J., "Evolution of Microscopic Heterogeneity and Dynamics in Choline Chloride-Based Deep Eutectic Solvents," *Nat. Commun.* **13**(1), 219 (2022). [CHRNS]
- Steinhardt, W., Maksimov, P.A., Dissanayake, S., Shi, Z., Butch, N.P., Graf, D., Podlesnyak, A., Liu, Y., Zhao, Y., Xu, G., Lynn, J.W., Marjerrison, C., Chernyshev, A.L., Haravifard, S., "Phase Diagram of YbZnGaO_4 in Applied Magnetic Field," *NPJ Quantum Mater.* **6**, 78 (2021).
- Sun, F., Yang, Y., Zhao, S., Wang, Y., Tang, M., Huang, Q., Ren, Y., Su, H., Wang, B., Zhao, N., Guo, X., Yu, H., "Local Li^+ Framework Regulation of a Garnet-Type Solid-State Electrolyte," *ACS Energy Lett.*, in press.
- Sun, N., Jin, Y., Wang, H., Yu, B., Wang, R., Wu, H., Zhou, W., Jiang, J., "Photoresponsive Covalent Organic Frameworks with Diarylethene Switch for Tunable Singlet Oxygen Generation," *Chem. Mater.* **34**(4), 1956 (2022).
- Sweeney, D.T., Krueger, S., Sen, K., Hackett, J.C., "Structures and Dynamics of Anionic Lipoprotein Nanodiscs," *J. Phys. Chem. B* **126**(15), 2850 (2022). [CHRNS]
- Takatsu, H., Goto, K., Sato, T.J., Lynn, J.W., Matsubayashi, K., Uwatoko, Y., Higashinaka, R., Matsuhira, K., Hiroi, Z., Kadowaki, H., "Universal Dynamics of Magnetic Monopoles in Two-Dimensional Kagomé Ice," *J. Phys. Soc. Jpn.* **90**(12), 123705 (2021).
- Tang, N., Liao, J.-W., Chui, S.-T., Ziman, T., Grutter, A.J., Liu, K., Lai, C.-H., Kirby, B.J., Gilbert, D.A., "Controlling Magnetic Configuration in Soft-Hard Bilayers Probed by Polarized Neutron Reflectometry," *APL Mater.* **10**(1), 011107 (2022).
- Tao, Y., Abernathy, D.L., Chen, T., Yildirim, T., Yan, J., Zhou, J., Goodenough, J.B., Louca, D., "Dynamics of Phase Transitions in YVO_3 Investigated via Inelastic Neutron Scattering and First-Principles Calculations," *Neutron News*, in press.
- Tao, Y., Abernathy, D.L., Chen, T., Yildirim, T., Yan, J., Zhou, J., Goodenough, J.B., Louca, D., "Lattice and Magnetic Dynamics in the YVO_3 Mott Insulator Studied by Neutron Scattering and First-Principles Calculations," *Phys. Rev. B* **100**(9), 094412 (2022).
- Testa, L., Babkevich, P., Kato, Y., Kimura, K., Favre, V., Rodriguez-Rivera, J.A., Ollivier, J., Raymond, S., Kimura, T., Motome, Y., Normand, B., Rønnow, H.M., "Spin Dynamics in the Square-Lattice Cupola System $\text{Ba}(\text{TiO})\text{Cu}_4(\text{PO}_4)_4$," *Phys. Rev. B* **105**(21), 214406 (2022). [CHRNS]

- Thorsen, M.K., Lai, A., Lee, M.W., Hoogerheide, D.P., Wong, G.C.L., Freed, J.H., Heldwein, E.E., "Highly Basic Clusters in the Herpes Simplex Virus 1 Nuclear Egress Complex Drive Membrane Budding by Inducing Lipid Ordering," *mBio* **12**(4), e01548-21 (2021).
- Torres, J.R., Buck, Z.N., Kaiser, H., Mamontov, E., Tyagi, M., Hansen, F.Y., Herwig, K.W., Daemen, L., Kidder, M.K., Taub, H., "Study of the Water Dynamics near Hydrophilic, Nanostructured CuO Surfaces by Quasielastic and Inelastic Neutron Scattering," *AIP Adv.* **12**(6), 065124 (2022). [CHNRNS]
- Upreti, P., Krogstad, M., Haley, C., Anitescu, M., Rao, V., Poudel, L., Chmaissem, O., Rosenkranz, S., Osborn, R., "Order-Disorder Transitions in $(\text{Ca}_x\text{Sr}_{1-x})\text{Rh}_4\text{Sn}_{13}$," *Phys. Rev. Lett.* **128**(9), 095701 (2022).
- Valeeva, A.A., Gusev, A.I., "Placement of H Atoms in the Crystal Lattice of Cubic Titanium Oxyhydride: Simulation and Diffraction Experiment," *Mendelev Commun.* **32**(3), 302 (2022).
- Vicenzi, E.P., Lam, T., Weaver, J.L., Herzing, A.A., McCloy, J.S., Sjöblom, R., Pearce, C.I., "Major to Trace Element Imaging and Analysis of Iron Age Glasses using Stage Scanning in the Analytical Dual Beam Microscope (Tandem)," *Herit. Sci.* **10**(1), 90 (2022).
- Wahane, A., Malik, S., Shih, K.-C., Gaddam, R.R., Chen, C., Liu, Y., Nieh, M.-P., Vikram, A., Bahal, R., "Dual-Modality Poly-L-Histidine Nanoparticles to Deliver Peptide Nucleic Acids and Paclitaxel for In Vivo Cancer Therapy," *ACS Appl. Mater. Interfaces* **13**(38), 45244 (2021).
- Wang, F., Blanc, L.E., Li, Q., Faraone, A., Ji, X., Chen-Mayer, H.H., Paul, R.L., Dura, J.A., Hu, E., Xu, K., Nazar, L.F., Wang, C., "Quantifying and Suppressing Proton Intercalation to Enable High-Voltage Zn-Ion Batteries," *Adv. Energy Mater.* **11**(41), 2102016 (2021).
- Wang, Z.-C., Been, E., Gaudet, J., Alqasseri, G.M.A., Fruhling, K., Yao, X., Stuhr, U., Zhu, Q., Ren, Z., Cui, Y., Jia, C., Moritz, B., Chowdhury, S., Devereaux, T., Tafti, F., "Anisotropy of the Magnetic and Transport Properties of EuZn_2As_2 ," *Phys. Rev. B* **105**(16), 165122 (2022).
- Wang, Z.-B., Mao, Y.-M., Li, X.-K., Li, Y.-G., Jarumaneeroj, C., Thitisak, B., Tiyaipiboonchaiya, P., Rungswang, W., Hsiao, B.S., "The Influence of Ethyl Branch on Formation of Shish-Kebab Crystals in Bimodal Polyethylene under Shear at Low Temperature," *Chinese J. Polym. Sci.* **39**(8), 1050 (2021).
- Watanabe, Y., Hyeon-Deuk, K., Yamamoto, T., Yabuuchi, M., Karakulina, O.M., Noda, Y., Kurihara, T., Chang, I.-Y., Higashi, M., Tomita, O., Tassel, C., Kato, D., Xia, J., Goto, T., Brown, C.M., Shimoyama, Y., Ogiwara, N., Hadermann, J., Abakumov, A.M., Uchida, S., Abe, R., Kageyama, H., "Polyoxocationic Antimony Oxide Cluster with Acidic Protons," *Sci. Adv.* **8**(24), eabm5379 (2022).
- Weaver, J.L., Job, A., Manandhar, K., Takeuchi, I., Downing, R.G., "Energy Broadening of Neutron Depth Profiles by Thin Polyamide Films," *J. Radioanal. Nucl. Ch.*, in press. [CHNRNS]
- Weaver, J., Job, A., "Adjustment to the Light Element Areal Concentration Calculation for Neutron Depth Profiles," *Microsc. Microanal.* **27**(Suppl 1), 2886 (2021). [CHNRNS]
- Wei, D.S., Saykin, D., Miller, O.Y., Ran, S., Saha, S.R., Agterberg, D.F., Schmalian, J., Butch, N.P., Paglione, J., Kapitulnik, A., "Interplay between Magnetism and Superconductivity in UTe_2 ," *Phys. Rev. B* **105**(2), 024521 (2022).
- Wissink, M., Goldenberger, K., Ferguson, L., Zhang, Y., Bilheux, H., LaManna, J., Jacobson, D., Kass, M., Finney, C., Willocks, J., "Fabrication of Black Body Grids by Thick Film Printing for Quantitative Neutron Imaging," *J. Imaging* **8**(6), 164 (2022).
- Wolf, C.M., Guio, L., Scheiwiler, S., Pakhnyuk, V., Luscombe, C., Pozzo, L.D., "Strategies for the Development of Conjugated Polymer Molecular Dynamics Force Fields Validated with Neutron and X-ray Scattering," *ACS Polymers Au* **1**(3), 134 (2021). [CHNRNS]
- Wong-Ng, W., Yang, Y., Lan, Y., Liu, G., Kafle, A., Liu, W., Hou, J., Windover, D., Huang, Q., Krylyuk, S., Kaduk, J.A., "Powder X-ray Structural Analysis and Bandgap Measurements for $(\text{Ca}_x\text{Sr}_{2-x})\text{MnWO}_6$ ($x = 0.25, 0.5, 0.75, 1.5, 1.75$)," *Powder Diff.*, in press.
- Wu, S., Xu, Z., Haley, S.C., Weber, S.F., Acharya, A., Maniv, E., Qiu, Y., Aczel, A.A., Settineri, N.S., Neaton, J.B., Analytis, J.G., Birgeneau, R.J., "Highly Tunable Magnetic Phases in Transition-Metal Dichalcogenide $\text{Fe}_{1/3+\delta}\text{NbS}_2$," *Phys. Rev. X* **12**(2), 021003 (2022). [CHNRNS]
- Xi, Y., Zhang, F., Ma, Y., Prabhu, V.M., Liu, Y., "Finely Tunable Dynamical Coloration using Bicontinuous Micrometer-Domains," *Nat. Commun.* **13**(1), 3619 (2022). [CHNRNS]
- Xu, A.Y., Rinee, K.C., Stemple, C., Castellanos, M.M., Bakshi, K., Krueger, S., Curtis, J.E., "Counting the Water: Characterize the Hydration Level of Aluminum Adjuvants using Contrast Matching Small-Angle Neutron Scattering," *Colloid Surface A*, in press.
- Xu, A.Y., Clark, N.J., Pollastrini, J., Espinoza, M., Kim, H.-J., Kanapuram, S., Kerwin, B., Treuheit, M.J., Krueger, S., McAuley, A., Curtis, J.E., "Effects of Monovalent Salt on Protein-Protein Interactions of Dilute and Concentrated Monoclonal Antibody Formulations," *Antibodies* **11**(2), 24 (2022). [CHNRNS]
- Yahne, D.R., Pereira, D., Jaubert, L.D.C., Sanjeeva, L.D., Powell, M., Kolis, J.W., Xu, G., Enjalran, M., Gingras, M.J.P., Ross, K.A., "Understanding Reentrance in Frustrated Magnets: The Case of the $\text{Er}_2\text{Sn}_2\text{O}_7$ Pyrochlore," *Phys. Rev. Lett.* **127**(27), 277206 (2021).
- Yanez, W., Ou, Y., Xiao, R., Koo, J., Held, J.T., Ghosh, S., Rable, J., Pillsbury, T., González Delgado, E., Yang, K., Chamorro, J., Grutter, A.J., Quarterman, P., Richardella, A., Sengupta, A., McQueen, T., Borchers, J.A., Mkhyan, K.A., Yan, B., Samarth, N., "Spin and Charge Interconversion in Dirac-Semimetal Thin Films," *Phys. Rev. Appl.* **16**(5), 054031 (2021).
- Yang, C., Wu, Q., Xie, W., Zhang, X., Brozena, A., Zheng, J., Garaga, M.N., Ko, B.H., Mao, Y., He, S., Gao, Y., Wang, P., Tyagi, M., Jiao, F., Briber, R., Albertus, P., Wang, C., Greenbaum, S., Hu, Y.-Y., Isogai, A., Winter, M., Xu, K., Qi, Y., Hu, L., "Copper-Coordinated Cellulose Ion Conductors for Solid-State Batteries," *Nature* **598**(7882), 590 (2021). [CHNRNS]
- Yin, X., Hewitt, D.R.O., Zheng, B., Yu, X., Carr, A.J., Grubbs, R.B., Bhatia, S.R., "Aqueous Assembly and Hydrogel Rheology of Sustainable Glyoxylate-Based Copolymers," *ACS Appl. Polym. Mater.*, in press. [CHNRNS]
- Yoshimune, W., Harada, M., "Temperature-Induced Shear-Thinning in Catalyst Inks," *Electrochem. Commun.* **130**, 107099 (2021).
- Yoshimune, W., Kato, S., Harada, M., "In Situ Small-Angle Neutron Scattering Analysis of Water Evaporation from Porous Exhaust-Gas-Catalyst Supports," *ACS Appl. Mater. Interfaces* **14**(15), 17396 (2022).
- Yu, B., Geng, S., Wang, H., Zhou, W., Zhang, Z., Chen, B., Jiang, J., "A Solid Transformation into Carboxyl Dimers Based on a Robust Hydrogen-Bonded Organic Framework for Propyne/Propylene Separation," *Angew. Chem. Int. Edit.* **60**(49), 25942 (2021).
- Yuan, X., Krueger, S., Shalaev, E., "Protein-Surfactant and Protein-Protein Interactions during Freeze and Thaw: A Small-Angle Neutron Scattering Study of Lysozyme Solutions with Polysorbate and Poloxamer," *J. Pharm. Sci.*, in press.

- Yusuf, M., LaManna, J., Paul, P., Agyeman-Budu, D., Toney, M., Weker, J., "Ex-Situ Li Plating Detection on Graphite Anodes in Extremely Fast-Charged Lithium-Ion Batteries using Simultaneous Neutron and X-ray Tomography," *Microsc. Microanal.* **27**(Suppl 1), 2732 (2021).
- Zajdel, P., Madden, D.G., Babu, R., Tortora, M., Mirani, D., Tsyren, N.N., Bartolomé, L., Amayuelas, E., Fairen-Jimenez, D., Lowe, A.R., Chorążewski, M., Leao, J.B., Brown, C.M., Bleuel, M., Stoudenets, V., Casciola, C.M., Echeverría, M., Bonilla, F., Grancini, G., Meloni, S., Grosu, Y., "Turning Molecular Springs into Nano-Shock Absorbers: The Effect of Macroscopic Morphology and Crystal Size on the Dynamic Hysteresis of Water Intrusion-Extrusion into-from Hydrophobic Nanopores," *ACS Appl. Mater. Interfaces* **14**(23), 26699 (2022). [CHNRNS]
- Zhai, Y., Luo, P., Waller, J., Self, J.L., Harriger, L.W., Z, Y., Faraone, A., "Dynamics of Molecular Associates in Methanol/Water Mixtures," *Phys. Chem. Chem. Phys.* **24**(4), 2287 (2022). [CHNRNS]
- Zhang, H.R., Liu, D.M., Zhang, Z.L., Wang, S.B., Yue, M., Huang, Q.Z., Lynn, J.W., "The Correlation between the Covalent Bonds and Magnetocaloric Properties of the $Mn_{2-x}Fe_xP_{1-y}Ge_{1-y}M_z$ Compounds," *J. Appl. Phys.* **130**(13), 133901 (2021).
- Zhang, L., Liu, Z., Yang, C., García Sakai, V., Tyagi, M., Hong, L., "Conduction Mechanism in Graphene Oxide Membranes with Varied Water Content: From Proton Hopping Dominant to Ion Diffusion Dominant," *ACS Nano*, in press. [CHNRNS]
- Zhang, R., Liu, S., Fan, L., Blach, T.P., Sang, G., "Unraveling High-Pressure Gas Storage Mechanisms in Shale Nanopores through SANS," *Environ. Sci. Nano* **8**(9), 2706 (2021). [CHNRNS]
- Zhang, S., Panda, D.K., Yadav, A., Zhou, W., Saha, S., "Effects of Intervalence Charge Transfer Interaction between π -Stacked Mixed Valent Tetrathiafulvalene Ligands on the Electrical Conductivity of 3D Metal-Organic Frameworks," *Chem. Sci.* **12**(40), 13379 (2021).
- Zhang, W., Ma, Y., Posey, N.D., Lueckheide, M.J., Prabhu, V.M., Douglas, J.F., "Combined Simulation and Experimental Study of Polyampholyte Solution Properties: Effects of Charge Ratio, Hydrophobic Groups, and Polymer Concentration," *Macromolecules*, in press.
- Zhang, X.H., Gao, T.R., Fang, L., Fackler, S., Borchers, J.A., Kirby, B.J., Maranville, B.B., Lofland, S.E., N'Diaye, A.T., Arenholz, E., Ullah, A., Cui, J., Skomski, R., Takeuchi, I., "Interfacial Magnetic Vortex Formation in Exchange-Coupled Hard-Soft Magnetic Bilayers," *J. Magn. Magn. Mater.*, in press.
- Zhang, X., Jiang, F., Torres-Luna, C., Nishiyama, Y., Briber, R.M., Wang, H., "Solvent-Assisted Fractionation of Oligomeric Cellulose and Reversible Transformation of Cellulose II and IV," *ACS Biomater. Sci. Eng.* **7**(10), 4792 (2021).
- Zhang, X., Mao, Y., Briber, R.M., "Efficient Production of Oligomeric Chitin with Narrow Distributions of Degree of Polymerization using Sonication-Assisted Phosphoric Acid Hydrolysis," *Carbohydr. Polym.* **276**, 118736 (2022).
- Zhang, X., Lin, R.-B., Wu, H., Huang, Y., Ye, Y., Duan, J., Zhou, W., Li, J.-R., Chen, B., "Maximizing Acetylene Packing Density for Highly Efficient C_2H_2/CO_2 Separation through Immobilization of Amine Sites within a Prototype MOF," *Chem. Eng. J.* **431**(Part 2), 134184 (2022).
- Zhang, Y., He, Z., Alexandridis, P., Tsiannou, M., "Polymeric Surfactant Micelle Structure Modulated by Ionic Liquids," *J. Mol. Liq.* **346**, 118195 (2022). [CHNRNS]
- Zhao, B., Lee, C., Lee, J.K., Fahy, K.F., LaManna, J.M., Baltic, E., Jacobson, D.L., Hussey, D.S., Bazylak, A., "Superhydrophilic Porous Transport Layer Enhances Efficiency of Polymer Electrolyte Membrane Electrolyzers," *Cell Rep. Phys. Sci.* **2**(10), 100580 (2021).
- Zheng, J., Wahiduzzaman, M., Barpaga, D., Trump, B.A., Gutiérrez, O.Y., Thallapally, P., Ma, S., McGrail, B.P., Maurin, G., Motkuri, R.K., "Porous Covalent Organic Polymers for Efficient Fluorocarbon-Based Adsorption Cooling," *Angew. Chem. Int. Edit.* **60**(33), 18037 (2021).
- Zheng, L., Liu, Z., Zhang, Q., Li, S., Huang, J., Zhang, L., Zan, B., Tyagi, M., Cheng, H., Zuo, T., García Sakai, V., Yamada, T., Yang, C., Tan, P., Jiang, F., Chen, H., Zhuang, W., Hong, L., "Universal Dynamical Onset in Water at Distinct Material Interfaces," *Chem. Sci.* **13**(15), 4341 (2022). [CHNRNS]
- Zimudzi, T.J., Sheffield, S.E., Feldman, K.E., Beaucage, P.A., DeLongchamp, D.M., Kushner, D.I., Stafford, C.M., Hickner, M.A., "Orientation of Thin Polyamide Layer-by-Layer Films on Non-Porous Substrates," *Macromolecules* **54**(24), 11296 (2021).
- Zoghlin, E., Schmeier, J., Holgate, C., Dally, R., Liu, Y., Laurita, G., Wilson, S.D., "Evaluating the Effects of Structural Disorder on the Magnetic Properties of $Nd_zZr_{2-z}O_7$," *Phys. Rev. Mater.* **5**(8), 084403 (2021).
- Zorn, R., Szymoniak, P., Kolmangadi, M.A., Malpass-Evans, R., McKeown, N.B., Tyagi, M., Böhring, M., Schönhals, A., "Low Frequency Vibrations and Diffusion in Disordered Polymers Bearing an Intrinsic Microporosity as Revealed by Neutron Scattering," *Crystals* **11**(12), 1482 (2021). [CHNRNS]
- Zou, H., Cui, Y., Wang, X., Zhang, Z., Yang, J., Xu, G., Okutani, A., Hagiwara, M., Matsuda, M., Wang, G., Mussardo, G., Hódsági, K., Kormos, M., He, Z., Kimura, S., Yu, R., Yu, W., Ma, J., Wu, J., "E_g Spectra of Quasi-One-Dimensional Antiferromagnet $BaCo_2V_2O_8$ under Transverse Field," *Phys. Rev. Lett.* **127**(7), 077201 (2021).

Instruments and Contacts

(name, tel. 301-975-xxxx, email)

High resolution powder diffractometer (BT-1):

- H. Wu, 2387, hui.wu@nist.gov
- Q. Z. Huang, 6164, qing.huang@nist.gov
- C. M. Brown, 5134, craig.brown@nist.gov

Engineering diffractometer (BT-8):

- T. Gnäupel-Herold, 5380, thomas.gnaeupel-herold@nist.gov

vSANS instrument (NG-3) (CHRS):

- E. Kelley, 8584, elizabeth.kelley@nist.gov
- Y. Liu, 6235, yun.liu@nist.gov
- J. Gaudet, 5010, jonathon.gaudet@nist.gov
- R. P. Murphy, 8544, ryan.murphy@nist.gov
- C. Gagnon, 2020, cedric.gagnon@nist.gov

30-m SANS instrument (NG-B):

- Y. Mao, 6017, yimin.mao@nist.gov
- S. Krueger, 6734, susan.krueger@nist.gov
- P. Beaucage, 8367, peter.beaucage@nist.gov
- P. D. Butler, 2028, paul.butler@nist.gov

10-m SANS instrument (NG-B) (nSoft):

- R. Jones, 4624, ronald.jones@nist.gov
- K. Weigandt, 8396, kathleen.weigandt@nist.gov
- T. Martin, 8866, tyler.martin@nist.gov
- P. Beaucage, 8367, peter.beaucage@nist.gov

uSANS, Perfect Crystal SANS (BT-5):

- J. G. Barker, 6732, john.barker@nist.gov
- P. D. Butler, 2028, paul.butler@nist.gov

30-m SANS instrument (NG-7):

- S. Teixeira, 4404, susana.marujoteixeira@nist.gov
- J. Gaudet, 5010, jonathon.gaudet@nist.gov
- J. G. Barker, 6732, john.barker@nist.gov
- J. R. Krzywon, 6650, jkrzywon@nist.gov

CANDOR, White-beam reflectometer/diffractometer (CHRS):

- A. Grutter, 4198, alexander.grutter@nist.gov
- D. Hoogerheide, 8839, david.hoogerheide@nist.gov
- B. Maranville, 6034, brian.maranville@nist.gov
- C. F. Majkrzak, 5251, charles.majkrzak@nist.gov

MAGIK, Off-Specular Reflectometer (NG-D):

- J. A. Dura, 6251, joseph.dura@nist.gov
- F. Heinrich, 4507, frank.heinrich@nist.gov

Polarized Beam Reflectometer/Diffractometer (NG-D):

- C. F. Majkrzak, 5251, cmajkrzak@nist.gov
- J. A. Borchers, 6597, julie.borchers@nist.gov

Neutron reflectometer-horizontal sample (NG-7):

- S. K. Satija, 5250, satija@nist.gov

HFBS, High-flux backscattering spectrometer (NG-2) (CHRS):

- M. Tyagi, 2046, madhusudan.tyagi@nist.gov
- R. Azuah, 5604, richard.azuah@nist.gov

NSE, Neutron spin echo spectrometer (NG-A) (CHRS):

- A. Faraone, 5254, antonio.faraone@nist.gov
- M. Nagao, 5505, michihiro.nagao@nist.gov

MACS, Multi-angle crystal spectrometer (BT-9) (CHRS):

- J. A. Rodriguez-Rivera, 6019, jose.rodriguez@nist.gov
- Y. Qiu, 3274, yiming.qiu@nist.gov

Double-focusing triple-axis Spectrometer (BT-7):

- Y. Zhao, 2164, yang.zhao@nist.gov
- R. Dally, 8369, rebecca.dally@nist.gov
- J. W. Lynn, 6246, jeff.lynn@nist.gov

SPINS, Spin-polarized triple-axis spectrometer (NG-5):

- G. Xu, 4144, guangyong.xu@nist.gov

Triple-axis spectrometer (BT-4):

- W. Ratcliff, 4316, william.ratcliff@nist.gov

FANS, Filter-analyzer neutron spectrometer (BT-4):

- C. M. Brown, 5134, craig.brown@nist.gov

DCS, Disk-chopper time-of-flight spectrometer (NG-4):

- N. Butch, 4863, nicholas.butch@nist.gov
- W. Zhou, 8169, wei.zhou@nist.gov
- C. M. Brown, 5134, craig.brown@nist.gov

Cold neutron depth profiling (NG-A):

- J. Weaver, 6311, jamie.weaver@nist.gov

Cold-neutron prompt-gamma neutron activation analysis (NG-D):

- R. L. Paul, 6287, rpaul@nist.gov
- H. H. Chen-Mayer, 5595, heather.chen-mayer@nist.gov

Thermal-neutron prompt-gamma activation analysis (VT-5):

- R. L. Paul, 6287, rpaul@nist.gov

Other activation analysis facilities:

- N. Sharp, 3926, nicholas.sharp@nist.gov
- R. L. Paul, 6287, rpaul@nist.gov

Thermal Neutron Imaging Facility (BT-2):

- J. LaManna, 6809, jacob.lamanna@nist.gov
- D. Jacobson, 6207, david.jacobson@nist.gov
- E. Baltic, 4842, eli.baltic@nist.gov
- D. Hussey, 6465, daniel.hussey@nist.gov

Cold Neutron Imaging Instrument (NG-6):

- D. Hussey, 6465, daniel.hussey@nist.gov
- E. Baltic, 4842, eli.baltic@nist.gov
- D. Jacobson, 6207, david.jacobson@nist.gov
- J. LaManna, 6809, jacob.lamanna@nist.gov

Neutron interferometer (NG-7):

- M. Huber, 5641, michael.huber@nist.gov
- S. Hoogerheide, 8582, shannon.hoogerheide@nist.gov

Quantum-based neutron interferometer facility (NG-7):

- M. Huber, 5641, michael.huber@nist.gov
- S. Hoogerheide, 8582, shannon.hoogerheide@nist.gov

Fundamental neutron physics station (NG-C):

- S. Hoogerheide, 8582, shannon.hoogerheide@nist.gov
- H. P. Mumm, 8355, hans.mumm@nist.gov
- M. S. Dewey, 4843, maynard.dewey@nist.gov
- J. Nico, 4663, jeffrey.nico@nist.gov

PhAND: Advanced Neutron Detector Development (NG-6a):

- H. P. Mumm, 8355, hans.mumm@nist.gov
- C. B. Shahi, 8194, chandra.shahi@nist.gov

α - γ : absolute neutron counter (NG-6m):

- M. S. Dewey, 4843, maynard.dewey@nist.gov
- H. P. Mumm, 8355, hans.mumm@nist.gov

Grating interferometer for fundamental physics (NG-6u):

- M. G. Huber, 5641, michael.huber@nist.gov
- D. Hussey, 6465, daniel.hussey@nist.gov

Theory and modeling:

- J. E. Curtis, 3959, joseph.curtis@nist.gov
- T. Yildirim, 6228, taner@nist.gov

Neutron test station (PHADES):

- R. Erwin, 6245, ross.erwin@nist.gov
- S. Watson, 6232, shannon.watson@nist.gov

Instruments under development:

SPINS-II:

- L. Harriger, 8360, leland.harriger@nist.gov

NIST Center For Neutron Research Contacts

Copies of annual reports, facility information, user information, and research proposal guidelines are available electronically.

Please visit our website: <http://www.ncnr.nist.gov>

For a paper copy of this report:

Steve Kline
301-975-6243
steven.kline@nist.gov

For general information on the facility:

Rob Dimeo
301-975-6210
robert.dimeo@nist.gov

Dan Neumann
301-975-5252
dan.neumann@nist.gov

For information on visiting the facility and/or user access questions:

Julie Keyser
301-975-8200
julie.keyser@nist.gov

Mary Ann FitzGerald
301-975-8200
maryann.fitzgerald@nist.gov

Becky Ogg
301-975-8200
rebecca.ogg@nist.gov

For information on performing research at the facility:

Yamali Hernandez
301-975-5295
yamali.hernandez@nist.gov

Facility address:

NIST Center for Neutron Research
National Institute of Standards and Technology
100 Bureau Drive, Mail Stop 6100
Gaithersburg, MD 20899-6100 USA

NIST
**National Institute of
Standards and Technology**
U.S. Department of Commerce

**NIST CENTER FOR
NEUTRON RESEARCH**

National Institute of
Standards and Technology
100 Bureau Drive, MS 6100
Gaithersburg, MD 20899-6100

www.ncnr.nist.gov

